REGULATION OF NUMERICAL DIFFUSION FOR COMPRESSIBLE-FLOW COMPUTATIONS

A thesis

submitted in partial fulfillment of the

requirements for the degree of

Doctor of Philosophy

by

Paragmoni Kalita

(Roll no. 10610301)

DEPARTMENT OF MECHANICAL ENGINEERING

INDIAN INSTITUTE OF TECHNOLOGY GUWAHATI

December 2017

CERTIFICATE

This is certified that the work contained in the thesis entitled **Regulation of Numerical Diffusion for Compressible-Flow Computations** and authored by **Paragmoni Kalita**, a student in the Department of Mechanical Engineering, Indian Institute of Technology Guwahati for the award of the degree of Doctor of Philosophy has been carried out under my supervision and that this work has not been submitted elsewhere for a degree.

Dr. Anoop Kumar Dass
Professor
Department of Mechanical Engineering
Indian Institute of Technology Guwahati

December 2017

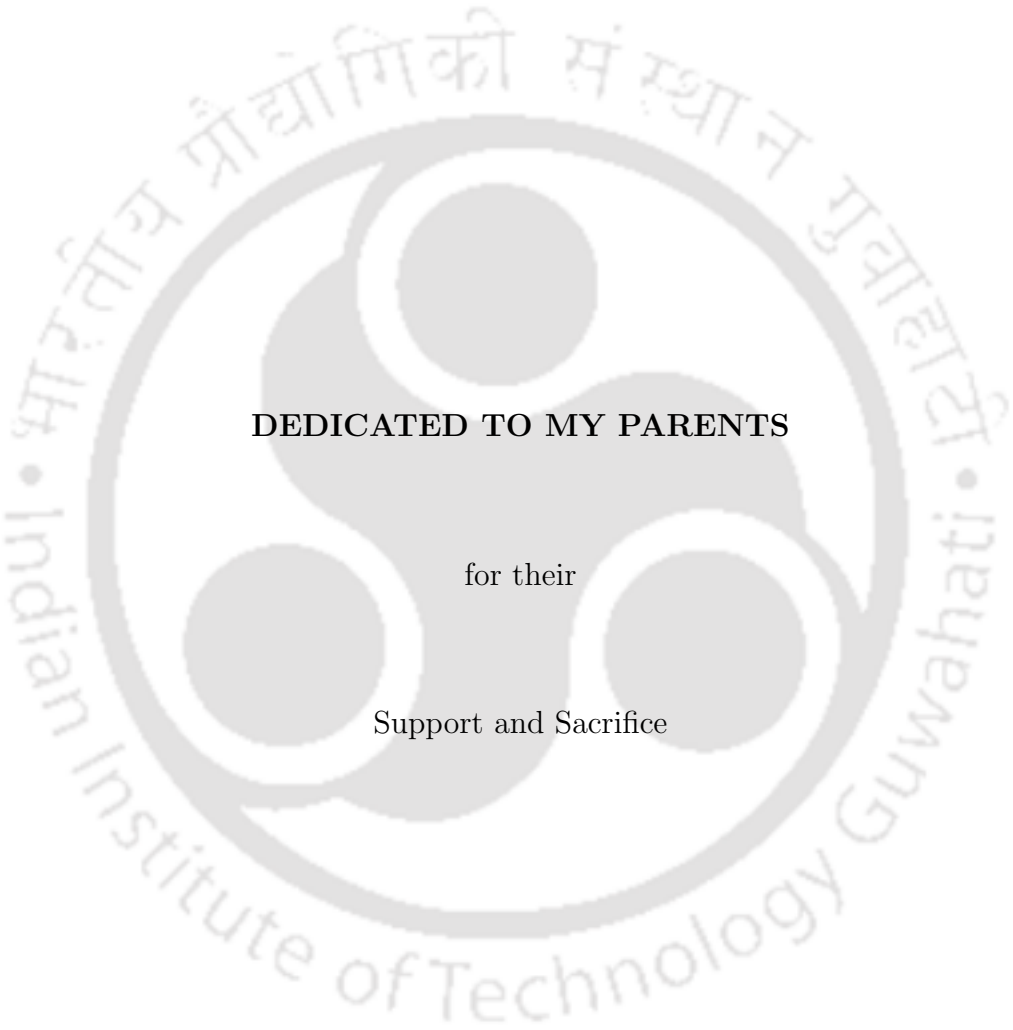

DEDICATED TO MY PARENTS

for their

Support and Sacrifice

Acknowledgements

A PhD work can only be accomplished through a lot of support, encouragement and inspiration from the well-wishers. At the outset I thank the Almighty for blessing me with the strength and patience required to complete a PhD work. I take this opportunity to thank from the core of my heart all those people who have directly or indirectly contributed in this direction.

Words are not enough to express my gratitude towards my PhD supervisor, Prof. Anoop Kumar Dass. He has been a constant source of support, inspiration and invaluable guidance. I thank him from the bottom of my heart for imparting the basics of the relevant subjects in the best possible way before I embarked on my thesis-work. He has imbibed in me the habit of scientific thinking and systematic analysis. Owing to the fact that I could not be available on week days as I was a part-time student, he spared his precious time on many weekends and holidays to mentor me, leaving aside his own personal assignments. Such gestures of kindness were indeed sources of motivation to me. At this juncture, I also take the opportunity to express my sincere thanks to Prof. Dass' family members for being very affectionate and for their kind hospitality.

I deeply thank my wife, Juli for her constant love, support, encouragement and patience during the course of my thesis-work. I can't thank her enough. I feel touched by the understanding shown by our daughter Dibyanshi, who, at such a tender age, bore so calmly the long hours of separation from father that the thesis-work inflicted on her. Lots of love to her.

All my family members have immensely contributed directly or indirectly towards the smooth completion of my PhD. My father, Late Amulya Kalita instilled in me strong values, self-belief and a thirst for knowledge. My mother, Mrs. Renu Kalita taught me the importance of sincerity, hard work and honesty. In spite of undergoing chemotherapy and radiation treatments for her Cancer diagnozed in 2014, she has not stopped encouraging me to focus on my thesis-work. Special thanks are due to my cousin Prof. Manoranjan Kalita, who motivated me to leave a career in the industry and join this exciting world of academics and research. I thank my elder sisters Archana and Gayatri and my brother-in-law Mr. Madan Chandra Baruah for their constant support and encouragement. I

gratefully acknowledge the words of wisdom and encouragement of my father-in-law Late Bhabendra Nath Deka, who remained a constant source of inspiration to me till the end.

I express my gratitude to the Tezpur University authorities for providing me the official permission to join PhD programme at Indian Institute of Technology (IIT) Guwahati as a part-time student and granting study leave for one semeseter to complete the necessary courseworks. Prof. Shyamanta M. Hazarika, former Head, Department of Mechanical Engineering at Tezpur University (and presently Professor in the Department of Mechanical Engineering, IIT Guwahati) provided the necessary support for obtaining the official permission for my study leave. I convey my deep sense of gratitude to him. I am grateful to Prof. Debabrata Chakraborty, former Head, Department of Mechanical Engineering, IIT Guwahati for guiding me on the official formalities for my admission into the PhD programme.

I thank the members of my Doctoral Committee, Prof. Manmohan Pandey (Department of Mechanical Engineering), Prof. Anugrah Singh (Department of Chemical Engineering) and Dr. Ganesh Natarajan (Department of Mechanical Engineering) for their invaluable comments and suggestions during my progress seminars. In this regard I wish to express my special thanks to Dr. Ganesh Natarajan for his invaluable help and suggestions on numerous occasions. Whether it is providing some research papers on my request or voluntarily on his own, or giving inputs on my thesis-work, he always gladly helped me in all possible ways.

I thank Dr. Kamaluddin Ahmed, Department of Civil Engineering, Tezpur University, for guiding me on the PhD Regulations while applying for my admission to IIT Guwahati. I also thank Prof. Mohammad Jawed in the Department of Civil Engineering, IIT Guwahati for his guidance on the application procedure for part-time PhD students. I am lucky to have friends like Mohd. Ashif Iqbal, Dr. Bhaskar Jyoti Bora, Mr. Debarshi Mallick, Mr. Subhra Sankar Kalita, Mr. Raushan Kumar, Mr. Kalpajyoti Borah, Dr. Sushen Kirtania, Mr. Polash Pratim Dutta, Dr. Simon Peter and many more, who all have been my co-research-scholars in the Department of Mechanical Engineering. They have always provided me great help and support. The support from Mr. Narayan Kalita, Hostel Affairs Board in providing me permissions for temporary-hostel accommodation without

a hitch during the last phase of my PhD is gratefully acknowledged. I also thank Dr. Partha Pratim Dutta, my senior colleague and present Head, Department of Mechanical Engineering at Tezpur University for his support, advice and encouragement. The help from Dr. Vivek K. Mehta, my colleague in the Department of Mechanical Engineering at Tezpur University in learning Latex for writing the present thesis is admiringly acknowledged.

I am grateful to Dr. Arnab Dey in the Department of Mechanical Engineering, IIT Guwahati for allowing me to register for his course on Advanced Computational Fluid Dynamics despite not having done any elementary-level course on the subject. The exposure that I received during the course was indeed very helpful to me during my thesis-work. I convey my gratitude to Dr. Bibin John and Dr. Bidyut B. Gogoi, former research scholars in the departments of Mechanical Engineering and Mathematics, for their inputs during my PhD. I also thank Mr. Raju Kumar, former MTech student in the Department of Mechanical Engineering, for his support during the initial phase of my thesis-work.

I feel fortunate to have received the love, cooperation and support from so many people in the completion of my PhD that it would not be possible for me to name them all. I thank all of them from the core of my heart.

Paragmoni Kalita

Indian Institute of Technology Guwahati

Abstract

This work is primarily concerned with the development of schemes and numerical methods for computing high-speed inviscid and viscous flows, computation of which frequently encounters various difficulties in the forms of discontinuities like shocks, contact surfaces, slip streams etc. Dynamics of inviscid compressible flows is governed by the Euler equations of gas dynamics and their discretization in the context of finite volume methods has attracted considerable attention of the CFD practitioners in the last four decades. This is because, for high-speed flows, Euler equations many a times give physically meaningful results and these can be used for aerodynamic-design purposes. It is now an accepted fact that for capturing shocks accurately, the conservative form of the Euler equations has to be numerically solved using conservative discretization schemes. Since the unsteady Euler equations are hyperbolic in nature admitting wave-like solution, simple central differencing of the fluxes leads to numerical instabilities necessitating the development of upwind schemes which comprise one-sided differencing that respects the direction of signal propagation. However, these schemes many a times smear various discontinuities greatly because of the presence of large amount of implicit numerical diffusion. This suggests alternative ways of flux differentiation. It has already been mentioned that simple central differencing of the flux terms lead to numerical instabilities. This is because central differencing is associated with very low amount of numerical diffusion and some amount is necessary for stability. This understanding led to a class of schemes that use central differencing of the flux term with (artificial) addition of some numerical viscosity for stabilization. This class of schemes is termed central schemes, in which the diffusion-term plays a very significant role. As already mentioned, if the diffusion is high it leads to smearing of the various discontinuities, and if the diffusion is low it leads to instabilities. This thesis attempts to address this problem encountered by central schemes, so that numerical diffusion can be controlled in such a way as to give a stable scheme, and at the same time produces accurate solution in the form of sharp discontinuities.

Local Lax-Friedrichs (LLF) scheme is one of the simplest, but highly diffusive central schemes, which leaves enough room for the diffusion to be reduced for accurate computation. In a relatively recent scheme called Diffusion-Regulated Local Lax-Friedrichs (DRLLF) scheme (J. Comput. Phys., Vol. 221, 2007), a method for regulating the numerical diffusion in the LLF scheme was proposed along with a prescribed value of a diffusion-regulating parameter. To gauge the influence of this parameter on various discontinuities in various problems, initially a series of 1D and 2D computations are carried out with different values of the parameter. These computations are also carried out with a relatively accurate upwind scheme, namely, Advection Upstream Splitting Method (AUSM) and a robust upwind scheme, namely, van Leer's Flux Vector Splitting (FVS) scheme for the sake of comparison. It is shown that the DRLLF scheme computes oblique (non-grid-aligned) and weak shocks more crisply than AUSM, however, it is the AUSM scheme that resolves grid-aligned strong shocks better. Besides establishing relative merits and demerits of the DRLLF scheme, we also show that the scheme can be used also to compute reacting-air flows at hypersonic speeds. In computing axisymmetric-hypersonic flow over a hemisphere the DRLLF scheme is found to produce numerical oscillations in the strong-shock zone. The formulation of the Diffusion-Regulation (DR) parameter is modified to overcome this problem.

In the second phase of the present work, the possibility of further reducing the numerical diffusion of the DRLLF scheme in the presence of physical diffusion for viscous-flow computations is investigated by computing supersonic laminar flow over a flat plate and hypersonic shock wave-boundary layer interaction (SWBLI) on a ramped surface. By scaling down the DR parameter throughout the computational domain below the original inviscid formulation we show that it is indeed possible to improve the accuracy of the DRLLF scheme for viscous-flow computations. Further, the effects of numerical diffusion on the performances of the AUSM, van Leer's FVS and DRLLF schemes in computing the adiabatic-wall temperature, skin friction coefficient, laminar-separation-bubble size are also investigated. It is demonstrated that the adiabatic-wall temperature and the laminar-separation-bubble size increase with numerical diffusion, whereas the skin friction decreases with the increase in numerical diffusion.

The nature of viscous flows suggests a possibility of differential regulation of numerical viscosity inside and outside the shear layer. As an important contribution from the present thesis-work, the differential control of the numerical diffusion of the DRLLF scheme is achieved by modifying the original DR parameter. The modified version of the DR parameter operates based on a new-boundary-layer sensor developed in such a way that the numerical diffusion is further reduced inside the viscous zone only, and in the outer inviscid zone the parameter reverts back to the original inviscid formulation. This new scheme is named as the DRLLF-Viscous (DRLLFV) scheme. The overall performance of the DRLLFV scheme is better than the AUSM scheme in that it resolves the boundary layer comparable with the latter and performs much better in resolving the leading-edge shocks. To implement the various flux schemes for computing a wide range of viscous-flow problems, a high-speed viscous flow solver (HSVFS) for structured grids is developed. The solver is flexible enough to incorporate as many inviscid flux schemes as one desires. The solver is capable of handling the first- and higher-order versions of the schemes using appropriate solution-reconstruction methods with different limiters. The viscous fluxes can be computed by using either the Green's theorem or the Cross-Diffusion Method. The solver is validated using ANSYS-FLUENT simulations as well as numerical and experimental results from literature.

The final important work of the present thesis addresses the need for an inexpensive scheme that can capture shocks and other discontinuities crisply irrespective of their strengh and grid-inclinations. For inviscid flows we develop a new scheme by hybridizing the AUSM and DRLLF schemes and coupling them through a novel shock switch that operates - unlike existing switches - on the gradient of the Mach number across the cell-interface. The AUSM and DRLLF schemes are chosen for the hybridization owing to their contrasting performances in resolving grid-aligned (and strong) and non-grid-aligned weaker shocks. It is our experience that if conventional shock switches based on variables like density, pressure or Mach number are used to combine the schemes, the desired effect of simultaneous crisp resolution of grid-aligned and non-grid-aligned discontinuities are not obtained. To circumvent this problem we design a shock switch based - for the first time - on the gradient of the cell-interface Mach number with very

impressive results. Thus the strategy of hybridizing two carefully selected schemes together with the innovative design of the shock switch that couples them, affords a method that produces the effects of a multidimensional scheme with a lower computational cost. The new hybrid scheme obtained for inviscid-flow computations is termed the AUSM-DRLLF Self-Adjusting Hybrid (ADSAH) scheme. It is further seen that hybridization of the AUSM scheme with the DRLLFV scheme using the present shock switch gives another scheme that provides crisp resolution for both shocks and boundary layers and the new scheme is termed the AUSM-DRLLF Self-Adjusting Hybrid Viscous (ADSAHV) scheme. Merits of the schemes are established through a carefully selected set of numerical experiments.

Contents

List of Figures

List of Tables

Nomenclature

$\mathbf{A}$	Flux Jacobian Matrix
A	Area of cross-section
a	Speed of sound
c_p	Specific heat at constant pressure
c_v	Specific heat at constant volume
e_m	Total energy per unit mass of the fluid
$\mathbf{F}$	Flux vector in the x-direction
$\mathbf{G}$	Flux vector in the y-direction
$\mathbf{H}$	Flux vector in the z-direction
$I+\frac{1}{2}$	Cell-interface between cells I and $I+1$ for 1D flow
$\mathbf{i}_x$	Unit vector in the x-direction
$\mathbf{i}_y$	Unit vector in the y-direction
$\mathbf{i}_z$	Unit vector in the z-direction
h_0	Stagnation enthalpy
L	Left state of a cell-interface
L	Characteristic length
$\mathbf{L}$	Matrix of left eigenvectors
M	Mach number
$\mathbf{n}$	Unit outward normal vector to a cell-interface
n_x	Component of unit normal vector in the x-direction
n_y	Component of unit normal vector in the y-direction
Pr	Prandtl number
p	Absolute pressure of the fluid
q	Heat flux
R	Right state of a cell interface
R	Characteristic gas constant
$\mathbf{R}$	Matrix of right eigenvectors

Re_L	Reynolds number based on the characteristic length
$\mathbf{r}$	Position vector
$\mathbf{Q}$	Resultant flux vector $\mathbf{i}_x\mathbf{F} + \mathbf{i}_y\mathbf{G} + \mathbf{i}_z\mathbf{H}$
T	Absolute temperature
T_0	Stagnation temperature
$\mathbf{U}$	Vector of conserved variables
u	Velocity component in the x-direction
$u_\perp$	Velocity component normal to a cell-interface
V	Cell-volume
v	Velocity component in the y-direction
w	Velocity component in the z-direction
$\overline{\Theta}$	Cell-averaged value of any parameter Θ
Θ^*	Non-dimensionalized form of any variable Θ

Greek Symbols

γ	Ratio of specific heats
Φ	Diffusion-Regulation (DR) parameter
Φ_d	Directional Diffusion Regulator (DDR)
$\mathbf{\Lambda}$	Diagonal matrix of the eigenvalues
λ	Eigenvalue
μ	Coefficient of dynamic viscosity
ψ	Weak-solution variable
ρ	Density of the fluid
τ	Stress on a fluid element
$\theta_{I+\frac{1}{2}}$	Shock switch across a cell-interface $I+\frac{1}{2}$

Subscripts

$\frac{1}{2}$	Cell-interface between a left and a right cell
∞	free-stream property
$\perp$	Component normal to a cell-interface
I	Inviscid terms
i	Space index in the x-direction
j	Space index in the y-direction
v	Viscous terms
x	Component in the x-direction
y	Component in the y-direction
z	Component in the z-direction
xx	Component acting on the x-plane in the x-direction
xy	Component acting on the x-plane in the y-direction
xz	Component acting on the x-plane in the z-direction
yx	Component acting on the y-plane in the x-direction
yy	Component acting on the y-plane in the y-direction
yz	Component acting on the y-plane in the z-direction
zx	Component acting on the z-plane in the x-direction
zy	Component acting on the z-plane in the y-direction
zz	Component acting on the z-plane in the z-direction

Superscripts

n	n^{th} time-level
$+$	Positive component
$-$	Negative component

Abbreviations

DDR	Directional Diffusion Regulator
DR	Diffusion-Regulation
FVM	Finite Volume Method
FDS	Flux-Difference Splitting
FVS	Flux-Vector Splitting
LSB	Laminar Separation Bubble
SWBLI	Shock Wave-Boundary Layer Interaction
1D	one-dimensional
2D	two-dimensional
3D	three-dimensional

Chapter 1

Introduction

1.1 Background

One of the main concerns of Computational Fluid Dynamics (CFD) practitioners is to improve the accuracy and resolution of the computed flow field. The accuracy and resolution of the computations are affected a great deal by the numerical scheme for discretizing the governing equations of the flow. In compressible-flow computations the issues of accuracy and resolution are more complex due to the presence of features like shocks, slip-lines, contact discontinuities, and various types of wave interactions- such as shock reflection, shock-shock interaction, shock-expansion interaction etc.

Historically, in the beginning the method of computing compressible flows involving shocks was that of "Shock Fitting", in which the states across the shock were connected using the Rankine-Hugoniot relations and the governing equations in the upstream and downstream zones of the shock were numerically solved at each time step. However, this approach has its own pitfalls in that the shock surface itself may be in motion relative to the network of points in space-time coordinates, and the differential equations as well as the boundary conditions are non-linear. Moreover, the shape and location of the shock surface is not always known in advance, which are determined by the governing equations and the boundary conditions themselves [1]. Consequently, the shock fitting approach involves lengthy calculations that are mostly done with trial and error at each time step.

In the presence of shocks or contact discontinuities, the flow variables become

non-differentiable at the locations of the discontinuities. Clearly, discontinuous solutions do not satisfy the partial differential equation (PDE) in the classical sense at all points, since the space-derivatives of the variables are not defined at these locations. To overcome these difficulties, "weak solution" to the governing PDE can be sought. A weak solution (also called a generalized solution) to an ordinary or partial differential equation is a function for which the derivatives may not all exist but which is nonetheless deemed to satisfy the equation in some precisely defined sense. One approach to obtain weak solutions is the "vanishing-viscosity method", where a diffusive term is introduced into the governing equations to obtain a unique-smooth solution and then the solution is sought at the limit when the coefficient of the diffusive term approaches zero. The addition of artificial viscosity results in smearing of the discontinuities. As a result of this the mathematical surfaces are replaced by thin layers where flow variables like pressure, velocity, density etc. change rapidly but smoothly. Addition of artificial viscosity and solving the governing equations in conservation form using a stable numerical scheme with properly posed initial and boundary conditions resulted in automatic capturing of the shock-shape and location during the space-time evolution. This new approach resulted to a shift of the computational paradigm from "Shock Fitting" to "Shock Capturing".

The dynamics of inviscid-compressible flows is governed by the unsteady Euler equations of gas dynamics that are hyperbolic in nature. For hyperbolic conservation laws, it is a well-established fact that the Forward-Time Central-Space (FTCS) method is unconditionally unstable. To impart numerical stability it is essential to add some numerical diffusion to the central dicretization of the space-derivatives associated with the inviscid fluxes. The major challenge in achieving high accuracy in compressible-flow computations is to ensure that a right amount of stabilizing diffusion is added in regions of sharp gradients to ensure stability, while in the rest of the computational domain the diffusion must be small enough not to spoil the solution accuracy. It has to be always borne in mind that too high numerical diffusion causes nonphysical smearing of the discontinuities.

To illustrate the point let us consider the one-dimensional (1D) linear advection

equation

$$\frac{\partial u}{\partial t} + c\frac{\partial u}{\partial x} = 0, \tag{1.1}$$

where c = constant > 0 is the wave speed. Let equation 1.1 be discretized by using a first-order-forward difference in time and first-order-rearward difference in space. Then equation 1.1 can be represented by the following difference equation:

$$\frac{u_j^{n+1} - u_j^n}{\Delta t} + c\frac{u_j^n - u_{j-1}^n}{\Delta x} = 0, \tag{1.2}$$

where u_j^n and u_{j-1}^n represent the discrete solutions for u at locations x_j and x_{j-1} at time t, respectively, Δx is the grid-spacing, Δt is the time-step, and u_j^{n+1} is the discrete solution at x_j at time $t + \Delta t$. Equation 1.2 is the first-order-upwind discretization of equation 1.1. It can be shown that equation 1.2 is actually equivalent to solving another partial differential equation of the form [2]:

$$\frac{\partial u}{\partial t} + c\frac{\partial u}{\partial x} = \frac{c\Delta x}{2}\left(1-\nu\right)\frac{\partial^2 u}{\partial x^2} + \frac{c\left(\Delta x\right)^2}{6}\left(3\nu - 2\nu^2 - 1\right)\frac{\partial^3 u}{\partial x^3} + \mathcal{O}\left[\left(\Delta t\right)^3, \left(\Delta t\right)^2\Delta x, \Delta t\left(\Delta x\right)^2, \left(\Delta x\right)^3\right], \tag{1.3}$$

where $\nu = \frac{c\Delta t}{\Delta x}$. The exact solution (free from any round-off error) of equation 1.2 can be viewed as the numerical solution of the *original* partial differential equation 1.1 with an error given by the truncation error. However, from another perspective, the exact solution (free from any round-off error) of the difference equation 1.2 constitutes an *exact solution* (no round-off error) of a *different* partial differential equation, namely, equation 1.3 that is called the *modified equation*. The leading-order term on the right-hand side of equation 1.3 contains a term $\frac{\partial^2 u}{\partial x^2}$ that has viscous-like effects. Though the original equation 1.1 was free from any viscous effects, the upwind discretization of the equation has artificially created viscous-like effects that are purely of numerical origin. The artificial viscosity or numerical diffusion results in smoothing of discontinuities in the marching procedure. Figure 1.1 shows a qualitative picture of the smearing of an initial discontinuity due to numerical diffusion in computing the 1D linear advection equation.

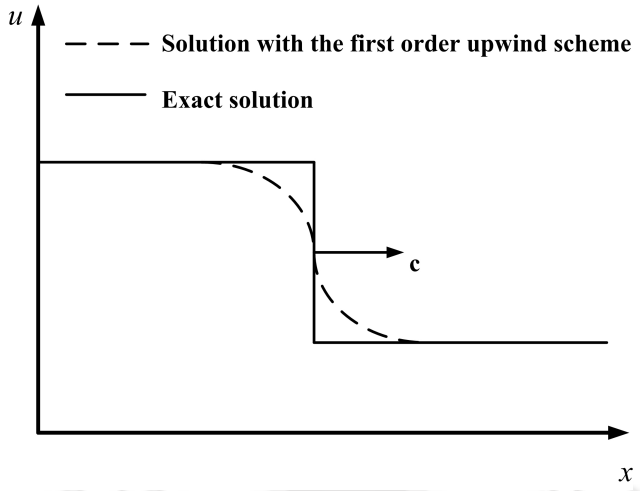

Fig. 1.1. Effect of numerical diffusion in computing the 1D linear wave equation with an initial discontinuity.

1.2 Literature review

The design of schemes that can accurately capture shocks and shear layers in the computation of inviscid and viscous-compressible flows has found importance in the recent developments of computational aerodynamics. The unsteady Euler equations that govern the dynamics of inviscid-compressible flows are hyperbolic in nature. Even for high-speed viscous applications governed by the compressible Navier-Stokes equations, the convective fluxes are numerically computed by using the same flux formulas developed for the Euler equations. The design of a stable, robust and accurate numerical flux scheme for nonlinear conservation laws is still a challenging research area. This is due to the fact that such equations admit discontinuous solutions in the forms of shocks, contact discontinuities, slip surfaces, and also may develop expansion waves with sonic points [3]. The idea of shock capturing in hyperbolic conservation laws by the addition of artificial viscosity was pioneered by von Neumann and Richtmyer [1]. As research in this field unfolded it gradually became clear that for numerical stability it is essential to add some explicit numerical or artificial diffusion to the central discretization of the flux terms [4–6]. However, excessive numerical diffusion spoils the solution accuracy by smearing the discontinuities and boundary layers [7, 8].

The initial attempts in designing numerical fluxes for the Euler equations resulted in schemes that had the same theoretical order of accuracy throughout the computational domain. Laney [9] termed these schemes the "first-generation methods". They can be classified as upwind and central schemes. The upwind schemes choose the stencil taking into account the directions of the wave propagation. These schemes can be viewed as equivalent to central discretization of the fluxes along with an "implicit" numerical-diffusion term. In contrast, the central schemes are mathematically simpler in formulation because the "wind-direction" is not an issue in the design of these schemes. Moreover, the central schemes employ a central discretization of the fluxes combined with an "explicitly" added numerical-diffusion term. An upwind scheme provides better nonlinear stability near shocks since it inherently satisfies the stencil adaptation required to fulfil the CFL criteria [9]. Although the upwind schemes are the natural choice for shock-capturing applications, the central schemes also have merits due to their algebraic simplicity and easier maneuverability of the numerical diffusion.

Godunov's scheme [10] laid the foundation for a class of upwind schemes. This scheme, although robust, was computationally expensive and complex owing to the requirement of using an exact Riemann solver [11]. Later on a series of upwind schemes like Steger and Warming's Flux Vector Splitting (FVS) [12], Roe's Flux Difference Splitting (FDS) [13], van Leer's FVS [14], Liou and Steffen's Advection Upstream Splitting Method (AUSM) [7], Edwards' Low-Diffusion Flux Splitting Scheme (LDFSS) [15] etc. were developed. Steger and Warming's pioneering idea in the field of FVS opened up the possibility of constructing upwind schemes based on the characteristic structure of the Euler equations. However, it suffered from the "sonic-glitch problem", which was overcome by van Leer [14]. The van Leer's FVS scheme was found to be robust but was found to be highly diffusive for inviscid and viscous computations. The AUSM scheme could produce much improved results for both inviscid and viscous computations. However, the AUSM scheme also needed various modifications for applicability to a wide range of speeds [16, 17]. It also needed other corrections like the entropy fix [18]. Roe's FDS scheme is considered a watershed event in the development of approximate Riemann solvers. In spite of offering high accuracy for a wide range of problems, Roe's FDS scheme

suffered from limitations like computational cost [7], carbuncle phenomenon and expansion shock [19]. Depending on the particular version used, Edwards' LDFSS scheme could reduce either numerical oscillations near strong shocks or carbuncle phenomenon but both the problems could not be simultaneously addressed [20]. Further, van Leer reported that although most of the FVS and FDS methods are good at resolving strong shocks aligned with the grid, they badly resolve shocks that are inclined to the grid [21].

The Lax family of schemes forms the basis of the central schemes. The Lax scheme [22], Lax-Wendroff scheme [23], Local Lax-Friedrichs or Rusanov's scheme [24], McCormack's scheme [25] etc. are some of the examples of central flux schemes. Although simple in mathematical formulation, these schemes suffer from the disadvantage of either excessive numerical diffusion or nonphysical oscillations near shocks [9]. Jameson carried out pioneering works in the development of central schemes with added artificial diffusion. One notable contribution from Jameson is the Convective Upwind and Split Pressure (CUSP) scheme [5]. Jameson's central schemes found a wide range of applicability. However, the performance of these schemes relied a great deal on the proper choice of the coefficients used in the evaluation of the numerical-diffusion terms [6] and as a result the skill and experience of the user was crucial in the proper use of these schemes.

The first-generation methods have one basic limitation that they "mindlessly" treat every part of the solution domain as the same. But a solution-sensitive scheme that can adjust its theoretical order of accuracy based on the smoothness of the flow field is more desirable in order to achieve high resolution. Many solution-sensitive methods combine a range of first-generation methods, varying the exact blend from place to place depending on the solution features such as shocks or smooth regions. For example, one such method may use Roe's first-order scheme at shocks and Lax-Wendroff scheme in smooth regions. The blending of the schemes is regulated based on the solution or the flux-gradients. This class of schemes can be called the second- and third-generation schemes [9].

The technique of designing high-resolution schemes by combining two schemes with complimentary properties is called flux-averaging [9]. Flux-averaged methods can further be classified as flux-limited, flux-corrected and self-adjusting hybrid

methods. On the basic philosophy level these three approaches are the same. The difference arises only in the ways of calculating the weight functions used for flux-averaging. Some of the examples of flux-limited methods are van-Leer's flux-limited method for the linear advection equation [26], Sweby's method [27], Osher-Chakravarthy TVD method [28] and Yee-Roe TVD scheme [29].

Boris and Book [30] started the era of flux-corrected methods by combining an upwind method with the Lax-Wendroff scheme and named their method as Flux-Corrected-Transport (FCT). Zalesak [31] generalized the original FCT to combine any two methods provided that one method always had more second-order-artificial viscosity than the other, so that the flux-correction plays the role of an anti-diffusive term in smooth regions. Another approach of FCT that corrected the physical flux rather than the numerical flux was proposed by Harten [4]. FCT methods are found suitable for simulating violent time-dependent flows, but they are less suited for steady-state calculations [21].

The self-adjusting hybrid methods obtain a convex combination of two schemes using a shock switch. As the name suggests the role of the shock switch is to distinguish shock or sharp-gradient regions from smooth regions, switching on at shocks and switching off in smooth regions. The pioneering work in the class of self-adjusting hybrid methods can be attributed to Harten and Zwas [32, 33], where they combined the Lax-Friedrichs and Lax-Wendroff schemes. Harten [34] combined a first-order-upwind scheme with the Lax-Wendroff scheme. Jameson et al. [35] proposed a scheme that combined a semidiscrete first-order-upwind scheme with a semidiscrete version of a central scheme plus fourth-order-artificial viscosity. This scheme is popularly known as the JST scheme. Radespiel and Kroll [18] hybridized the AUSM and the van Leer's FVS schemes to extract the benefits of both in resolving boundary layers as well as strong shocks. However, the weight factor used in this scheme for hybridization is constant rather than being solution-sensitive. Development of hybrid schemes continues to find importance as evidenced from the recent literature [36, 37] on this area.

Apart from the flux-averaged methods, other approaches to regulate the numerical diffusion for achieving high shock resolution also exist. The solution-averaging (also called reconstruction-evolution) [38, 39] and diffusion-regulation of central

and upwind schemes [40–44] are two common approaches in this direction. The quest for designing Riemann solvers that can accurately capture a discontinuity irrespective of its grid-inclination has led to the development of "multidimensional" upwind schemes [21]. These schemes have resulted from attempts to redeem the fact that in the extension of conventional upwind strategies to multidimensional equations using traditional finite volume method (FVM), discontinuities oblique to grid faces are mostly worse resolved than those aligned with the grid [21]. As one remedy to this problem rotated Riemann solvers [45, 46] were developed to achieve directional upwinding. Flux formulas based on rotated frames do achieve the goal of uniform resolution of shocks and shears independent of direction, but are not robust when used in higher-order schemes [21]. The class of residual distribution (RD) schemes [47, 48] is considered a fundamental and robust approach and these schemes possess "genuinely multidimensional" features. The residual distribution schemes are best formulated on finite-element grids [21]. Though elegant, the RD approach works mainly for the Euler equations and it requires a considerable amount of reformulation for extension to any other hyperbolic systems [49]. The multidimensional HLLE/HLLEM/HLLC Riemann solvers [49–53] are some recently developed truly multidimensional schemes that are versatile and robust.

1.3 Motivation and objectives

Literature survey reveals that numerical diffusion plays a significant role in the accurate computation of both inviscid and viscous-compressible flows. A scope exists to regulate the numerical diffusion of schemes for achieving higher accuracy. In case of central schemes like the Local Lax-Friedrichs (LLF) scheme, it is relatively easy to maneuver the numerical-diffusion term. Schemes like the Diffusion-Regulated LLF (DRLLF) and Directional Diffusion-Regulated LLF (DDRLLF) schemes have been recently developed in order to regulate numerical diffusion of the LLF scheme. However, systematic studies on the possibility of further reducing the numerical-diffusion level of the DRLLF scheme for viscous-flow computations is not available in reported literature. In addition, a scope exists to design a robust yet simple

and cost-effective numerical flux scheme with controlled diffusion that can capture both strong and weak shocks irrespective of their grid-inclinations. In this backdrop the motivation for the present thesis work is primarily drawn from the need for the analysis and regulation of numerical diffusion in computing inviscid and viscous-compressible flows. Based on the literature review and the existing research gap, the present thesis aims at achieving the following major objectives:

- To develop an understanding on the effects of numerical diffusion in the computation of inviscid-compressible flows.
- To compare the performances of some of the existing numerical schemes, namely, van Leer's FVS, AUSM, DRLLF and DDRLLF schemes in inviscid-flow computations and qualitatively correlate the shock resolutions with the numerical diffusion present in these schemes.
- To study the effects of numerical diffusion in the computation of viscous-compressible flows.
- To investigate whether it is possible to reduce the numerical diffusion of the DRLLF scheme for viscous-flow computations lower than the level originally prescribed for the Euler equations.
- To develop a structured grid high-speed viscous flow solver and use the same with both existing and newly-developed schemes.
- To design a simple and robust numerical flux methodology that can adjust its numerical diffusion for accurate capturing of a shock irrespetive of its strength and grid-inclination.

1.4 Organization of the thesis

The thesis is organized in seven chapters. Chapter 2 presents the governing equations of compressible flows and background information on various numerical methods used in the present work. The role of numerical diffusion in inviscid-flow computations along with performance comparison of several upwind and central

schemes in computing 1D, quasi-1D, 2D and axisymmetric flows are presented in Chapter 3. Chapter 4 discusses various aspects of viscous-flow computations including the effects of numerical diffusion, the possibility of reducing the numerical diffusion in presence of physical viscosity and performance comparison of different limiters in the higher-order-solution-reconstruction methods. Chapter 5 presents a new diffusion-regulated scheme for accurate computation of the compressible Navier-Stokes equations using a novel-boundary-layer sensor. To address the need for a simple yet robust finite-volume based scheme with multidimensional-like effects, a novel hybrid approach using a new shock switch is introduced in Chapter 6. Chapter 7 summarizes the thesis and highlights the major achievements. Some scopes for future work are also mentioned in this chapter. Seven appendices are added to improve the clarity of the thesis.

Chapter 2

The Governing Equations and Background Information

This chapter begins with the governing equations for three-dimensional (3D) inviscid and viscous compressible flows in differential forms. This is followed by a discussion on some upwind and central schemes for numerical computation of the convective flux terms present in the governing equations. Special emphasis is laid on the artificial viscosity or numerical diffusion associated with different schemes. Finally the flux-reconstruction and solution-averaging techniques for obtaining higher order of accuracy are discussed.

2.1 The Euler equations of gas dynamics

Dynamics of inviscid compressible flows is governed by the Euler equations of gas dynamics. For 3D flows these equations are written in non-dimensional form as

$$\frac{\partial \mathbf{U}}{\partial t} + \frac{\partial \mathbf{F}}{\partial x} + \frac{\partial \mathbf{G}}{\partial y} + \frac{\partial \mathbf{H}}{\partial z} = 0, \tag{2.1}$$

where $\mathbf{U}$ is the vector of conserved variables, and $\mathbf{F}, \mathbf{G}$ and $\mathbf{H}$ are the flux vectors along the x-, y- and z-directions, respectively. The expressions for these vectors are as follows:

$$\mathbf{U} = \begin{bmatrix} \rho \\ \rho u \\ \rho v \\ \rho w \\ \rho e_m \end{bmatrix}, \tag{2.2a}$$

$$\mathbf{F} = \begin{bmatrix} \rho u \\ p + \rho u^2 \\ \rho uv \\ \rho uw \\ (p + \rho e_m)u \end{bmatrix}, \tag{2.2b}$$

$$\mathbf{G} = \begin{bmatrix} \rho v \\ \rho uv \\ p + \rho v^2 \\ \rho vw \\ (p + \rho e_m)v \end{bmatrix}, \tag{2.2c}$$

$$\mathbf{H} = \begin{bmatrix} \rho w \\ \rho uw \\ \rho vw \\ p + \rho w^2 \\ (p + \rho e_m)w \end{bmatrix}. \tag{2.2d}$$

The symbols have their usual meanings. Details of the non-dimensionalization of the Euler equations are provided in Appendix A.

2.2 The Compressible Navier-Stokes equations

The non-dimensional form of the 3D Navier-Stokes equations for compressible flows can be expressed as

$$\frac{\partial \mathbf{U}}{\partial t} + \frac{\partial \mathbf{F}_\mathrm{I}}{\partial x} + \frac{\partial \mathbf{G}_\mathrm{I}}{\partial y} + \frac{\partial \mathbf{H}_\mathrm{I}}{\partial z} = \frac{\partial \mathbf{F}_\mathrm{v}}{\partial x} + \frac{\partial \mathbf{G}_\mathrm{v}}{\partial y} + \frac{\partial \mathbf{H}_\mathrm{v}}{\partial z}, \tag{2.3}$$

where $\mathbf{U}$, $\mathbf{F}$, $\mathbf{G}$ and $\mathbf{H}$ have the same meanings as before and suffices I and v indicate inviscid and viscous parts, respectively. The expressions for the flux vectors

are as follows:

$$\mathbf{F}_{\mathrm{I}} = \begin{bmatrix} \rho u \\ p + \rho u^2 \\ \rho uv \\ \rho uw \\ (p + \rho e_m)u \end{bmatrix}, \tag{2.4a}$$

$$\mathbf{G}_{\mathrm{I}} = \begin{bmatrix} \rho v \\ \rho uv \\ p + \rho v^2 \\ \rho vw \\ (p + \rho e_m)v \end{bmatrix}, \tag{2.4b}$$

$$\mathbf{H}_{\mathrm{I}} = \begin{bmatrix} \rho w \\ \rho uw \\ \rho vw \\ p + \rho w^2 \\ (p + \rho e_m)w \end{bmatrix}, \tag{2.4c}$$

$$\mathbf{F}_{\mathrm{v}} = \begin{bmatrix} 0 \\ \tau_{xx} \\ \tau_{xy} \\ \tau_{xz} \\ u\tau_{xx} + v\tau_{xy} + w\tau_{xz} - q_x \end{bmatrix}, \tag{2.5a}$$

$$\mathbf{G}_{\mathrm{v}} = \begin{bmatrix} 0 \\ \tau_{yx} \\ \tau_{yy} \\ \tau_{yz} \\ u\tau_{yx} + v\tau_{yy} + w\tau_{yz} - q_y \end{bmatrix}, \tag{2.5b}$$

$$\mathbf{H}_{\mathrm{v}} = \begin{bmatrix} 0 \\ \tau_{zx} \\ \tau_{zy} \\ \tau_{zz} \\ u\tau_{zx} + v\tau_{zy} + w\tau_{zz} - q_z \end{bmatrix}. \tag{2.5c}$$

Assuming Stokes' hypothesis for a Newtonian fluid, the stress and heat-flux terms in the viscous-flux vectors can be expressed as

$$\tau_{xx} = \frac{\mu}{\mathrm{Re}_L}\left\{\frac{4}{3}\frac{\partial u}{\partial x} - \frac{2}{3}\left(\frac{\partial v}{\partial y} + \frac{\partial w}{\partial z}\right)\right\}, \tag{2.6a}$$

$$\tau_{yy} = \frac{\mu}{\mathrm{Re}_L}\left\{\frac{4}{3}\frac{\partial v}{\partial y} - \frac{2}{3}\left(\frac{\partial u}{\partial x} + \frac{\partial w}{\partial z}\right)\right\}, \tag{2.6b}$$

$$\tau_{zz} = \frac{\mu}{\mathrm{Re}_L}\left\{\frac{4}{3}\frac{\partial w}{\partial z} - \frac{2}{3}\left(\frac{\partial u}{\partial x} + \frac{\partial v}{\partial y}\right)\right\}, \tag{2.6c}$$

$$\tau_{xy} = \frac{\mu}{\mathrm{Re}_L}\left(\frac{\partial u}{\partial y} + \frac{\partial v}{\partial x}\right) = \tau_{yx}, \tag{2.6d}$$

$$\tau_{yz} = \frac{\mu}{\mathrm{Re}_L}\left(\frac{\partial v}{\partial z} + \frac{\partial w}{\partial y}\right) = \tau_{zy}, \tag{2.6e}$$

$$\tau_{zx} = \frac{\mu}{\mathrm{Re}_L}\left(\frac{\partial w}{\partial x} + \frac{\partial u}{\partial z}\right) = \tau_{xz}, \tag{2.6f}$$

$$q_x = -\left\{\frac{\mu}{\mathrm{Re}_L\,\mathrm{Pr}\,(\gamma-1)\,M_\infty^2}\right\}\frac{\partial T}{\partial x}, \tag{2.7a}$$

$$q_y = -\left\{\frac{\mu}{\mathrm{Re}_L\,\mathrm{Pr}\,(\gamma-1)\,M_\infty^2}\right\}\frac{\partial T}{\partial y}, \tag{2.7b}$$

$$q_z = -\left\{\frac{\mu}{\mathrm{Re}_L\,\mathrm{Pr}\,(\gamma-1)\,M_\infty^2}\right\}\frac{\partial T}{\partial z}, \tag{2.7c}$$

where μ is the non-dimensionalized coefficient of dynamic viscosity, Re_L is the Reynolds number based on the characteristic length L and Pr is the Prandtl number. If Re_∞ is the Reynolds number with length 1, then $\mathrm{Re}_L = \mathrm{Re}_\infty L = \frac{\rho_\infty U_\infty L}{\mu_\infty}$. The quantities U_∞, M_∞, ρ_∞ and μ_∞ represent the velocity, Mach number, density and coefficient of dynamic viscosity under the free-stream conditions, respectively.

It may be noted that the terms $\mathbf{F}_{\mathrm{I}}$, $\mathbf{G}_{\mathrm{I}}$ and $\mathbf{H}_{\mathrm{I}}$ are identical with the-Euler flux terms. The details of the non-dimensionalization of the Navier-Stokes equations are provided in Appendix B. In Finite Volume Method (FVM) the viscous fluxes require the computation of the flow-variable gradients across the cell-interface (Appendix D). The Green's theorem [54] and the cross-diffusion technique [55] for the gradient computation are described in Appendix E.

2.3 Upwind schemes

The unsteady Euler equations are hyperbolic in nature. Owing to hyperbolicity these equations admit wave-like solutions. Some analytical aspects of 1D Euler equations are presented in Appendix C. It is seen that they can be recast in characteristic form with wave-speeds u, $u+a$ and $u-a$, where u is the fluid-velocity and a is the sonic speed. The wave-speeds are the eigenvalues of the Flux-Jacobian matrix. For solving the 2D Euler equations using FVM, the interfacial numerical fluxes can be determined following exactly the same procedure as in 1D, except that one has to use the flux vector $\mathbf{Q}_\perp$ normal to the cell-interface (see Appendix D). It can be shown that for 2D flows the Jacobian of the normal flux $\mathbf{Q}_\perp$ possesses four real eigenvalues $u_\perp$, $u_\perp$, $u_\perp + a$ and $u_\perp - a$, where $u_\perp$ is the contravariant velocity [54]. Depending on the sign and magnitude of the contravariant Mach number $M_\perp$, the waves or characteristics across a cell-interface may be left-running or right-running. An upwind method must somehow decompose the solution into component waves, approximating the right-running waves with a leftward bias and the left-running waves with a rightward bias. However, the differential equations appearing in the characteristic form of the Euler equations do not have analytical solutions except for simple waves [9]. Therefore, for the upwind stencil selection, most vector upwind methods access the characteristics indirectly using techniques like the Flux-Vector Splitting (FVS) and Flux-Difference Splitting (FDS). This section describes the FVS and FDS techniques for 1D flows in such a way that the numerical-viscosity term is clearly visible. The same concepts can be easily extended to multiple dimensions. The 2D versions of some FVS schemes, namely, van Leer's FVS [14], Liou and Steffen's Advection Upstream Spliting Method (AUSM) [7] and Radespiel-Kroll's Hybrid Method [18] are also described as they are used for comparing our results with.

2.3.1 Flux-Vector Splitting schemes

Here the Flux-Vector Splitting (FVS) approach will be explained based on the concept introduced by Steger and Warming [12] in the context of the 1D unsteady

Euler equations given by

$$\frac{\partial \mathbf{U}}{\partial t} + \frac{\partial \mathbf{F}}{\partial x} = 0. \tag{2.8}$$

In quasi-linear form equation 2.8 can be expressed as

$$\begin{aligned} \frac{\partial \mathbf{U}}{\partial t} + \frac{\mathrm{d}\mathbf{F}}{\mathrm{d}\mathbf{U}}\frac{\partial \mathbf{U}}{\partial x} &= 0 \\ \frac{\partial \mathbf{U}}{\partial t} + \mathbf{A}\frac{\partial \mathbf{U}}{\partial x} &= 0. \end{aligned} \tag{2.9}$$

Figure 2.1 shows typical 1D finite volume cells and a cell-interface along with the corresponding left and right states. Like the other numerical-flux schemes the purpose of the FVS approach also is to approximate the flux $\mathbf{F}_{I+\frac{1}{2}}$ across the cell-interface $I + \frac{1}{2}$ between the left and right states L and R, respectively. The Jacobian matrix $\mathbf{A}$ can be written in the canonical form as

$$\mathbf{A} = \mathbf{T}\mathbf{\Lambda}\mathbf{T}^{-1}, \tag{2.10}$$

where $\mathbf{\Lambda}$ is the diagonal matrix with the eigenvalues of $\mathbf{A}$ as its diagonal elements, $\mathbf{T}$ is the concatenation of the right eigenvectors and $\mathbf{T}^{-1}$ is the concatenation of the left eigenvectors of $\mathbf{A}$ [56]. The details are presented in Appendix C.

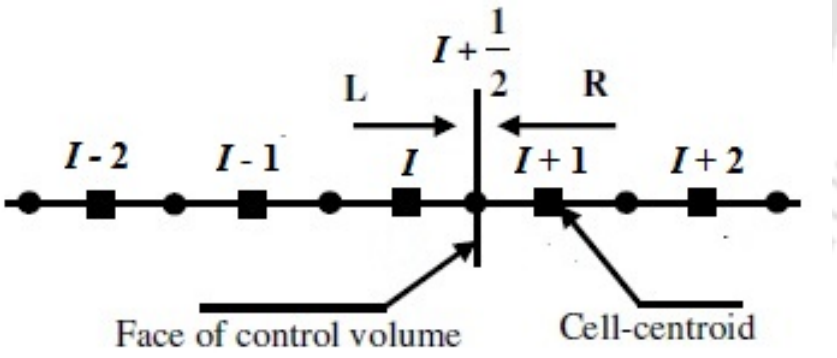

Fig. 2.1. 1D finite volumes with a cell-interface.

The matrix $\mathbf{\Lambda}$ can be written as

$$\mathbf{\Lambda} = \begin{bmatrix} \lambda_1 & 0 & 0 \\ 0 & \lambda_2 & 0 \\ 0 & 0 & \lambda_3 \end{bmatrix}, \tag{2.11}$$

where

$$\lambda_1 = u, \lambda_2 = u + a, \lambda_3 = u - a. \tag{2.12}$$

In general, the characteristic velocities or eigenvalues can be split into positive and negative parts as

$$\lambda_i = \lambda_i^+ + \lambda_i^-, \;\; i=1,2,3, \tag{2.13}$$

where

$$\lambda_i^+ = \frac{\lambda_i + |\lambda_i|}{2}, \tag{2.14a}$$

$$\lambda_i^- = \frac{\lambda_i - |\lambda_i|}{2}. \tag{2.14b}$$

From equations 2.14a and 2.14b one can easily deduce

$$|\lambda_i| = \lambda_i^+ - \lambda_i^-. \tag{2.15}$$

Using equations 2.11 and 2.13 the diagonal matrix $\mathbf{\Lambda}$ can be recast as

$$\mathbf{\Lambda} = \mathbf{\Lambda}^+ + \mathbf{\Lambda}^-, \tag{2.16}$$

where $\mathbf{\Lambda}^+$ and $\mathbf{\Lambda}^-$ are the diagonal matrices with diagonal elements λ_i^+ and λ_i^- $(i = 1, 2, 3)$, so that

$$\mathbf{\Lambda}^+ = \begin{bmatrix} \lambda_1^+ & 0 & 0 \\ 0 & \lambda_2^+ & 0 \\ 0 & 0 & \lambda_3^+ \end{bmatrix}, \tag{2.17a}$$

$$\mathbf{\Lambda}^- = \begin{bmatrix} \lambda_1^- & 0 & 0 \\ 0 & \lambda_2^- & 0 \\ 0 & 0 & \lambda_3^- \end{bmatrix}. \tag{2.17b}$$

Also using equations 2.10 and 2.16 the Jacobian $\mathbf{A}$ can be written as

$$\begin{aligned} \mathbf{A} &= \mathbf{T}\left(\mathbf{\Lambda}^+ + \mathbf{\Lambda}^-\right)\mathbf{T}^{-1} \\ &= \mathbf{T}\mathbf{\Lambda}^+\mathbf{T}^{-1} + \mathbf{T}\mathbf{\Lambda}^-\mathbf{T}^{-1} \\ &= \mathbf{A}^+ + \mathbf{A}^-, \end{aligned} \tag{2.18}$$

where

$$\mathbf{A}^+ = \mathbf{T}\mathbf{\Lambda}^+\mathbf{T}^{-1}, \tag{2.19a}$$

$$\mathbf{A}^- = \mathbf{T}\mathbf{\Lambda}^-\mathbf{T}^{-1}. \tag{2.19b}$$

If we define a diagonal matrix $|\mathbf{\Lambda}|$ in such a way that

$$|\mathbf{\Lambda}| = \begin{bmatrix} |\lambda_1| & 0 & 0 \\ 0 & |\lambda_2| & 0 \\ 0 & 0 & |\lambda_3| \end{bmatrix}, \tag{2.20}$$

then using equations 2.15, 2.17a, 2.17b and 2.20 the following expression is obtained:

$$|\mathbf{\Lambda}| = \mathbf{\Lambda}^+ - \mathbf{\Lambda}^-. \tag{2.21}$$

Subtracting equation 2.19b from 2.19a and using equation 2.21, we obtain

$$\begin{aligned} \mathbf{A}^+ - \mathbf{A}^- &= \mathbf{T}\left(\mathbf{\Lambda}^+ - \mathbf{\Lambda}^-\right)\mathbf{T}^{-1} \\ &= \mathbf{T}|\mathbf{\Lambda}|\mathbf{T}^{-1} \\ &= |\mathbf{A}|\,, \end{aligned} \tag{2.22}$$

where

$$|\mathbf{A}| = \mathbf{T}|\mathbf{\Lambda}|\mathbf{T}^{-1}. \tag{2.23}$$

Now using the homegeneity property of the Euler equations [12] the flux vector can be expressed in terms of the Jacobian matrix $\mathbf{A}$ and the vector of conserved variables $\mathbf{U}$ as

$$\mathbf{F} = \mathbf{A}\mathbf{U}. \tag{2.24}$$

Using equation 2.18 the flux vector obtained in equation 2.24 can be recast as

$$\begin{aligned} \mathbf{F} &= \left(\mathbf{A}^+ + \mathbf{A}^-\right)\mathbf{U} \\ &= \mathbf{A}^+\mathbf{U} + \mathbf{A}^-\mathbf{U} \\ \mathbf{F} &= \mathbf{F}^+ + \mathbf{F}^-, \end{aligned} \tag{2.25}$$

where

$$\mathbf{F}^+ = \mathbf{A}^+\mathbf{U}, \tag{2.26a}$$

$$\mathbf{F}^- = \mathbf{A}^-\mathbf{U}. \tag{2.26b}$$

Equation 2.25 is the basic expression for any FVS method. For 1D FVM, with reference to figure 2.1, the interface flux $\mathbf{F}_{I+\frac{1}{2}}$ can be expressed using the FVS approach as

$$\mathbf{F}_{I+\frac{1}{2}} = \mathbf{F}^+_{\mathrm{L}} + \mathbf{F}^-_{\mathrm{R}}, \tag{2.27}$$

where $\frac{\mathrm{d}\mathbf{F}^+}{\mathrm{d}\mathbf{U}}$ has all positive eigenvalues and $\frac{\mathrm{d}\mathbf{F}^-}{\mathrm{d}\mathbf{U}}$ has all negative eigenvalues. Now using equation 2.27 one can write

$$\mathbf{F}_{I+\frac{1}{2}} = \frac{1}{2}\left(\mathbf{F}_{\mathrm{L}}^{+} + \mathbf{F}_{\mathrm{L}}^{-}\right) + \frac{1}{2}\left(\mathbf{F}_{\mathrm{R}}^{+} + \mathbf{F}_{\mathrm{R}}^{-}\right) - \frac{1}{2}\left\{\left(\mathbf{F}_{\mathrm{R}}^{+} - \mathbf{F}_{\mathrm{L}}^{+}\right) - \left(\mathbf{F}_{\mathrm{R}}^{-} - \mathbf{F}_{\mathrm{L}}^{-}\right)\right\}. \quad (2.28)$$

It follows from equation 2.25 that

$$\mathbf{F}_{\mathrm{L}}^{+} + \mathbf{F}_{\mathrm{L}}^{-} = \mathbf{F}_{\mathrm{L}}, \quad (2.29a)$$

$$\mathbf{F}_{\mathrm{R}}^{+} + \mathbf{F}_{\mathrm{R}}^{-} = \mathbf{F}_{\mathrm{R}}. \quad (2.29b)$$

Substituting equations 2.29a and 2.29b in equation 2.28

$$\mathbf{F}_{I+\frac{1}{2}} = \frac{1}{2}\left(\mathbf{F}_{\mathrm{L}} + \mathbf{F}_{\mathrm{R}}\right) - \frac{1}{2}\left(\Delta_{I+\frac{1}{2}}\mathbf{F}^{+} - \Delta_{I+\frac{1}{2}}\mathbf{F}^{-}\right), \quad (2.30)$$

where

$$\Delta_{I+\frac{1}{2}}\mathbf{F}^{+} = \mathbf{F}_{\mathrm{R}}^{+} - \mathbf{F}_{\mathrm{L}}^{+}, \quad (2.31a)$$

$$\Delta_{I+\frac{1}{2}}\mathbf{F}^{-} = \mathbf{F}_{\mathrm{R}}^{-} - \mathbf{F}_{\mathrm{L}}^{-}. \quad (2.31b)$$

In general the operator $\Delta_{I+\frac{1}{2}}()$ can be written as follows:

$$\Delta_{I+\frac{1}{2}}() = ()_{\mathrm{R}} - ()_{\mathrm{L}}. \quad (2.32)$$

Using equations 2.26a, 2.26b in equations 2.31a and 2.31b we can write

$$\Delta_{I+\frac{1}{2}}\mathbf{F}^{+} = \mathbf{A}_{\mathrm{R}}^{+}\mathbf{U}_{\mathrm{R}} - \mathbf{A}_{\mathrm{L}}^{+}\mathbf{U}_{\mathrm{L}}, \quad (2.33a)$$

$$\Delta_{I+\frac{1}{2}}\mathbf{F}^{-} = \mathbf{A}_{\mathrm{R}}^{-}\mathbf{U}_{\mathrm{R}} - \mathbf{A}_{\mathrm{L}}^{-}\mathbf{U}_{\mathrm{L}}. \quad (2.33b)$$

Substituting equations 2.22, 2.33a and 2.33b in equation 2.30 one obtains

$$\begin{aligned}
\mathbf{F}_{I+\frac{1}{2}} &= \frac{1}{2}\left(\mathbf{F}_{\mathrm{L}} + \mathbf{F}_{\mathrm{R}}\right) - \frac{1}{2}\left(\mathbf{A}_{\mathrm{R}}^{+}\mathbf{U}_{\mathrm{R}} - \mathbf{A}_{\mathrm{L}}^{+}\mathbf{U}_{\mathrm{L}} - \mathbf{A}_{\mathrm{R}}^{-}\mathbf{U}_{\mathrm{R}} + \mathbf{A}_{\mathrm{L}}^{-}\mathbf{U}_{\mathrm{L}}\right) \\
&= \frac{1}{2}\left(\mathbf{F}_{\mathrm{L}} + \mathbf{F}_{\mathrm{R}}\right) - \frac{1}{2}\left\{\left(\mathbf{A}_{\mathrm{R}}^{+} - \mathbf{A}_{\mathrm{R}}^{-}\right)\mathbf{U}_{\mathrm{R}} - \left(\mathbf{A}_{\mathrm{L}}^{+} - \mathbf{A}_{\mathrm{L}}^{-}\right)\mathbf{U}_{\mathrm{L}}\right\} \\
&= \frac{1}{2}\left(\mathbf{F}_{\mathrm{L}} + \mathbf{F}_{\mathrm{R}}\right) - \frac{1}{2}\left(\left|\mathbf{A}_{\mathrm{R}}\right|\mathbf{U}_{\mathrm{R}} - \left|\mathbf{A}_{\mathrm{L}}\right|\mathbf{U}_{\mathrm{L}}\right). \quad (2.34)
\end{aligned}$$

Equation 2.34 can be recast in artificial-viscosity form of the FVS methods as

$$\mathbf{F}_{I+\frac{1}{2}} = \frac{1}{2}\left(\mathbf{F}_{\mathrm{L}} + \mathbf{F}_{\mathrm{R}}\right) - \frac{1}{2}\Delta_{I+\frac{1}{2}}\left(\left|\mathbf{A}\right|\mathbf{U}\right). \quad (2.35)$$

The second term in the right-hand side of equation 2.35 represents the numerical diffusion implicitly added to the central discretization of the interface flux in case of FVS schemes.

2.3.2 Flux-Difference Splitting schemes

We shall now explain the construction of the Flux-Difference Splitting (FDS) schemes based on the Roe-linearization [13] for quasi-linear form of the 1D unsteady Euler equations given by equation 2.9. In the context of FDS schemes the coefficient matrix $\mathbf{A}$ can be approximated by a linearized matrix $\widetilde{\mathbf{A}}\left(\mathbf{U}_{\mathrm{L}}, \mathbf{U}_{\mathrm{R}}\right)$. The matrix $\widetilde{\mathbf{A}}\left(\mathbf{U}_{\mathrm{L}}, \mathbf{U}_{\mathrm{R}}\right)$ can be considered as a representative of the local conditions with the following properties [13]:

1. It constitutes a linear mapping from vector space $\mathbf{U}$ to vector space $\mathbf{F}$.
2. As $\mathbf{U}_{\mathrm{L}} \rightarrow \mathbf{U}_{\mathrm{R}} \rightarrow \mathbf{U}$, $\widetilde{\mathbf{A}}\left(\mathbf{U}_{\mathrm{L}}, \mathbf{U}_{\mathrm{R}}\right) \rightarrow \mathbf{A}\left(\mathbf{U}\right)$.
3. For any $\mathbf{U}_{\mathrm{L}}$ and $\mathbf{U}_{\mathrm{R}}$, $\widetilde{\mathbf{A}}\left(\mathbf{U}_{\mathrm{L}}, \mathbf{U}_{\mathrm{R}}\right) \times \left(\mathbf{U}_{\mathrm{L}} - \mathbf{U}_{\mathrm{R}}\right) \rightarrow \mathbf{F}_{\mathrm{L}} - \mathbf{F}_{\mathrm{R}}$.
4. The eigenvectors of $\widetilde{\mathbf{A}}$ are linearly independent.

With the aforementioned properties of $\widetilde{\mathbf{A}}\left(\mathbf{U}_{\mathrm{L}}, \mathbf{U}_{\mathrm{R}}\right)$, the nonlinear system of hyperbolic conservation laws given by equation 2.9 can be linearized in an approximate sense as

$$\frac{\partial \mathbf{U}}{\partial t} + \widetilde{\mathbf{A}}_{\mathrm{RL}} \frac{\partial \mathbf{U}}{\partial x} = 0, \tag{2.36}$$

where $\widetilde{\mathbf{A}}_{\mathrm{RL}} = \widetilde{\mathbf{A}}\left(\mathbf{U}_{\mathrm{L}}, \mathbf{U}_{\mathrm{R}}\right)$. Similar to equation 2.10 the matrix $\widetilde{\mathbf{A}}_{\mathrm{RL}}$ can be expressed as

$$\widetilde{\mathbf{A}}_{\mathrm{RL}} = \mathbf{T}_{\mathrm{RL}} \mathbf{\Lambda}_{\mathrm{RL}} \mathbf{T}_{\mathrm{RL}}^{-1}, \tag{2.37}$$

where $\mathbf{\Lambda}_{\mathrm{RL}}$ is the diagonal matrix having the eigenvalues $\left(\lambda_{\mathrm{RL}}\right)_i$ of $\widetilde{\mathbf{A}}_{\mathrm{RL}}$ as its diagonal elements. For $i = 1, 2, 3$ the linearized eigenvalues can be split as

$$\left(\lambda_{\mathrm{RL}}^{+}\right)_i = \frac{\left(\lambda_{\mathrm{RL}}\right)_i + \left|\left(\lambda_{\mathrm{RL}}\right)_i\right|}{2}, \tag{2.38a}$$

$$\left(\lambda_{\mathrm{RL}}^{-}\right)_i = \frac{\left(\lambda_{\mathrm{RL}}\right)_i - \left|\left(\lambda_{\mathrm{RL}}\right)_i\right|}{2}. \tag{2.38b}$$

Thus

$$\left(\lambda_{\mathrm{RL}}\right)_i = \left(\lambda_{\mathrm{RL}}^{+}\right)_i + \left(\lambda_{\mathrm{RL}}^{-}\right)_i, \tag{2.39a}$$

$$\left(\left|\lambda_{\mathrm{RL}}\right|\right)_i = \left(\lambda_{\mathrm{RL}}^{+}\right)_i - \left(\lambda_{\mathrm{RL}}^{-}\right)_i. \tag{2.39b}$$

The diagonal matrices $\mathbf{\Lambda}_{\mathrm{RL}}^{+}$ and $\mathbf{\Lambda}_{\mathrm{RL}}^{-}$ are defined as follows:

$$\mathbf{\Lambda}_{\mathrm{RL}}^{+} = \begin{bmatrix} \left(\lambda_{\mathrm{RL}}^{+}\right)_1 & 0 & 0 \\ 0 & \left(\lambda_{\mathrm{RL}}^{+}\right)_2 & 0 \\ 0 & 0 & \left(\lambda_{\mathrm{RL}}^{+}\right)_3 \end{bmatrix}, \tag{2.40a}$$

$$\mathbf{\Lambda}_{\mathrm{RL}}^{-} = \begin{bmatrix} \left(\lambda_{\mathrm{RL}}^{-}\right)_1 & 0 & 0 \\ 0 & \left(\lambda_{\mathrm{RL}}^{-}\right)_2 & 0 \\ 0 & 0 & \left(\lambda_{\mathrm{RL}}^{-}\right)_3 \end{bmatrix}. \tag{2.40b}$$

Using equations 2.39a, 2.40a and 2.40b it is seen that

$$\mathbf{\Lambda}_{\mathrm{RL}} = \mathbf{\Lambda}_{\mathrm{RL}}^{+} + \mathbf{\Lambda}_{\mathrm{RL}}^{-}. \tag{2.41}$$

Using equation 2.41 in equation 2.37 the linearized matrix $\widetilde{\mathbf{A}}_{\mathrm{RL}}$ can be expressed as follows:

$$\begin{aligned} \widetilde{\mathbf{A}}_{\mathrm{RL}} &= \mathbf{T}_{\mathrm{RL}} \left(\mathbf{\Lambda}_{\mathrm{RL}}^{+} + \mathbf{\Lambda}_{\mathrm{RL}}^{-}\right) \mathbf{T}_{\mathrm{RL}}^{-1} \\ &= \mathbf{T}_{\mathrm{RL}} \mathbf{\Lambda}_{\mathrm{RL}}^{+} \mathbf{T}_{\mathrm{RL}}^{-1} + \mathbf{T}_{\mathrm{RL}} \mathbf{\Lambda}_{\mathrm{RL}}^{-} \mathbf{T}_{\mathrm{RL}}^{-1} \\ &= \widetilde{\mathbf{A}}_{\mathrm{RL}}^{+} + \widetilde{\mathbf{A}}_{\mathrm{RL}}^{-}, \end{aligned} \tag{2.42}$$

where

$$\widetilde{\mathbf{A}}_{\mathrm{RL}}^{+} = \mathbf{T}_{\mathrm{RL}} \mathbf{\Lambda}_{\mathrm{RL}}^{+} \mathbf{T}_{\mathrm{RL}}^{-1}, \tag{2.43a}$$

$$\widetilde{\mathbf{A}}_{\mathrm{RL}}^{-} = \mathbf{T}_{\mathrm{RL}} \mathbf{\Lambda}_{\mathrm{RL}}^{-} \mathbf{T}_{\mathrm{RL}}^{-1}. \tag{2.43b}$$

From equations 2.39b, 2.40a and 2.40b it is seen that

$$\mathbf{\Lambda}_{\mathrm{RL}}^{+} - \mathbf{\Lambda}_{\mathrm{RL}}^{-} = \left|\mathbf{\Lambda}_{\mathrm{RL}}\right|, \tag{2.44}$$

where $\left|\mathbf{\Lambda}_{\mathrm{RL}}\right|$ is a diagonal matrix with $\left(\left|\lambda_{\mathrm{RL}}\right|\right)_i$, $i = 1, 2, 3$ as its diagonal elements. Subtracting equation 2.43b from equation 2.43a and using equation 2.44 we obtain

$$\begin{aligned} \widetilde{\mathbf{A}}_{\mathrm{RL}}^{+} - \widetilde{\mathbf{A}}_{\mathrm{RL}}^{-} &= \mathbf{T}_{\mathrm{RL}} \left(\mathbf{\Lambda}_{\mathrm{RL}}^{+} - \mathbf{\Lambda}_{\mathrm{RL}}^{-}\right) \mathbf{T}_{\mathrm{RL}}^{-1} \\ &= \mathbf{T}_{\mathrm{RL}} \left|\mathbf{\Lambda}_{\mathrm{RL}}\right| \mathbf{T}_{\mathrm{RL}}^{-1} \\ &= \left|\widetilde{\mathbf{A}}_{\mathrm{RL}}\right|, \end{aligned} \tag{2.45}$$

where

$$\left|\widetilde{\mathbf{A}}_{\mathrm{RL}}\right| = \mathbf{T}_{\mathrm{RL}} \left|\mathbf{\Lambda}_{\mathrm{RL}}\right| \mathbf{T}_{\mathrm{RL}}^{-1}. \tag{2.46}$$

The linearized flux vectors $\mathbf{F}_{\mathrm{L}}$ and $\mathbf{F}_{\mathrm{R}}$ are expressed in terms of the matrix $\widetilde{\mathbf{A}}_{\mathrm{RL}}$ as

$$\mathbf{F}_{\mathrm{L}} = \widetilde{\mathbf{A}}_{\mathrm{RL}} \mathbf{U}_{\mathrm{L}}, \tag{2.47a}$$

$$\mathbf{F}_{\mathrm{R}} = \widetilde{\mathbf{A}}_{\mathrm{RL}} \mathbf{U}_{\mathrm{R}}. \tag{2.47b}$$

In FDS methods the difference of the flux vectors across the cell-interface $I+\frac{1}{2}$ is split using equations 2.42, 2.47a and 2.47b as

$$\begin{aligned}\Delta_{I+\frac{1}{2}}\mathbf{F} &= \mathbf{F}_{\mathrm{R}} - \mathbf{F}_{\mathrm{L}} \\ &= \widetilde{\mathbf{A}}_{\mathrm{RL}}\mathbf{U}_{\mathrm{R}} - \widetilde{\mathbf{A}}_{\mathrm{RL}}\mathbf{U}_{\mathrm{L}} \\ &= \left(\widetilde{\mathbf{A}}^{+}_{\mathrm{RL}} + \widetilde{\mathbf{A}}^{-}_{\mathrm{RL}}\right)(\mathbf{U}_{\mathrm{R}} - \mathbf{U}_{\mathrm{L}}) \\ &= \widetilde{\mathbf{A}}^{+}_{\mathrm{RL}}(\mathbf{U}_{\mathrm{R}} - \mathbf{U}_{\mathrm{L}}) + \widetilde{\mathbf{A}}^{-}_{\mathrm{RL}}(\mathbf{U}_{\mathrm{R}} - \mathbf{U}_{\mathrm{L}}) \\ &= \Delta_{I+\frac{1}{2}}\mathbf{F}^{+} + \Delta_{I+\frac{1}{2}}\mathbf{F}^{-}, \end{aligned} \tag{2.48}$$

where

$$\Delta_{I+\frac{1}{2}}\mathbf{F}^{+} = \widetilde{\mathbf{A}}^{+}_{\mathrm{RL}}(\mathbf{U}_{\mathrm{R}} - \mathbf{U}_{\mathrm{L}}), \tag{2.49a}$$

$$\Delta_{I+\frac{1}{2}}\mathbf{F}^{-} = \widetilde{\mathbf{A}}^{-}_{\mathrm{RL}}(\mathbf{U}_{\mathrm{R}} - \mathbf{U}_{\mathrm{L}}). \tag{2.49b}$$

It can be observed from equations 2.27 and 2.48 that the FVS approach splits the flux vector itself into right-running and left-running components, whereas the FDS methods decompose the difference of the flux vector into two parts. This is the reason behind the nomenclature of FVS and FDS. The FVS and FDS methods differ also in their artificial-viscosity forms. Here we describe how the FDS methods can be presented in the artificial-viscosity form. Based on the linearized matrix $\widetilde{\mathbf{A}}_{\mathrm{RL}}$ the interface flux $\mathbf{F}_{I+\frac{1}{2}}$ can be expressed with the FDS approach as

$$\mathbf{F}_{I+\frac{1}{2}} = \mathbf{F}_{\mathrm{L}} + \widetilde{\mathbf{A}}^{-}_{\mathrm{RL}}(\mathbf{U}_{\mathrm{R}} - \mathbf{U}_{\mathrm{L}}), \tag{2.50a}$$

$$\mathbf{F}_{I+\frac{1}{2}} = \mathbf{F}_{\mathrm{R}} - \widetilde{\mathbf{A}}^{+}_{\mathrm{RL}}(\mathbf{U}_{\mathrm{R}} - \mathbf{U}_{\mathrm{L}}). \tag{2.50b}$$

Equations 2.50a and 2.50b can be finally recast in the artificial-viscosity form of FDS methods using equation 2.45 as

$$\begin{aligned}\mathbf{F}_{I+\frac{1}{2}} &= \frac{1}{2}(\mathbf{F}_{\mathrm{L}} + \mathbf{F}_{\mathrm{R}}) - \frac{1}{2}\left|\widetilde{\mathbf{A}}_{\mathrm{RL}}\right|(\mathbf{U}_{\mathrm{R}} - \mathbf{U}_{\mathrm{L}}) \\ &= \frac{1}{2}(\mathbf{F}_{\mathrm{L}} + \mathbf{F}_{\mathrm{R}}) - \frac{1}{2}\left|\widetilde{\mathbf{A}}_{\mathrm{RL}}\right|\Delta_{I+\frac{1}{2}}\mathbf{U}. \end{aligned} \tag{2.51}$$

The second term in the right-hand side of equation 2.51 corresponds to the numerical diffusion associated with the FDS methods. A comparison of equation 2.51 with the artificial-viscosity form of the FVS methods given by equation 2.35 clearly shows the differences of these two schemes in the their present forms. However,

irrespective of these differences, the common properties shared by both FVS and FDS approaches are:

1. Both the methods are upwind.
2. The numerical-diffusion terms in both the approaches are implicity formed by the basic formulation of these methods themselves.

2.3.3 van Leer's FVS scheme

van Leer [14] split the flux vector into two parts based upon the split Mach Number as:

$$\mathbf{Q}_\perp = \left(\mathbf{Q}_\perp^+\right)_{\mathrm{L}} + \left(\mathbf{Q}_\perp^-\right)_{\mathrm{R}}, \tag{2.52}$$

where $\mathbf{Q}_\perp$ is the flux normal to a cell-interface between upstream and downstream states L and R, respectively. The contravariant Mach number at the cell-interface is split as

$$\begin{aligned} M_\perp &= \left(M_\perp^+\right)_{\mathrm{L}} + \left(M_\perp^-\right)_{\mathrm{R}}, \\ \text{with } M_\perp^\pm &= \begin{cases} \frac{1}{2}\left(M_\perp \pm |M_\perp|\right) & \text{for } |M_\perp| \geq 1 \\ \pm\frac{1}{4}\left(M_\perp \pm 1\right)^2 & \text{otherwise} \end{cases}. \end{aligned} \tag{2.53}$$

In case of 2D subsonic flow, i.e., $|M_\perp| < 1$ the split fluxes are obtained as [57]

$$\mathbf{Q}_\perp^\pm = \pm\frac{\rho a}{4}\left(M_\perp\right)^2 \begin{bmatrix} 1 \\ u + \frac{n_x(u_\perp \pm 2a)}{\gamma} \\ v + \frac{n_y(u_\perp \pm 2a)}{\gamma} \\ \frac{\{(\gamma-1)u_\perp \pm 2a\}^2}{2(\gamma^2-1)} + \frac{u^2+v^2-u_\perp^2}{2} \end{bmatrix}. \tag{2.54}$$

For supersonic flow across the cell-interface, i.e. $|M_\perp| \geq 1$ the fluxes are split in the following manner to obtain upwinding:

$$\left.\begin{aligned} \mathbf{Q}_\perp^+ = \mathbf{Q}_\perp, \mathbf{Q}_\perp^- = 0 \text{ if } M_\perp \geq 1 \\ \mathbf{Q}_\perp^+ = 0, \mathbf{Q}_\perp^- = \mathbf{Q}_\perp \text{ if } M_\perp \leq -1 \end{aligned}\right\}. \tag{2.55}$$

In equation 2.54, n_x and n_y are the x- and y-components of the unit vector normal to the cell-interface and $u_\perp$ is the contravariant velocity as mentioned in Appendix D.

2.3.4 Advection Upstream Splitting Method (AUSM)

Liou and Steffen [7] pointed out that the inviscid flux vector at the cell-interface can be split into two physically distinct components, namely, the convective and acoustic parts. For 2D flow, this splitting can be represented as

$$\mathbf{Q}_\perp = u_\perp \begin{bmatrix} \rho \\ \rho u \\ \rho v \\ \rho h_0 \end{bmatrix} + \begin{bmatrix} 0 \\ p_{\frac{1}{2}} n_x \\ p_{\frac{1}{2}} n_y \\ 0 \end{bmatrix} = \mathbf{Q}^c_\perp + \mathbf{Q}^p_\perp, \tag{2.56}$$

where $p_{\frac{1}{2}}$ is the pressure at the cell-interface. The convective terms $\mathbf{Q}^c_\perp$ can be considered as passive scalar quantities convected by a suitably defined velocity $u_\perp$ at the cell-interface. On the other hand, the pressure terms $\mathbf{Q}^p_\perp$ are governed by the acoustic-wave speeds. The convective terms can be effectively written as

$$\begin{aligned} \mathbf{Q}^c_\perp &= u_\perp \begin{bmatrix} \rho \\ \rho u \\ \rho v \\ \rho h_0 \end{bmatrix}_{\mathrm{L/R}} = M_\perp \begin{bmatrix} \rho a \\ \rho u a \\ \rho v a \\ \rho h_0 a \end{bmatrix}_{\mathrm{L/R}}, \\ \text{where } \{*\}_{\mathrm{L/R}} &= \begin{cases} \{*\}_{\mathrm{L}} & \text{if } M_\perp \geq 0 \\ \{*\}_{\mathrm{R}} & \text{otherwise} \end{cases}. \end{aligned} \tag{2.57}$$

The contravariant Mach number $M_\perp$ can be obtained using equation 2.53 as in van Leer's FVS scheme. The pressure at the interface in the flux-vector component $\mathbf{Q}^p_\perp$ is split as follows:

$$\begin{aligned} p_{\frac{1}{2}} &= p^+_{\mathrm{L}} + p^-_{\mathrm{R}}, \\ \text{with } p^\pm &= \begin{cases} \frac{p}{2}\left(\frac{M \pm |M|}{M}\right) & \text{if } |M_\perp| \geq 1 \\ \frac{p}{4}\left(M \pm 1\right)^2 \left(2 \mp M\right) & \text{otherwise} \end{cases}. \end{aligned} \tag{2.58}$$

To express the AUSM scheme in artificial-viscosity form, firstly the contravariant Mach number may be split in the form:

$$\begin{aligned} M_\perp &= M^+_\perp + M^-_\perp, \\ \text{where } M^\pm_\perp &= \frac{1}{2}\left(M_\perp \pm |M_\perp|\right). \end{aligned} \tag{2.59}$$

It is evident from equation 2.59 that

$$M_\perp = \begin{cases} M_\perp^+ & \text{if } M_\perp \geq 0 \\ M_\perp^- & \text{otherwise} \end{cases}, \tag{2.60}$$

and

$$|M_\perp| = M_\perp^+ - M_\perp^-. \tag{2.61}$$

Substituting equations 2.59, 2.60 and 2.61 in equation 2.57 the convective part of the flux vector can be written as

$$\begin{aligned} \mathbf{Q}_\perp^c &= M_\perp^+ \begin{bmatrix} \rho a \\ \rho u a \\ \rho v a \\ \rho h_0 a \end{bmatrix}_{\mathrm{L}} + M_\perp^- \begin{bmatrix} \rho a \\ \rho u a \\ \rho v a \\ \rho h_0 a \end{bmatrix}_{\mathrm{R}} \\ &= \frac{1}{2} M_\perp \left[\begin{Bmatrix} \rho a \\ \rho u a \\ \rho v a \\ \rho h_0 a \end{Bmatrix}_{\mathrm{L}} + \begin{Bmatrix} \rho a \\ \rho u a \\ \rho v a \\ \rho h_0 a \end{Bmatrix}_{\mathrm{R}} \right] - \frac{1}{2} |M_\perp| \, \Delta_{\frac{1}{2}} \begin{Bmatrix} \rho a \\ \rho u a \\ \rho v a \\ \rho h_0 a \end{Bmatrix}, \end{aligned} \tag{2.62}$$

where

$$\Delta_{\frac{1}{2}} \{*\} = \{*\}_{\mathrm{R}} - \{*\}_{\mathrm{L}}. \tag{2.63}$$

In the right-hand side of equation 2.62 the first term is a Mach-number-weighted average and the second term is the numerical diffusion associated with the numerical approximation of the convective part of the flux vector. Comparing the numerical-diffusion term of the AUSM scheme with the corresponding term for the FDS approach (equation 2.51), it is seen that for 2D Euler equations the AUSM scheme requires 4 operations whereas the FDS approach requires $4^2 = 16$ operations. Finally using equations 2.62 and 2.58 in equation 2.56 the interface-flux with the AUSM scheme can be expressed as

$$\mathbf{Q}_\perp = \frac{1}{2} M_\perp \left[\begin{Bmatrix} \rho a \\ \rho u a \\ \rho v a \\ \rho h_0 a \end{Bmatrix}_{\mathrm{L}} + \begin{Bmatrix} \rho a \\ \rho u a \\ \rho v a \\ \rho h_0 a \end{Bmatrix}_{\mathrm{R}} \right]$$

$$- \frac{1}{2} |M_\perp| \Delta_{\frac{1}{2}} \begin{Bmatrix} \rho a \\ \rho u a \\ \rho v a \\ \rho h_0 a \end{Bmatrix} + \begin{bmatrix} 0 \\ \left(p_{\mathrm{L}}^{+} + p_{\mathrm{R}}^{-}\right) n_x \\ \left(p_{\mathrm{L}}^{+} + p_{\mathrm{R}}^{-}\right) n_y \\ 0 \end{bmatrix}. \quad (2.64)$$

2.3.5 Radespiel and Kroll's Hybrid scheme

The AUSM scheme, though less robust, is generally more accurate than van Leer's FVS scheme in predicting viscous and inviscid flows. The former scores over the other in terms of low computational complexity and low numerical diffusion [18]. However, it is found that the AUSM scheme suffers from the limitation of producing pressure-oscillations in the vicinity of strong shocks under adverse-grid situations and flow-alignment. Radespiel and Kroll [18] designed a hybrid flux vector scheme that switched from AUSM to van Leer's FVS at shock waves. In this scheme, the interface-flux is written using the following expression:

$$\mathbf{Q}_\perp = \frac{1}{2} M_\perp \left[\begin{Bmatrix} \rho a \\ \rho u a \\ \rho v a \\ \rho h_0 a \end{Bmatrix}_{\mathrm{L}} + \begin{Bmatrix} \rho a \\ \rho u a \\ \rho v a \\ \rho h_0 a \end{Bmatrix}_{\mathrm{R}} \right] - \frac{1}{2} \phi_{\frac{1}{2}} \Delta_{\frac{1}{2}} \begin{Bmatrix} \rho a \\ \rho u a \\ \rho v a \\ \rho h_0 a \end{Bmatrix} + \begin{bmatrix} 0 \\ \left(p_{\mathrm{L}}^{+} + p_{\mathrm{R}}^{-}\right) n_x \\ \left(p_{\mathrm{L}}^{+} + p_{\mathrm{R}}^{-}\right) n_y \\ 0 \end{bmatrix}. \quad (2.65)$$

The contravariant Mach number $M_\perp$ and split pressures $p^{\pm}$ are obtained using the equations 2.53 and 2.58, respectively. The coefficient of the numerical-diffusion term for the convective part of the flux vetor $\phi_{\frac{1}{2}}$ is obtained using the following expressions:

$$\phi_{\frac{1}{2}} = (1 - \omega)\, \phi_{\frac{1}{2}}^{\mathrm{vL}} + \omega \phi_{\frac{1}{2}}^{\mathrm{modAUSM}}, \quad (2.66)$$

with

$$\phi_{\frac{1}{2}}^{\mathrm{vL}} = \begin{cases} |M_\perp| & \text{if } |M_\perp| \geq 1 \\ |M_\perp| + \frac{1}{2} \left\{ (M_\perp)_{\mathrm{R}} - 1 \right\}^2 & \text{if } 0 \leq M_\perp < 1 \\ |M_\perp| + \frac{1}{2} \left\{ (M_\perp)_{\mathrm{L}} + 1 \right\}^2 & \text{if } -1 < M_\perp \leq 0 \end{cases}, \quad (2.67)$$

and

$$\phi_{\frac{1}{2}}^{\text{modAUSM}} = \begin{cases} |M_\perp| & \text{if } |M_\perp| > \tilde{\delta} \\ \frac{M_\perp^2 + \tilde{\delta}^2}{2\tilde{\delta}} & \text{if } 0 \leq |M_\perp| \leq \tilde{\delta} \end{cases}, \tag{2.68}$$

where $\tilde{\delta}$ $\left(0 < \tilde{\delta} \leq 0.5\right)$ is a small parameter required to avoid the numerical diffusion approaching zero as $M_\perp \to 0$, and ω $(0 \leq \omega \leq 0.5)$ is a constant. It may be noted that for $\omega = 0$ the scheme given by equation 2.65 becomes the van Leer's FVS and for $\omega = 1$ it reverts back to the AUSM scheme.

2.4 Central schemes

In central schemes the interface-flux is computed by using a symmetric stencil without considering the directions of the associated characteristic velocities. An upwind scheme provides better nonlinear stability near shocks since it inherently satisfies the stencil adaptation required to satisfy the CFL criteria [9]. On the other hand the central schemes enjoy the merit of simplicity without bothering about the 'wind direction' for hyperbolic conservation laws. For a system of hyperbolic conservation laws the coupled nature of the characteristic equations is an integral part to be considered in the design of upwind schemes. On the contrary the central schemes can handle each equation of a system of hyperbolic conservation laws as a separate scalar equation. P. D. Lax was the pioneer of the central schemes [22, 23]. Later on Jameson played a pivotal role in the development of high-resolution central schemes [5, 35]. This section presents a general mathematical framework of the central schemes followed by the formulations of the Local Lax-Friedrichs (LLF) [24], Diffusion-Regulated Local Lax-Friedrichs (DRLLF) [40] and Directional Diffusion-Regulated Local Lax-Friedrichs (DDRLLF) [41] schemes.

2.4.1 Artificial-viscosity form of central schemes

It is well-known that pure central discretization of the fluxes for hyperbolic conservation laws lead to numerical instabilities. The stabilizing effect is imparted to a central scheme by the addition of a numerical-diffusion term. The numerical-diffusion terms lead to second-order derivatives or viscous-like effects in the discrete

form of the governing equations. However, excessive numerical diffusion degrades the solution accuracy by smearing the discontinuities and shear layers. In central schemes it is simpler to control the numerical diffusion explicitly so that it is maximum at shocks or discontinuities and minimum in smooth-flow regions. The introduction of viscous-like effects by the numerical-diffusion terms can be explained with the example of a central scheme having a constant numerical-diffusion coefficient applied to a 1D hyperbolic scalar coservation law. Consider a 1D hyperbolic scalar conservation law

$$\frac{\partial u}{\partial t} + \frac{\partial f(u)}{\partial x} = 0, \tag{2.69}$$

where u is the conserved variable, $f(u)$ is the flux and $\frac{\mathrm{d}f(u)}{\mathrm{d}u} = a$ is real. With reference to figure 2.1, the discrete form of equation 2.69 with the first-order Euler-explicit time-discretization becomes

$$\frac{\overline{u}_I^{n+1} - \overline{u}_I^n}{\Delta t} + \frac{\widehat{f}^n_{I+\frac{1}{2}} - \widehat{f}^n_{I-\frac{1}{2}}}{\Delta x} = 0, \tag{2.70}$$

where $\overline{u}_I^{n+1}$ and $\overline{u}_I^n$ are the cell-averaged values of u in the cell I at time levels $n+1$ and n, $\widehat{f}^n_{I+\frac{1}{2}}$ and $\widehat{f}^n_{I-\frac{1}{2}}$ are the conservative numerical fluxes at cell faces $I+\frac{1}{2}$ and $I-\frac{1}{2}$ at time level n, respectively. Considering a constant numerical-diffusion coefficient Γ the conservative numerical fluxes can be expressed in artificial-viscosity form [9] as

$$\widehat{f}^n_{I-\frac{1}{2}} = \frac{1}{2}\left\{f\left(\overline{u}^n_{I-1}\right) + f\left(\overline{u}^n_I\right)\right\} - \frac{1}{2}\Gamma\left(\overline{u}^n_I - \overline{u}^n_{I-1}\right), \tag{2.71a}$$

$$\widehat{f}^n_{I+\frac{1}{2}} = \frac{1}{2}\left\{f\left(\overline{u}^n_I\right) + f\left(\overline{u}^n_{I+1}\right)\right\} - \frac{1}{2}\Gamma\left(\overline{u}^n_{I+1} - \overline{u}^n_I\right). \tag{2.71b}$$

Substituting equations 2.71a 2.71b in equation 2.70 one obtains

$$\begin{aligned}\frac{\overline{u}_I^{n+1} - \overline{u}_I^n}{\Delta t} + \frac{f\left(\overline{u}^n_{I+1}\right) - f\left(\overline{u}^n_{I-1}\right)}{2\Delta x} &= \frac{\Gamma\left(\overline{u}^n_{I+1} - 2\overline{u}^n_I + \overline{u}^n_{I-1}\right)}{2\Delta x} \\ &= \frac{\Gamma\Delta x}{2}\left\{\frac{\overline{u}^n_{I+1} - 2\overline{u}^n_I + \overline{u}^n_{I-1}}{(\Delta x)^2}\right\}.\end{aligned} \tag{2.72}$$

Equation 2.72, written in discrete form can be recast in the form of a partial differential equation with a truncation error as

$$\frac{\partial u}{\partial t} + \frac{\partial f(u)}{\partial x} = \frac{\Gamma\Delta x}{2}\frac{\partial^2 u}{\partial x^2} + \mathcal{O}\left\{\Delta t, (\Delta x)^2\right\}. \tag{2.73}$$

The first term on the right-hand side of equation 2.73 corresponds to the artificial viscosity caused by the numerical-diffusion terms in equations 2.71a and 2.71b. It

is to be noted that the original equation 2.69 is inviscid, whereas the addition of numerical diffusion in the approximation of the discrete numerical fluxes leads to the dissipative effects seen in equation 2.73. The numerical-diffusion terms in the central schemes also create the upwinding-like effect without bothering about the characteristic velocities. This is evident from the similarilty of the correponding terms in equations 2.71a, 2.71b, 2.51 and 2.35. These equations can also be written in a more general aritificial-viscosity form of the conservative numerical flux as

$$\widehat{f}^{n}_{I+\frac{1}{2}} = \frac{1}{2}\left\{f\left(\overline{u}^{n}_{I}\right) + f\left(\overline{u}^{n}_{I+1}\right)\right\} - D_{I+\frac{1}{2}}, \tag{2.74}$$

where $D_{I+\frac{1}{2}}$ is the numerical diffusive flux.

2.4.2 Local Lax-Friedrichs scheme

The Local Lax-Friedrichs (LLF) scheme was proposed by Rusanov [24]. This is an improved version of the Lax-Friedrichs (LxF) method [22]. For the 1D Euler equations the interface-flux can be computed by using the LxF method as:

$$\mathbf{F}_{I+\frac{1}{2}} = \frac{1}{2}\left(\mathbf{F}_{\mathrm{L}} + \mathbf{F}_{\mathrm{R}}\right) - \frac{1}{2}\frac{\Delta x}{\Delta t}\left(\mathbf{U}_{\mathrm{R}} - \mathbf{U}_{\mathrm{L}}\right). \tag{2.75}$$

For a constant grid-spacing and a global time-stepping, the numerical-diffusion coefficient for this scheme is constant and is $\frac{\Delta x}{\Delta t}$. However, using the CFL condition across a cell-interface it can be written that

$$\begin{aligned} \frac{|\lambda_{\max}|\,\Delta t}{\Delta x} &\leq 1 \\ |\lambda_{\max}| &\leq \frac{\Delta x}{\Delta t}, \end{aligned} \tag{2.76}$$

where $|\lambda_{\max}|$ is the maximum of the moduli of eigenvalues of the flux Jacobian matrices across the cell-interface $I + \frac{1}{2}$ given by

$$|\lambda_{\max}| = \max\left(|u_{\mathrm{L}}| + a_{\mathrm{L}}, |u_{\mathrm{R}}| + a_{\mathrm{R}}\right). \tag{2.77}$$

The LLF scheme replaces the constant numerical-diffusion coefficient of the LxF method with a reduced one whose value changes locally with the cell-interface in view of equation 2.76. For the 1D Euler equations the interface-flux is computed by using the LLF scheme as

$$\mathbf{F}_{I+\frac{1}{2}} = \frac{1}{2}\left(\mathbf{F}_{\mathrm{L}} + \mathbf{F}_{\mathrm{R}}\right) - \frac{1}{2}\left|\lambda_{\max}\right|\left(\mathbf{U}_{\mathrm{R}} - \mathbf{U}_{\mathrm{L}}\right). \tag{2.78}$$

For the 2D Euler equations the flux vector normal to the cell-interface between the given left and right states L and R, respectively, is computed by using the LLF scheme as

$$\mathbf{Q}_\perp = \frac{1}{2}\left\{(\mathbf{Q}_\perp)_\mathrm{L} + (\mathbf{Q}_\perp)_\mathrm{R}\right\} - \frac{1}{2}\left|\lambda_\perp\right|_{\max}(\mathbf{U}_\mathrm{R} - \mathbf{U}_\mathrm{L}), \tag{2.79}$$

where $|\lambda_\perp|_{\max} = \max\left\{(u_\perp)_\mathrm{L} + a_\mathrm{L}, (u_\perp)_\mathrm{R} + a_\mathrm{R}\right\}$. Equations 2.78 and 2.79 ensure that in the case of LLF scheme the numerical-diffusion coefficients for the Euler equations are always positive real numbers. This helps in avoiding expansive sonic points without using any entropy fix [4].

2.4.3 Diffusion-Regulated Local Lax-Friedrichs scheme

The interface-flux using any numerical scheme can be written in a general form:

$$\mathbf{Q}_\perp = \frac{1}{2}\left\{(\mathbf{Q}_\perp)_\mathrm{L} + (\mathbf{Q}_\perp)_\mathrm{R}\right\} - \mathbf{D}_\perp, \tag{2.80}$$

where $\mathbf{D}_\perp$ is the diffusive flux. Jaisankar and Raghurama Rao [40] introduced the Diffusion-Regulation (DR) parameter Φ to regulate the numerical diffusion, leading to a diffusion-regulated scheme of the form:

$$\mathbf{Q}_\perp = \frac{1}{2}\left\{(\mathbf{Q}_\perp)_\mathrm{L} + (\mathbf{Q}_\perp)_\mathrm{R}\right\} - \Phi\mathbf{D}_\perp. \tag{2.81}$$

For effective shock capturing the numerical diffusion should satisfy three requirements:

1. In most of the accurate schemes, including those by Roe or Osher, the diffusive flux is of the form $\alpha\Delta U$ and therefore assumes small values away from the shock discontinuities, where ΔU is amall. Hence a minimal dissipation for stable solution is sufficient in the zones away from shock discontinuities.

2. For a greater accuracy the dissipation near to a shock, but not at the shock discontinuity itself, must be adequate and do the job of diminishing the influence of left state on right state and *vice-versá*. But most of the schemes for the vector conservation laws fail to completely eliminate this influence and as a result the shock becomes smeared owing to the contributions from both sides of the shock.

3. The numerical dissipation at the steady contact discontinuities should be zero to have an exact capture.

The DR parameter is modelled to fulfil the first two requirements to a great extent. This leads to a low dissipative, yet robust, scheme. In addition, the numerical dissipation is also driven to zero at a steady contact discontinuity, with the use of an exponential function of an average Mach number at the cell-interface. This makes possible the 'exact' capturing of the steady contact discontinuities. The parameter Φ is modelled as a simple function of the jump in normal Mach number across the cell-interface $\Delta M_\perp$ as follows:

$$\Phi = \begin{cases} \frac{\left\{(\Delta M_\perp)^2+\delta^2\right\}}{2\delta}\left\{1-e^{-\kappa(M_\perp)_{\mathrm{a}}}\right\} & \text{when } |\Delta M_\perp| \leq \delta \\ |\Delta M_\perp| & \text{when } \delta < |\Delta M_\perp| \leq 1.0 \\ 1 & \text{when } |\Delta M_\perp| > 1.0 \end{cases}, \tag{2.82}$$

where $(M_\perp)_{\mathrm{a}}$ is the average normal Mach number across the cell-interface. The suggested value of δ when solving the Euler equations is 0.5 [40], which is reported to have worked well for most of the test cases. Unless otherwise mentioned in the present thesis, the DRLLF scheme is implemented with $\delta = 0.5$ throughout. The parameter κ is empirically assigned a value of 10 that works well for the supersonic test cases. For subsonic flows higher value of κ is desirable. It may be noted that the exponential term $\left\{1-e^{-\kappa(M_\perp)_{\mathrm{a}}}\right\}$ improves quality of results only for slow moving contact discontinuities in inviscid flows. For high-speed flow applications, such situation is absent. Further, in certain viscous applications such as near a solid boundary and flow-separation across a cell-interface, the exponential term may give rise to an anti-diffusive term that is potentially destabilizing. Accordingly, the present thesis uses the DR parameter Φ without the exponential term so that

$$\Phi = \begin{cases} \frac{\left\{(\Delta M_\perp)^2+\delta^2\right\}}{2\delta} & \text{when } |\Delta M_\perp| \leq \delta \\ |\Delta M_\perp| & \text{when } \delta < |\Delta M_\perp| \leq 1.0 \\ 1 & \text{when } |\Delta M_\perp| > 1.0 \end{cases}. \tag{2.83}$$

With the introduction of the DR parameter given by equation 2.83 the diffusion-regulated version of the LLF scheme, named as DRLLF scheme becomes

$$\mathbf{Q}_{\perp} = \frac{1}{2}\left\{(\mathbf{Q}_{\perp})_{\mathrm{L}} + (\mathbf{Q}_{\perp})_{\mathrm{R}}\right\} - \frac{1}{2}\Phi\,|\lambda_{\perp}|_{\max}\,(\mathbf{U}_{\mathrm{R}} - \mathbf{U}_{\mathrm{L}})\,. \tag{2.84}$$

The variation of Φ as a function of $\Delta M_{\perp}$ without the exponential term is shown in figure 2.2. A minimum residual dissipation is retained, except when the average Mach number is close to zero, to prevent the violation of the entropy condition.

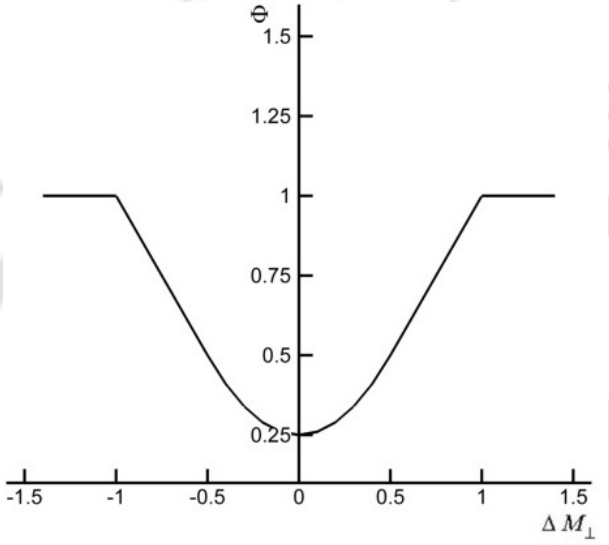

Fig. 2.2. DR parameter Φ without the exponential term.

2.4.4 Directional Diffusion-Regulated Local Lax-Friedrichs scheme

Jaisankar and Sheshadri [41] introduced a computational parameter called Directional Diffusion Regulator (DDR) for some numerical solvers of systems of hyperbolic conservation laws. The aim of this new method was to bring forth real multidimensional physics into the upwind discretization. The basic idea of this regulator-driven method is to retain a full upwind scheme across local discontinuities, with the upwind bias decreasing smoothly to a minimum away from the discontinuity. The DDR is designed with the following properties:

1. On the application of DDR to a solver, the full numerical diffusion of the parent scheme is retained in the normal direction to a discontinuity.

2. The diffusive flux should vary smoothly to a low value when moving away from the direction of maximum gradient.

These design requirements are incorporated by considering the ratio of the gradient across a finite volume interface to the local maximum gradient. Considering any weak-solution variable ψ (could be pressure, temperature or density) the ratio of the gradient across the cell-interface to the local maximum gradient (μ_{g}) is expressed as

$$\mu_{\mathrm{g}} = \frac{\left|\frac{\Delta\psi}{\Delta s}\right|_{\mathrm{int}}}{\left|\frac{\Delta\psi}{\Delta s}\right|_{\mathrm{int\_max}}}, \tag{2.85}$$

where $\left|\frac{\Delta\psi}{\Delta s}\right|_{\mathrm{int}}$ is the gradient of ψ across a finite volume interface and $\left|\frac{\Delta\psi}{\Delta s}\right|_{\mathrm{int\_max}}$ is the maximum of gradients at the interface.

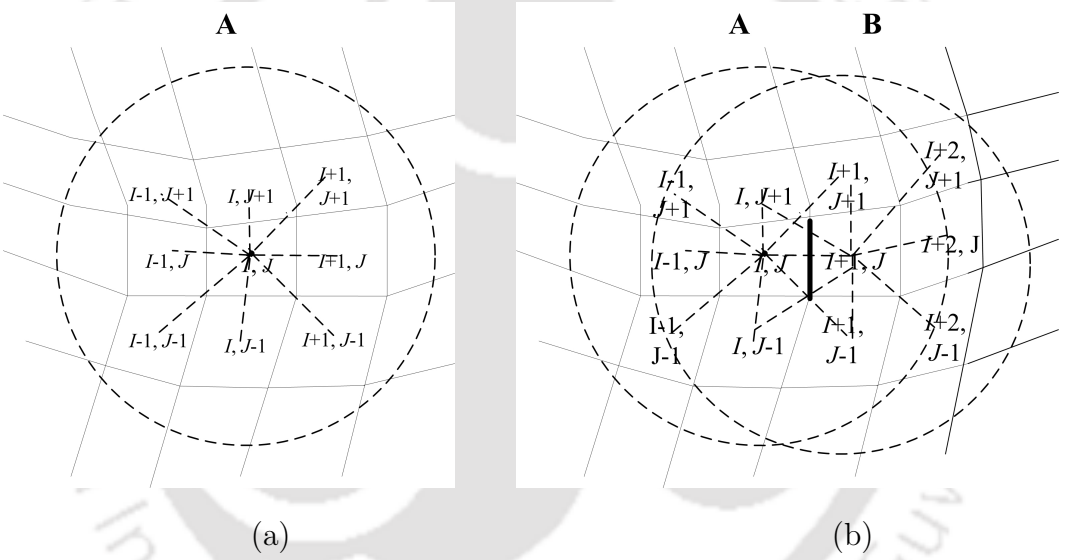

(a) (b)

Fig. 2.3. (a) Circle 'A' encloses a typical finite volume update point (I, J) connected with its immediate neighbours through dotted lines along which gradients are computed to obtain maximum gradient about (I, J) (b) Region (A∪B) shows (a)-like figures for points (I, J) and $(I + 1, J)$, which are intersecting to form an interface (thick line) where DDR is computed.

With reference to figure 2.3, the left and right cells of the cell-interface (shown by the thick line) are (I, J) and $(I+1, J)$, respectively. Representing any arbitrary cell by the symbol P, and immediate neighbours by 'k' the highest value of the maximum gradient about P is obtained by

$$\left|\frac{\Delta\psi}{\Delta s}\right|_{\mathrm{max\_P}} = \max\left(\left|\frac{\psi_{\mathrm{P}} - \psi_k}{d_{\mathrm{P},k}}\right|, k = 1, 2, 3, ..., n\right), \tag{2.86}$$

'$d_{\mathrm{P},k}$' is the distance between points P and k. The quantity $\left|\frac{\Delta\psi}{\Delta s}\right|_{\mathrm{int\_max}}$ is then obtained as an arithmetic mean of maximum gradients about the left and right states of the cell-interface.

$$\left|\frac{\Delta\psi}{\Delta s}\right|_{\mathrm{int\_max}} = \mathrm{mean}\left(\left|\frac{\Delta\psi}{\Delta s}\right|_{\mathrm{max\_left}}, \left|\frac{\Delta\psi}{\Delta s}\right|_{\mathrm{max\_right}}\right). \tag{2.87}$$

The parameter μ_{g} is then utilized to obtain the DDR Φ_{d}, which defines the directional bias to the diffusive-flux term.

$$\Phi_{\mathrm{d}} = \begin{cases} \frac{\mu_{\mathrm{g}}^2+(b-1)\delta^2}{b\delta} & \text{for } \mu_{\mathrm{g}} \leq \delta \\ |\mu_{\mathrm{g}}| & \text{for } \delta < |\mu_{\mathrm{g}}| \leq 1.0 \\ 1 & \text{for } \mu_{\mathrm{g}} > 1.0 \end{cases}. \tag{2.88}$$

The value of μ_{g} is assumed to be zero whenever $\left|\frac{\Delta\psi}{\Delta s}\right|_{\mathrm{int\_max}} \leq 10^{-12}$ to avoid blow-up. The suggested range of δ is 0.5 to 0.65. Usually b is taken as 2. In very fine grids the suggested value of b is in the range 3 to 4 [41]. The DDR given by equation 2.88 is used with the diffusive flux of the LLF scheme to obtain the Directional Diffusion-Regulated Local Lax-Friedrichs (DDRLLF) scheme. For 2D flows the interface-flux using the DDRLLF scheme is expressed as

$$\mathbf{Q}_{\perp} = \frac{1}{2}\left\{(\mathbf{Q}_{\perp})_{\mathrm{L}} + (\mathbf{Q}_{\perp})_{\mathrm{R}}\right\} - \frac{1}{2}\Phi_{\mathrm{d}}\left|\lambda_{\perp}\right|_{\max}(\mathbf{U}_{\mathrm{R}} - \mathbf{U}_{\mathrm{L}}). \tag{2.89}$$

2.5 Flux-averaged schemes

It is an established fact that a first-order-upwind scheme such as van Leer's FVS is stable even near shocks, but it may be too diffusive to cause large smearing of discontinuities. On the other hand a second-order-accurate scheme like MacCormack's scheme [25] captures steeper shocks, albeit with numerical oscillations in its vicinity. In other words, these schemes, named as the first-generation methods [9] have a basic limitation that they 'mindlessly' treat every part of the solution as same, thereby maintaining a constant theoretical order of accuracy throughout the computational domain. Flux-averaging is a technique of designing high-resolution schemes by using a combination of two schemes having complimentary properties. These schemes belong to the second- and third-generation schemes [9].

Let us consider a cell-interface $I+\frac{1}{2}$ shared by two adjoining cells having centroids at I and $I+1$ as shown in figure 2.1. For the sake of lucidity we consider 1D control volumes; but the same methodology can be easily extended to cell-centred finite volume methods in multiple dimensions. If $\widehat{f}^{(1)}_{I+\frac{1}{2}}$ and $\widehat{f}^{(2)}_{I+\frac{1}{2}}$ are the conservative numerical fluxes of two schemes with complementary properties, then the flux-averaged conservative numerical flux at the cell-interface is given by [9]

$$\widehat{f}^{n}_{I+\frac{1}{2}} = \mathrm{avg}^{n}_{I+\frac{1}{2}} \left(\widehat{f}^{(1)}_{I+\frac{1}{2}}, \widehat{f}^{(2)}_{I+\frac{1}{2}} \right), \tag{2.90}$$

where $\mathrm{avg}^{n}_{I+\frac{1}{2}}$ is some averaging function. Equation 2.90 can also be recast in the form

$$\widehat{f}^{n}_{I+\frac{1}{2}} = \widehat{f}^{(1)}_{I+\frac{1}{2}} + \phi_{I+\frac{1}{2}} \left(\widehat{f}^{(2)}_{I+\frac{1}{2}} - \widehat{f}^{(1)}_{I+\frac{1}{2}} \right), \tag{2.91}$$

where $\phi_{I+\frac{1}{2}}$ is some averaging function that provides a suitable combination of $\widehat{f}^{(1)}_{I+\frac{1}{2}}$ and $\widehat{f}^{(2)}_{I+\frac{1}{2}}$. In the artificial-viscosity forms the fluxes $\widehat{f}^{(1)}_{I+\frac{1}{2}}$ and $\widehat{f}^{(2)}_{I+\frac{1}{2}}$ can be written as

$$\widehat{f}^{(1)}_{I+\frac{1}{2}} = \frac{1}{2}\left(f_{\mathrm{L}} + f_{\mathrm{R}}\right) - \frac{1}{2}\varepsilon^{(1)}_{I+\frac{1}{2}}\left(u_{\mathrm{R}} - u_{\mathrm{L}}\right), \tag{2.92a}$$

$$\widehat{f}^{(2)}_{I+\frac{1}{2}} = \frac{1}{2}\left(f_{\mathrm{L}} + f_{\mathrm{R}}\right) - \frac{1}{2}\varepsilon^{(2)}_{I+\frac{1}{2}}\left(u_{\mathrm{R}} - u_{\mathrm{L}}\right), \tag{2.92b}$$

where $\varepsilon^{(1)}_{I+\frac{1}{2}}$ and $\varepsilon^{(2)}_{I+\frac{1}{2}}$ are numerical-diffusion coefficients of the corresponding schemes. If $\widehat{f}^{(1)}_{I+\frac{1}{2}}$ is chosen as more diffusive than $\widehat{f}^{(2)}_{I+\frac{1}{2}}$ then $\varepsilon^{(1)}_{I+\frac{1}{2}} \geq \varepsilon^{(2)}_{I+\frac{1}{2}}$. Substituting equations 2.92a and 2.92b in equation 2.91 one obtains

$$\widehat{f}^{n}_{I+\frac{1}{2}} = \widehat{f}^{(1)}_{I+\frac{1}{2}} + \frac{1}{2}\phi_{I+\frac{1}{2}}\left(\varepsilon^{(1)}_{I+\frac{1}{2}} - \varepsilon^{(2)}_{I+\frac{1}{2}}\right)\left(u_{\mathrm{R}} - u_{\mathrm{L}}\right). \tag{2.93}$$

The second term in the above equation is anti-diffusive. Now for numerical stability and high resolution, the parameter $\phi_{I+\frac{1}{2}}$ can be so chosen that $\phi_{I+\frac{1}{2}} \to 0$ near shocks and $\phi_{I+\frac{1}{2}} \to 1$ in smooth regions. In other words the flux-averaged schemes belong to the class of solution-sensitive methods, which vary the theoretical order of accuracy as per the flow-field configuration.

2.5.1 Flux-limited methods

For simplicity the flux-limited framework is discussed here for the 1D hyperbolic scalar conservation law given by equation 2.69. In the context of flux-limited

methods the averaging parameter $\phi_{I+\frac{1}{2}}$ is called a *flux limiter*. By tradition, flux-limited methods often 'bump' the spatial index on the flux limiter up or down by one half, depending on wind direction [9]. In particular, if the wave speed $a > 0$, then

$$\widehat{f}^n_{I+\frac{1}{2}} = \widehat{f}^{(1)}_{I+\frac{1}{2}} + \phi^n_I \left(\widehat{f}^{(2)}_{I+\frac{1}{2}} - \widehat{f}^{(1)}_{I+\frac{1}{2}} \right), \tag{2.94}$$

and if $a < 0$, then

$$\widehat{f}^n_{I+\frac{1}{2}} = \widehat{f}^{(1)}_{I+\frac{1}{2}} + \phi^n_{I+1} \left(\widehat{f}^{(2)}_{I+\frac{1}{2}} - \widehat{f}^{(1)}_{I+\frac{1}{2}} \right). \tag{2.95}$$

Equations 2.94 and 2.95 are only the starting points for flux-limited methods, rather than a rigid framework. It can also be observed that neither of these two equations satisfy the condition required to compute the interface-flux $\widehat{f}^n_{I+\frac{1}{2}}$ across sonic points, i.e. $a = 0$. To satisfy these requirements a range of flux-limited methods are available that use different notations that appear to deviate from the basic form of this class of schemes shown by equations 2.94 and 2.95. The choice of the constituent schemes and the flux limiter is crucial in the design of this class of schemes. The flux limiter is to be so chosen that the flux-limited scheme switches to one constituent scheme near shocks and to the other one in smooth regions. In this regard it is crucial for the flux limiter to distinguish shocks from smooth regions. In the case of flux-limited methods the parameter $\phi_{I+\frac{1}{2}}$ is chosen as some function of the ratios of the neighbouring solution or flux differences. In terms of solution differences these ratios can be expressed as follows:

$$r^+_I = \frac{\overline{u}^n_I - \overline{u}^n_{I-1}}{\overline{u}^n_{I+1} - \overline{u}^n_I}, \tag{2.96a}$$

$$r^-_I = \frac{\overline{u}^n_{I+1} - \overline{u}^n_I}{\overline{u}^n_I - \overline{u}^n_{I-1}}. \tag{2.96b}$$

The ratios r^+_I and r^-_I can also be expressed in terms of the ratios of the neighbouring flux differences as

$$r^+_I = \frac{\widehat{f}^{(2)}_{I-\frac{1}{2}} - \widehat{f}^{(1)}_{I-\frac{1}{2}}}{\widehat{f}^{(2)}_{I+\frac{1}{2}} - \widehat{f}^{(1)}_{I+\frac{1}{2}}}, \tag{2.97a}$$

$$r^-_I = \frac{\widehat{f}^{(2)}_{I+\frac{1}{2}} - \widehat{f}^{(1)}_{I+\frac{1}{2}}}{\widehat{f}^{(2)}_{I-\frac{1}{2}} - \widehat{f}^{(1)}_{I-\frac{1}{2}}}. \tag{2.97b}$$

It can be shown that for the linear advection equation and for constant differences between the numerical-diffusion coefficients of the constituent flux schemes the

ratios computed based on solution differences and flux differences are equivalent. From equations 2.96a, 2.96b, 2.97a and 2.97b it can be noticed that $r_I^+ = 1/r_I^-$. The flux-limiter function can be expressed in terms of the ratio of the solution or flux differences as follows:

$$\phi_I^n = \phi\left(r_I^+\right), \tag{2.98a}$$

$$\phi_{I+1}^n = \phi\left(r_{I+1}^-\right). \tag{2.98b}$$

Various limiters like minmod, superbee, van Leer etc. can be used as flux limiters in designing the flux-limited methods.

2.5.2 Flux-Corrected-Transport methods

Boris and Book [30] started the era of flux-corrected methods by designing a two-step, flux-corrected blend of the first-order-upwind method and Lax-Wendroff scheme [23]. They named their scheme as Flux-Corrected Transport (FCT). The flux-corrected methods for scalar conservation laws can be written in the general form:

$$\begin{aligned} \widehat{f}_{I+\frac{1}{2}}^n &= \widehat{f}_{I+\frac{1}{2}}^{(1)} + \widehat{f}_{I+\frac{1}{2}}^{(\mathrm{C})} \\ &= \widehat{f}_{I+\frac{1}{2}}^{(1)} + \mathrm{diff}_{I+\frac{1}{2}}^n \left(\widehat{f}_{I+\frac{1}{2}}^{(1)}, \widehat{f}_{I+\frac{1}{2}}^{(2)}\right), \end{aligned} \tag{2.99}$$

where $\widehat{f}_{I+\frac{1}{2}}^{(\mathrm{C})}$ is corrective-numerical flux and $\mathrm{diff}_{I+\frac{1}{2}}^n$ is a differencing function. Equation 2.99 can also be written in flux-limited-like form:

$$\widehat{f}_{I+\frac{1}{2}}^n = \widehat{f}_{I+\frac{1}{2}}^{(1)} + \phi_{I+\frac{1}{2}}^n \left(\widehat{f}_{I+\frac{1}{2}}^{(2)} - \widehat{f}_{I+\frac{1}{2}}^{(1)}\right), \tag{2.100}$$

where the second term on the right-hand side of equation 2.100 represents the corrective-numerical flux of equation 2.99. It is to be noted that a traditional difference exists between the flux-limited and flux-corrected-transport methods. The function $\phi_{I+\frac{1}{2}}^n$ in case of flux-limited methods depends on the *ratios of the solution or flux differences* $r_I^{\pm}$. On the other hand for the flux-corrected-transport methods the function $\phi_{I+\frac{1}{2}}^n$ relies on the *solution or flux differences* of neighbouring cells. Of course the limiter functions like minmod, superbee, van Leer etc. can also be used for these methods.

2.5.3 Self-adjusting-hybrid methods

The self-adjusting-hybrid methods use convex linear combinations of two numerical schemes having complimentary properties. This class of schemes can be obtained from the flux-averaged form given by equation 2.91. For this purpose a new parameter $\theta_{I+\frac{1}{2}}$ is used that is related to the parameter $\phi_{I+\frac{1}{2}}$ as

$$\theta_{I+\frac{1}{2}} = 1 - \phi_{I+\frac{1}{2}}. \tag{2.101}$$

Substituting equation 2.101 in equation 2.91 we obtain a self-adjusting-hybrid method:

$$\widehat{f}^{n}_{I+\frac{1}{2}} = \theta_{I+\frac{1}{2}} \widehat{f}^{(1)}_{I+\frac{1}{2}} + \left(1 - \theta_{I+\frac{1}{2}}\right) \widehat{f}^{(2)}_{I+\frac{1}{2}}. \tag{2.102}$$

The parameter $\theta_{I+\frac{1}{2}}$ is called the shock switch. The convexity condition requires that $\theta_{I+\frac{1}{2}} \leq 1$. Near shocks $\theta_{I+\frac{1}{2}} \to 1$ and in smooth-flow regions $\theta_{I+\frac{1}{2}} \to 0$. Accordingly, the self-adjusting hybrid scheme given by equation 2.102 acts close to $\widehat{f}^{(1)}_{I+\frac{1}{2}}$ and $\widehat{f}^{(2)}_{I+\frac{1}{2}}$ near shocks and smooth-flow regions, respectively.

Fig. 2.4. The same discrete data may represent both smooth and discontinuous solutions.

The governing principle behind the design of a shock switch is that it should be close to 1 near shocks and close to zero in smooth regions. In general, shock switches distinguish shocks from smooth-flow regions, switching on at shocks and switching off in smooth regions. However, a shock switch that operates in this fashion is far from perfect. When handling discrete points the same data set may represent both smooth and shock solutions as shown in figure 2.4 owing to the reason that any sampling contains only limited information about the solution, especially solutions with jump discontinuities.

There are various approaches for designing shock switches. One such approach is presented here. This is based on the proven fact that large divided differences indicate discontinuous derivatives and accordingly the shock switches are made

functions of first- or second-divided differences [9]. Let us consider

$$\theta^n_{I+\frac{1}{2}} = \max\left(\theta^n_I, \theta^n_{I+1}\right), \tag{2.103}$$

where for any solution-variable u,

$$\theta^n_I = \frac{\overline{u}^n_{I+1} - 2\overline{u}^n_I + \overline{u}^n_{I-1}}{(\Delta x)^2}.$$

To ensure $\theta^n_{I+\frac{1}{2}} \geq 0$ the absolute value of the second-divided differences are considered as follows:

$$\theta^n_I = \frac{\left|\overline{u}^n_{I+1} - 2\overline{u}^n_I + \overline{u}^n_{I-1}\right|}{(\Delta x)^2}.$$

To satisfy the condition $\theta_{I+\frac{1}{2}} \leq 1$ the divided difference is normalized using the triangle inequality

$$\frac{\left|\left(\overline{u}^n_{I+1} - \overline{u}^n_I\right) - \left(\overline{u}^n_I - \overline{u}^n_{I-1}\right)\right|}{(\Delta x)^2} \leq \frac{\left|\overline{u}^n_{I+1} - \overline{u}^n_I\right| + \left|\overline{u}^n_I - \overline{u}^n_{I-1}\right|}{(\Delta x)^2}.$$

One possible expression for θ^n_I is

$$\theta^n_I = \frac{\left|\left(\overline{u}^n_{I+1} - \overline{u}^n_I\right) - \left(\overline{u}^n_I - \overline{u}^n_{I-1}\right)\right|}{\left|\overline{u}^n_{I+1} - \overline{u}^n_I\right| + \left|\overline{u}^n_I - \overline{u}^n_{I-1}\right|}. \tag{2.104}$$

2.6 Solution-averaging: Reconstruction-evolution methods

The solution-averaging approach, also called reconstruction-evolution or solution-reconstruction is explained here using the 1D unsetady Euler equations given by equation 2.8. Any equation from the system of 1D Euler equations can be written in the form:

$$\frac{\partial U}{\partial t} + \frac{\partial F}{\partial x} = 0, \tag{2.105}$$

where U is the conserved variable and F is the corresponding flux. The semi-discrete version of equation 2.105 on a cell-centred FVM approach is given by

$$\frac{d\overline{U}_I}{dt} + \frac{F_{I+\frac{1}{2}} - F_{I-\frac{1}{2}}}{\Delta x} = 0, \tag{2.106}$$

where $\overline{U}_I$ is the volume-averaged value of the conserved variable over a cell (refer figure 2.1), having centroid at I given by

$$\overline{U}_I = \frac{1}{V_I}\int_{V_I} U dx,$$

where V_I is the volume of the cell, and $F_{I\pm\frac{1}{2}}$ is the corresponding spatial flux quadrature. It may be noted from Appendix C that the flux vector $\mathbf{F}$ is a function of the conserved varables U_1, U_2 and U_3, which in turn can be expressed in terms of the solution or primitive variables.

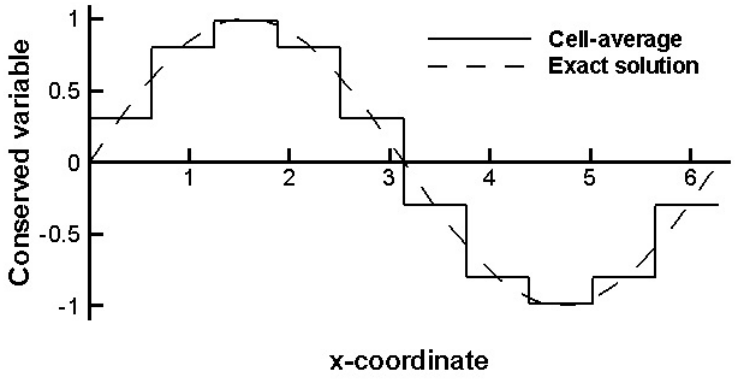

Fig. 2.5. Exact function $U(x) = \sin x$ and cell-averaged $\overline{U}_I$.

The discretization of the domain as shown in figure 2.1 and introduction of volume-averages $\overline{U}_I$ lead to loss of information regarding $U(x,t)$. Let us consider, for example, the periodic function $U(x) = \sin x$ within the domain $0 \leq x \leq 2\pi$. The exact function $U(x)$ and the cell-averaged values $\overline{U}_I$, assuming the decomposition of the domain into ten cells is shown in figure 2.5. From the figure it is evident that the cell-averaged value is only an approximation of the exact solution. Of course, the appoximation improves if the size of the cells is reduced. In computational methods, however, there is a constraint on refining the cell-size because of higher-memory requirement. This also leads to increased computational cost and round-off errors. Consequently, it is a standard practice to work with finite number of cells. Solution-reconstruction is one technique that can improve the solution-accuracy in spite of using volume-averages.

From equation 2.106 it is seen that finding the time-evolution of $\overline{U}_I$ requires the fluxes $F_{I\pm\frac{1}{2}}$, which in turn must be computed by using $U_{\mathrm{L/R}}$ in the vicinity of $x_{I\pm\frac{1}{2}}$. Within each cell I, a local approximate *reconstruction* $U_I(x)$ of the exact function $U(x)$ can be used to compute the fluxes. In doing so it is quite possible that a local discontinuity may exist at each cell-face, i.e. $U_{\mathrm{L}} \neq U_{\mathrm{R}}$. Thus each cell-interface may pose a Riemann problem. The numerical-flux scheme to compute $F_{I\pm\frac{1}{2}}$, must take this discontinuous behaviour into consideration [56].

The simplest approximations for the left and right states are $U_{\mathrm{L}} = \overline{U}_I$ and $U_{\mathrm{R}} = \overline{U}_{I+1}$, which are first-order accurate. However, this method leads to excessive numerical diffusion, and generally leads to inaccurate results, especially for viscous-flow computations [54]. In the solution-averaging approach higher-order accuracy is achieved by computing the numerical fluxes $F_{I\pm\frac{1}{2}}$ based on U_{L} and U_{R}, which are obtained by *suitable interpolation* of the $\overline{U}$ from the neighbouring cells. There are various approaches to solution-averaging. van Leer's Monotone Upstream-centred Scheme for Conservation Laws (MUSCL) [38], Colella-Woodward's Piecewise Parabolic Method (PPM) [58], Anderson-Thomas-van Leer's Modified Upwind Scheme for Conservation Laws [57], Harten-Osher's UNO method [59], Harten-Engquist-Osher-Chakravarthy's ENO method [60], Barth and Jasperson's piecewise linear reconstruction [61] etc. are a few of the many solution-averaging methods.

It may be noted that both flux-averaging and solution-averaging aim at obtaining higher order of accuracy in computing the numerical-flux terms. Flux-averaging combines two numerical-flux schemes with complimentary properties based on solution-sensitive algorithms. On the other hand in case of solution-averaging or solution-reconstruction, variation of the solution within a cell is reconstructed from the cell-average and the variables at the cell-interface are then interpolated from both the upstream and downstream sides. To ensure monotonous solution, some slope limiters are required.

2.6.1 van Leer's MUSCL approach

One possibility to compute the left and right states is to carry out linear interpolation using the same number of values to the left and right of the face. In other words, the interpolation is centred at the face. It can be shown that for hyperbolic conservation laws the central interpolation is unconditionally unstable [56]. On the other hand, upwind interpolations are based on the characteristics of the Euler equations. In this approach flow variables are interpolated separately from the left and the right sides of the face using non-symmetric stencil. van Leer's Monotone Upstream-centred Schemes for Conservation Laws (MUSCL) approach [38] is

based on characteristic-based interpolation of the flow variables. With reference to Figure 2.1, the left and right states for the cell-interface between the cells I and $I+1$ are computed by using the MUSCL approach as [54]:

$$U_{\mathrm{L}} = \overline{U}_I + \frac{\epsilon}{4}\left[(1+\widehat{\kappa})\,\Delta_{I+\frac{1}{2}}\overline{U} + (1-\widehat{\kappa})\,\Delta_{I-\frac{1}{2}}\overline{U}\right], \tag{2.107a}$$

$$U_{\mathrm{R}} = \overline{U}_{I+1} - \frac{\epsilon}{4}\left[(1+\widehat{\kappa})\,\Delta_{I+\frac{1}{2}}\overline{U} + (1-\widehat{\kappa})\,\Delta_{I+\frac{3}{2}}\overline{U}\right], \tag{2.107b}$$

where $\Delta_{I\pm\frac{1}{2}}\overline{U}$ is given by equation 2.32. If $\epsilon = 0$ the discretization becomes first-order accurate. For $\epsilon = 1$, the stencil size and the nature of the reconstruction varies depending on the value of the parameter $\widehat{\kappa}$. This is summarized in Table 2.1 [56].

Table. 2.1. Dependence of the type of reconstruction on the value of $\widehat{\kappa}$

$\widehat{\kappa}$	**Type of reconstruction**
1	Centered
1/3	Upwind-biased
0	Upwind-biased
-1	Upwind

2.6.2 Piecewise-linear reconstruction

In this approach reconstruction is done assuming that the solution is piecewise linearly distributed over the control volume. Here the reconstructed value of a variable U is computed as follows:

$$U_{\mathrm{L}} = \overline{U}_I + (\mathbf{r}_{\mathrm{c}} - \mathbf{r}_I)\,.\,(\underline{\nabla}U)_I\,, \tag{2.108a}$$

$$U_{\mathrm{R}} = \overline{U}_{I+1} + (\mathbf{r}_{\mathrm{c}} - \mathbf{r}_{I+1})\,.\,(\underline{\nabla}U)_{I+1}\,, \tag{2.108b}$$

where $\mathbf{r}_{\mathrm{c}}$, $\mathbf{r}_I$ and $\mathbf{r}_{I+1}$ represent the position vectors of the cell-face centre, and the cell-centroids of the left and right cells, respectively. $\underline{\nabla}U$ is the gradient of the variable U within a cell, which is computed by using the Green's theorem presented in Appendix E. But this reconstruction may lead to numerical oscillations. Barth

and Jasperson [61] suggested the use of a *limiter function* Φ to ensure monotone solution. Introducing limiters, equations 2.108a and 2.108b are recast as

$$U_{\mathrm{L}} = \overline{U}_I + \Phi_I \left(\mathbf{r}_{\mathrm{c}} - \mathbf{r}_I\right) . \left(\underline{\nabla} U\right)_I , \tag{2.109a}$$

$$U_{\mathrm{R}} = \overline{U}_{I+1} + \Phi_{I+1} \left(\mathbf{r}_{\mathrm{c}} - \mathbf{r}_{I+1}\right) . \left(\underline{\nabla} U\right)_{I+1} . \tag{2.109b}$$

The concept of limiters and some of their variants are presented in section 2.6.3.

2.6.3 Limiters

For a monotone solution, maxima in the flow field must be non-increasing and minima non-decreasing, and no new local extrema should arise during the time evolution. The Godunov's theorem [10], however, states that monotone linear numerical schemes for solving partial differential equation (PDE)s can be at most first-order accurate. Thus, higher-order accurate numerical schemes require non-linear limiter functions to suppress the numerical oscillations in the regions of high gradients like shocks. The function of a limiter is to reduce the slope $\left(\text{i.e., } \left(\overline{U}_{I+1} - \overline{U}_I\right)/\Delta x\right)$ used to interpolate a flow variable to the face of a control volume, in order to constrain the solution variations. In other words a limiter should carry out the following functions:

1. At strong discontinuities, the limiter has to reduce slopes to zero to prevent the generation of a new extremum. This implies for the solution-reconstruction schemes that the (monotone) first-order-upwind scheme is recovered in the immediate vicinity of high gradients.

2. In order to maintain a low level of numerical dissipation, the original unlimited discretization has to be obtained in smooth-flow regions.

The effect of a limiter on the interpolation of the left and right states is sketched in figure 2.6. In figure 2.6a the slope of local variation of U changes across the cells I and $I+1$. The use of a limiter enforces the slope of the variable inside cell I as zero and minimizes the slope-differences across adjacent cells as shown in figure 2.6b.

van Leer's MUSCL approach is converted to a monotonicity-preserving scheme by employing a limiter function to control the differences $\Delta_{I\pm\frac{1}{2}}U$ as per the re-

quirement. The MUSCL interpolation formulae given by equations 2.107a and 2.107b are modified by setting $\epsilon = 1$ and using a limiter function as follows:

$$U_{\mathrm{L}} = \overline{U}_I + \frac{1}{4}\left[(1+\widehat{\kappa})\,\Phi^{-}_{I+\frac{1}{2}}\Delta_{I+\frac{1}{2}}\overline{U} + (1-\widehat{\kappa})\,\Phi^{+}_{I-\frac{1}{2}}\Delta_{I-\frac{1}{2}}\overline{U}\right], \tag{2.110a}$$

$$U_{\mathrm{R}} = \overline{U}_{I+1} - \frac{1}{4}\left[(1+\widehat{\kappa})\,\Phi^{+}_{I+\frac{1}{2}}\Delta_{I+\frac{1}{2}}\overline{U} + (1-\widehat{\kappa})\,\Phi^{-}_{I+\frac{3}{2}}\Delta_{I+\frac{3}{2}}\overline{U}\right], \tag{2.110b}$$

where $\Phi^{\pm}_{I\pm\frac{1}{2}}$ are slope limiters, which are functions of ratios of consecutive solution variations, i.e. $\Phi^{\pm}_{I\pm\frac{1}{2}} = \Phi\left(r^{\pm}_{I\pm\frac{1}{2}}\right)$ with [62]

$$r^{+}_{I+\frac{1}{2}} = \frac{\overline{U}_{I+2} - \overline{U}_{I+1}}{\overline{U}_{I+1} - \overline{U}_I}, \tag{2.111a}$$

$$r^{-}_{I+\frac{1}{2}} = \frac{\overline{U}_I - \overline{U}_{I-1}}{\overline{U}_{I+1} - \overline{U}_I}. \tag{2.111b}$$

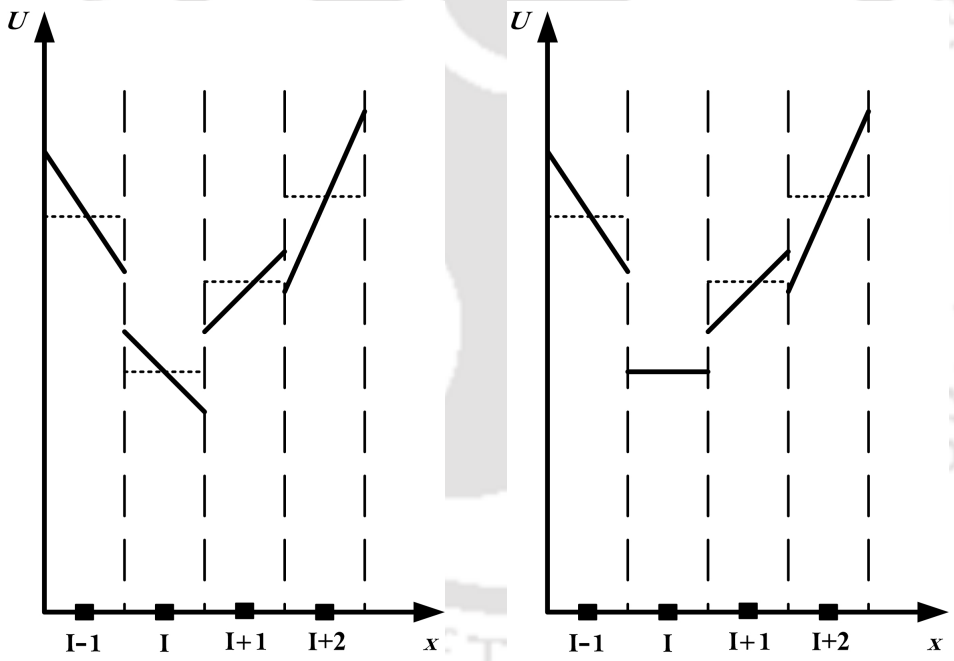

(a) (b)

Fig. 2.6. Comparison of (a) direct and (b) limited interpolation to the cell faces. (Thick lines represent the reconstructed solution, dotted horizontal lines represent cell-averages, and vertical-dashed lines represent the cell-interfaces.)

If $r_{\mathrm{L}} = r^{+}_{I-\frac{1}{2}}$ and $r_{\mathrm{R}} = r^{-}_{I+\frac{3}{2}}$, i.e.

$$r_{\mathrm{L}} = \frac{\overline{U}_{I+1} - \overline{U}_I}{\overline{U}_I - \overline{U}_{I-1}}, \tag{2.112a}$$

$$r_{\mathrm{R}} = \frac{\overline{U}_{I+1} - \overline{U}_I}{\overline{U}_{I+2} - \overline{U}_{I+1}}, \tag{2.112b}$$

then equations 2.110a and 2.110b can be recast in the form [54]

$$U_{\mathrm{L}} = \overline{U}_I + \frac{1}{4}\left[(1+\widehat{\kappa})\, r_{\mathrm{L}} \Phi\left(1/r_{\mathrm{L}}\right) + (1-\widehat{\kappa})\, \Phi\left(r_{\mathrm{L}}\right)\right]\left(\overline{U}_I - \overline{U}_{I-1}\right), \tag{2.113a}$$

$$U_{\mathrm{R}} = \overline{U}_{I+1} - \frac{1}{4}\left[(1+\widehat{\kappa})\, r_{\mathrm{R}} \Phi\left(1/r_{\mathrm{R}}\right) + (1-\widehat{\kappa})\, \Phi\left(r_{\mathrm{R}}\right)\right]\left(\overline{U}_{I+2} - \overline{U}_{I+1}\right). \tag{2.113b}$$

If $\Phi(r)$ is designed with symmetric property $\Phi(r) = \Phi(1/r)$, then equations 2.113a and 2.113b can be rewrttten as

$$U_{\mathrm{L}} = \overline{U}_I + \frac{1}{2}\Psi_{\mathrm{L}}\left(\overline{U}_I - \overline{U}_{I-1}\right), \tag{2.114a}$$

$$U_{\mathrm{R}} = \overline{U}_{I+1} - \frac{1}{2}\Psi_{\mathrm{R}}\left(\overline{U}_{I+2} - \overline{U}_{I+1}\right), \tag{2.114b}$$

where

$$\Psi_{\mathrm{L/R}} = \frac{1}{2}\left[(1+\widehat{\kappa})\, r_{\mathrm{L/R}} + (1-\widehat{\kappa})\right] \Phi_{\mathrm{L/R}}. \tag{2.115}$$

In the case of van Albada limiter $\widehat{\kappa} = 0$ and the slope limiter function is taken as

$$\Phi\left(r\right) = \frac{2r}{r^2+1}. \tag{2.116}$$

In this case the function $\Psi(r)$ corresponds to the van Albada limiter [63]

$$\Psi(r) = \frac{r^2 + r}{1 + r^2}. \tag{2.117}$$

With this definition of $\Psi(r)$ the left and right states of cell-interface are calculated using the van Albada limiter as [63]

$$U_{\mathrm{L}} = \overline{U}_I + \frac{1}{2}\delta_{\mathrm{L}}, \tag{2.118a}$$

$$U_{\mathrm{R}} = \overline{U}_{I+1} - \frac{1}{2}\delta_{\mathrm{R}}. \tag{2.118b}$$

The function δ is typically the same for both the states given by

$$\delta = \frac{a\left(b^2+\varepsilon\right) + b\left(a^2+\varepsilon\right)}{a^2 + b^2 + 2\varepsilon}, \tag{2.119}$$

so that

$$a_{\mathrm{R}} = \overline{U}_{I+2} - \overline{U}_{I+1},\ b_{\mathrm{R}} = \overline{U}_{I+1} - \overline{U}_I, \tag{2.120a}$$

$$a_{\mathrm{L}} = \overline{U}_{I+1} - \overline{U}_I,\ b_{\mathrm{L}} = \overline{U}_I - \overline{U}_{I-1}. \tag{2.120b}$$

The additional parameter ε is required to prevent the activation of the limiter in smooth-flow regions owing to small-scale oscillations. It has to be set proportional to the local-grid scale. In the present work it is taken proportional to the cell-volume V as

$$\varepsilon = 10 \times (V)^{1.25}. \tag{2.121}$$

In the case of Hemker and Koren limiter function $\widehat{\kappa} = 1/3$. The slope limiter is given by

$$\Phi(r) = \frac{3r}{2r^2 - r + 2}. \tag{2.122}$$

Following van Albada limiter the reconstruction formulae using the Hemker-Koren limiter become identical to equations 2.118a and 2.118b, with the function δ now having the form [54]

$$\delta = \frac{a\left(b^2 + 2\varepsilon\right) + b\left(2a^2 + \varepsilon\right)}{2a^2 + 2b^2 - ab + 3\varepsilon}. \tag{2.123}$$

The definitions of the parameters a, b and ε are retained as in equations 2.120a, 2.120b and 2.121.

The minmod limiter [64] presents an alternate formulation for the MUSCL approach. This form can be obtained using the symmetric property of the the slope limiter $\Phi(r)$ in equations 2.113a and 2.113b, which can be expressed as [56]

$$\begin{aligned} U_{\mathrm{L}} &= \overline{U}_I + \frac{1}{4}\left[(1+\widehat{\kappa})\,\Phi(r_{\mathrm{L}})\,\Delta_{I+\frac{1}{2}}\overline{U} + (1-\widehat{\kappa})\,\Phi(r_{\mathrm{L}})\,\Delta_{I-\frac{1}{2}}\overline{U}\right] \\ &= \overline{U}_I + \frac{1}{4}\left[(1+\widehat{\kappa})\,\widehat{\Delta}_{I+\frac{1}{2}}\overline{U} + (1-\widehat{\kappa})\,\widehat{\Delta}_{I-\frac{1}{2}}\overline{U}\right], \end{aligned} \tag{2.124a}$$

$$\begin{aligned} U_{\mathrm{R}} &= \overline{U}_{I+1} - \frac{1}{4}\left[(1+\widehat{\kappa})\,\Phi(r_{\mathrm{R}})\,\Delta_{I+\frac{1}{2}}\overline{U} + (1-\widehat{\kappa})\,\Phi(r_{\mathrm{R}})\,\Delta_{I+\frac{3}{2}}\overline{U}\right] \\ &= \overline{U}_{I+1} - \frac{1}{4}\left[(1+\widehat{\kappa})\,\widehat{\Delta}_{I+\frac{1}{2}}\overline{U} + (1-\widehat{\kappa})\,\widehat{\Delta}_{I+\frac{3}{2}}\overline{U}\right], \end{aligned} \tag{2.124b}$$

where

$$\widehat{\Delta}_{I-\frac{1}{2}}\overline{U} = \Phi(r_{\mathrm{L}})\,\Delta_{I-\frac{1}{2}}\overline{U} = \mathrm{minmod}\left(\Delta_{I-\frac{1}{2}}\overline{U}, b\Delta_{I+\frac{1}{2}}\overline{U}\right), \tag{2.125a}$$

$$\widehat{\Delta}_{I+\frac{1}{2}}\overline{U} = \Phi(r_{\mathrm{L}})\,\Delta_{I+\frac{1}{2}}\overline{U} = \mathrm{minmod}\left(b\Delta_{I-\frac{1}{2}}\overline{U}, \Delta_{I+\frac{1}{2}}\overline{U}\right), \tag{2.125b}$$

so that $b = \frac{3-\widehat{\kappa}}{1-\widehat{\kappa}}$ and

$$\text{minmod}(x,y) = \begin{cases} x & \text{if } |x| \leq |y| \text{ and } \text{sign}(x) = \text{sign}(y) \\ y & \text{if } |y| \leq |x| \text{ and } \text{sign}(x) = \text{sign}(y) \\ 0 & \text{if } \text{sign}(x) \neq \text{sign}(y) \end{cases}. \tag{2.126}$$

The Venkatakrishnan limiter function [39] is used with the piecewise-linear reconstruction given by equations 2.109a and 2.109b. It is given by

$$\Phi_I = \min_{J \in \mathrm{N}_I} \begin{cases} L\left(\overline{U}_I^M - \overline{U}_I, \Delta_{J\mathrm{c}}\right) & \text{if } \Delta_{J\mathrm{c}} > 0 \\ L\left(\overline{U}_I^m - \overline{U}_I, \Delta_{J\mathrm{c}}\right) & \text{if } \Delta_{J\mathrm{c}} < 0 \\ 1 & \text{otherwise} \end{cases}, \tag{2.127}$$

where

$$L(a,b) = \frac{a^2 + 2ab + \omega}{a^2 + b^2 + ab + \omega}, \tag{2.128a}$$

$$\Delta_{J\mathrm{c}} = (\mathbf{r}_\mathrm{c} - \mathbf{r}_J) \,.\, (\underline{\nabla} U)_J \,, \tag{2.128b}$$

$$\overline{U}_I^M = \max_{J \in \mathrm{N}_I} \left(\overline{U}_J - \overline{U}_I\right), \; \overline{U}_I^m = \min_{J \in \mathrm{N}_I} \left(\overline{U}_J - \overline{U}_I\right). \tag{2.128c}$$

In equation 2.127, N_I refers to all the neighbouring cells of the cell I and the subscript 'c' refers to the centre of the cell-face. The parameter ω is introduced to control the amount of limiting. Setting $\omega = 0$ leads to full limiting. On the other hand a large value of ω returns a weak limiter function. In the present work ω is assigned a value

$$\omega = (Kh)^3, \tag{2.129}$$

where K is a constant $\mathcal{O}(1)$ set equal to 5 [54] and the parameter h is equal to the square-root of the cell-volume in 2D.

In the framework of the CUSP scheme [5] the left and right states are evaluated to second-order accuracy using the following expressions:

$$U_\mathrm{L} = \overline{U}_I + \frac{1}{2} L\left(\Delta_{I+\frac{3}{2}} \overline{U}, \Delta_{I+\frac{1}{2}} \overline{U}\right), \tag{2.130a}$$

$$U_\mathrm{R} = \overline{U}_{I+1} - \frac{1}{2} L\left(\Delta_{I+\frac{3}{2}} \overline{U}, \Delta_{I+\frac{1}{2}} \overline{U}\right), \tag{2.130b}$$

where $L(a,b)$ is a limited average given by

$$L(a,b) = \frac{1}{2} \Psi(a,b)(a+b), \tag{2.131}$$

and $\Psi(a, b)$ is the limiter defined by

$$\Psi(a, b) = 1 - \left| \frac{a - b}{|a| + |b| + \varepsilon} \right|^2 . \tag{2.132}$$

The constant ε is assigned a very small value ($\varepsilon \approx 10^{-20}$) to avoid division by zero. Equation 2.132 shows that when a and b are of equal magnitude but opposite in sign, then the limiter becomes $\Psi(a, b) = 0$. This results in only first-order-accurate approximations to the left and right states.

Chapter 3

Role of Numerical Diffusion in Inviscid-Flow Computations

3.1 Introduction

In this chapter we present a preliminary study on the role of numerical diffusion in the computation of inviscid compressible flows. For the study initially the DRLLF scheme [40] is chosen. This is due to the fact that it is straighforward to control numerical diffusion of the DRLLF scheme by regulating the DR parameter as shown by equation 2.83. With the physical understanding developed through the DRLLF scheme on the effect of numerical diffusion in resolving flow features like shocks, contact discontinuities and expansion waves we compare its results with the AUSM [7], van Leer's FVS [14, 57], LLF [24], and DDRLLF [41] schemes and then make comments on the numerical-diffusion behaviour of these schemes. The numerical results are also compared with the analytical solutions, if available. We carry out the study through a range of carefully selected 1D, quasi-1D, 2D and axisymmetric-flow problems. The schemes are tested for subsonic to hypersonic regimes. The test cases include problems involving both grid-aligned and oblique shocks, which serve to study the performances of schemes in capturing shocks of varied strengths. In all the cases discretizations of the Euler equations of gas

dynamics governing the flow are done on the cell-centred FVM framework. We compute the flows numerically using solvers based on the programming language "C".

For study on 1D and quasi-1D flows the test cases considered are Sod's 1st shock tube problem [65] and quasi-1D flow through a converging-diverging nozzle [2]. Sod's shock tube problem is a classic-bench-marking problem to test the performances of numerical schemes for hyperbolic conservation laws. It finds its importance because it offers a variety of compressible-flow features like shocks, contact discontinuities and expansion waves, which can be used to study the efficacies of various numerical schemes. Sod's 1st shock tube problem involves an unsteady shock, where the absolute flows across the shock remain subsonic. In the computation of high-speed flow through nozzles quasi-1D approximations are known to give physically meaningful results [2, 66, 67]. We consider flow through a converging-diverging nozzle with a standing shock in the divergent portion of the nozzle. Both the test cases possess analytical solutions for validation of the numerical results [68].

For 2D flows the role of numerical diffusion is investigated with supersonic test cases of a converging-diverging nozzle, a forward-facing stepped channel [11], a 2D wedge and a ramped channel. Here the converging-diverging-nozzle flow considered for the quasi-1D case is computed by using a 2D formulation. Flow through a forward-facing-stepped channel involves a Mach reflection and a centred-expansion fan. Flow over a 2D wedge is an external-flow problem with an attached-weak shock and a centred-expansion wave. The ramped-channel problem involves an internal flow with interaction of a weak-reflected shock and a centered-expansion fan. These problems are chosen because the boundary conditions for these problems have to be handled differently and are as important as the numerical-flux schemes. The accuracy and robustness of the AUSM, van Leer's FVS, DRLLF and DDRLLF schemes to capture shocks of varied strengths are studied. Comparisons of the computational time for different test cases using these schemes are also made.

The study on effects of numerical-diffusion regulation is extended to inviscid-hypersonic flows. The test cases considered are flows over a semi-cylinder and a

hemisphere governed by the 2D and axisymmetric Euler equations, respectively. Inviscid analysis of hypersonic flow is found relevant in calculating the pressure coefficients, wave-drag coefficients of hypersonic-blunt bodies and also in establishing the Mach-number-independence principle [69]. The numerical solution of the governing equations for inviscid-hypersonic flow is also given importance by various researchers for studying the numerical stability of various flux schemes, especially at very high Mach numbers [7, 40, 70–72]. One significant feature of hypersonic speeds is that in the nose region of the blunt bodies the air temperature may reach extremely high levels so that chemical reactions like dissociation of oxygen and nitrogen molecules may occur [69]. If the vibrational excitation and chemical reactions take place very rapidly in comparison to the time it takes for a fluid element to move through the flow-field, we have vibrational and chemical-equilibrium flow. For an equilibrium-air model properties of high-temperature air are calculated using the polynomial correlation of Tannehill and Mugge [73]. Correlated and tabulated data of Tannehill and Mugge are widely used in practical computation of properties of high-temperature air. The ability of the DRLLF scheme to compute reacting-air flows is not available in reported literature. This motivates us to study the aspects of the DRLLF scheme in computing inviscid-hypersonic flows using the equilibrium-air model of Tannehill and Mugge. Although significant variations in the temperature fields obtained by the perfect gas and the equilibrium-air models are reported, the perfect-gas model is found to predict the pressure-field within 2% of the latter one [74]. Keeping this in view comparsions of results with the equilibrium-air and perfect-gas models are done.

This chapter is organized in five sections. The effects of varying the level of numerical diffusion on the computation of 1D and quasi-1D flow problems are presented in section 3.2. The effects of numerical diffusion in resolving strong and weak shocks for 2D supersonic flows are discussed in section 3.3. Application of the DRLLF scheme for computing 2D and axisymmetric-hypersonic flows over a semi-cylinder and a hemisphere, respectively, using an equlibrium-air model is explored in section 3.4. Concluding remarks are made in section 3.5.

3.2 Aspects of numerical-diffusion regulation for 1D and quasi-1D flows

This section first presents the governing equations for 1D and quasi-1D flows, followed by the problem statements for the shock tube and quasi-1D flow through a converging-diverging nozzle, the application of the boundary conditions for the quasi-1D flow problem and the results with discussion. In case of 1D and quasi-1D flows the discontinuities, if they exist, are normal to the flow-direction. Therefore analysis of the 1D and quasi-1D flows depict the performances of numerical schemes in resolving grid-aligned discontinuities.

3.2.1 The 1D and Quasi-1D Euler equations

For 1D flow the Euler equations of gas dynamics are given by:

$$\frac{\partial \mathbf{U}}{\partial t} + \frac{\partial \mathbf{F}}{\partial x} = 0, \tag{3.1}$$

where

$$\mathbf{U} = \begin{bmatrix} \rho \\ \rho u \\ \rho e_m \end{bmatrix}, \tag{3.2a}$$

$$\mathbf{F} = \begin{bmatrix} \rho u \\ p + \rho u^2 \\ (p + \rho e_m) u \end{bmatrix}. \tag{3.2b}$$

The Euler equations for quasi-1D flows are given by

$$\frac{\partial \mathbf{U}}{\partial t} + \frac{\partial \mathbf{F}}{\partial x} = \mathbf{J}, \tag{3.3}$$

where

$$\mathbf{U} = \begin{bmatrix} \rho A \\ \rho u A \\ \rho e_m A \end{bmatrix}, \tag{3.4a}$$

$$\mathbf{F} = \begin{bmatrix} \rho u A \\ (p + \rho u^2) A \\ (p + \rho e_m) u A \end{bmatrix}, \tag{3.4b}$$

$$\mathbf{J} = \begin{bmatrix} 0 \\ p\frac{\partial A}{\partial x} \\ 0 \end{bmatrix}. \tag{3.4c}$$

In equations 3.1 and 3.3, **U** and **F** are the flux vectors. It may be noted that an additional source term **J** appears in the quasi-1D Euler equations given by equation 3.3. The term A in equations 3.4a-3.4c represents the area of cross-section.

3.2.2 The shock tube problem

Figure 3.1 shows a shock tube of length $L = 10$ m, in the middle ($x = 5$ m) of which there exists a diaphragm that separates two gases of different pressures and densities. The gas on the left-hand side is at a higher pressure (p) and density (ρ) than the one on the right-hand side. Initially the gases on both sides of the diaphragm are at rest ($u = 0$). Subscript L indicates the left state and R the right state. The gases can exist at different pressures and densities and initially they are at zero velocity because they are separated by the diaphragm and the tube has closed ends. In the present problem we consider the gases on both the sides to be air whose specific-heat ratio is $\gamma = 1.4$. The diaphragm breaks at time $t = 0$. This makes a flow take place in the tube from the left (higher-pressure side) to right (lower-pressure side). The Mach number in the flow is high and inviscid-flow assumption gives physically realistic results. Hence we assume that the flow in the problem is governed by the 1D Euler equations (1DEE) given by equation 3.1.

A complex flow pattern develops in the tube. A series of expansion waves move to the left, and a shock wave and contact surface (a wave across which pressures are identical but density varies) move to the right. As the flow involves discontinuities like a shock and a contact surface, one needs to discretize the conservative form of the governing equations using a conservative scheme. The initial conditions are:

$$p_{\mathrm{L}} = 10^5 \text{ Pa}, \quad \rho_{\mathrm{L}} = 1.0 \text{ kg/m}^3, \quad u_{\mathrm{L}} = 0,$$

$$p_{\mathrm{R}} = 10^4 \text{ Pa}, \rho_{\mathrm{R}} = 0.125 \text{ kg/m}^3, u_{\mathrm{R}} = 0.$$

The flow is to be computed upto time $t = 0.0061$ sec. The time is so chosen that at that instant the waves do not reach the ends of the tube and at both the ends of

the tube, even at $t > 0$, the initial values of $\mathbf{U}$ can be used as boundary conditions.

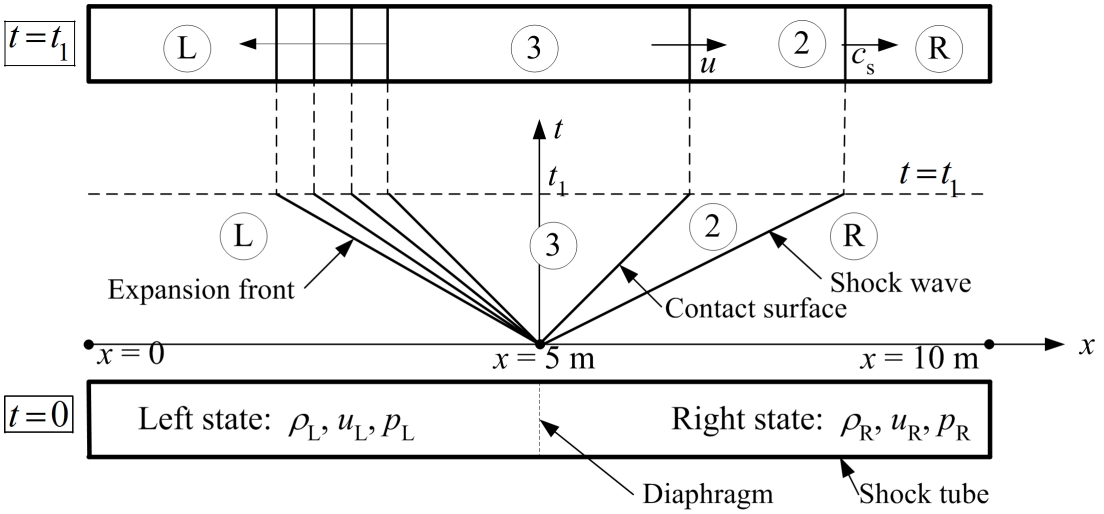

Shock-tube at instants $t = 0$ and $t = t_1$

Fig. 3.1. The schematic of the shock tube problem.

3.2.3 The Quasi-1D converging-diverging nozzle-flow problem

A converging-diverging nozzle of a prescribed geometry given by the following equation is taken [2]:

$$A(x) = 1 + 2.2(x - 1.5)^2,\ 0 \leq x \leq 3.0. \tag{3.5}$$

The reservoir pressure and temperature are taken as 101325 N/m^2 and 300 K, respectively. The back pressure is specified as 0.7 times the reservoir pressure. All the flow variables are functions of the distance along the nozzle axis (x) only. In addition, the cross-sectional area is also a function of x only. Such a flow is called quasi-1D flow. For the given nozzle geometry and back pressure, a standing normal shock wave is generated in the diverging portion of the nozzle at steady state. The flow is subsonic in the converging portion, sonic at the throat, supersonic in the diverging portion upto the normal shock and again subsonic thereafter. The steady state is to be computed both numerically and analytically.

3.2.4 Boundary conditions for quasi-1D flow

The inlet and outlet boundary conditions for computing the Euler equations of gas dynamics are specified depending on the number of characteristics entering and leaving the domain through the boundary. The number of variables to be specified at a boundary is equal to the number of characteristics entering the computational domain through that boundary. The number of variables extrapolated from within the computational domain at a boundary is the number of characteristics leaving the computational domain through that boundary [75].

For the quasi-1D nozzle-flow problem governed by the equations 3.3 there are three characteristic waves crossing any point in the flow domain simultaneously. The wave speeds are given by u, $u+a$ and $u-a$. Since the flow is considered to enter the nozzle from a reservoir where the gas is stagnant, hence the inlet flow is always subsonic ($u < a$). Hence at the inlet two characteristics will enter and one will leave the computational domain. Accordingly two variables are fixed at the inlet and one variable is extrapolated from inside. In this work, the pressure and temperature at inlet are specified as those of the reservoir conditions. The conserved variable for the momentum equation is extrapolated from within the computational domain. Owing to the presence of a standing normal shock in the divergent section the flow is subsonic at the nozzle exit. Therefore, two characteristics leave and one characteristic enters the computational domain. Accordingly the pressure at the outlet is specified as 0.7 times the reservoir pressure. The conserved variables for the continuity and momentum equations at the outlet are extrapolated from within the computational domain.

3.2.5 Effects of numerical diffusion in 1D and quasi-1D flows

All the numerical solutions for Sod's 1st problem are obtained with 200 cells and a CFL number of 0.2. Figure 3.2 shows the plot for the variations of density for Sod's 1st problem computed by using the DRLLF scheme for different values of δ (see equation 2.83) with increments of 0.1. The figure shows that as the numerical diffusion is reduced the numerical oscillations grow, especially near dis-

continuities[1]. Accordingly numerical oscillations are the maximum for $\delta = 0.1$ and as the numerical-diffusion level is raised these oscillations get reduced. There is only slight difference in the smearing of the shock and the contact discontinuity captured with δ=0.7 and δ=0.9. However the numerical oscillations are greatly reduced for $\delta = 0.9$. It may be noted that for $\delta = 1.0$ the DRLLF scheme becomes equivalent to the fully diffusive LLF scheme. Thus for the computation of the 1D shock tube problem using DRLLF scheme, the value of $\delta = 0.9$ is found to be the most appropriate in terms of reduction in spurious numerical oscillations with slight compromise in the resolution of the captured discontinuities. The reason for oscillations produced near the shock using the DRLLF scheme even at higher values of δ is that the jump in absolute Mach number across the shock is much less than unity for Sod's 1st problem since the absolute flows are subsonic.

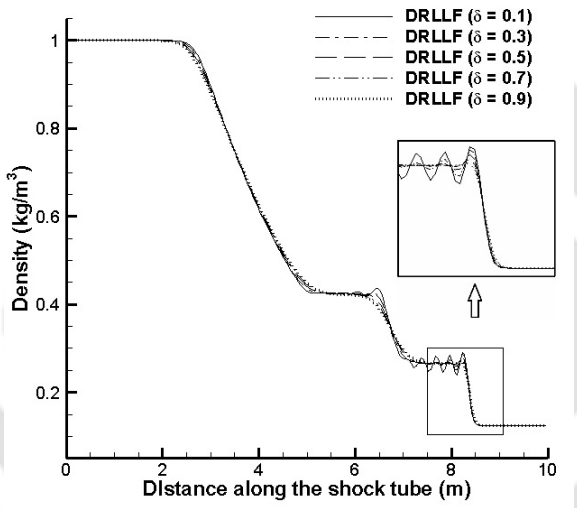

Fig. 3.2. Comparison of densities for the shock tube problem given by the DRLLF scheme using different values of δ.

Figure 3.3 shows the comparison of the density-variation plots with the LLF, DRLLF ($\delta = 0.9$) and DDRLLF schemes for the same problem. For the DDRLLF scheme, since the DDR assumes the value of unity for values of $\mu_g \geq 1$ and for 1D flow $\mu_g \geq 1$, hence Φ_d will always be close to unity. Thus this method works as an unregulated method for 1D problems. This is demonstrated in figure 3.3, where the density-variation plots for LLF and DDRLLF schemes are very close to each

[1]This work has been published in the proceedings of the 40th National Conference on Fluid Mechanics and Fluid Power (2013), National Institute of Technology Hamirpur, India

other. It is evident that among the LLF, DRLLF ($\delta = 0.9$) and DDRLLF schemes the DRLLF ($\delta = 0.9$) scheme outperforms the other two in computing Sod's 1st problem.

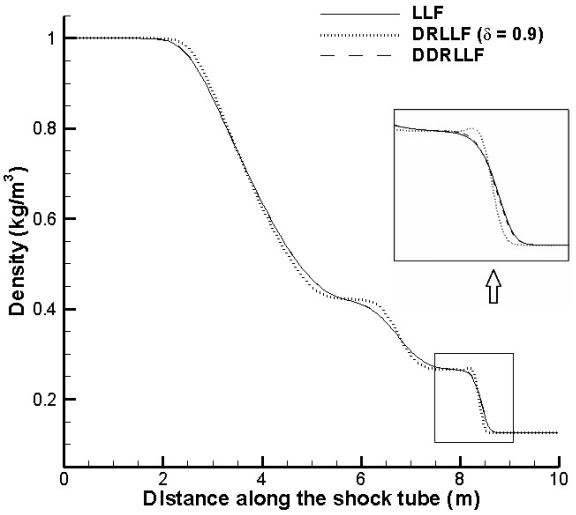

Fig. 3.3. Comparison of densities for the shock tube problem given by the LLF, DRLLF (δ=0.9) and DDRLLF schemes.

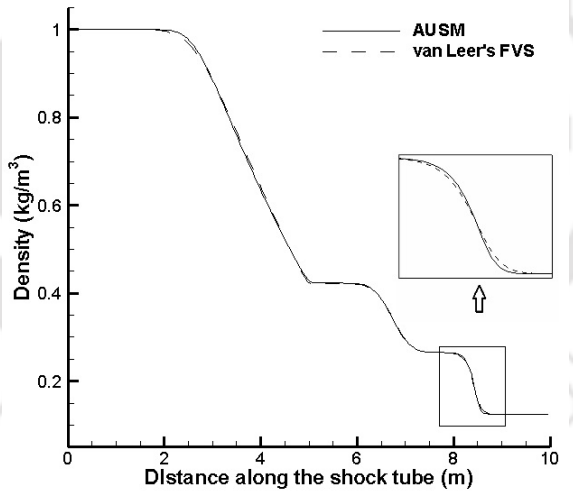

Fig. 3.4. Comparison of densities for the shock tube problem given by van Leer's FVS and AUSM schemes.

At this point it makes sense to make a comparison between the robust van Leer's FVS scheme [14] with the accurate AUSM [7] scheme. Figure 3.4 plots the density variations for Sod's 1st problem using the two schemes. It shows that the AUSM scheme, being less dissipative, resolves the expansion fan, contact discontinuity and the normal shock wave better than van Leer's FVS scheme.

With these observations we compare the AUSM and DRLLF ($\delta = 0.9$) schemes with the analytical solution for Sod's 1st problem in the density-variation plot shown in figure 3.5. The smearing of the shock captured by the DRLLF scheme is found to be less than that by AUSM. The resolutions of the contact discontinuity and the expansion fan captured by the two schemes are very much comparable to each other. Thus the DRLLF scheme appears to be a promising alternative for computation of inviscid-flux terms in the computation of high-speed flows.

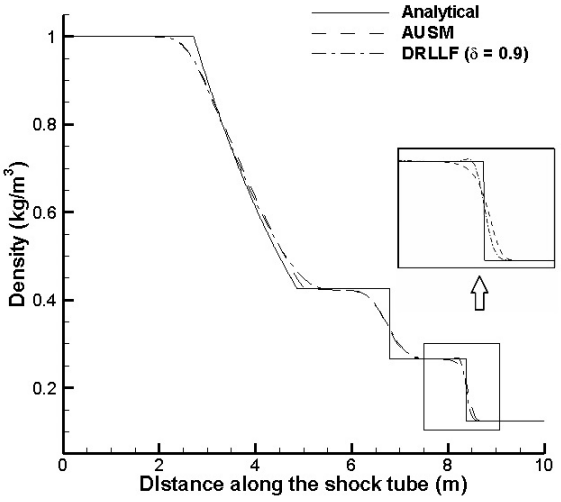

Fig. 3.5. Comparison of densities for the shock tube problem given by the AUSM scheme, DRLLF (δ=0.9) scheme and the analytical method.

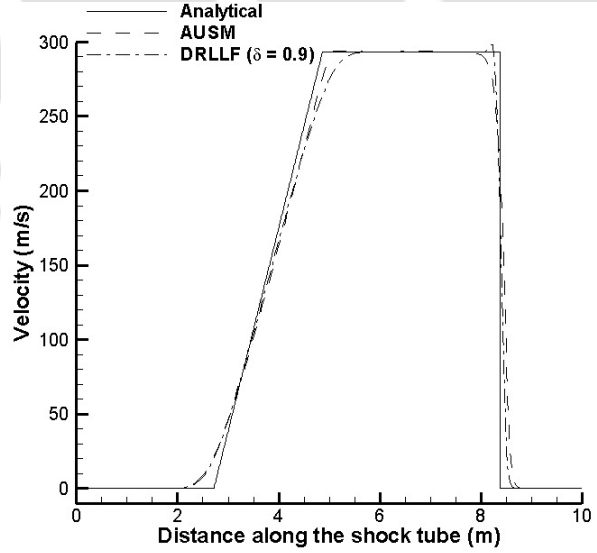

Fig. 3.6. Comparison of velocities for the shock tube problem given by the AUSM scheme, DRLLF (δ=0.9) scheme and the analytical method.

Figure 3.6 compares the computed velocity profiles for Sod's 1st problem using the AUSM and DRLLF ($\delta = 0.9$) schemes with the analytical results. The

continuity of the velocity field across the contact discntinuity is maintained by both the schemes. Along the flow-direction the downstream end of the expansion wave is marginally smeared by the DRLLF scheme. However the shock smearing is less with the DRLLF scheme compared with AUSM. At the same time the small-numerical oscillations near the shock produced by the DRLLF scheme leave a scope for further improvement of the scheme.

The numerical computations for the quasi-1D nozzle-flow problem are carried out using 60 cells with a CFL number of 0.2. In order to assess the effects of numerical diffusion in computing quasi-1D flows, figure 3.7 presents a comparison of the density variation along the nozzle, computed with the DRLLF scheme using various values of δ. For $\delta = 0.1$ and $\delta = 0.3$, although the smearing of the captured normal shock is less, the numerical oscillations near the shock are more. For $\delta = 0.5$, with slight reduction in the shock resolution these oscillations are almost eliminated. At higher values of δ, the smearing of the shock increases. Thus from figure 3.7 it appears that for the computation of quasi-1D converging-diverging nozzle-flow using the DRLLF scheme, the value $\delta = 0.5$ produces a reasonably accurate result.

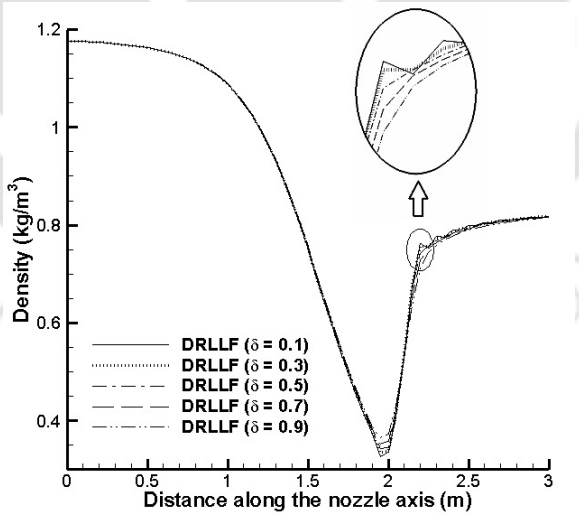

Fig. 3.7. Comparison of densities for the quasi-1D nozzle-flow problem given by the DRLLF scheme using different values of δ.

Figure 3.8 compares the density variations for the quasi-1D nozzle-flow computed with the LLF, DRLLF ($\delta = 0.5$) and DDRLLF schemes. As observed for the shock tube problem, in this case also the DDRLLF scheme acts like an unregulated

scheme. The DRLLF ($\delta = 0.5$) scheme outperforms the other two in resolving the shock. Thus it gets reinforced as reported in [41] that there is no scope to regulate the numerical diffusion with the DDRLLF scheme for 1D and quasi-1D flows. On the other hand the DRLLF scheme has a scope for improvement over the LLF scheme for this class of problems.

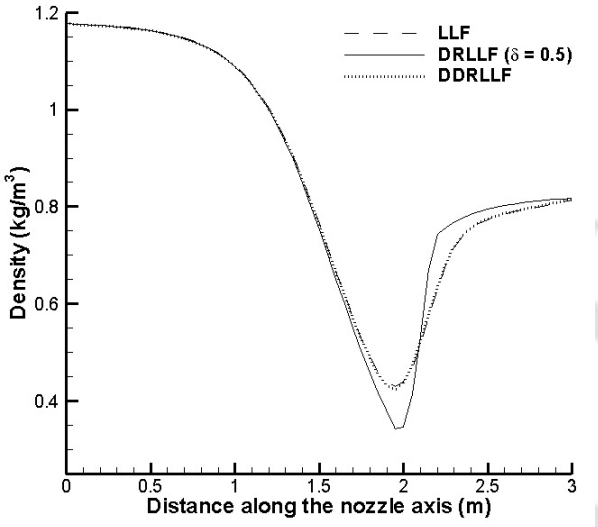

Fig. 3.8. Comparison of densities for the quasi-1D nozzle-flow problem given by the LLF, DRLLF (δ=0.5) and DDRLLF schemes.

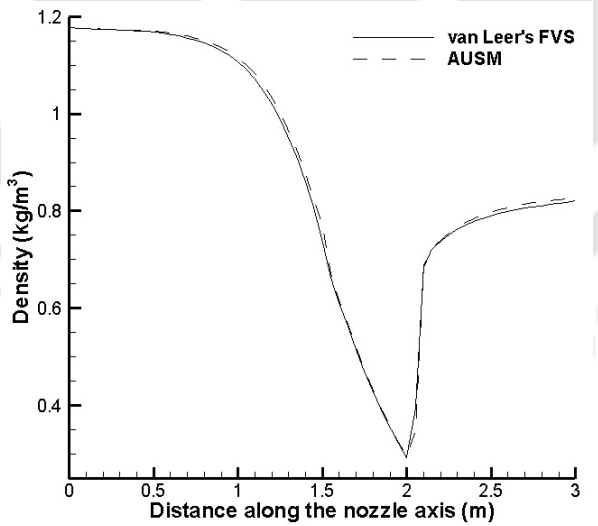

Fig. 3.9. Comparison of densities for the quasi-1D nozzle-flow problem given by van Leer's FVS and AUSM schemes.

Figure 3.9 shows the comparison of density variations for the quasi-1D nozzle-flow problem computed by using the AUSM and van Leer's FVS schemes and the curves are in close agreement. AUSM, being less diffusive, captures the normal shock with marginally less smearing. The density profiles for the problem using the

AUSM and DRLLF ($\delta = 0.5$) are compared with the analytical solution in figure 3.10. In this case since the flow upstream of the shock is supersonic hence the jump in Mach number is larger compared with Sod's 1st problem. As a result near the shock the DRLLF scheme is more diffusive and therefore the shock captured by the scheme gets more smeared compared with the AUSM scheme. Similar observations can be made from the Mach-number profile comparison of the AUSM and DRLLF ($\delta = 0.5$) schemes and the analytical results for the quasi-1D flow problem as shown by figure 3.11.

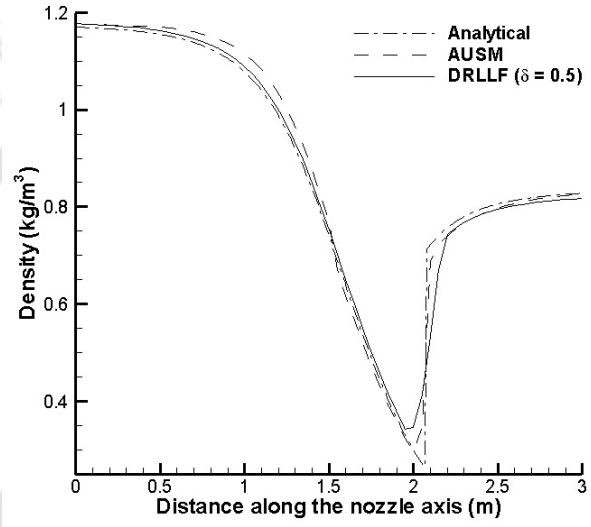

Fig. 3.10. Comparison of densities for the quasi-1D nozzle-flow problem given by the AUSM and DRLLF (δ=0.5) schemes and the analytical method.

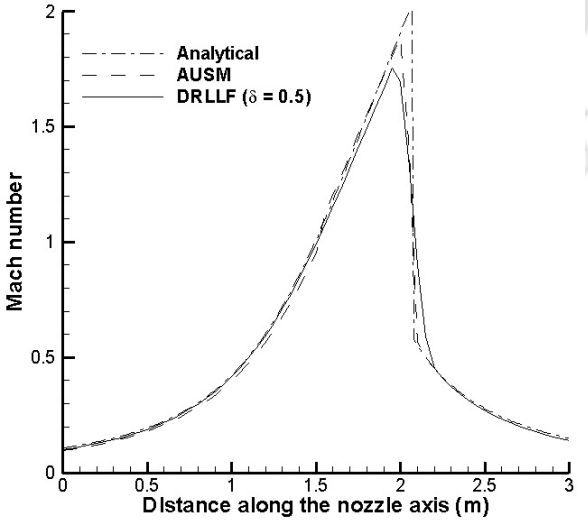

Fig. 3.11. Comparison of axial variations of Mach number for the quasi-1D nozzle-flow problem given by the AUSM and DRLLF (δ=0.5) schemes and the analytical method.

A study on the computational time taken by van Leer's FVS, AUSM, DRLLF and DDRLLF schemes for the 1D shock tube and quasi-1D nozzle-flow problems is done. The same machine and compiler are used for the comparison exercise. The processor is Intel(R) Core (TM) 2 Duo T5550 with processor speed of 1.83 GHz, and having 1GB RAM. The Microsoft Visual C++ 6 compiler is used to compile all the codes. Table 3.1 lists the CPU-time for these test problems taken by the four schemes. For Sod's 1st problem apparently there is no difference among the schemes in terms of the CPU-time. For the quasi-1D flow case the DRLLF scheme competes well with the AUSM and van Leer's FVS schemes in terms of the computational time. The DDRLLF scheme falls in between the DRLLF and AUSM schemes in terms of computational time. However there is hardly any point in focusing on this observation since the DDRLLF scheme does not actually control the numerical diffusion of the LLF scheme for the 1D and quasi-1D flows.

Table. 3.1. Comparison of CPU-time for 1D and quasi-1D flows

Test Problem	**Scheme**	**CPU-time (s)**
Sod's 1st problem	AUSM	0.281
	van Leer's FVS	0.281
	DRLLF	0.281
	DDRLLF	0.281
Quasi-1D flow	AUSM	7.187
	van Leer's FVS	7.406
	DRLLF	6.890
	DDRLLF	7.359

3.3 Aspects of numerical-diffusion regulation for 2D supersonic flows

In this section we first present the 2D planar and axisymmetric forms of the Euler equations of gas dynamics. This is followed by the problem statements for the

2D nozzle-flow, forward-facing-stepped channel, flow past a 2D wedge and the ramped-channel problems. Subsequently the treatments of boundary conditions are presented, followed by the results and discussion. The test problems are chosen in such a way that the performances of the various numerical schemes can be studied in resolving both grid-aligned and inclined shocks.

3.3.1 2D and Axisymmetric forms of the Euler equations

For 2D and axisymmetric flows the Euler equations are given by [76]

$$\frac{\partial \mathbf{U}}{\partial t} + \frac{\partial \mathbf{F}}{\partial x} + \frac{\partial \mathbf{G}}{\partial y} + \alpha \mathbf{S} = 0, \tag{3.6}$$

where $\mathbf{U}$, $\mathbf{F}$, $\mathbf{G}$, $\mathbf{S}$, α are the conserved-variable vector, flux vector along the x-direction, flux vector along the y-direction, source vector and a parameter governed by the nature of flow, respectively. These are given by

$$\mathbf{U} = \begin{bmatrix} \rho \\ \rho u \\ \rho v \\ \rho e_m \end{bmatrix}, \tag{3.7a}$$

$$\mathbf{F} = \begin{bmatrix} \rho u \\ p + \rho u^2 \\ \rho uv \\ (p + \rho e_m)u \end{bmatrix}, \tag{3.7b}$$

$$\mathbf{G} = \begin{bmatrix} \rho v \\ \rho uv \\ p + \rho v^2 \\ (p + \rho e_m)v \end{bmatrix}, \tag{3.7c}$$

$$\mathbf{S} = \frac{1}{y_c} \begin{bmatrix} \rho v \\ \rho uv \\ \rho v^2 \\ (p + \rho e_m)v \end{bmatrix}, \tag{3.7d}$$

$$\alpha = \begin{cases} 0 & \text{for 2D planar flow} \\ 1 & \text{for axisymmetric flow} \end{cases}, \tag{3.7e}$$

where y_c is the distance from the axis of symmetry.

3.3.2 The problem statements

For the nozzle-flow, the same problem considered in section 3.2.3 is computed with a 2D formulation. Owing to the curvature of the nozzle wall the streamlines become more curved at locations away from the axis. The standing normal shock becomes curved in order to maintain the perpendicularity between the streamline and the shock at the point of crossing. This problem offers a means to test the ability of the flux schemes to capture grid-aligned strong shocks.

In the case of forward-facing-stepped-channel problem [11] supersonic flow at Mach 3 enters a tunnel having a step facing the incoming flow. A detached curved shock is formed upstream of the step that causes a Mach reflection from the top wall. A centred expansion fan occurs at the step-corner. The flow configuration is a strong function of time. We compare the solutions obtained by the AUSM, van Leer's FVS, DRLLF and DDRLLF schemes at time $t = 8.1$ s. Table 3.2 lists the free-stream and geometric parameters for this problem.

Table. 3.2. The geometric and free-stream parameters for the forward-facing-stepped-channel problem

Parameter	**Value**
Length of the channel (L)	3 m
Height of the channel (H)	1 m
Distance of the step from the entrance (L_s)	0.6 m
Height of the step (H_s)	0.2 m
free-stream Mach number (M_∞)	3
free-stream pressure (p_∞)	101325 N/m^2
free-stream temperature (T_∞)	300 K

The supersonic flow past a 2D wedge involves interaction between a leading-edge shock and a centred-expansion fan emanating from the expansion-corner of the wedge. The interaction leads to gradual weakening of the leading-edge shock till it becomes a Mach wave at some finite distance from the wedge surface. The

incidence angle is zero and therefore the flow is symmetric. This problem tests the performances of the flux schemes in resolving weak shocks for external flows. The geometric and free-stream parameters for this problem are listed in Table 3.3.

In the supersonic flow through a ramped channel an oblique shock emanates from the ramp corner. This shock reflects from the top wall and interacts with the expansion fan centered at the expansion-corner of the channel. The performances of the flux schemes in resolving discontinuities inclined to the grid for internal flows are studied through this test problem. Table 3.4 shows the geometric and free-stream parameters for this problem.

Table. 3.3. The geometric and free-stream parameters for supersonic flow past a 2D wedge

Parameter	**Value**
Total length of the object (L)	20 m
Length of the wedged portion (L_w)	1 m
Half-wedge angle (α_w)	10^0
free-stream Mach number (M_∞)	2
free-stream pressure (p_∞)	101325 N/m^2
free-stream temperature (T_∞)	300 K

Table. 3.4. The geometric and free-stream parameters for supersonic flow through a ramped channel

Parameter	**Value**
Total length of the channel (L)	3 m
Height of the channel (H)	1 m
Location of the ramp from the entrance of the channel (X_R)	1 m
Length of the ramped portion along the channel (L_R)	1 m
Ramp angle (θ)	20^0
free-stream Mach number (M_∞)	3
free-stream pressure (p_∞)	101325 N/m^2
free-stream temperature (T_∞)	300 K

3.3.3 Boundary conditions for 2D flows

We begin with the treatments of inlet and outlet-boundary conditions. These are formulated based on the eigenvalues of the convective-flux Jacobian for the 2D Euler equations. For a stationary grid the eigenvalues of the convective-flux Jacobian are given by [54]

$$\begin{aligned} \lambda_1 = \lambda_2 &= u_\perp \\ \lambda_3 &= u_\perp + a \\ \lambda_4 &= u_\perp - a. \end{aligned} \tag{3.8}$$

Depending on the sign of the eigenvalues information is transported out of or into the computational domain along the characteristics. The number of conditions to be imposed from outside or extrapolated from within the computational domain are governed by the theory mentioned in section 3.2.4. It may be noted that the problem will be well posed only if the full information on the ingoing and outgoing characteristics can be recovered from the imposed combinations of conservative or primitive variables [62].

Figures 3.12a and 3.12b show schematics of inlet and outlet boundaries, respectively. Depending on the local Mach number four different kinds of boundary conditions may appear:

- Subsonic inflow
- Supersonic inflow
- Subsonic outflow
- Supersonic outflow

Subsonic inflow

For 2D subsonic inflow there are three incoming characteristics and one outgoing (λ_4 in equation 3.8). Therefore, three characteristic variables are imposed based on the free-stream values and one characteristic variable is extrapolated from within the computational domain. The three variables specified are the stagnation pressure, stagnation temperature and the flow angle. The outgoing Riemann invariant

is extrapolated from the interior, which is defined by [54]

$$\Re_{\mathrm{d}}^{-} = \mathbf{v}_{\mathrm{i}}.\mathbf{n} - \frac{2a_{\mathrm{i}}}{\gamma - 1}, \tag{3.9}$$

where $\mathbf{v}_{\mathrm{i}}$ and a_{i} are the fluid-velocity and the acoustic speed in the interior cell, respectively. The speed of sound in the dummy cell is obtained using the outgoing Riemann invariant as

$$a_{\mathrm{d}} = -\frac{\Re_{\mathrm{d}}^{-}(\gamma - 1)}{(\gamma - 1)\cos^2\theta + 2}\left\{1 + \cos\theta\sqrt{\frac{[(\gamma - 1)\cos^2\theta + 2]\,a_0^2}{(\gamma - 1)\left(\Re_{\mathrm{d}}^{-}\right)^2} - \frac{\gamma - 1}{2}}\right\}, \tag{3.10}$$

where θ is the flow angle relative to the boundary and a_0 denotes the stagnation speed of sound, which are given by

$$\cos\theta = -\frac{\mathbf{v}_{\mathrm{i}}.\mathbf{n}}{|\mathbf{v}_{\mathrm{i}}|}, \tag{3.11}$$

and

$$a_0^2 = a_{\mathrm{i}}^2 + \frac{\gamma - 1}{2}|\mathbf{v}_{\mathrm{i}}|^2, \tag{3.12}$$

The static temperature, pressure, density and absolute velocity at the dummy cell (see figure 3.12a) are evaluated as follows:

$$\begin{aligned} T_{\mathrm{d}} &= T_0\frac{a_{\mathrm{d}}^2}{a_0^2} \\ p_{\mathrm{d}} &= p_0\left(\frac{T_{\mathrm{d}}}{T_0}\right)^{\frac{\gamma}{\gamma-1}} \\ \rho_{\mathrm{d}} &= \frac{p_{\mathrm{d}}}{RT_{\mathrm{d}}}\ \text{(Equation of state)} \\ |\mathbf{v}_{\mathrm{d}}| &= \sqrt{2c_p\,(T_0 - T_{\mathrm{d}})}. \end{aligned} \tag{3.13}$$

where T_0 and p_0 are the stagnation temperature and pressure, R is the characteristic gas constant and c_p is the specific heat at constant pressure. The velocity components at the dummy cell can be obtained by decomposing $|\mathbf{v}_{\mathrm{d}}|$ according to the prescribed flow angle. This type of boundary condition is to be implemented in the case of 2D-nozzle-flow problem.

Supersonic inflow

For supersonic inflow, all eigenvalues are of the same sign. Since the flow is entering the physical domain, the conservative variables in the dummy cell located on the

inlet boundary are determined by specifying the free-stream values only. Therefore one can write

$$\mathbf{U}_{\mathrm{d}} = \mathbf{U}_{\infty}, \tag{3.14}$$

where the subscript ∞ refers to the free-stream conditions. This type of inlet boundary condition can be implemented in all supersonic and hypersonic inflow problems.

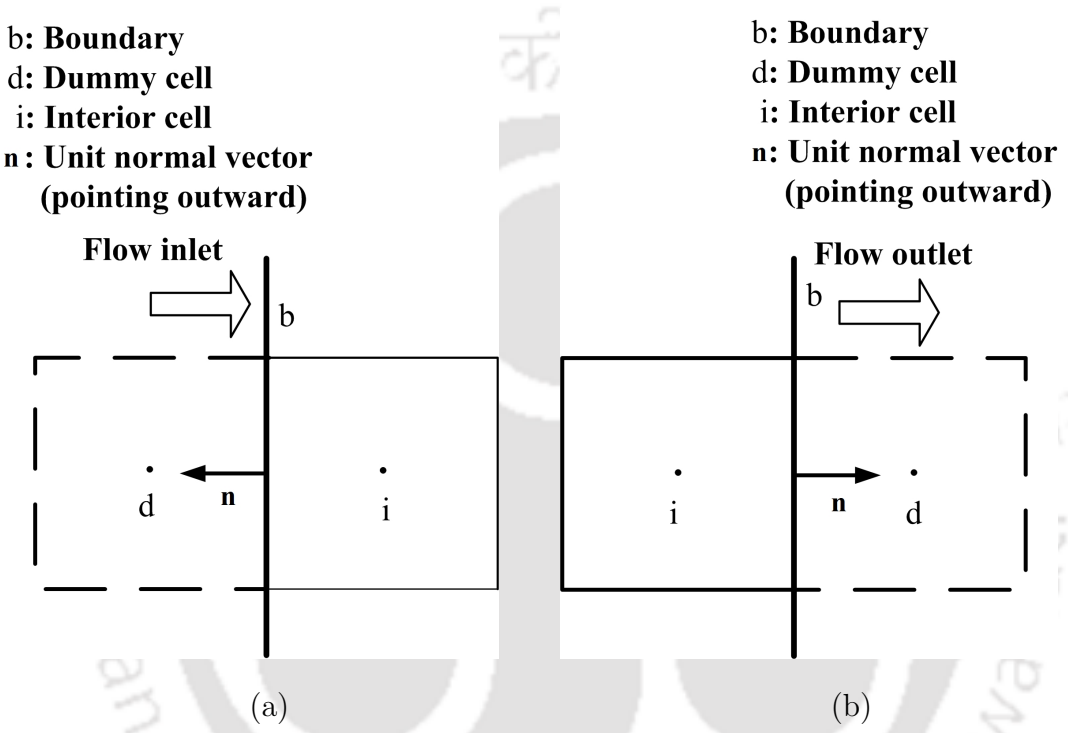

Fig. 3.12. Schematics of dummy cells and interior cells: (a) Inlet boundary and (b) Outlet boundary.

Subsonic outflow

In this case one characteristic enters the domain and three characteristics leave the domain through the outlet boundary. Accordingly, one variable is to be imposed on the boundary and three variables are to be extrapolated from the interior. It is customary to specify the outlet pressure and extrapolate the x- and y-velocity components and either the density or temperature from the interior. This type of outlet boundary condition is to be implemented for 2D subsonic flow through a nozzle, 2D flow through a converging-diverging nozzle with a standing normal

shock in the divergent passage and in some cases of supersonic flow through a forward-facing-stepped channel.

Supersonic outflow

In the case of supersonic outflow, all the eigenvalues are of the same sign and hence all the four characteristics leave the boundary from the interior. Therefore all the conserved variables in the dummy cell attached to the outflow boundary are extrapolated from the interior, i.e.,

$$\mathbf{U}_{\mathrm{d}} = \mathbf{U}_{\mathrm{i}}. \tag{3.15}$$

For a solid wall, the wall pressure can be extrapolated from the interior cells and velocity component normal to the wall can be imposed as zero. This approach is called the pressure extrapolation boundary condition. However, the accuracy of the pressure extrapolation boundary condition is highly sensitive to the wall-curvature [54]. The mirror-image boundary condition scores over the former. This boundary condition is discussed below.

The mirror-image boundary condition

As shown in figure 3.13 the velocity component parallel to the wall in the dummy cell is equal to that in the interior cell. On the other hand, the velocity component normal to the wall in the dummy cell is equal in magnitude but opposite in sign to that in the interior cell. In this situation the solid wall acts like a mirror for the velocity vector and this is the reason behind the naming of this boundary condition. In figure 3.13, $\left(u_{\parallel}\right)_{\mathrm{i}}$ and $(u_{\perp})_{\mathrm{i}}$ represent the velocity components in the interior cell parallel and normal to the wall, respectively. The symbols $\left(u_{\parallel}\right)_{\mathrm{d}}$ and $(u_{\perp})_{\mathrm{d}}$ are the corresponding velocity components in the dummy cell. The wall is inclined at angle θ with the x-axis. Using the mirror-image boundary condition the x- and y-velocity components, pressure, temperature and density are evaluated as follows:

$$
\begin{aligned}
u_{\mathrm{d}} &= u_{\mathrm{i}} \cos 2\theta + v_{\mathrm{i}} \sin 2\theta \\
v_{\mathrm{d}} &= u_{\mathrm{i}} \sin 2\theta - v_{\mathrm{i}} \cos 2\theta \\
p_{\mathrm{d}} &= p_{\mathrm{i}} \\
T_{\mathrm{d}} &= T_{\mathrm{i}} \\
\rho_{\mathrm{d}} &= \frac{p_{\mathrm{d}}}{RT_{\mathrm{d}}} \text{ (Equation of state).}
\end{aligned}
\tag{3.16}
$$

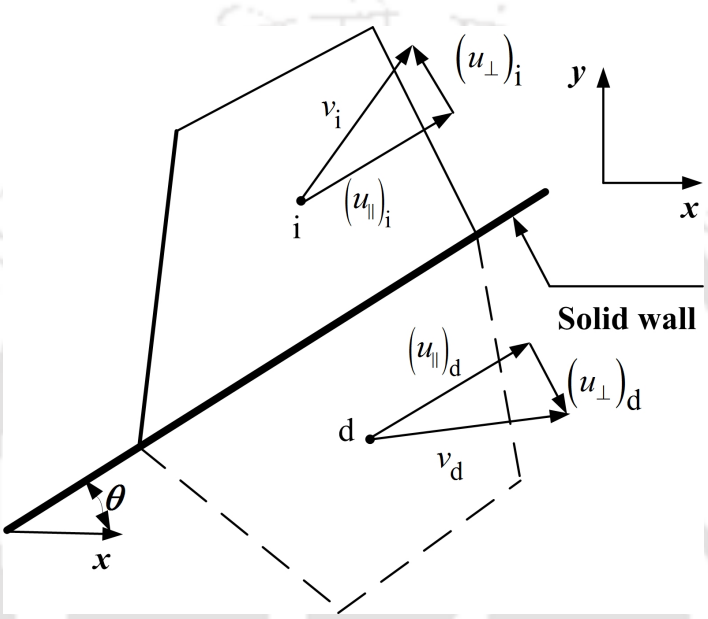

Fig. 3.13. The mirror-image boundary condition for an inviscid wall.

In addition to the standard inlet, outlet and wall boundary conditions the upper boundary in the 2D wedge and the expansion-corner in the forward-facing-stepped-channel problems require special care. These are discussed in the following sections.

Treatment of upper boundary for the 2D supersonic wedge problem

For the supersonic flow past a 2D wedge the flow is supersonic at both inlet and outlet. Accordingly, the boundary conditions are set as per the standard procedure discussed in the preceding sections. The wall is treated with the mirror-image boundary condition. The upper boundary condition for this problem has to be

implemented in conjunction with a careful choice of the computational domain. Far away from the surface the shock becomes a Mach wave leading to isentropic flow. Therefore, the upper boundary condition can be specified in such a way that the variables equal the free-stream parameters. However, care must be exercised that the length and height of the computational domain are taken sufficient enough. In this work the length and height of the computational domain are taken as 20 m and 10 m, respectively, through exhaustive numerical tests that suggest a 540×400 mesh.

Special-boundary condition at the expansion-corner

The special boundary condition at the expansion corner is required for the forward-facing-stepped-channel flow. At the inlet since the flow is supersonic the free-stream conditions are specified. At the outlet the Mach number is checked at every iteration for each cell and either the supersonic or the subsonic outflow boundary condition is implemented depending on the outlet Mach number. The mirror-image boundary condition is used for the upper and lower walls.

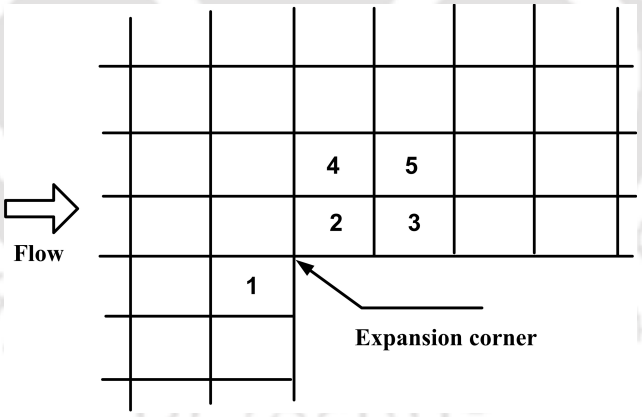

Fig. 3.14. Special boundary condition near the expansion corner.

The upper corner of the step is the centre of a sharp expansion fan and hence is a singular point of the flow. The generation of numerical errors at this corner of the step may be reduced by applying an additional boundary condition near the corner. With reference to figure 3.14, in the zones 2 to 5 the density is reset so that the total enthalpy has the same value as in zone 1. The magnitudes of velocities are also reset, so that the sum of enthalpy and kinetic energy per unit

mass has the same value as in the same zone to set the entropy. This condition is based on the assumption of a nearly steady flow near the corner. Similar boundary condition was applied by Woodward and Collela [11].

3.3.4 Performances of schemes in computing 2D supersonic flows

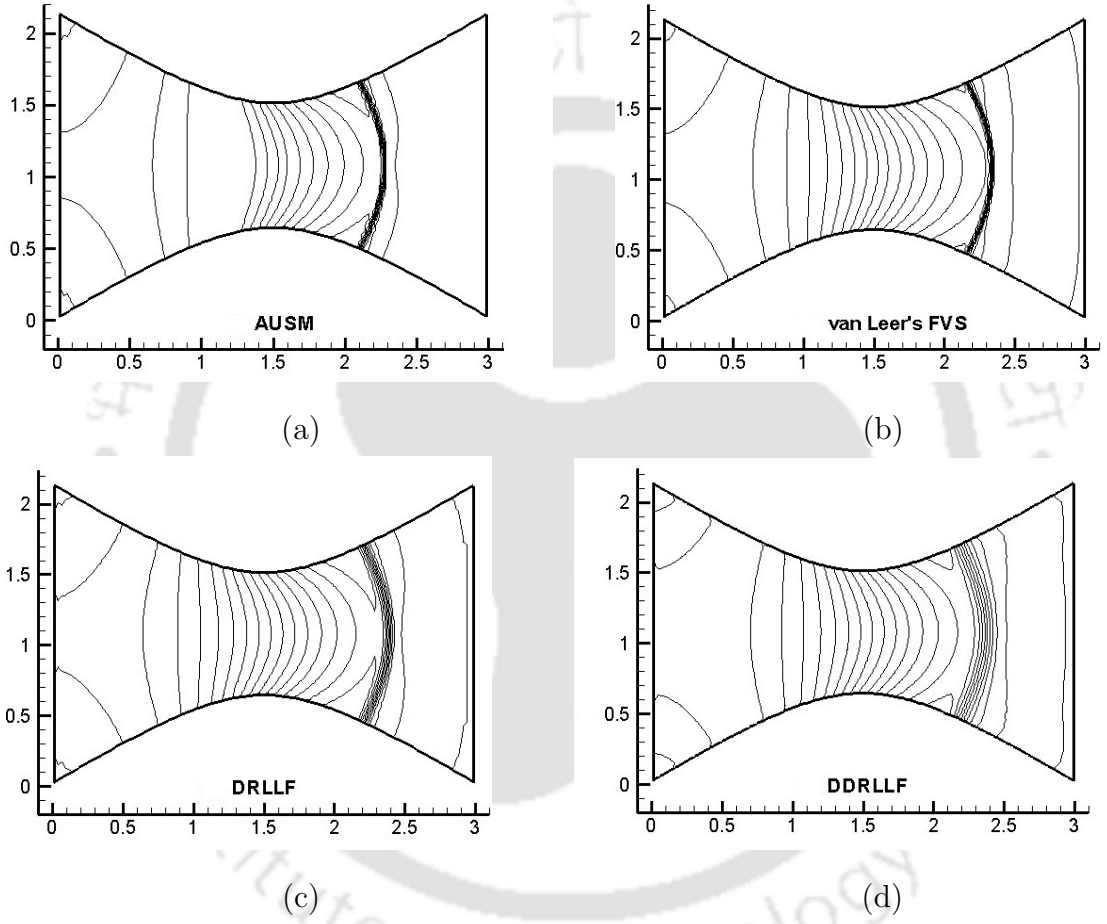

Fig. 3.15. Pressure contours for 2D flow through a converging-diverging nozzle using (a) AUSM, (b) van Leer's FVS, (c) DRLLF and (d) DDRLLF schemes.

The 2D converging-diverging nozzle-flow problem is computed with first-order-accurate van Leer's FVS, AUSM, DRLLF and DDRLLF schemes. The problem is solved on a 170×51 grid for all the methods with a CFL number of 0.1. Figures 3.15(a)-(d) show the pressure contours obtained with these schemes, showing that the resolutions of the shocks captured by AUSM and van Leer's FVS are better than those by DRLLF and DDRLLF schemes. The DRLLF scheme resolves the

shock relatively better than the DDRLLF scheme. The reason for this observation is that the DR parameter approaches its maximum value of unity as the jump in normal Mach number across the cell interface, i.e., $\Delta M_{\perp}$ approaches unity (see equation 2.83). Similarly the DDR approaches its maximum value of unity as the value of μ_{g} in equation 2.88 exceeds a value of unity. Equation 2.85 suggests that $\mu_{\mathrm{g}} \geq 1$ in the vicinity of a normal shock and hence the DDR also assumes its maximum value. As the DR parameter and DDR tend towards unity, the DRLLF and DDRLLF schemes behave like the fully diffusive LLF scheme. Therefore, it can be stated that the strong shocks are resolved better by the AUSM and van Leer's FVS schemes than the DRLLF and DDRLLF schemes. This fact gets reinforced from figures 3.16(a)-(b) that plot the pressure and Mach-number variations along the nozzle axis, respectively, using the four schemes. Further figures 3.16(a)-(b) reaffirm the sonic-glitch problem exibited by the AUSM scheme, which is not present with the DRLLF and DDRLLF schemes, as shown by the encircled regions.

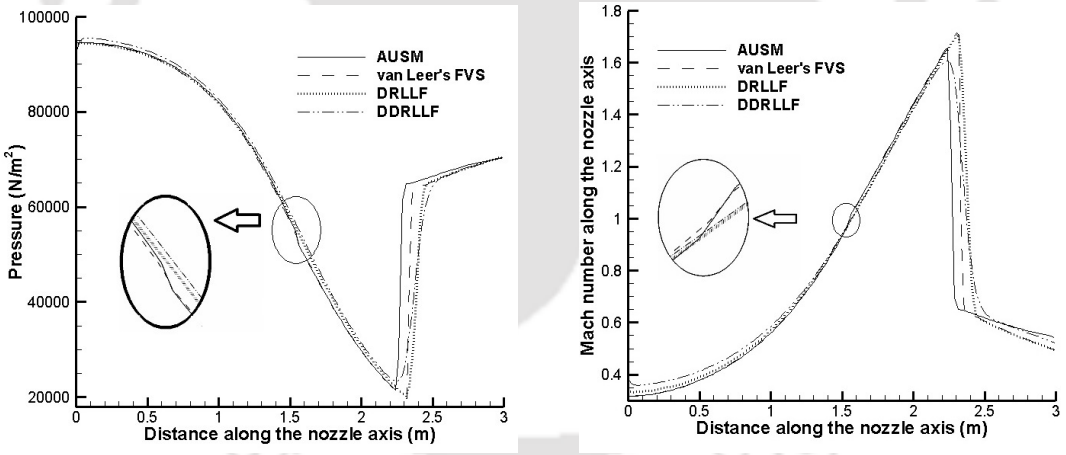

(a) (b)

Fig. 3.16. Axial variations using first-order-accurate AUSM, van Leer's FVS, DRLLF and DDRLLF schemes: (a) Pressure and (b) Mach number.

Figures 3.17(a-d) compare the pressure contours for the supersonic flow through a forward-facing stepped channel presented in Table 3.2. A 120×40 grid is used for the computations. The CFL number is 0.2. Overall the detached strong shock upstream of the step is better resolved by the AUSM and van Leer's FVS schemes. The AUSM scheme, being less diffusive, produces marginally better results than van Leer's FVS.

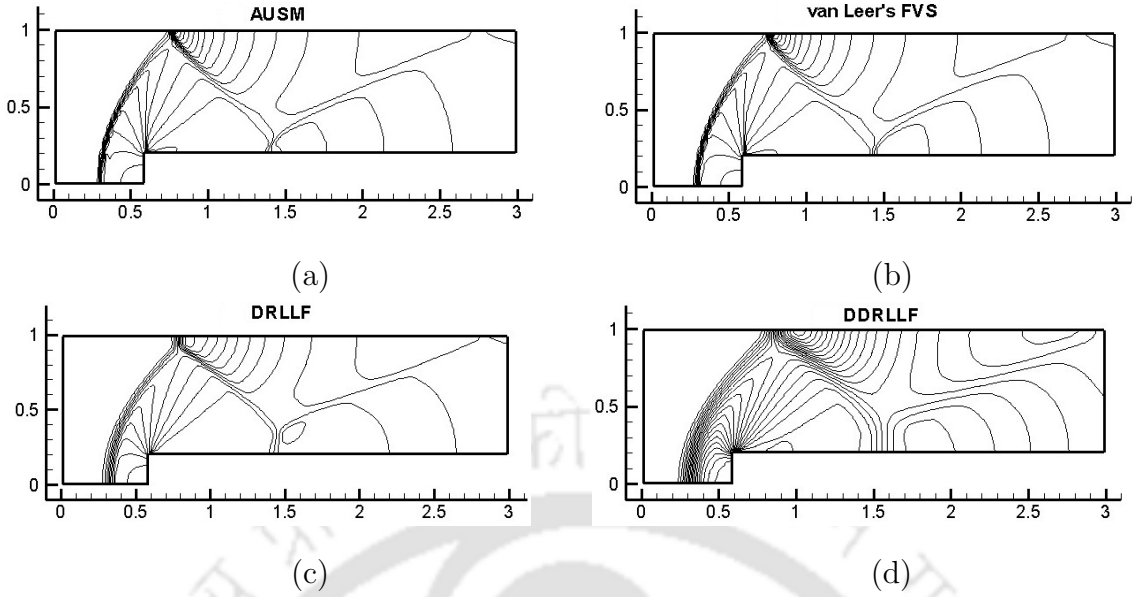

Fig. 3.17. Pressure contours for supersonic flow through a forward-facing-stepped channel using (a) AUSM, (b) van Leer's FVS, (c) DRLLF, and (d) DDRLLF schemes.

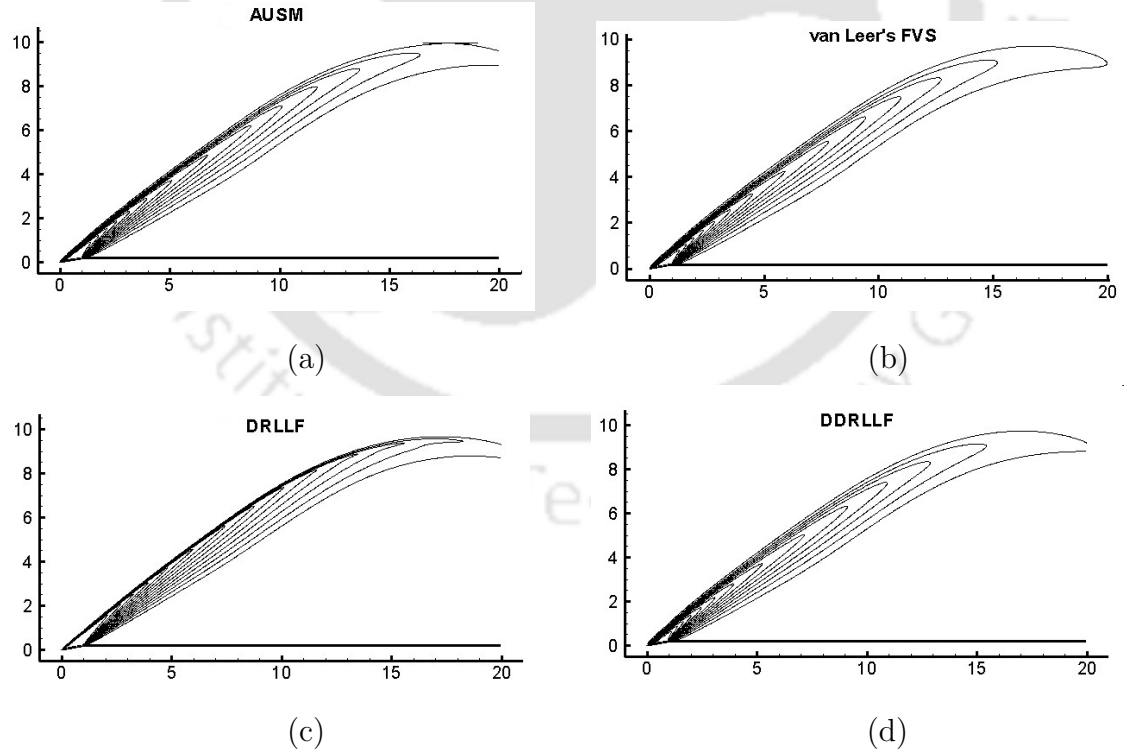

Fig. 3.18. Pressure contours for supersonic flow past a 2D wedge using (a) AUSM, (b) van Leer's FVS, (c) DRLLF and (d) DDRLLF schemes.

Figures 3.18(a-d) compare the steady-state pressure contours of the AUSM, van Leer's FVS, DRLLF and DDRLLF schemes for supersonic flow over the 2D wedge problem (Table 3.3). The flow is symmetric about the axis as the wedge is considered at zero-incidence angle. Hence the flow is computed over the upper half of the body only. The gradual weakening of the leading-edge shock due to interaction with the expansion fan centered at the convex corner till it becomes a Mach wave is captured by all the schemes. Further it can be seen that the DRLLF scheme produces a much better resolution of the weak leading-edge-shock compared with rest of the schemes. It can be inferred that in the vicinity of weak shocks the DRLLF scheme offers less numerical diffusion to produce crisp resolution of grid-inclined shocks.

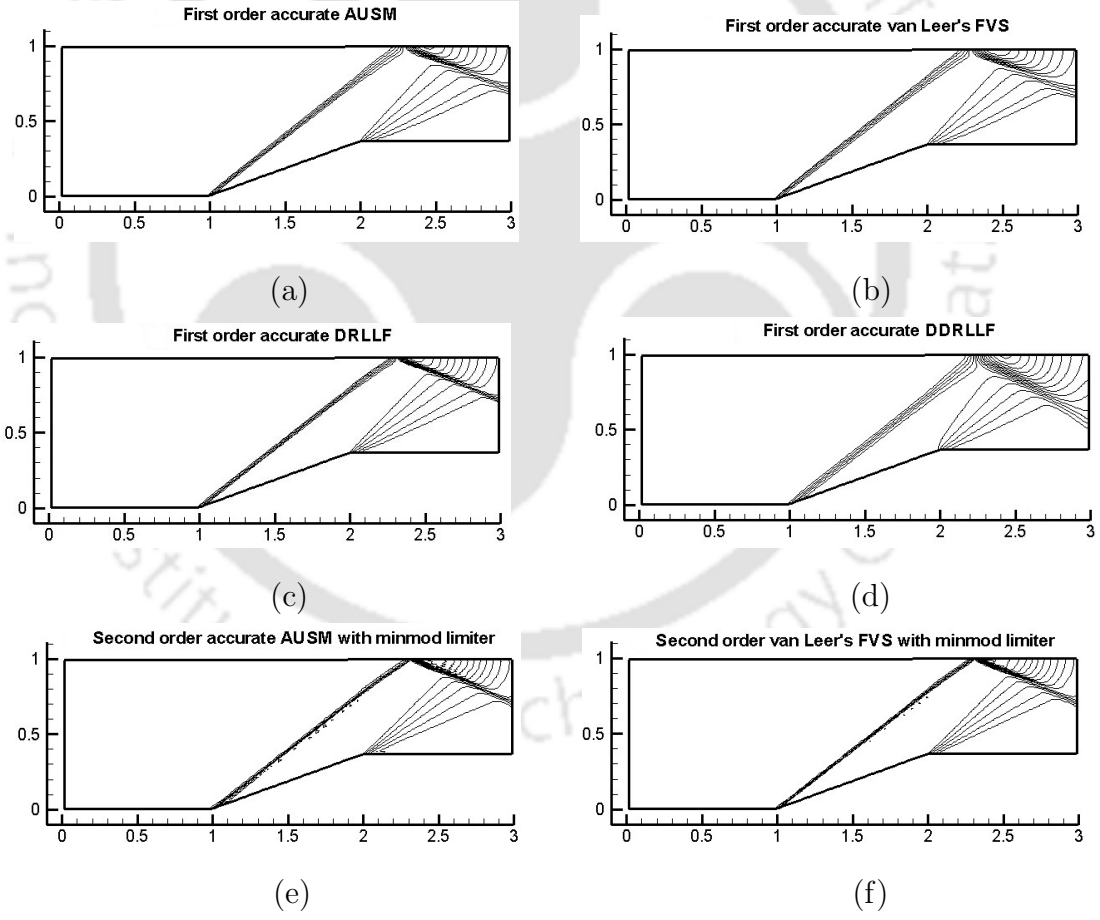

Fig. 3.19. Pressure contours for supersonic flow through a ramped surface using first-order-accurate: (a) AUSM, (b) van Leer's FVS, (c) DRLLF,(d) DDRLLF schemes, and higher-order-accurate: (e) AUSM, (f) van Leer's FVS schemes.

The 2D ramp-in-a-channel problem (Table 3.4) is computed with the first-order-accurate AUSM, van Leer's FVS, DRLLF and DDRLLF schemes and higher-order-accurate AUSM and van Leer's FVS schemes with minmod limiter through the MUSCL approach. A 120×80 grid is used for all the methods with a CFL number of 0.2. Figures 3.19(a-f) show the pressure contours for this flow computed with different schemes[2]. For the first-order-accurate versions, the oblique shocks are best captured by the DRLLF scheme compared with the other three schemes. The DDRLLF scheme also captures the oblique shocks with improved resolution compared with the normal shocks in the shock tube, quasi-1D and 2D nozzle-flow problems. From figures 3.19(a-f) it is also evident that the first-order-accurate DRLLF scheme resolves the oblique shocks almost as good as the second-order-accurate van Leer's FVS and AUSM schemes. Moreover, in the contours obtained by the second-order-accurate AUSM and van Leer's FVS schemes, oscillations are seen, especially near the shock. The first-order DRLLF scheme is free from such oscillations.

The reason for the improved performances of the DRLLF and DDRLLF schemes in resolving weak shocks over strong shocks is that the jump in normal Mach number $\Delta M_\perp$ for the former type of shocks is less compared with that in case of the latter ones. As a result the DR parameter across an oblique shock assumes smaller values (see equation 2.83) and therefore the DRLLF scheme is more effective for oblique shocks. Similarly across oblique shocks, the gradients of flow variables across the interface are not as strong as that in case of normal shocks. Thus the value of μ_g (see equation 2.88) in the case of oblique shocks is also on the smaller side. Accordingly the value of the DDR is smaller and thus the DDRLLF scheme is more effective for oblique shock waves, especially when these are not aligned with the grid. Figures 3.19c and 3.19d also indicate that even in oblique-shock resolution the DRLLF scheme outperforms the DDRLLF scheme. Thus the DRLLF scheme is found to be more effective for diffusion regulation in both 1D and 2D flow problems compared with the more recent DDRLLF scheme that is useful for 2D (or 3D) problems with grid-inclined shocks only.

[2]This work has been published in the proceedings of the 40th National Conference on Fluid Mechanics and Fluid Power (2013), National Institute of Technology Hamirpur, India

Table. 3.5. Comparison of CPU-time for 2D supersonic flows

Test Problem	**Scheme**	**CPU-time (s)**
Converging-diverging nozzle-flow	AUSM	365.48
	van Leer's FVS	339.17
	DRLLF	322.84
	DDRLLF	893.61
Forward-facing stepped channel	AUSM	68.64
	van Leer's FVS	62.34
	DRLLF	60.39
	DDRLLF	183.24
2D wedge	AUSM	1782.61
	van Leer's FVS	1690.74
	DRLLF	1602.39
	DDRLLF	3743.67
Ramped channel	AUSM	267.12
	van Leer's FVS	245.87
	DRLLF	233.41
	DDRLLF	1394.92

Table 3.5 lists the CPU-time for the 2D supersonic flow problems by the four schemes. The convergence behaviour of the schemes is found similar. Accordingly for a particular problem the CPU-time is reported for the same number of iterations for all the schemes. This data is a representation of the relative algorithmic simplicity of the different schemes. The DRLLF scheme consumes the least CPU-time owing to its algorithmic simplicity. The CPU-time of the AUSM and van-Leer's FVS schemes are close. The DDRLLF scheme consumes large CPU-time for 2D-flow computations owing to its increased programming complexity, since the flow-gradients have to be computed across more number of neighbouring points to compute the value of μ_g. The saving in computational time by the DRLLF scheme becomes more prominent as the number of grid points increases.

Thus the DRLLF scheme holds promise for computation of more complex flows involving a large number of grid points.

3.4 Aspects of the DRLLF scheme applied to hypersonic flows

The promising performance of the DRLLF scheme for computing 1D and quasi-1D flows, and 2D supersonic-flow computations provides the motivation for investigating its performance in computing hypersonic flows. In this section some aspects of the DRLLF scheme applied to compute hypersonic flows over a semi-cylinder and a hemisphere are presented. A comparison of the performance of the DRLLF scheme with the robust van Leer's FVS is made. The computations are done for the perfect-gas model and the high temperature equilibrium chemically reacting air model proposed by Tannehill and Mugge [73]. The ability of the DRLLF scheme to compute reacting gas models is demonstrated for the first time[3].

3.4.1 The equilibrium-air model of Tannehill and Mugge

For a given free-stream Mach number, computations are initiated by a prescribed value of γ. As the iterations proceed, γ is calculated using density and internal energy per unit mass, which are given by the Euler solver. Remaining thermodynamic properties such as pressure, sonic velocity and temperature are calculated using correlated formulae suggested by Tannehill and Mugge [73].

3.4.2 Flow over a semi-cylinder

Hypersonic flow at a free-stream Mach number, pressure and temperature of 15, 1197 Pa and 226.5 K, respectively over a semi-cylinder of diameter 10 m is considered [77]. A 201×201 mesh in the r-θ plane is used. The CFL number is 0.2 for all the computations. The flow is governed by the 2D planar Euler equations of gas dynamics given by equation 3.6. Figures 3.20 and 3.21 show the pressure and Mach contours, respectively, for the two gas models using van Leer's FVS and DRLLF

[3]This work has been published in the proceedings of the 5th International and 41st National Conference on Fluid Mechanics and Fluid Power (2014), Indian Institute of Technology Kanpur, India

schemes. It is seen that the shock stand-off distance is less for the equilibrium-air model compared with the perfect-gas model. The DRLLF scheme captures the detached bow shock without any numerical oscillations, but with more smearing than van Leer's FVS scheme.

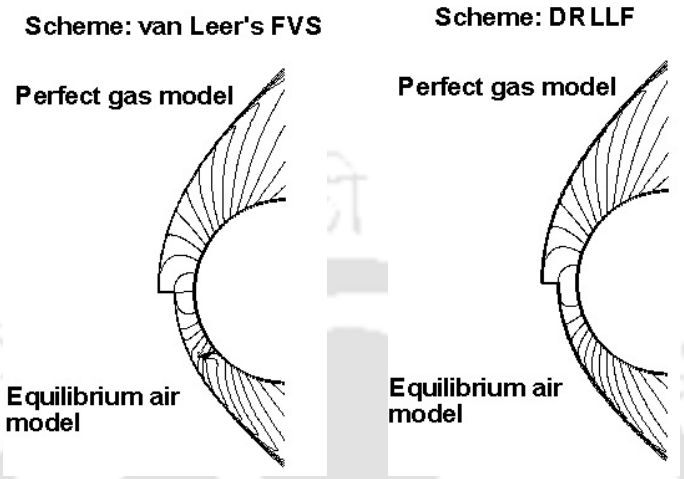

(a) (b)

Fig. 3.20. Pressure contours for inviscid-hypersonic flow over a semi-cylinder for the perfect-gas model and equilibrium-air model using (a) van Leer's FVS scheme and (b) DRLLF scheme.

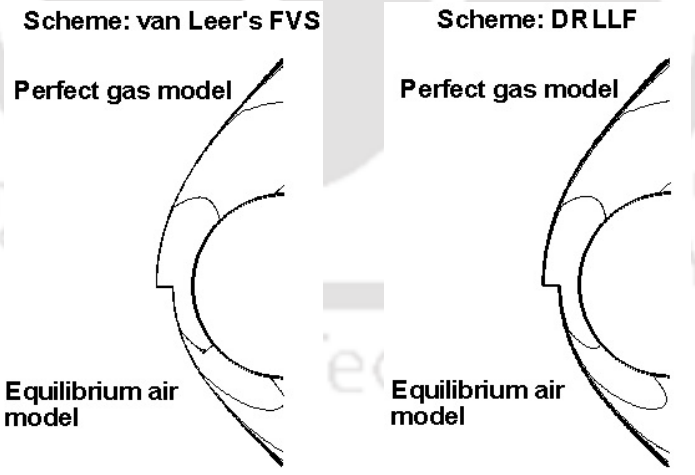

(a) (b)

Fig. 3.21. Mach contours for inviscid-hypersonic flow over a semi-cylinder for the perfect-gas model and equilibrium-air model using (a) van Leer's FVS scheme and (b) DRLLF scheme.

3.4.3 Flow over a hemisphere

Hypersonic flow at the same free-stream Mach number, pressure and temperature as in section 3.4.2 over a hemisphere of diameter 10 m is considered [77]. A 201×200 mesh in the r-θ plane is used. The CFL number is 0.2 for all the computations. The flow over a hemisphere are governed by the axisymmetric Euler equations of gas dynamics given by equation 3.6. Figures 3.22 and 3.23 show the pressure and Mach contours, respectively, computed with van Leer's FVS and DRLLF schemes for the two gas models. The contour plots reveal that for axisymmetric-hypersonic-flow computations numerical oscillations are produced by the DRLLF scheme near the shock.

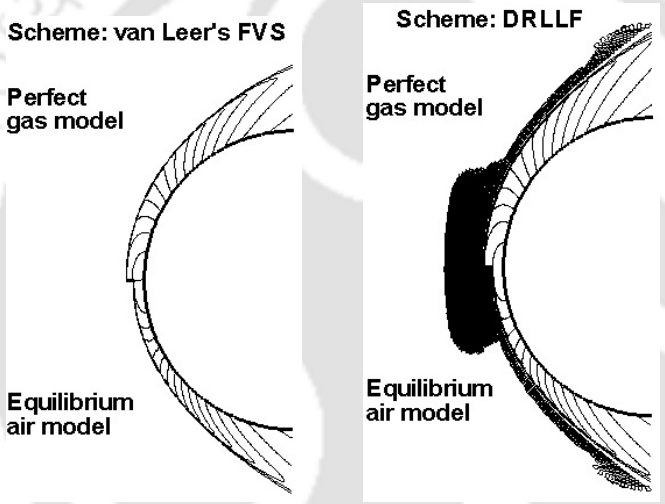

Fig. 3.22. Pressure contours for inviscid-hypersonic flow over a hemisphere for the perfect-gas model and equilibrium-air model using (a) van Leer's FVS scheme and (b) DRLLF scheme.

To overcome the problem of the numerical oscillations in the DRLLF scheme, the mathematical formulation for the DR parameter is modified. In the modified algorithm the DR parameter is assigned a value of unity in non-monotonous zones, so that the DRLLF scheme reverts back to the original dissipative LLF scheme. This is done as follows:

First the monotonicity at a cell is checked. Let us define a parameter $\Delta_{\text{left}}U = U_{\text{cell}} - U_{\text{leftcell}}$, where the subscripts 'cell' and 'leftcell' represent the cell immediately to the left of the cell-interface and the next left cell, respectively. Also let $\Delta_{\text{right}}U =$

$U_{\text{rightcell}} - U_{\text{cell}}$, where the subscript 'rightcell' represents the cell immediately to the right of the cell-interface. Then in case of non-monotonic solution at a cell,

$$\Delta_{\text{left}} U_i \times \Delta_{\text{right}} U_i < 0, \quad i = 1 \text{ or } 2 \text{ or } 3 \text{ or } 4. \tag{3.17}$$

Now the DR parameter is computed by modifying equation 2.83 as follows.

$$\begin{aligned} &\Phi = 1 \text{ if } \Delta_{\text{left}} U_i \times \Delta_{\text{right}} U_i < 0, \quad i = 1 \text{ or } 2 \text{ or } 3 \text{ or } 4, \\ &\text{else } \Phi = \begin{cases} \frac{\left\{(\Delta M_\perp)^2 + \delta^2\right\}}{2\delta} & \text{when } |\Delta M_\perp| \leq \delta \\ |\Delta M_\perp| & \text{when } \delta < |\Delta M_\perp| \leq 1.0 \\ 1 & \text{when } |\Delta M_\perp| > 1.0 \end{cases} . \end{aligned} \tag{3.18}$$

Here $i = 1, 2, 3$ and 4 correspond to the continuity, x-momentum, y-momentum and energy equations, respectively. With the modified DR parameter we term the DRLLF scheme as the Modified DRLLF scheme. It can be seen from equation 3.18 that wherever the solution becomes non-monotonic, the modified algorithm drives the scheme locally to the LLF scheme.

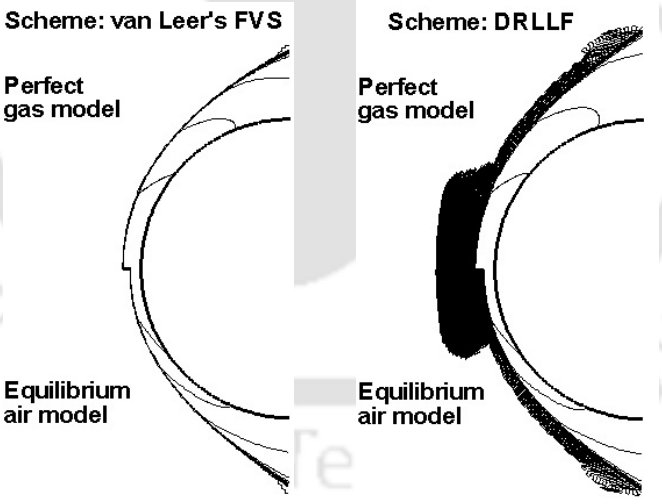

(a) (b)

Fig. 3.23. Mach contours for inviscid-hypersonic flow over a hemisphere for the perfect-gas model and equilibrium-air model using (a) van Leer's FVS scheme and (b) DRLLF scheme.

With modification of the algorithm for computing the DR parameter, the numerical oscillations could be avoided as shown in the pressure and Mach contours

for the Modified DRLLF (DRLLFM) scheme shown in figure 3.24. The results are found in good agreement with the literature [74, 77].

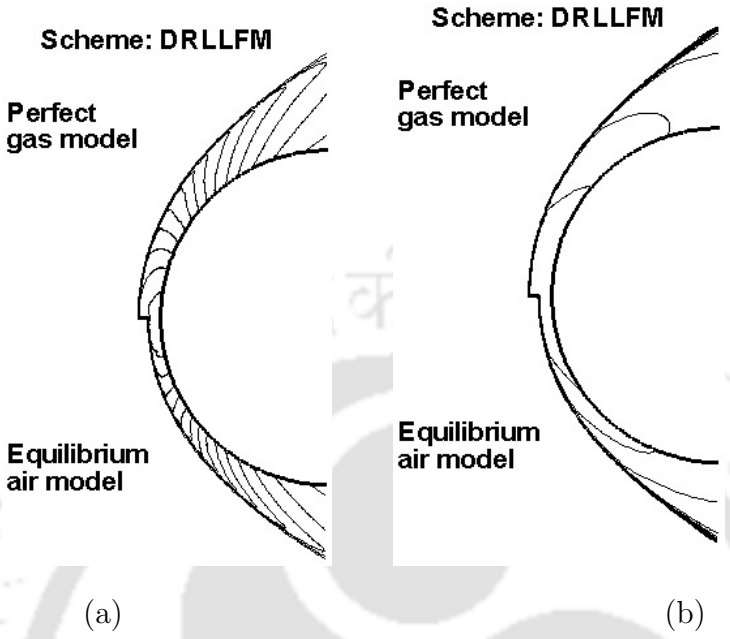

Fig. 3.24. Inviscid-hypersonic flow over a hemisphere with the Modified DRLLF scheme using the perfect-gas model and equilibrium-air model: (a) Pressure contours and (b) Mach contours.

3.5 Conclusions

The objectives of the present chapter are to study the role of numerical diffusion and its regulation in the computation of high-speed inviscid flow problems, and to compare the performances of two recent diffusion-regulated methods with established numerical flux schemes. The study is done at various levels, namely, 1D and quasi-1D flows, 2D supersonic flows, and hypersonic flows. For the 1D and quasi-1D flows Sod's 1st shock tube problem and flow through a converging-diverging nozzle, both having analytical solutions are chosen as the test cases. The performance of the Diffusion-Regulated Local Lax-Friedrichs (DRLLF) scheme is studied with varying levels of numerical diffusion. It is seen that as the level of numerical diffusion is reduced, the smearing of the captured discontinuities reduces but the numerical oscillations get augmented. The choice of the extent of artificial diffusion to be added is based upon a balance between the resolution and numerical

stability. The most appropriate value of the quantity δ for computing the DR parameter is found to be problem-dependent. The DRLLF scheme is also compared with the AUSM, van Leer's FVS and the more recent DDRLLF schemes. The DRLLF scheme significantly improves the resolution of the captured discontinuities compared with original LLF scheme with little added computational complexity. For moving normal shocks where the absolute flows across the shock remain subsonic (e.g. Sod's 1^{st} problem) the DRLLF scheme captures the shock with the least smearing, albeit with small numerical oscillations in the shock-vicinity. On the other hand, in the case of a stationary shock (e.g. the normal shock standing in the divergent section of a converging-diverging nozzle), the jump in Mach number across the cell-interface is large and hence the DR parameter assumes higher values. As a result the benefits of the DRLLF scheme may not appear prominent for stationary normal shocks aligned with the grid, where the AUSM and van Leer's FVS schemes perform better. The DDRLLF scheme works like an unregulated method for 1D and quasi-1D flows and the DRLLF scheme scores over the former in such cases.

Also 2D supersonic flows are computed by using the AUSM, van Leer's FVS, DRLLF and DDRLLF schemes. Four test problems of external and internal flows are chosen so that they provide cases of both strong and weak shocks. The test problems considered are flow through a converging-diverging nozzle with a standing normal shock, flow through a forward-facing stepped channel, flow over a 2D wedge and flow through a ramped channel. For the computation of supersonic flow over a 2D wedge, the boundary conditions can be correctly implemented only after a careful choice of the computational domain size. For all flows the AUSM scheme resolves the strong shocks (e.g. the standing-normal shock in the converging-diverging nozzle, and the detached shock upstream of the step and the Mach-stem in the stepped channel) better than the rest of the schemes, especially for grid-aligned shocks, since it is less diffusive. However the DRLLF scheme scores over the rest of the schemes in resolving weak shocks, e.g. the leading-edge shock in the 2D wedge, and the incident as well as the reflected shocks in the ramped channel problems. The DDRLLF scheme resolves the normal shocks without any significant improvements and the weak shocks almost as good as the AUSM and

van Leer's FVS schemes. The oblique shocks captured by the first-order-accurate DRLLF scheme are comparable to the second-order-accurate AUSM and van Leer's FVS schemes, as shown with the example of the 2D-ramped-channel problem. Among the four schemes tested, the computational time for the DRLLF scheme is competitive for different types of flow problems. Although the DDRLLF scheme is developed later to bring in multidimensional physics still DRLLF appears a better choice from the point of view of accuracy, robustness and computational cost.

Owing to the promise shown by the DRLLF scheme through its simplicity and robustness, the applicability of the scheme for the Euler equations to compute hypersonic flows including chemical equilibrium-air model is investigated. The results are compared with the robust van Leer's FVS scheme. It is found that for inviscid-hypersonic flow over a semi-cylinder the DRLLF scheme captures the detached bow shock without any numerical oscillations, but with more smearing compared with van Leer's FVS scheme for both the perfect gas and the equilibrium-air models. For the computation of axisymmetric-hypersonic flow the DRLLF scheme is found to produce numerical oscillations. The original algorithm to compute the DR parameter is modified to successfully enforce monotonicity for such cases. The ability of the DRLLF scheme to compute reacting-air flows is demonstrated. It is seen that a scope exists to design a robust and versatile scheme based on the DRLLF scheme for accurate-shock capturing irrespective of its strength or grid-inclination. This is going to be explored in subsequent chapters.

Chapter 4

Aspects of Viscous-Flow Computations

4.1 Introduction

In this chapter we present a study on the role of numerical diffusion in computing viscous-compressible flows. The study begins with a test case of supersonic-laminar flow over a flat plate at zero incidence. The inviscid-flux terms in the Navier-Stokes equations governing the flow are computed by using first-order-accurate van Leer's FVS, AUSM and DRLLF schemes. The results are correlated with the inherent numerical diffusion of these schemes. The study is also motivated by the necessity to examine whether reduced artificial viscosity can be used with the DRLLF scheme in computing viscous flows than was suggested in the original paper on inviscid computation. It is demonstrated that reduced artificial viscosity is not only possible, but it results in a scheme that is very efficient in the computation of the standard supersonic viscous flow over a flat plate, in that it is comparable in accuracy to the AUSM scheme in the boundary layer and better than the latter in shock resolution. Even with the reduced artificial viscosity suggested in this study the DRLLF scheme shows good convergence behaviour comparable with the other two schemes. Motivated by the encouraging results, similar study is extended to hypersonic shock wave-boundary layer interaction (SWBLI) on a ramped surface. The study affirms that in the presence of physical viscosity, scope exists to reduce

the numerical diffusion of the DRLLF scheme than the level originally suggested for the Euler solvers. Before making the concluding remarks of the chapter, a study on the performances of some limiters for the higher-order-accurate computations of viscous supersonic flow over a flat plate with the AUSM scheme is presented.

For viscous flow over a flat plate, because of the no-slip condition on the wall, fluid at the wall and some neighbourhood has to be necessarily subsonic. In the case of a supersonic free-stream this can happen only through a shock emanating from the leading edge of the flat plate. The region between the surface and the shock is the shock layer. Also owing to the viscous effects, a boundary layer develops on the surface. In general, the shock layer can be characterized by the region of viscous flow and inviscid flow as shown in figure 4.1. It may be noted, that dissipation of kinetic energy within the boundary layer can cause high-temperature gradients near the solid surface. This may lead to high-heat transfer rates.

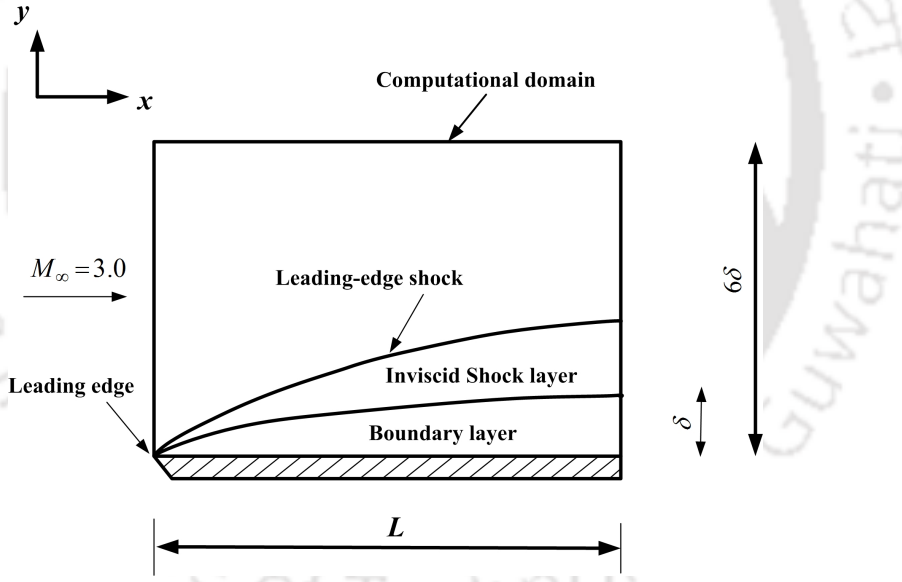

Fig. 4.1. The various zones for viscous supersonic flow over a flat plate.

Aircrafts flying through the atmosphere at supersonic speeds have slender shapes with very low-wall curvature resembling the flow over a flat plate. Eckert [78] suggested that the solution of supersonic-viscous flow over a flat plate could be extended to obtain parameters like skin friction coefficient, recovery factor, and convective heat transfer coefficient for high-speed flow over slender surfaces maintained at constant temperatures. This reaffirms the importance of the classical problem of boundary layer over a flat plate.

Various studies have been done on computation of high-speed viscous flows over flat plates. Aliabadi et al. [79] presented a finite-element-based computation of viscous-compressible flows based upon the conservation and entropy-variables formulations. Savelyev [80] showed numerical simulation of laminar viscous supersonic flow over a flat plate with a rectangular cavity. Drikakis and Durst [81] presented a numerical assessment of the effect of angle of incidence and Reynolds number on the flow-separation for viscous supersonic flow past a flat plate. Aoki et al. [82] carried out numerical analysis of supersonic-rarefied-gas flow past a flat plate. Deshpande et al. [83] carried out a computational study of viscous supersonic flow over a flat plate with moving protrusion. Abbas and Nordström [84] demonstrated that in the numerical computation of the Navier-Stokes equations involving boundary layers it is advantageous to use weak no-slip boundary conditions. Arnal and Vermeerch [85] gave an overview of the compressibility effects, free-stream Mach number and wall-temperature effects, on boundary layer laminar-turbulent transition from incompressible flow to low supersonic Mach number. Tsoutsanis et al. [86] developed Weighted-Essentially-Non-Oscillatory (WENO) schemes on arbitrary unstructured meshes for computing laminar, transitional and turbulent flows. John and Kulkarni [87] carried out numerical assessment of correlations for shock wave-boundary layer interaction. Matsuyama [88] reported the performance of all-speed AUSM family schemes for direct numerical simulation of low Mach number turbulent channel flow. Iyer et al. [89] investigated the boundary-layer transition in high-speed flows due to roughness. Fang et al. [90] presented an optimized low-dissipation monotonicity-preserving scheme for numerical simulations of high-speed turbulent flows. Xu and Weng [91] proposed a high-order-accurate and low-dissipation method for unsteady compressible viscous-flow computation on helicopter rotor in forward flight. However, a comprehensive study of the effects of numerical diffusion on the computation of viscous supersonic flows over a flat plate under isothermal- and adiabatic-wall conditions is not available in the literature.

The study on the effects of numerical diffusion for viscous-flow computations is relatively straightforward with the DRLLF scheme, since the level of diffusion can be controlled just the way in case of inviscid flows presented in Chapter 3.

Moreover, the promising performance of the DRLLF scheme, especially for weak-shock capuring provides motivation for further investigations on this scheme for viscous-flow applications. Kannan and Wang [92] used the DR parameter to improve the high-order-spectral-volume formulation and demonstrated the potential of the diffusion-regulation for viscous subsonic test cases. The performance of the DRLLF scheme for computing viscous supersonic flows, however, is an unexplored area. van Leer's FVS scheme is known to be robust, although more diffusive especially for viscous flows. The AUSM scheme was designed with less numerical diffusion to make it suitable for viscous-flow computations as well [7]. In the present work, a comparison of the computations of viscous supersonic flow over a flat plate with a laminar boundary layer [93] using first-order-accurate van Leer's FVS, AUSM and DRLLF schemes is done. Based upon the comparison, an analysis of the effect of numerical diffusion on the flow features captured by the different schemes is presented. Emphasis on further improvement of the flow-field resolution by the DRLLF scheme is done because of its algorithmic simplicity compared with the other two schemes.

In the computation of viscous flows, physical diffusion is always present. Motivation is drawn from this fact to investigate the possibility of reducing the numerical diffusion of the DRLLF scheme for the computation of supersonic viscous flows lower than the level reported in the original paper for inviscid computations. Many methods exist for the computation of the gradients in the viscous flux terms [94]. In this chapter these terms are computed by using simple central discretization and using the Green's theorem [54]. Both these methods are combined with the three inviscid flux schemes and the results are compared. The equivalence of the two methods for computing the gradients across the cell-interfaces in a uniform Cartesian grid is verified.

In hypersonic flows viscous interactions are prominent, especially for thin-shock-layer problems [69]. At very high speeds, the viscous dissipation on a solid surface leads to substantially high temperature, leading to increased viscosity. Thus the boundary layer becomes thicker and displaces the outer inviscid flow. This type of viscous interaction, also called pressure interaction, influences the pressure field around the solid surface. Apart from the leading-edge shock, the

boundary layer may also interact with external shocks as well as shocks generated at other locations of the surface. This type of viscous interaction, also known as shock wave-boundary layer interaction (SWBLI) influences the dynamics of hypersonic flights a great deal.

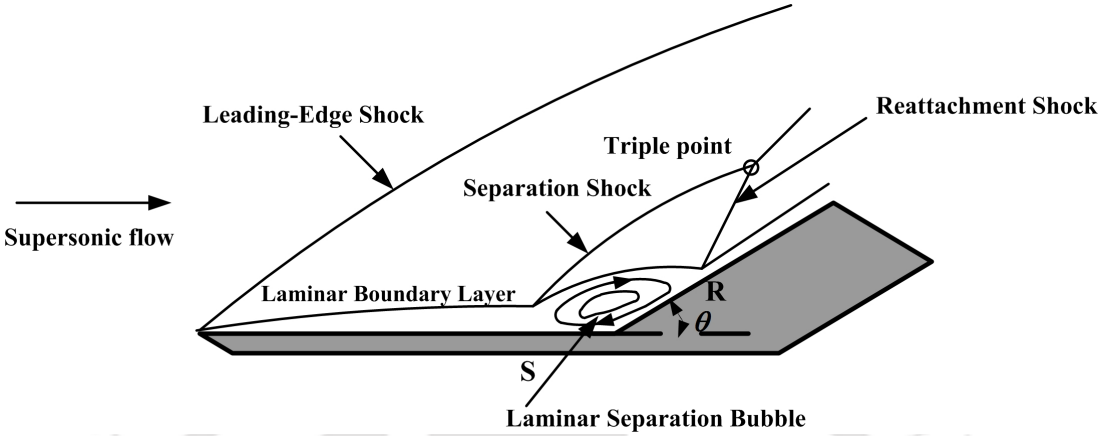

Fig. 4.2. Schematic diagram representing ramp-based SWBLI.

Many subsystems for high-speed applications involve flow over a ramped surface. Some examples of such flows are engine-inlets, wing-body junctions, control-surfaces etc. Figure 4.2 shows the schematic of a ramp-induced SWBLI with flow-separation. The viscous effects give rise to a relatively weak shock emanating from the sharp-leading edge of the plate. Additionally, the abrupt deflection of flow by the ramp at the compression-corner induces an oblique shock. The boundary layer experiences adverse pressure gradient near the region of flow deceleration or oblique shock. The ramp-induced shock interacts with the flat-plate boundary layer. Due to the upstream propagation of pressure-disturbances across the subsonic portion of the boundary layer, flow-separation may occur [95], which depends on many parameters including Mach number, Reynolds number, ramp angle, wall-temperature and boundary-layer stability. For ramp-induced hypersonic SWBLI Needham and Stollery [96] suggested an expression for the incipient-separation angle beyond which flow-separation occurs under certain flow-conditions. Boundary-layer separation affects the lift- and drag-characteristic of the vehicle by creating separation and reattachment shocks, expansion waves and slip lines. Apart from boundary-layer separation, the SWBLI phenomenon also leads to enhanced heating load [97] or even a turbulent re-attachment [98]. Both internal as well as

external aerodynamics get affected by such interactions.

Holden [99, 100] performed theoretical and experimental studies to understand the effects of free-stream Mach number, Reynolds number, wedge-angle and leading-edge bluntness on SWBLI phenomena. Rizzeta and Mach [101] computed the laminar hypersonic flowfield for ramp-induced SWBLI using four different numerical algorithms. John et al. [102] presented a numerical study of the effects of free-stream Mach number and stagnation temperature on the boundary-layer separation and heat transfer. In this chapter a study on the effect of numerical diffusion on the laminar-separation-bubble (LSB) length for a SWBLI problem [98] is presented using first-order-accurate van Leer's FVS, AUSM and DRLLF schemes. The possibility of using lower levels of numerical diffusion with the DRLLF scheme for hypersonic viscous-flow computations than the level prescribed originally for the Euler solvers is also explored.

First-order-accurate methods are not so accurate for viscous-flow computations owing to their diffusive nature. Higher-order accuracy of the schemes can be achieved using suitable variable interpolation techniques like the MUSCL [38] and piecewise linear reconstruction [61] with limiters. Various limiter functions can be used for implementing the MUSCL approach. In this chapter three limiter functions, namely the minmod limiter, the van Albada limiter and the Hemker-Koren limiter functions [54] are used. The piecewise linear reconstruction is also tested along with the Venkatakrishnan limiter function [39]. The performances of these limiters in computing high-speed viscous flows by taking the test case of laminar-boundary layer over a flat plate is investigated. Corresponding improvements over the first-order-accurate solutions are marked.

This chapter is organized in five sections. Section 4.2 presents the effects of numerical diffusion in computing viscous supersonic flow over a flat plate. The extension of a similar study for hypersonic SWBLI on a ramped surface is discussed in section 4.3. A study on the performance of limiters in the computation of viscous supersonic flow over a flat plate is presented in 4.4, before making the concludig remarks for the present chapter in section 4.5.

4.2 Effects of numerical diffusion in the computation of viscous-supersonic flow over a flat plate

This section presents the 2D Navier-Stokes equations governing viscous-compressible flows, followed by the implementation of the boundary conditions for viscous-compressible flows and the problem statement for viscous-supersonic flow over a flat plate along with the grid used. Subsequently an analysis on the effects of numerical diffusion and its regulation in the computation of viscous supersonic flow over a flat plate with a laminar boundary layer [93] is presented. The steady state velocity, temperature and entropy profiles at the trailing edge of the plate under adiabatic- and isothermal-wall conditions with the AUSM, van Leer's FVS and DRLLF schemes are presented, and the results are correlated with the relative numerical diffusion of the schemes. The equivalence of the central differencing and Green's theorem [54] on Cartesian grids for viscous flux evaluation is also demonstrated. A comparison of the CPU-time with the different flux schemes is also presented .

4.2.1 The 2D compressible Navier-Stokes equations

The non-dimensionalized form of the Navier-Stokes equations for 2D compressible flow is given by:

$$\frac{\partial \mathbf{U}}{\partial t} + \frac{\partial \mathbf{F}_\mathrm{I}}{\partial x} + \frac{\partial \mathbf{G}_\mathrm{I}}{\partial y} = \frac{\partial \mathbf{F}_\mathrm{v}}{\partial x} + \frac{\partial \mathbf{G}_\mathrm{v}}{\partial y}. \tag{4.1}$$

The expressions for the inviscid and viscous-flux vectors are as follows:

$$\mathbf{F}_\mathrm{I} = \begin{bmatrix} \rho u \\ p + \rho u^2 \\ \rho uv \\ (p + \rho e_m)u \end{bmatrix}, \tag{4.2a}$$

$$\mathbf{G}_{\mathrm{I}} = \begin{bmatrix} \rho v \\ \rho u v \\ p + \rho v^2 \\ (p + \rho e_m) v \end{bmatrix}, \tag{4.2b}$$

$$\mathbf{F}_{\mathrm{v}} = \begin{bmatrix} 0 \\ \tau_{xx} \\ \tau_{xy} \\ u\tau_{xx} + v\tau_{xy} - q_x \end{bmatrix}, \tag{4.2c}$$

$$\mathbf{G}_{\mathrm{v}} = \begin{bmatrix} 0 \\ \tau_{yx} \\ \tau_{yy} \\ u\tau_{yx} + v\tau_{yy} - q_y \end{bmatrix}. \tag{4.2d}$$

The stress and heat-flux terms in the viscous-flux vectors can be expressed as

$$\tau_{xx} = \frac{\mu}{\mathrm{Re}_L} \left\{ \frac{4}{3}\frac{\partial u}{\partial x} - \frac{2}{3}\frac{\partial v}{\partial y} \right\}, \tag{4.3a}$$

$$\tau_{yy} = \frac{\mu}{\mathrm{Re}_L} \left\{ \frac{4}{3}\frac{\partial v}{\partial y} - \frac{2}{3}\frac{\partial u}{\partial x} \right\}, \tag{4.3b}$$

$$\tau_{xy} = \frac{\mu}{\mathrm{Re}_L} \left(\frac{\partial u}{\partial y} + \frac{\partial v}{\partial x} \right) = \tau_{yx}, \tag{4.3c}$$

$$q_x = -\left\{ \frac{\mu}{\mathrm{Re}_L \,\mathrm{Pr}\,(\gamma - 1)\, M_\infty^2} \right\} \frac{\partial T}{\partial x}, \tag{4.4a}$$

$$q_y = -\left\{ \frac{\mu}{\mathrm{Re}_L \,\mathrm{Pr}\,(\gamma - 1)\, M_\infty^2} \right\} \frac{\partial T}{\partial y}, \tag{4.4b}$$

where μ is the non-dimensionalized coefficient of dynamic viscosity and Re_L is the Reynolds number based on the characteristic length L given by $\mathrm{Re}_L = \mathrm{Re}_\infty L = \frac{\rho_\infty U_\infty L}{\mu_\infty}$. The parameters Re_∞ and Pr are the unit Reynolds number and Prandtl number, respectively. The quantities U_∞, M_∞, ρ_∞ and μ_∞ represent the velocity, Mach number, density and coefficient of dynamic viscosity of the free-stream, respectively.

4.2.2 Implementation of boundary conditions for viscous-compressible-flow computations

At the farfield the inviscid-compressible-flow boundary conditions can be used when the boundaries are placed far enough from the immersed body [103, 104]. In other words, the characteristic-based boundary conditions for subsonic and supersonic flows as discussed in section 3.3.3 can be implemented at the inlet and outlet. The height of the computational domain may be so chosen that no discontinuity, including the leading-edge shock crosses the top boundary. Accordingly either the free-stream conditions or the zero-gradient boundary condition may be implemented depending on the chosen height of the domain above the solid surface. The boundary conditions at the solid wall under adiabatic and isothermal conditions for viscous-flow computations have to be handled differently. Figure 4.3 shows a picture on a solid wall showing the interior and dummy cells.

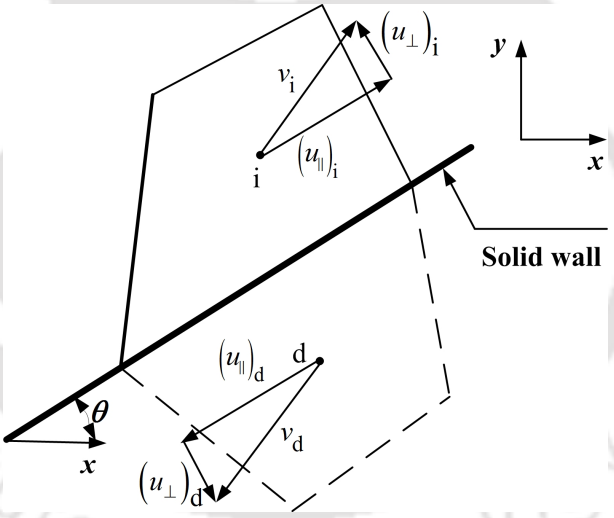

Fig. 4.3. The no-slip boundary condition for viscous flows.

As shown in figure 4.3, the velocity components both parallel and normal to the wall in the dummy cell are equal in magnitude but opposite in sign to the corresponding quantities in the interior cell. In the figure, $\left(u_\parallel\right)_{\rm i}$ and $(u_\perp)_{\rm i}$ represent the velocity components in the interior cell parallel and normal to the wall, respectively. The symbols $\left(u_\parallel\right)_{\rm d}$ and $(u_\perp)_{\rm d}$ are the corresponding velocity components in the dummy cell. The wall is inclined at any arbitrary angle θ with the x-axis. To enforce the no-slip boundary condition the x- and y-velocity

components are evaluated as follows:

$$\begin{aligned} u_{\mathrm{d}} &= -u_{\mathrm{i}} \\ v_{\mathrm{d}} &= -v_{\mathrm{i}}. \end{aligned} \tag{4.5}$$

For an isothermal wall the temperature in the dummy cell is specified the same as the specified wall condition. For the adiabatic-wall condition, since heat-flux along the wall-normal direction is zero, hence the temperature in the dummy cell T_{d} is given by

$$T_{\mathrm{d}} = T_{\mathrm{i}}, \tag{4.6}$$

where T_{i} is the temperature at the interior cell. After assigning the temperature at the dummy cell the pressure p_{d} and density ρ_{d} are computed as follows:

$$\begin{aligned} p_{\mathrm{d}} &= p_{\mathrm{i}} \\ \rho_{\mathrm{d}} &= \frac{p_{\mathrm{d}}}{RT_{\mathrm{d}}}. \end{aligned} \tag{4.7}$$

where p_{i} is the pressure in the interior cell.

4.2.3 The problem statement and the grid used

Viscous flow of air at Mach 3 over a flat plate of length $L = 2.85 \times 10^{-5}$ m is computed. The free-stream pressure and temperature are taken as 101325 Pa and 288.15 K, respectively. This corresponds to a Reynolds number Re_L of around 2000. The Prandtl number is taken as 0.71. Thus, the boundary layer developed on the plate can be considered laminar. Table 4.1 lists the geometric and free-stream parameters for this problem [93].

Table. 4.1. The geometric and free-stream parameters for viscous supersonic flow over a flat plate

Parameter	**Value**
Length of the plate L	0.0000285 m
free-stream pressure p_∞	101325 Pa
free-stream temperature T_∞	288.15 K
free-stream Mach number M_∞	3
Wall-temperature for isothermal condition T_{w}	288.15 K

The height of the computational domain normal to the plate is taken as six times the boundary-layer thickness at the trailing edge, so that the free-stream conditions can be imposed in the top boundary. The boundary-layer thickness at the trailing edge can be computed as follows [93]:

$$\delta_h = \frac{5L}{\sqrt{\mathrm{Re}_L}} = 3.186 \times 10^{-6}\ \mathrm{m}. \tag{4.8}$$

To accurately capture the sharp velocity gradients near the solid surface along the wall-normal direction, grid-refinement is done near the plate. The grid is formed using the following stretching function [103]:

$$\begin{aligned} x &= \xi \\ \frac{y}{h} &= \frac{(\beta+1) - (\beta-1)B^{1-\eta}}{1 + B^{1-\eta}}, \end{aligned} \tag{4.9}$$

where h is the height of the computational domain, ξ and η are the transformed co-ordinates, and $B = \frac{\beta+1}{\beta-1}$, β $(1 < \beta < \infty)$ is the stretching parameter. As β gets closer to unity, grid-point clustering is higher near the wall. In the present work β is taken as 1.1. Figure 4.4 shows a typical 40×40 grid obtained using equation 4.9 along with the boundary conditions used in the edges of the computational domain.

The first-order Euler-explicit time-integration method is used with a CFL number of 0.2 for all the computations. Both isothermal- and adiabatic-wall conditions are considered. In the computation of the Navier-Stokes equations, since physical viscosity is already present, it is preferable to use a scheme with small numerical diffusion. From equation 2.83 it can be observed that a reduction in the value of δ implies reduced numerical diffusion in the DRLLF scheme. Hence in the present work, the DRLLF scheme is adopted by gradually decreasing δ from 0.5 to 0.1 in steps of 0.1. The gradients at the cell-interfaces in the viscous-flux terms are computed by using both central differencing and Green's theorem. The results with these two techniques are presented in the following sections.

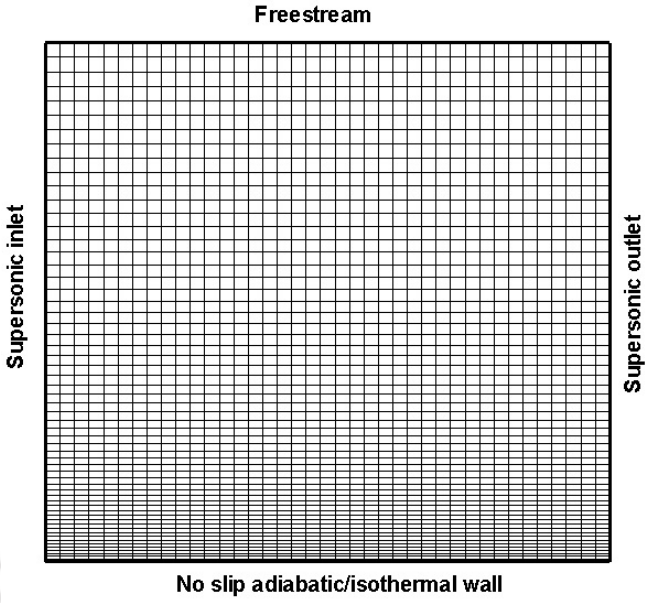

Fig. 4.4. A typical 40×40 grid for supersonic-laminar flow over a flat plate showing the computational domain and the boundary conditions.

4.2.4 Results with gradient computation at cell-interfaces using central differencing

A typical-grid-independence study is presented in figure 4.5 that shows the steady state normalized temperature ($\overline{T} = T/T_\infty$) profile at the trailing edge of the plate under adiabatic condition using the first-order AUSM scheme. The results are shown for the 40×60, 60×80, 80×100, 100×120 and 120×140 grids. It is found that the 80×100 grid produces the grid-independent results. All the subsequent results for this problem are presented on the 80×100 grid. As suggested by Van Driest [105] the non-dimensionalized y-distance is given by

$$\overline{y} = \frac{y}{x}\sqrt{\mathrm{Re}_x}, \tag{4.10}$$

where $\mathrm{Re}_x = \frac{\rho_\infty U_\infty x}{\mu_\infty}$.

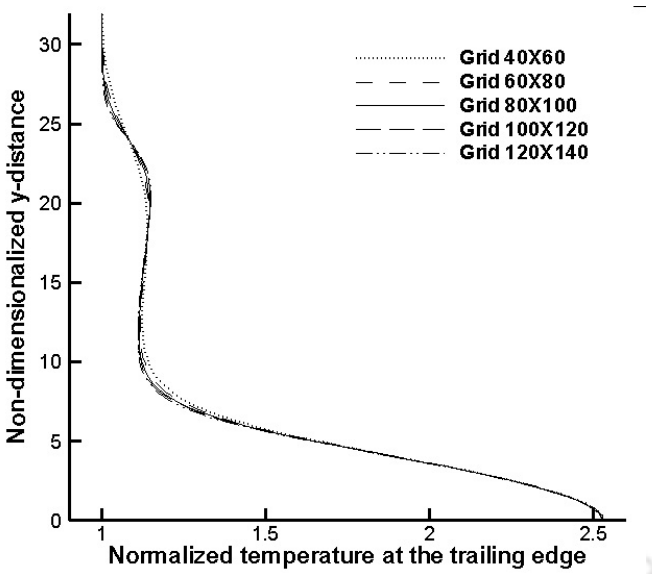

Fig. 4.5. Grid-independence test for computation of supersonic-laminar flow over a flat plate.

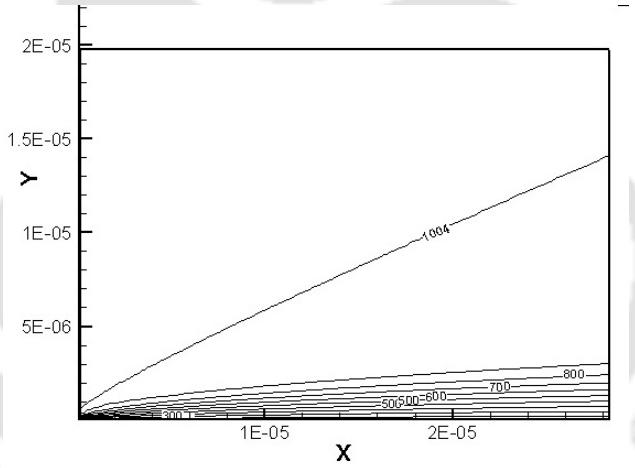

Fig. 4.6. u-velocity contours for supersonic-laminar flow over a flat plate under the isothermal-wall condition computed by using the DRLLF scheme ($\delta = 0.5$).

The u-velocity contours using the DRLLF scheme with $\delta = 0.5$ for the isothermal- and adiabatic-wall conditions are shown in figures 4.6 and 4.7, respectively[1]. The leading-edge shock and the boundary layer captured by the scheme can be seen clearly in the figures.

[1]This work is published in *International Journal of Applied and Computational Mathematics*, Springer, Vol. 2 (2016)

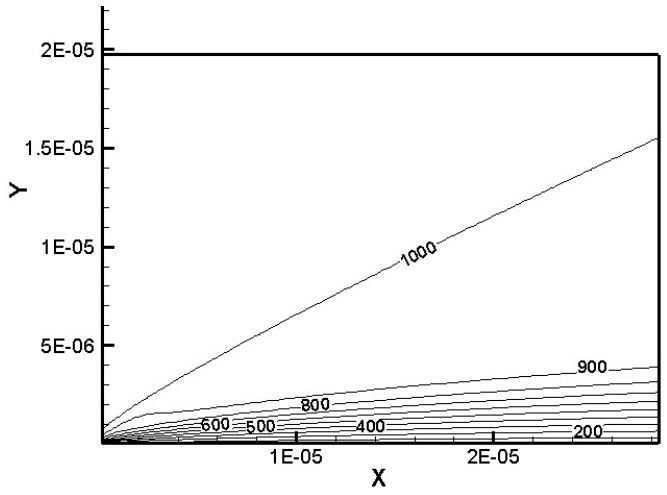

Fig. 4.7. u-velocity contours for supersonic-laminar flow over a flat plate under the adiabatic-wall condition computed by using the DRLLF scheme ($\delta = 0.5$).

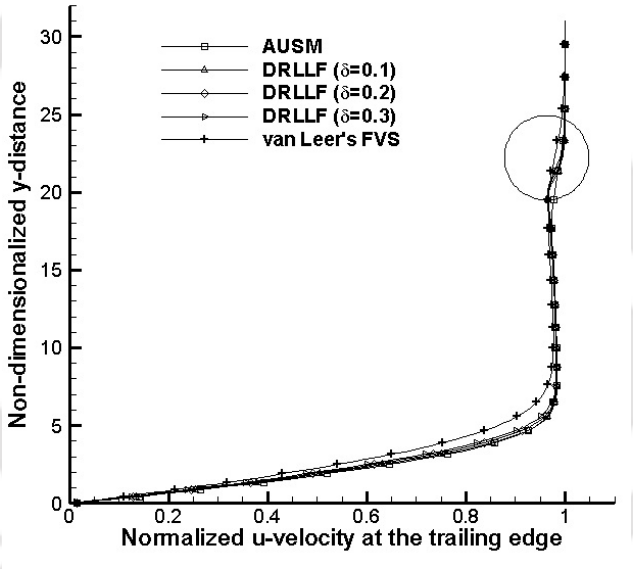

Fig. 4.8. Trailing-edge-u-velocity profile for supersonic-laminar flow over a flat plate under the isothermal-wall condition. Gradients at the cell-interfaces are computed by using central differencing.

Figures 4.8 and 4.9 show the steady-state normalized u-velocity ($\overline{u} = u/U_\infty$) profiles at the trailing edge of the plate vs. the non-dimensionalized y-distance for the isothermal- and adiabatic-wall conditions, respectively. For clarity of the figures, the results of the DRLLF scheme with $\delta = 0.1$, 0.2 and 0.3 only are shown along with those of AUSM and van Leer's FVS schemes. It is seen that the DRLLF scheme with $\delta = 0.1$ and $\delta = 0.2$ are in very close agreement with the AUSM scheme. This shows that by using a value of δ much lower than what was reported

in the original paper for inviscid computations, it is possible to bring down the numerical diffusion of the DRLLF scheme and hence improve accuracy without causing numerical instability. The van Leer's FVS scheme predicts a much higher hydrodynamic-boundary-layer thickness, depicting the highly diffusive nature of the scheme.

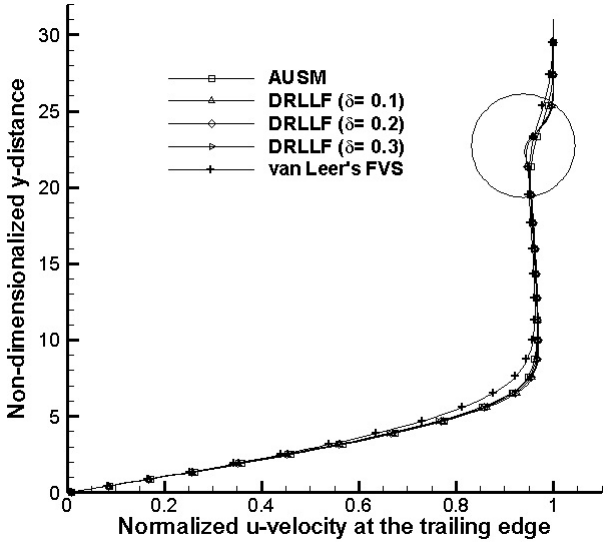

Fig. 4.9. Trailing-edge-u-velocity profile for supersonic-laminar flow over a flat plate under the adiabatic-wall condition. Gradients at the cell-interfaces are computed by using central differencing..

Figures 4.10 and 4.11 show the steady-state-normalized-temperature profiles at the trailing edge for the isothermal- and adiabatic-wall conditions, respectively. Comparing figures 4.10 and 4.11, two interesting differences in the temperature profiles for the isothermal- and adiabatic-wall conditions can be noticed, which are correlated with the numerical diffusion of the different inviscid flux schemes as follows.

Figure 4.10 shows that for the isothermal-wall condition, a point of maximum temperature is reached at some distance above the wall. It is seen that as the numerical diffusion increases the point of maximum temperature shifts upwards. Thus for the AUSM scheme this point is nearest to the wall, it moves up for the DRLLF scheme with increasing values of δ and is farthest from the wall for van Leer's FVS scheme. It is known that the ratio of the thicknesses of the hydrodynamic and thermal boundary layers is a function of the Prandtl number. Accordingly with increasing numerical diffusion, both the hydrodynamic- as well

as the thermal-boundary-layer thicknesses increase. When the thermal-boundary-layer thickness is high, the temperature gradients normal to the wall are less and *vice-versá*. This explains the reason for the upward shifting of the point of the maximum temperature with increasing numerical diffusion. The second observation is that the temperature-variation trends above and below the point of the maximum temperature reverse for the isothermal-wall condition. Below the point of maximum temperature, at a certain distance from the wall, the highest diffusive scheme shows the lowest temperature and *vice-versá*. This can be ascribed to the fact that for a scheme with lower diffusion the rate of increase of temperature to the maximum point is sharper. On the other hand, above the point of maximum temperature, at a certain y-location, the more diffusive scheme shows higher temperature. This can be attributed to the gradual rate of decrease of temperature from the maximum point for a scheme with higher diffusion.

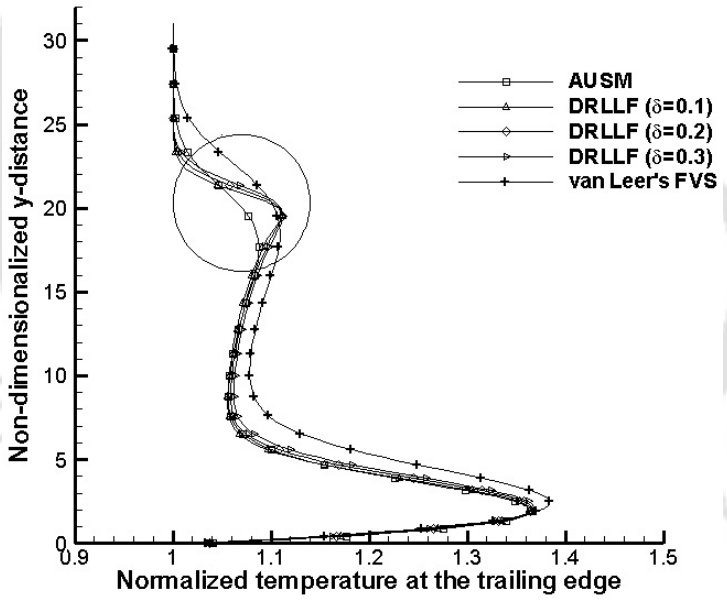

Fig. 4.10. Trailing-edge-temperature profile for supersonic-laminar flow over a flat plate under the isothermal-wall condition. Gradients at the cell-interfaces are computed by using central differencing.

Figure 4.11 shows that for the adiabatic-wall condition, the point of maximum temperature is located on the wall itself. This is thermodynamically justifiable since the high velocity of the incoming free-stream is decelerated by the viscous effects on the wall, thereby converting large part of the kinetic energy into enthalpy. If we consider a streamline connecting the free-stream and the first cell-centre

above the wall, the summation of the kinetic energy and the static enthalpy at the grid point is equal to the free-stream-stagnation enthalpy. Since the free-stream-stagnation enthalpy is constant, hence if the fluid-velocity shown by a scheme at the grid point is less, the static enthalpy obtained is more and *vice-versá*. For the highest diffusive scheme, because the fluid-velocity at the cell-centroid just above the wall is the least, hence the static enthalpy is the maximum. Since temperature is proportional to the static enthalpy, hence the temperature shown at that point is also the maximum for the most diffusive scheme. For an adiabatic wall, the temperature gradient at the wall is zero. Therefore the temperature at the wall is also equal to the temperature at the cell-centroid just above the wall. The second observation from figure 4.11 is that trend of the temperature variation for the adiabatic-wall condition remains the same throughout the thermal boundary layer, i.e. the more diffusive scheme predicts a higher temperature. The reason for this occurrence is the lower temperature gradient within the thermal boundary layer for the more diffusive scheme. It can be noted that the van Leer's FVS scheme predicts erroneously high adiabatic-wall temperature. However, the DRLLF scheme with $\delta = 0.1$ and 0.2 agrees well with the AUSM scheme.

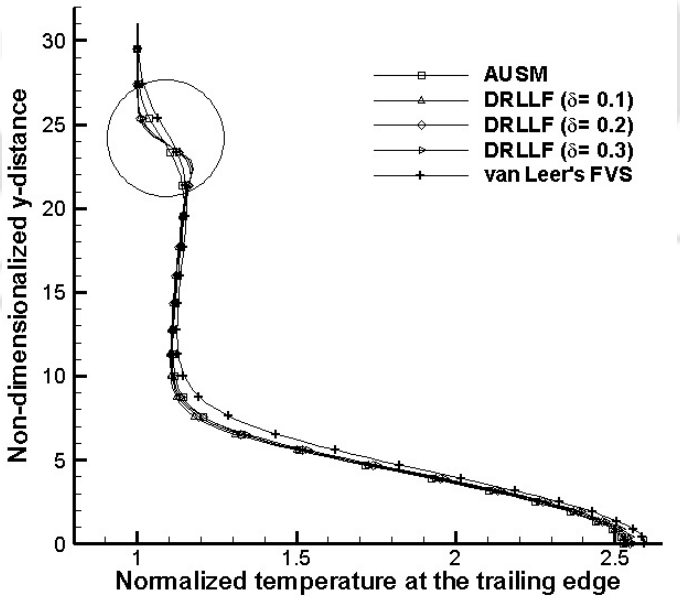

Fig. 4.11. Trailing-edge-temperature profile for supersonic-laminar flow over a flat plate under the adiabatic-wall condition. Gradients at the cell-interfaces are computed by using central differencing.

From figures 4.8-4.11 it can be further observed that the DRLLF scheme captures the leading-edge shock better than the AUSM and van Leer's FVS schemes as shown by the encircled portions in these figures. The better performance of the DRLLF scheme in capturing weak shocks for inviscid flows has been demonstrated in section 3.3.4. Even for the present-viscous-flow problem, since the shock is weak, the DRLLF scheme is seen to resolve the shock better than the other two schemes.

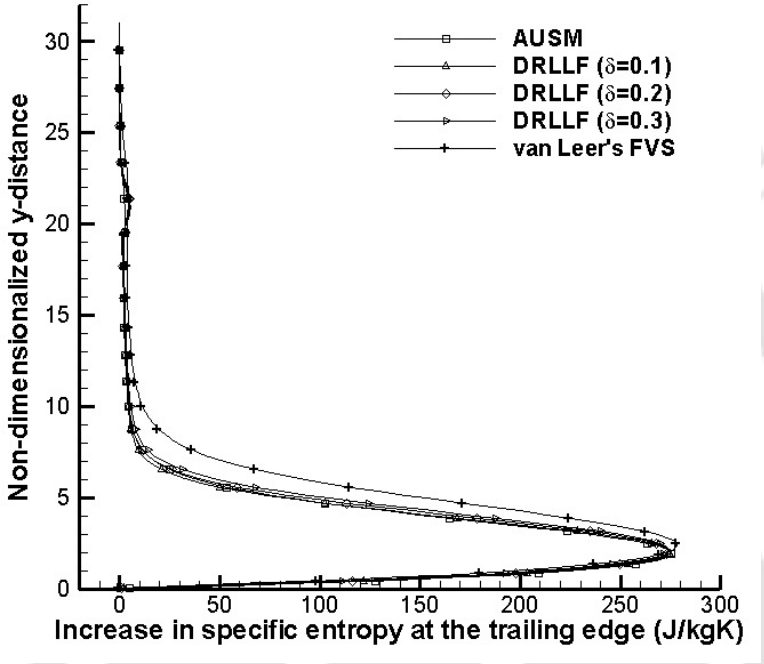

Fig. 4.12. Trailing-edge-specific-entropy profile for supersonic-laminar flow over a flat plate under the isothermal-wall condition. Gradients at the cell-interfaces are computed by using central differencing.

Entropy generation along the flow may be considered as a parameter to quantify the relative numerical diffusion of various schemes [6, 106]. However, in viscous-flow computations, the numerical diffusion may not be the only factor influencing the entropy profile since there may be other effects such as heat transfer across the wall. Still it will not be out of place to study the change of entropy for the different schemes as it will provide an insight into the entropy generation due to diffusion. The free-stream conditions are considered as the datum and increase in specific entropy at any point over this datum is computed by using the

thermodynamic identity:

$$\Delta s = c_p \ln\left(\frac{T}{T_\infty}\right) - R \ln\left(\frac{p}{p_\infty}\right). \tag{4.11}$$

For compressible-laminar-boundary layer over a flat plate, the pressure ratios are small compared with the temperature gradients. Thus, the effect of the pressure-term in equation 4.11 is not prominent compared with that of the temperature-term. As a result, the trend of the specific-entropy profile is expected to be similar to the temperature profile as corroborated by figures 4.12 and 4.13.

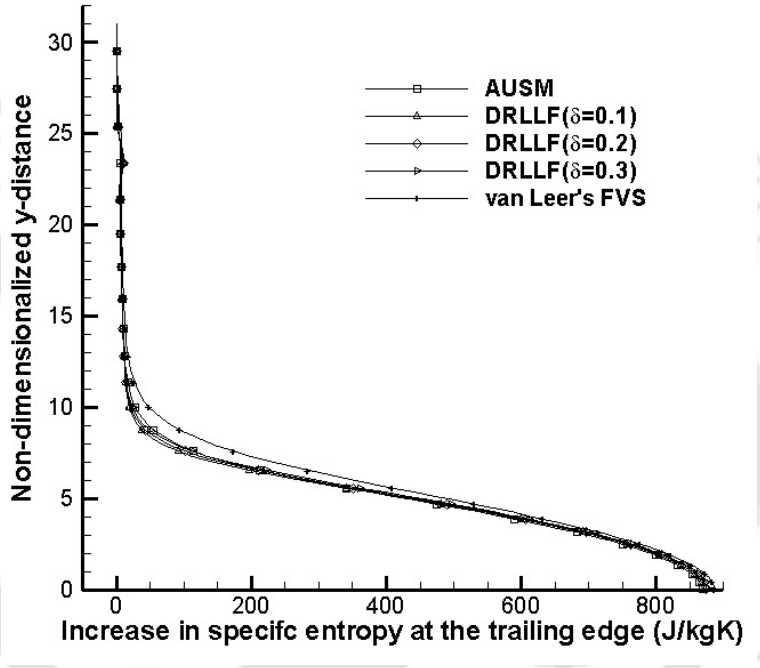

Fig. 4.13. Trailing-edge-specific-entropy profile for supersonic-laminar flow over a flat plate unnder the adiabatic-wall condition. Gradients at the cell-interfaces are computed by using central differencing.

It appears from figures 4.8-4.13 that for the DRLLF scheme, $\delta = 0.1$ gives the results closest to the AUSM scheme. However at such low value of δ the residual diminishes in an oscillatory fashion. This is evident from figures 4.14 and 4.15, which show the L_2-norm-residual-history plots for the isothermal- and adiabatic-wall conditions using the different schemes. However at higher values of δ, the convergence of the DRLLF scheme is found similar to van Leer's FVS and AUSM schemes. Thus based on a trade-off between accuracy and smooth convergence rate, $\delta = 0.2$ is the most suitable value for evaluating the DR parameter in the computation of this class of problems.

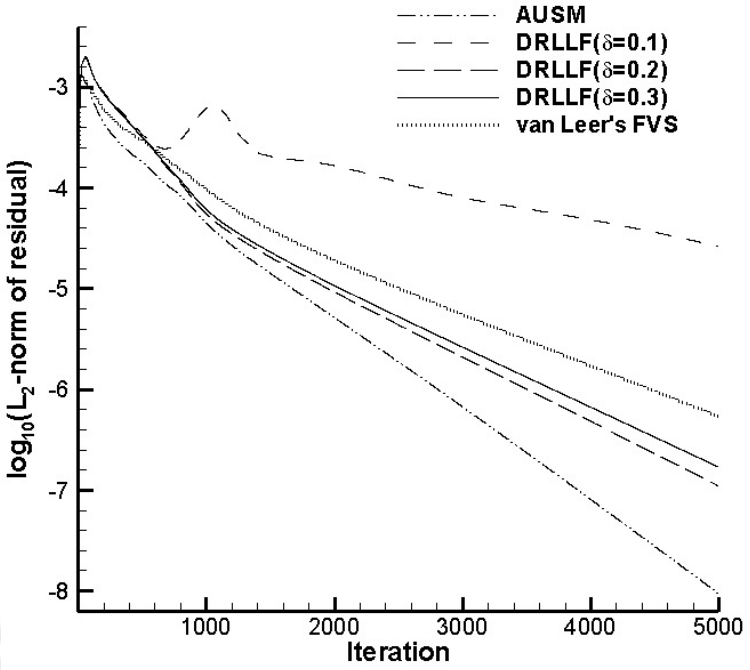

Fig. 4.14. Residual-history plots for supersonic-laminar flow over a flat plate under the isothermal-wall condition. Gradients at the cell-interfaces are computed by using central differencing.

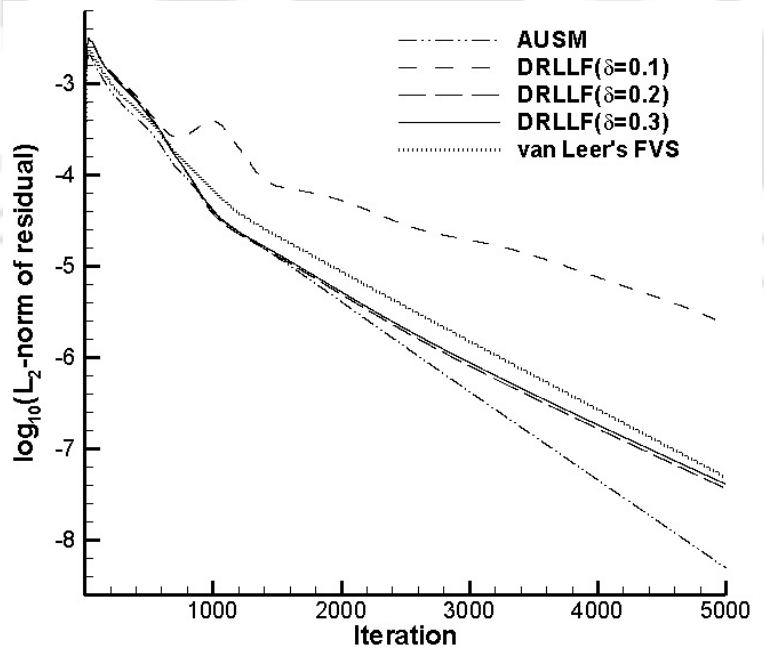

Fig. 4.15. Residual-history plots for supersonic-laminar flow over a flat plate under the adiabatic-wall condition. Gradients at the cell-interfaces are computed by using central differencing.

4.2.5 Results with gradient computation at cell-interfaces using Green's theorem

The u-velocity profile at the trailing edge for the isothermal- and adiabatic-wall conditions using the different inviscid flux schemes are shown in figures 4.16 and 4.17, where the gradients in the viscous fluxes are computed with Green's theorem. The very high boundary-layer thickness computed by using the van Leer's FVS scheme affirms that the scheme is not suitable for viscous-flow computations. The velocity profiles obtained by using central differencing and Green's theorem as shown in figure 4.8, 4.9, 4.16 and 4.17, respectively, are similar. The temperature and entropy profiles at the trailing edge as well as the residual-history plots for the Green's theorem are also found similar to those for the central differencing method, which demonstrate the equivalence of the two gradient-computation methods on a regular Cartesian grid.

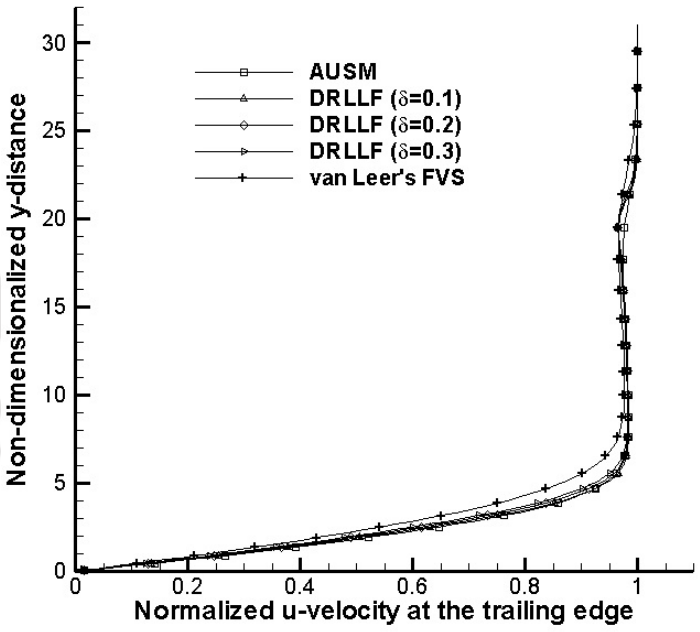

Fig. 4.16. Trailing-edge-u-velocity profile for supersonic-laminar flow over a flat plate under the isothermal-wall condition. Gradients at the cell-interfaces are computed by using Green's theorem.

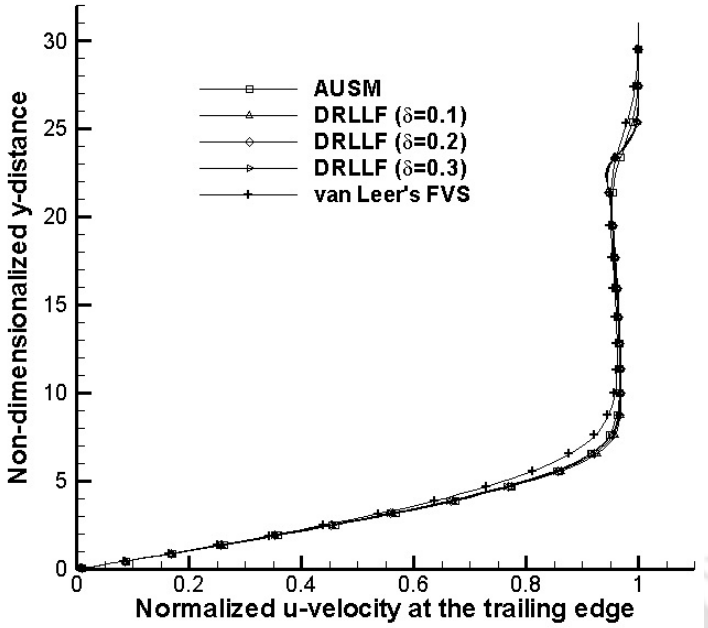

Fig. 4.17. Trailing-edge-u-velocity profile for supersonic-laminar flow over a flat plate under the adiabatic-wall condition. Gradients at the cell-interfaces are computed by using Green's theorem.

4.2.6 Comparison of CPU-time

Table. 4.2. Comparison of CPU-time for computing viscous supersonic flow over an isothermal-flat plate

Inviscid-flux scheme	**Gradient-computation scheme**	**CPU-time (s)**
AUSM	central differencing	145.61
	Green's theorem	160.08
DRLLF($\delta = 0.2$)	central differencing	141.39
	Green's theorem	155.987
van Leer's FVS	central differencing	139.183
	Green's theorem	150.476

The same machine and compiler are used for the comparison of the computational time for the different scheme-combinations. The processor is Intel(R) Core (TM) 2 Duo T5550 with a processor speed of 1.83 GHz, and having 1GB RAM. The

Microsoft Visual C++ 6 compiler is used to compile all the codes. Table 4.2 lists the CPU-time for 5000 iterations by the different scheme-combinations for the isothermal-wall condition. A similar trend is observed for the adiabatic-wall condition also.

From the residual-history plots, it is seen that the AUSM, DRLLF ($\delta = 0.2$) and van Leer's FVS schemes converge almost after the same number of time-steps. However, van Leer's FVS is found to give poor accuracy for viscous-flow computations. For the present computations, the DRLLF ($\delta = 0.2$) scheme is found with higher overall accuracy than the AUSM scheme. In addition table 4.2 reveals that the DRLLF scheme consumes marginally less CPU-time per iteration than the AUSM scheme. This can be attributed to the algorithmic simplicity of the former scheme. For large-viscous computations, the saving in computational time by using DRLLF scheme may be significant compared with the AUSM scheme without any loss of accuracy.

4.3 Effects of numerical diffusion in the computation of hypersonic shock-wave boundary layer interaction

This section presents the problem statement for a ramp-induced hypersonic SWBLI problem and the grid used along with the boundary conditions. This is followed by the results and discussion on the effects of numerical diffusion in the computation of hypersonic SWBLI with laminar separation. The level of numerical diffusion in the DRLLF scheme is regulated by changing the parameter δ in equation 2.83 and a qualitative analysis is offered on its effects on the computed-skin-friction profile, laminar-separation-bubble (LSB) size, pressure-coefficient profile and convergence behaviour. Comparisons are made with the AUSM and van Leer's FVS schemes as well.

4.3.1 The problem statement and the grid used with the boundary conditions

A ramp-induced hypersonic SWBLI problem as discussed in section 4.1 is considered. The length of the flat surface from the ramp upto the compression-corner is 0.05 m. The total length of the ramped passage is 0.12 m. The unit Reynolds number $Re_\infty = \frac{\rho_\infty U_\infty}{\mu_\infty}$ is $8 \times 10^5\ \mathrm{m}^{-1}$. The free-stream Mach number M_∞ is 6. The free-stream stagnation temperature $(T_0)_\infty$ is 1080 K. The wall is maintained isothermally at 300 K. The ramp angle is 15^0, which, under the given free-stream and wall conditions, is greater than the incipient-separation angle suggested by Needham ans Stollery [96]. Table 4.3 lists the geometric and free-stream parameters for this problem [98].

The problem statement is given again in table 4.3. Computations are carried out on a stretched grid with clustering near the solid wall and the ramp junction. For the mesh generation, the grid-stretching function given by equation 4.9 is used in this problem also. Figure 4.18 shows a typical coarse grid with 120×80 cells along with the boundary conditions for the computation of the hypersonic SWBLI problem. The height of the computational domain is taken as 1.2 times the length of the flat-plate portion from the leading edge up to the ramp junction [102]. This is done to ensure that at the top the free-stream boundary condition can be used without causing significant error.

Table. 4.3. The geometric and free-stream parameters for the hypersonic SWBLI problem.

Parameter	**Value**
Length of the plate upto the compression-corner (L_c)	0.05 m
Total length of the ramped surface	0.12 m
Ramp angle θ	15^0
free-stream stagnation temperature $(T_0)_\infty$	1080 K
Unit Reynolds number Re_∞	$8 \times 10^5\ \mathrm{m}^{-1}$
free-stream Mach number M_∞	6
Wall-temperature T_w	300 K

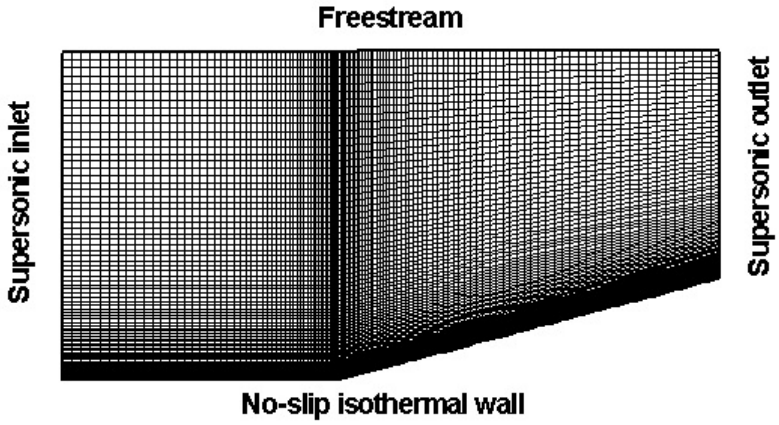

Fig. 4.18. A typical coarse grid for computing the hypersonic SWBLI problem.

Since the problem involves non-orthogonal grids, the method of central differencing for gradient-computation will not work in this case. Therefore, the gradient-terms in the viscous fluxes are computed by using the Green's theorem. First-order Euler explicit time-integration method with a CFL number of 0.2 is used for all the computations. Figure 4.19 shows the grid-independence test for the variation of skin friction coefficient along the ramped surface computed with the first-order-accurate AUSM scheme. The plot shows that grid-independent solutions are achieved for the 192×140 mesh. Hence subsequent results are shown for this grid only.

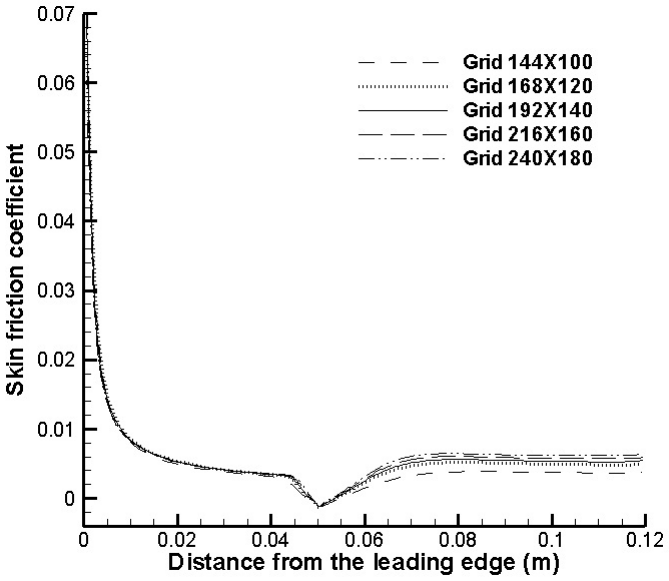

Fig. 4.19. Grid-independence test for the hypersonic SWBLI problem with the first-order AUSM scheme.

4.3.2 Effects of numerical diffusion on the skin-friction profile

Figure 4.20 shows the skin-friction-coefficient profiles for the problem using the DRLLF scheme[2] with $\delta = 0.1$, 0.3 and 0.5. Numerical experiments suggest that the DRLLF scheme becomes numerically unstable for $\delta < 0.1$. It is seen that in the attached region, the computed-skin-friction coefficient is the maximum for $\delta = 0.1$ and its value decreases with increasing δ. Since the numerical diffusion decreases with the reduction of δ, therefore the computed-boundary-layer thickness also decreases, leading to increased velocity gradients at the solid wall. As a result the computed-wall-shear stress increases and hence the skin friction coefficient also increases.

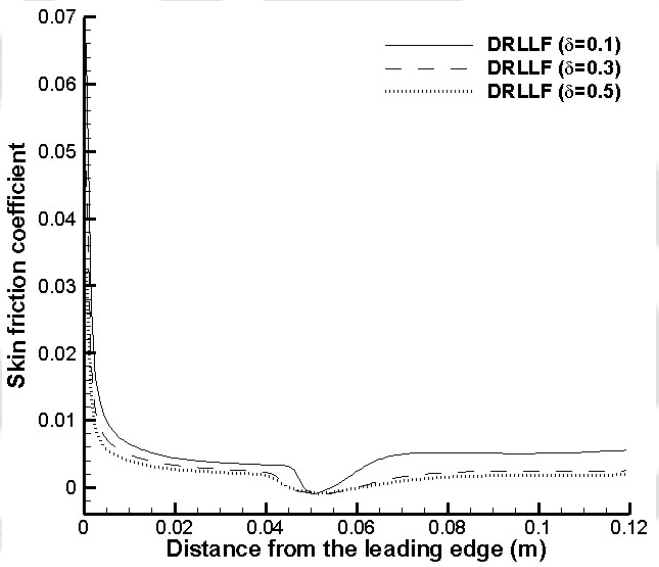

Fig. 4.20. skin-friction profiles for the hypersonic SWBLI problem using the DRLLF scheme with different values of δ.

Figure 4.21 shows the skin-friction-coefficient profiles computed with the AUSM, DRLLF ($\delta = 0.1$), DRLLF ($\delta = 0.2$), DRLLF ($\delta = 0.5$) and van Leer's FVS schemes. The DRLLF($\delta = 0.5$) scheme highly underpredicts the skin-friction-coefficient profile similar to van Leer's FVS scheme, indicating comparable levels of numerical diffusion of the two schemes. The DRLLF scheme with ($\delta = 0.1$) provides a much crisper resolution of the skin-friction-coefficient profile compara-

[2]This work is published in the proceedings of the International Symposium on Aspects of Mechanical Engineering and Technology for Industry (2014), NERIST, Arunachal Pradesh, India

ble with the AUSM scheme. The performance of the DRLLF ($\delta = 0.2$) is close to the DRLLF ($\delta = 0.1$) scheme upstream of the separation point. However, in the post re-attachement zone the former scheme underpredicts the skin-friction profile compared with the latter. It is evident that in the presence of physical viscosity, there is ample scope for reducing the numerical diffusion of the DRLLF scheme compared with the level originally suggested for the Euler solvers by Jaisankar and Raghurama Rao [40].

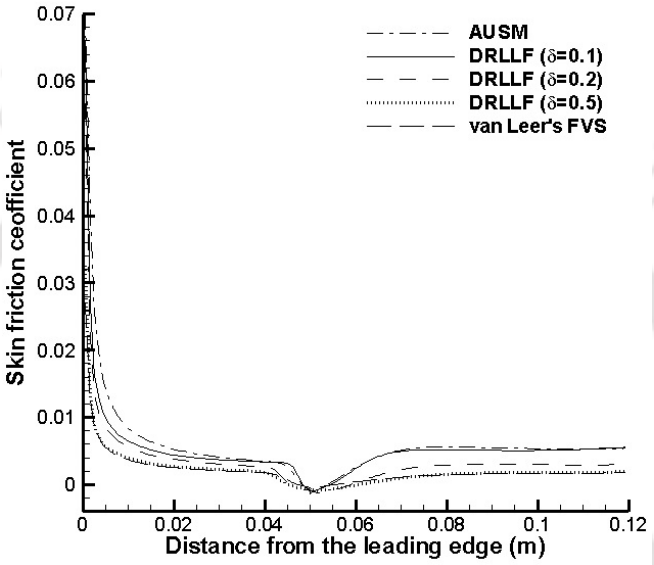

Fig. 4.21. skin-friction profiles for the hypersonic SWBLI problem using the AUSM, van Leer's FVS, DRLLF ($\delta = 0.1$), DRLLF ($\delta = 0.2$) and DRLLF ($\delta = 0.5$) schemes.

4.3.3 Effects of numerical diffusion on the size of laminar separation bubble (LSB)

A study of the effect of numerical diffusion on the computed LSB length is done. Table 4.4 lists the LSB lengths obtained by the AUSM, van Leer's FVS and DRLLF schemes. For the DRLLF scheme, the values are reported for different values of δ by decreasing the parameter from 0.5 to 0.1 in steps of 0.1. The length of the LSB is calculated as the difference between the extrema of the x-coordinates where the skin friction coefficient remains negative. It can be seen that the computed LSB

length increases with the increase in the numerical-diffusion level.

Table. 4.4. Comparison of LSB length for the hypersonic SWBLI problem

Scheme	LSB length (mm)
AUSM	5.24
van Leer's FVS	14.42
DRLLF (δ=0.5)	15.19
DRLLF (δ=0.4)	12.18
DRLLF (δ=0.3)	9.46
DRLLF (δ=0.2)	7.26
DRLLF (δ=0.1)	5.56

4.3.4 Effects of numerical diffusion on the pressure-coefficient profile

Figure 4.22 shows the wall-pressure-coefficient profiles with the AUSM, DRLLF ($\delta = 0.1$), DRLLF ($\delta = 0.2$), DRLLF ($\delta = 0.5$) and van Leer's FVS schemes. It is seen that with increased level of numerical diffusion, the separation zone (encircled) in the pressure-coefficient profile increases in size.

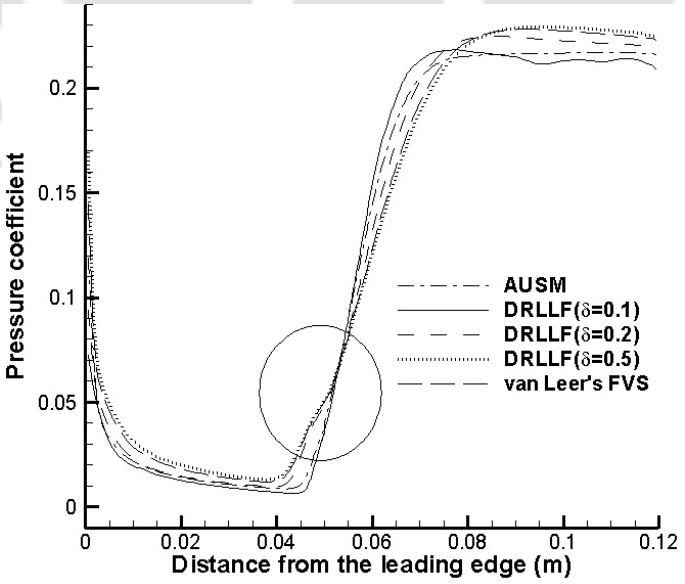

Fig. 4.22. pressure-coefficient profiles for the hypersonic SWBLI problem using the AUSM, DRLLF ($\delta = 0.1$), DRLLF ($\delta = 0.2$), DRLLF ($\delta = 0.5$) and van Leer's FVS schemes.

4.3.5 Effects of numerical diffusion on convergence

Figure 4.23 shows the residual-history plots for computing the SWBLI problem with the AUSM, DRLLF ($\delta = 0.1$) and van Leer's FVS schemes. It can be noted that the residual-history plots for the DRLLF scheme with $\delta = 0.2$, 0.3, 0.4 and 0.5 are almost the same and therefore the residual-history plots for the DRLLF scheme with these values of δ are not shown for clarity of the figure. The schemes have markedly similar convergence behaviour.

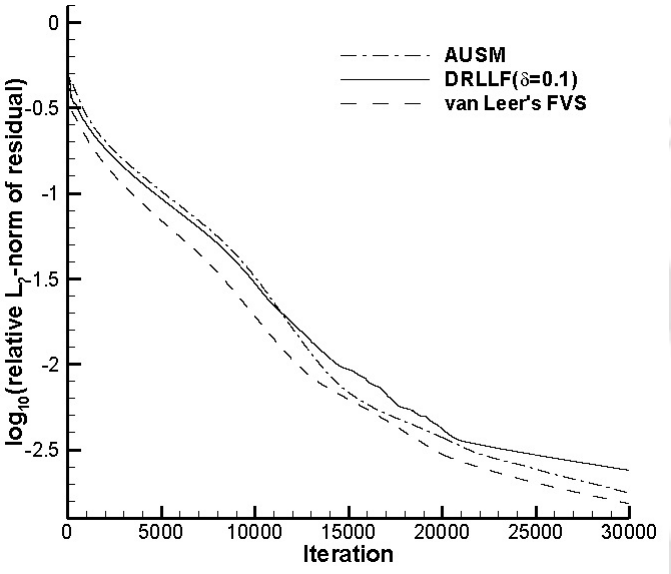

Fig. 4.23. Residual-history plots for the hypersonic SWBLI problem with the AUSM, DRLLF ($\delta = 0.1$) and van Leer's FVS schemes.

4.4 Effects of limiters in the computation of viscous supersonic flow over a flat plate using higher-order-reconstruction methods

In this section the performances of some limiters in the higher-order reconstruction of the variables for computing the inviscid fluxes of viscous-compressible flows are studied. The supersonic-flow problem over a flat plate given in table 4.1 is considered as the test problem. The inviscid fluxes of the 2D Navier-Stokes equations, governing the flow are computed with the AUSM scheme. The Green's theorem described in Appendix E is used to compute the gradients in the viscous fluxes.

The minmod, van Albada and Hemker-Koren limiters presented in section 2.6.3 are employed with the MUSCL approach described in section 2.6.1. In addition, the Venkatakrishnan limiter (see section 2.6.3) is used with the piecewise-linear-reconstruction techninque presented in section 2.6.2.

Figure 4.24 presents the normalized-velocity ($\overline{u} = u/U_\infty$) profile at the trailing edge of the plate for the isothermal-wall condition, using the second-order AUSM with the four limiter functions and the first-order accurate method[3]. The non-dimensionalized y-distance is obtained by equation 4.10 as suggested by Van Driest [105]. As anticipated, the second-order computations with all the limiter functions yield a less diffused boundary layer compared with the first-order method. As seen in the encircled portion, the van Albada, minmod and Hemker-Koren limiters are found to produce similar velocity profiles for the isothermal case, but the one given by the Venkatakrishnan limiter is more diffused.

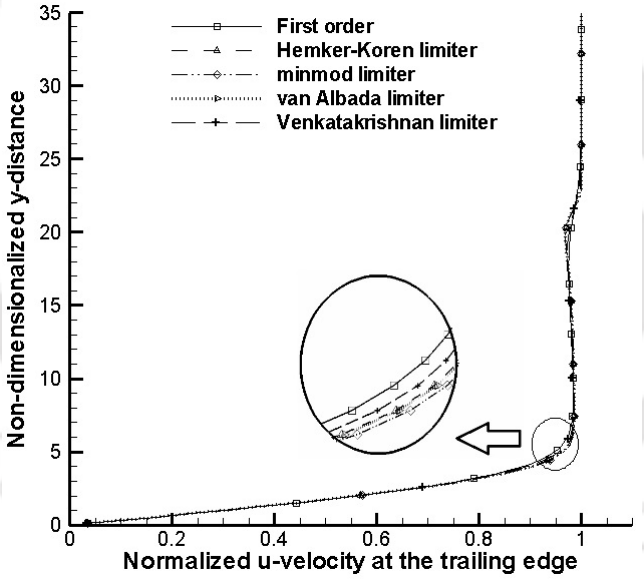

Fig. 4.24. Normalized-u-velocity profile at the trailing edge for supersonic-laminar flow over a flat plate under the isothermal-wall condition.

The normalized temperature ($\overline{T} = T/T_\infty$) profiles for the isothermal-wall condition computed by using the first-order method and the higher-order methods with the four limiters are shown in Figure 4.25. The plot shows that for the first-order scheme, which is the most diffusive of the methods tested, the maximum temperature computed within the boundary layer is the highest. This is evident

[3]This work is published in the proceedings of the International Conference on Frontiers in Mathematics (2015), Gauhati University, India

from the encircled portion in Figure 4.25. The computed temperature profiles by the minmod, van Albada and the Hemker-Koren limiters are very close to each other. This suggests that these three limiters have similar diffusive nature. For the Venkatakrishnan limiter the maximum computed temperature is close to that with the first-order method. This observation affirms that for this type of viscous computations the Venkatakrishnan limiter is more diffusive than the other three limiters.

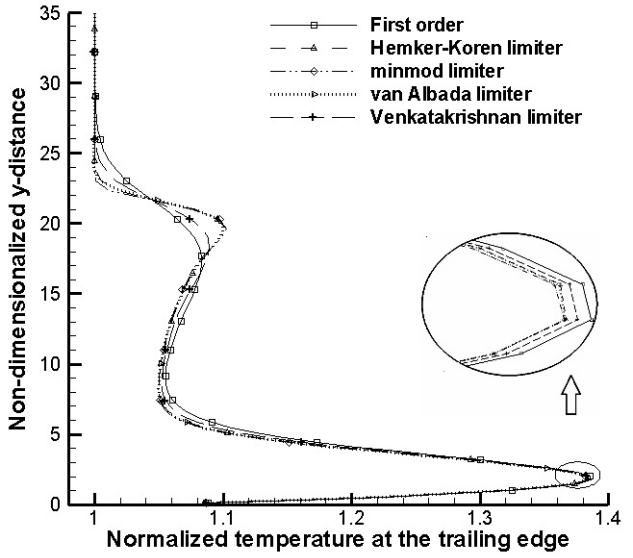

Fig. 4.25. Normalized-temperature profile at the trailing edge for supersonic-laminar flow over a flat plate under the isothermal-wall condition.

The normalized u-velocity profiles at the trailing edge of the plate for the adiabatic-wall condition are shown in Figure 4.26. The Venkatakrishnan limiter is found to be the most diffusive of the four limiters. The differences in the results of the Hemker-Koren, minmod and the van Albada limiters are not significant. However, on a resolved scale the minmod limiter is found to produce the least diffused results among these three functions. Figure 4.27 presents the normalized-temperature profiles at the trailing edge for the adiabatic-wall condition using different methods. It has been demonstrated in section 4.2.4 that a scheme with more numerical diffusion computes a higher-wall temperature. Accordingly, it can be seen that the first-order method gives the highest-wall temperature. The wall-temperature using the Venkatakrishnan limiter is in between the first-order-accurate result and those using the other three limiters. In the case of adiabatic-wall condition also, no appreciable differences in the results obtained using the

minmod, van Albada and Venkatakrishnan limiter functions are seen. However, among the three, the minmod limiter exhibits slightly less diffusive nature as can be seen in the encircled portion near the wall.

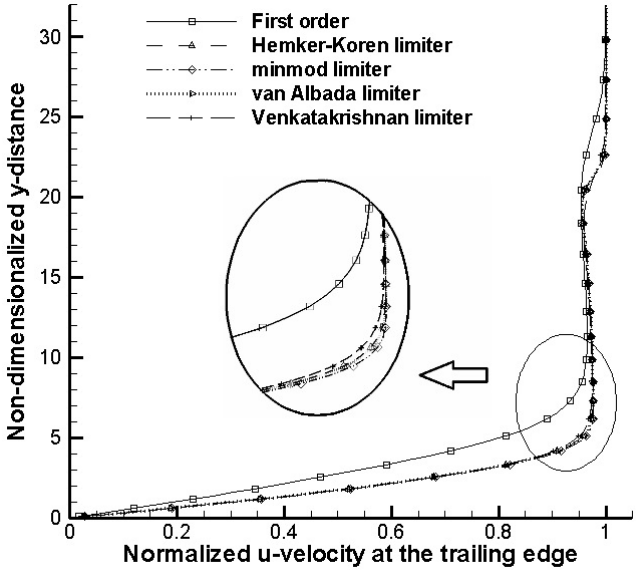

Fig. 4.26. Normalized u-velocity profile at the trailing edge for supersonic-laminar flow over a flat plate under the adiabatic-wall condition.

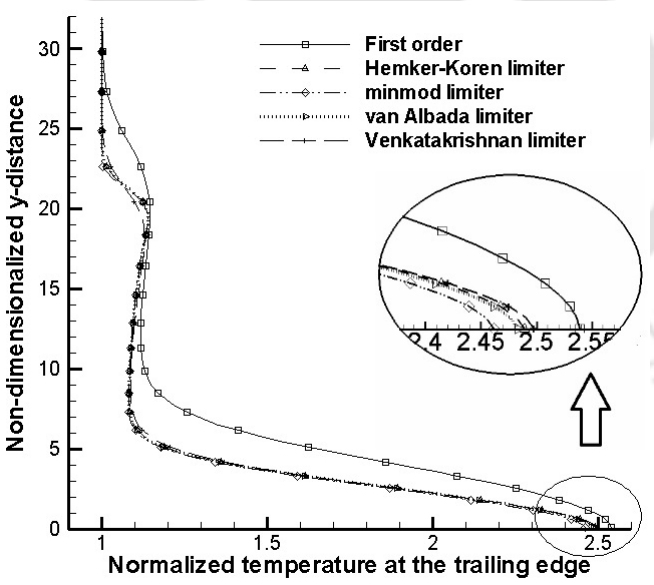

Fig. 4.27. Normalized temperature profile at the trailing edge for supersonic-laminar flow over a flat plate under the adiabatic-wall condition.

The convergence behaviour of the limiters are shown in figures 4.28 and 4.29 for the isothermal- and adiabatic-wall conditions, respectively. The L_2-norm-residual-history plots show that all the limiters behave in similar fashion for both

wall conditions. This indicates that the performances of these limiters from the convergence point of view are similar.

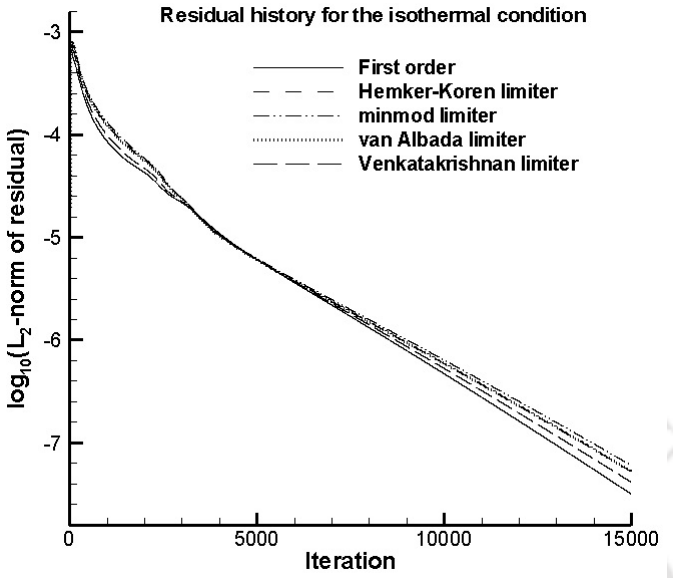

Fig. 4.28. L_2-norm residual-history for supersonic-laminar flow over a flat plate under the isothermal-wall condition.

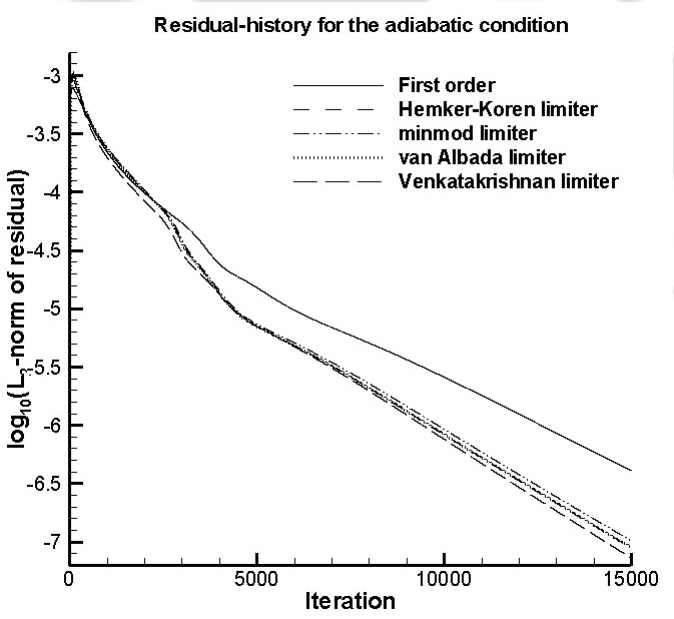

Fig. 4.29. L_2-norm residual-history for supersonic-laminar flow over a flat plate under the adiabatic-wall condition.

4.5 Conclusions

This chapter presents some aspects of viscous-compressible-flow computations in three stages. The first stage investigates the effects of numerical diffusion in the computation of viscous supersonic flow over a flat plate with a laminar boundary layer. In the second stage, similar study is carried out for computing hypersonic shock wave-boundary layer interaction with a laminar separation. The third stage presents a study on the performances of some limiters in the computation of the viscous supersonic flow over a flat-plate problem computed with higher-order AUSM scheme using solution-reconstruction.

In the computation of viscous-supersonic flow past a flat plate, a study is carried out to examine whether it is possible to use lower levels of numerical diffusion in the DRLLF scheme, than stability permits in the computation of inviscid flows. This study shows that reduced artificial viscosity is indeed a possibility. Considering both accuracy and smooth convergence a lower value of the numerical-diffusion parameter ($\delta = 0.2$) is suggested for computing such flows. However, a comprehensive mathematical formulation for the regulation of the numerical diffusion applicable to a wide range of compressible-flow conditions can further be framed. The overall accuracy of the computation using a smaller DR parameter is higher because it resolves the boundary layer as accurately as the AUSM scheme and additionally resolves the shock better than the AUSM and van Leer's FVS schemes. The DRLLF scheme is also comparable with the AUSM and van Leer's FVS schemes in terms of CPU-time per iteration. Limitation of the van Leer's FVS scheme for viscous-flow computations due to high-numerical diffusion is affirmed again. For the isothermal-wall condition, the location of the point of maximum temperature shifts upward when the numerical diffusion increases and the trends of the temperature profiles above and below this point reverse for different numerical schemes. For the adiabatic-wall condition, a more diffusive scheme predicts a higher-wall temperature. Also it is found that on a regular-orthogonal grid, the Green's theorem is comparable with the central-differencing method for the computation of the gradients across cell-interfaces.

Hypersonic shock wave-boundary layer interaction over a ramped surface is

computed by using the DRLLF, AUSM and van Leer's FVS schemes. It is seen that for hypersonic-viscous-flow computations the numerical diffusion of the DRLLF scheme can be further reduced below the level prescribed originally for inviscid-flow computations. A reduced value of $\delta = 0.1$ used to compute the DR parameter is suggested for computing the SWBLI problem. However, the most suitable value of δ for any problem is to be chosen based upon the various flow parameters such as free-stream Mach number, pressure, temperature, wall-temperature etc. It is shown that high-numerical diffusion results in under-prediction of the wall-shear-stress profile due to a diffused boundary layer. Further, a qualitative analysis of the effect of numerical diffusion on the laminar-separation-bubble (LSB) length is done. The LSB-length is found to increase with the increase in numerical diffusion. The convergence rate of the DRLLF scheme for hypersonic-viscous computations like the SWBLI problem is also comparable with the AUSM and van Leer's FVS schemes.

For the study on the performances of limiters in the higher-order-accurate computations of viscous-compressible flows, the problem on supersonic flow over a flat plate at zero incidence producing a laminar boundary layer is computed with the first-order AUSM and higher-order methods of AUSM scheme using solution-reconstruction. For computation, the MUSCL approach and the piecewise-linear-reconstruction technique are used. The MUSCL approach is implemented using the Hemker-Koren, minmod and van Albada limiter functions. The piecewise-linear reconstruction is applied with the Venkatakrishnan limiter function. The Venkatakrishnan limiter is the most diffusive among the four functions tested. The minmod limiter exhibits marginally less diffusive nature than the others. The convergence behaviour of all the limiters are found similar with the first-order method.

Chapter 5

A Diffusion-Regulated Scheme for Viscous Compressible Flows With a Novel Boundary-Layer Sensor

5.1 Introduction

Heretofore the DRLLF scheme is used in such a way that the Diffusion-Regulation (DR) parameter is scaled down equally throughout the computational domain. However, in flows involving boundary layer the viscous effects are the most prominent on the fluid-solid interface and away from the interface these effects gradually diminish as one moves towards the edge of the boundary layer. Accordingly, the nature of viscous flows suggest the possibility of differential regulation of numerical viscosity inside and outside the shear layer. Here the differential control of the numerical diffusion of the DRLLF scheme is achieved by modifying the original DR parameter. The modified version of the DR parameter operates based on a new boundary-layer sensor developed in such a way that the numerical diffusion is further reduced inside the viscous zone only and in the outer inviscid zone the parameter reverts back to the original inviscid formulation. This new scheme is named as the DRLLF-Viscous (DRLLFV) scheme[1]. Earlier investigations on viscous-flow computations using the finite volume framework suggest scaling down

[1]This work is published in *Computers & Fluids*, Elsevier, Vol. 129 (2016)

the numerical diffusion in the wall-normal direction only [107]. In conformity with the same principle, this work also suggests the reduction of the numerical diffusion of the DRLLF scheme within the boundary layer only along the wall-normal direction.

To implement the idea we undertake the development of a structured grid high-speed viscous flow solver (HSVFS) that can compute the inviscid and viscous fluxes using as many number of schemes as one desires. The present solver incorporates the van Leer's FVS, AUSM, DRLLF and DRLLFV schemes. The solver is capable of handling the first- and higher-order-accurate methods of the schemes using appropriate-reconstruction methods with different limiters. For the higher-order computation using the van Leer's FVS and AUSM schemes, the minmod limiter [64] and van Albada limiter [63] can be used through the MUSCL approach [38]. In addition, the Venkatakrishnan limiter [39] can be used through the piecewise-linear-reconstruction approach [61]. High resolutions of the DRLLF and DRLLFV schemes can be obtained by combining these two schemes with the aforesaid limiters as well as Jameson's limiter originally suggested for the CUSP scheme [5]. The viscous fluxes can be computed by using either the Green's theorem [54] or the Cross-Diffusion Method [55].

For the validation of the solver and checking the numerical performance of the DRLLFV scheme, the present work considers two test cases. The first test case is viscous supersonic flow past a flat plate [93] at zero incidence. The second problem is ramp-induced hypersonic shock wave-boundary layer interaction (SWBLI) under different free-stream and wall conditions [98, 108, 109]. Throughout the rest of this chapter, the first and second test cases are referred to as problem-1 and problem-2, respectively.

For problem-1, the computed results of the HSVFS are compared with corresponding ANSYS-FLUENT simulations for code-validation. In both the HSVFS as well as the ANSYS-FLUENT simulations, the inviscid fluxes are computed by using the higher-order AUSM schemes. The results are found in excellent agreement, which validates the code. Additionally, the trailing-edge velocity and temperature profiles computed by the HSVFS through the first- and higher-order-accurate DRLLFV schemes are analyzed along with the corresponding results of the AUSM,

van Leer's FVS and DRLLF schemes. From the analysis, it is found that the DRLLFV scheme resolves the boundary layer far more accurately than the van Leer's FVS and DRLLF schemes. The DRLLFV scheme also outperforms the AUSM scheme both within and outside the boundary layer in that it resolves the skin-friction profile and the leading-edge shock cripser than the latter.

Further evaluation of the HSVFS is done by comparing the computed skin-friction, pressure-coefficient and wall-heat flux profiles with corresponding published numerical and experimental results for problem-2 [98, 108, 109]. In the case of hypersonic SWBLI problems as well, the DRLLFV scheme is able to resolve the boundary layer more accurately than the AUSM scheme. As a result, the skin-friction profile in the attached zone computed by using the DRLLFV scheme is higher than the AUSM scheme. The wall-heat flux obtained by the DRLLFV scheme is also higher than the published computed results and closer to the available experimental data. Thus, the superior performance of the DRLLFV scheme in computing high-speed-viscous flows is demonstrated.

This chapter is organized in four sections. The philosophy and working of the boundary-layer sensor and the newly proposed DRLLFV scheme are presented in section 5.1. The superior performance the DRLLFV scheme compared with the AUSM scheme for viscous-flow computations and the validation of the HSVFS are demonstrated in section 5.3. The improved results with the new scheme are summarized in section 5.4.

5.2 The boundary-layer sensor and the newly proposed diffusion-control methodology

The proposed method controls the diffusion-regulation parameter Φ based upon the parameter r_{vg} which is the absolute value of the ratio of the velocity gradient across the cell-interface and velocity gradient at the wall:

$$r_{\text{vg}} = \left| \frac{(\partial U_{\text{par}}/\partial \eta)_{\text{interface}}}{(\partial U_{\text{par}}/\partial \eta)_{\text{wall}}} \right|, \tag{5.1}$$

where U_{par} is the velocity component parallel to the wall, η is the direction normal to the wall, and the subscripts 'interface' and 'wall' represent the cell-interface and

the fluid-solid interface, respectively. The parameter r_{vg} is used as a boundary-layer sensor. The inviscid fluxes at the cell-faces that 'face' the flow are computed by using the DR parameter given in equation 2.83 only. Inside the boundary layer, the numerical diffusion in the convective-flux computation at the cell-faces that are 'aligned' with the flow is controlled as follows:

1. The location of the edge of the boundary layer is tracked using the parameter r_{vg}. At the wall $r_{\text{vg}} = 1$ and it decreases asymptotically from the wall till the edge of the boundary layer. Thus, a critical height Y_{critical} is identified at the cell for which, $r_{\text{vg}} \leq 0.01$.

2. In the cells where $Y < Y_{\text{critical}}$, the computed value of r_{vg} is returned. For $Y \geq Y_{\text{critical}}$ the value of r_{vg} is taken as zero.

3. A scaling function f is computed by using the following expression:

$$f = 1 - 2.25 r_{\text{vg}} + 1.3 r_{\text{vg}}^2. \tag{5.2}$$

From equation 5.2 it may be seen that $f = 1$ for $r_{\text{vg}} = 0$ and $f = 0.05$ for $r_{\text{vg}} = 1$. The DR parameter is now computed by modifying equation 2.83 as

$$\Phi = \begin{cases} f\frac{\left\{(\Delta M_\perp)^2 + \delta^2\right\}}{2\delta}, & \text{when } |\Delta M_\perp| \leq \delta \\ f\,|\Delta M_\perp|\,, & \text{when } \delta < |\Delta M_\perp| \leq 1.0 \\ 1 & \text{when } |\Delta M_\perp| > 1.0 \end{cases}. \tag{5.3}$$

Equation 5.3 reveals that outside the boundary layer the DR parameter is computed based upon the original inviscid formulation given by equation 2.83.

4. The formulation given by equation 5.2 and equation 5.3 works very well for viscous flows without boundary-layer separation. However for separated flows, at some locations, the parameter r_{vg} becomes greater than 1. This is due to the change of sign of U_{par} across adjacent cells close to the separated zone. Now Equation 5.2 returns a value of $f > 1$, when $r_{\text{vg}} > 1$. This in turn scales up the DR parameter instead of regulating it inside the boundary

layer. Thus, a more generalized formulation is prescribed by modifying the function f as follows:

$$f = \begin{cases} 1 - 2.25 r_{\text{vg}} + 1.3 r_{\text{vg}}^2, & \text{for } r_{\text{vg}} \leq 1 \\ 0.05 & \text{otherwise} \end{cases} . \tag{5.4}$$

It is to be noted that the numerical coefficients in equations 5.2 and 5.4 are empirically obtained based upon a set of numerical experiments and analysis. This procedure is briefly described in Appendix F.

5.3 Results and discussion

Parameters concerned with problem-1 and problem-2 are listed in tables 4.1, 4.3 and 5.1. Problem-1 is chosen with a reasonably small Reynolds number based on the characteristic length. For problem-2 the ramp angle is chosen in such a way that it is greater than the incipient-separation angle suggested by Needham and Stollery [96] for some cases [98, 108] and less than the incipient-separation angle for the other cases [109]. The test cases have both experimental as well as computational results for the performance evaluation of the DRLLFV scheme.

Table. 5.1. The geometric and free-stream parameters for problem-2.

Parameter	**Value**
Length of the plate upto the compression-corner (L_c)	0.05 m, 0.4389 m
Total length of the ramped surface	0.12 m, 0.8778 m
Ramp angle θ	15^0
free-stream stagnation temperature	1080 K, 1747 K, 1800 K
Unit Reynolds number Re_∞	8×10^5 m^{-1}, 236200 m^{-1}
free-stream Mach number M_∞	6, 14.1
Wall-temperature T_{w}	300 K, 298 K, 297.22 K

For both the problems, the convective fluxes are computed by using van Leer's FVS, AUSM, DRLLF and DRLLFV schemes. The gradients in the viscous fluxes are computed by using the Green's theorem [54]. The Euler explicit time integration is done with a CFL number of 0.2. For the better resolution of the boundary

layer, grid clustering near the wall is done using the stretching function given by equation 4.9.

In section 4.2.4 it was shown that the 80×100 grid produced the mesh-independent solution for problem-1. Henceforth, all the subsequent results for problem-1 are computed on a 80×100 grid only. Figures 5.1 and 5.2 show the normalized temperature $\left(\overline{T} = T/T_\infty\right)$ and normalized-u-velocity $(\overline{u} = u/U_\infty)$ profiles, respectively at the trailing edge under the adiabatic-wall condition for problem-1, obtained by using the HSVFS and ANSYS-FLUENT simulations. Both the computations are done on a computational domain of size 2.85×10^{-5} m $\times$ 1.91×10^{-5} m by using higher-order-accurate AUSM schemes. The results are found to be in good agreement to support the accuracy of the solver.

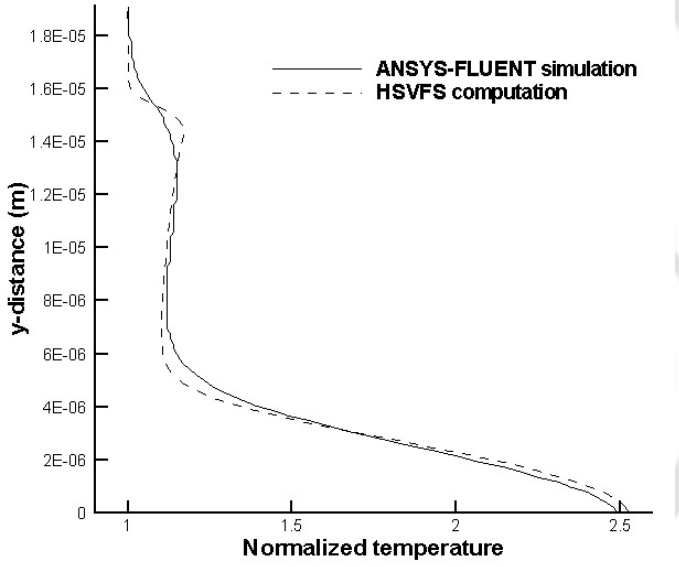

Fig. 5.1. Normalized-temperature profiles at the trailing edge for problem-1 under adiabatic-wall condition using HSVFS and ANSYS-FLUENT.

Figure 5.3 shows the normalized-temperature profiles at the trailing edge under the adiabatic-wall condition for problem-1 by using first-order-accurate DRLLF, DRLLFV, van Leer's FVS and AUSM schemes. Comparison of the results is made for the first-order methods as it helps isolate the effects of the relative numerical diffusion of the schemes from the effects of limiters used for the higher-order methods. It is seen that the adiabatic-wall temperature computed by using the DRLLF and van Leer's FVS schemes are much higher compared with the DRLLFV and AUSM schemes. The DRLLFV scheme estimates an adiabatic-wall

temperature close to the AUSM scheme.

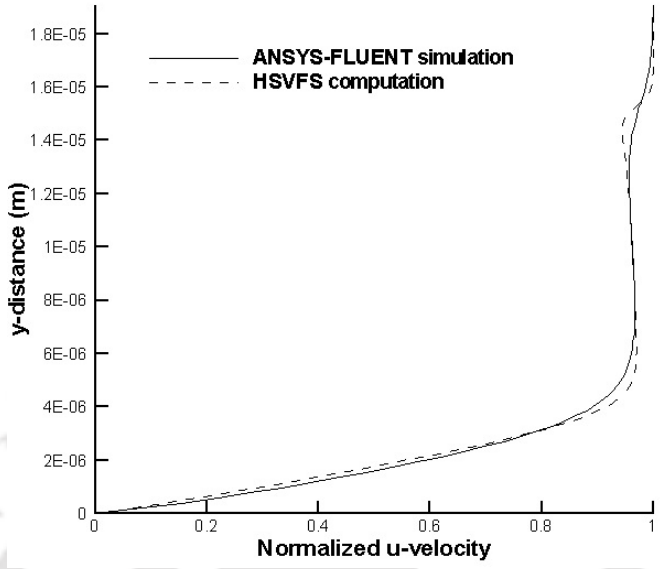

Fig. 5.2. Normalized-velocity profiles at the trailing edge for problem-1 under adiabatic-wall condition using HSVFS and ANSYS-FLUENT.

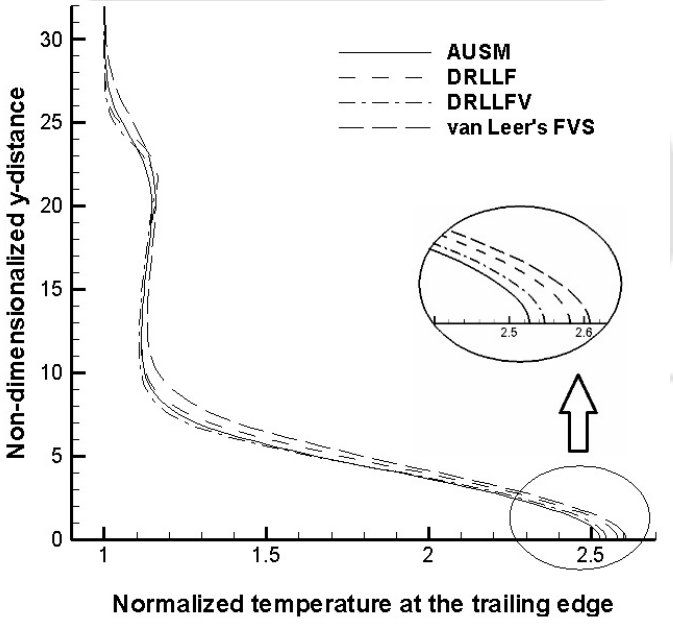

Fig. 5.3. Normalized-temperature profiles at the trailing edge for problem-1 under adiabatic-wall condition using first-order-accurate schemes.

Figure 5.4 shows the normalized-u-velocity profiles at the trailing edge for problem-1 under the adiabatic condition using the first-order methods of the four schemes mentioned in figure 5.3. The plots suggest that the DRLLFV scheme resolves the hydrodynamic boundary layer much better than the rest of the schemes.

The encircled portion shows a zoomed view of the edge of the hydrodynamic boundary layer. The van Leer's FVS scheme computes the most diffused edge of the hydrodynamic boundary layer and the present scheme resolves the edge of the boundary layer most sharply, followed by the DRLLF and AUSM schemes. It can be further noticed from figures 5.3 and 5.4 that apart from the accurate computation of the boundary layer (comparable with the AUSM scheme), the DRLLFV scheme resolves the leading-edge shock in the inviscid zone better than AUSM.

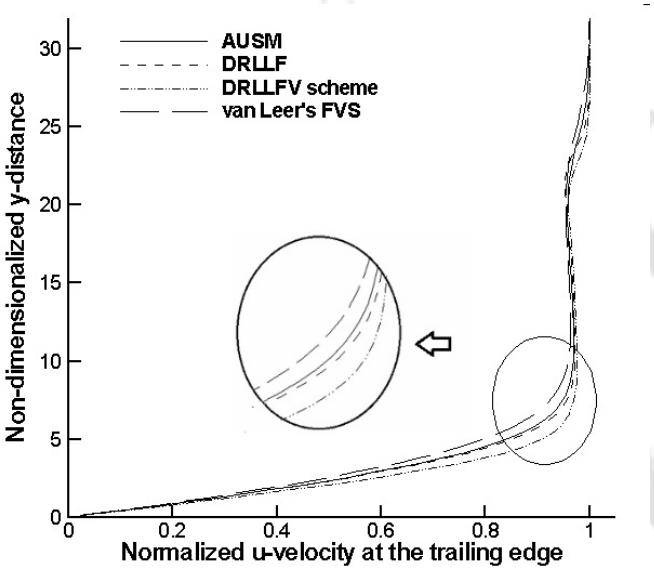

Fig. 5.4. Normalized-u-velocity profiles at the trailing edge for problem-1 under adiabatic-wall condition using first-order-accurate schemes.

Viscosity increases the thicknesses of hydrodynamic and thermal boundary layers. Thus, owing to numerical diffusion the boundary-layer thickness computed by using any numerical scheme is always higher than the actual value. In other words, a numerical scheme which predicts the lowest value of the boundary-layer thickness is generally preferable. Higher hydrodynamic boundary-layer thickness leads to lesser velocity gradient on the wall. This in turn leads to the underestimation of the wall-skin-friction coefficient. Figure 5.5 shows the variation of the skin-friction coefficient along the flat plate computed with the first-order-accurate AUSM, DRLLF, DRLLFV and van Leer's FVS schemes. As expected the van Leer's FVS scheme underpredicts the skin-friction coefficient. The skin-friction coefficients computed by using the DRLLFV scheme at corresponding locations are the highest.

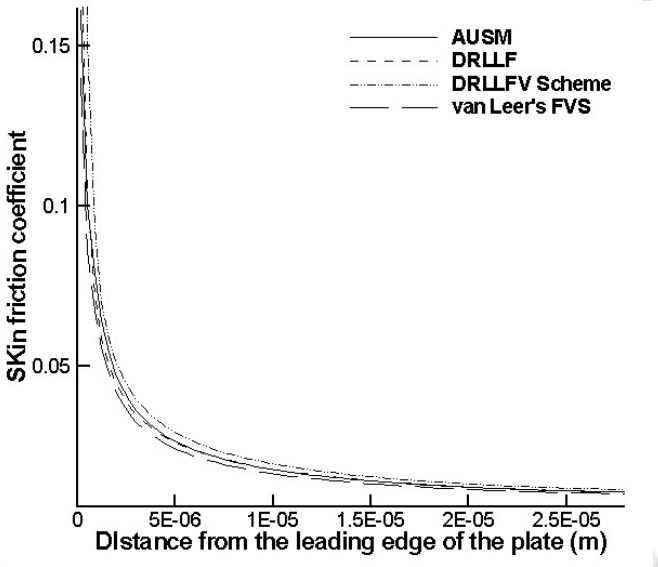

Fig. 5.5. Variations of the skin-friction coefficient along the flat plate for problem-1 under adiabatic-wall condition using first-order-accurate schemes.

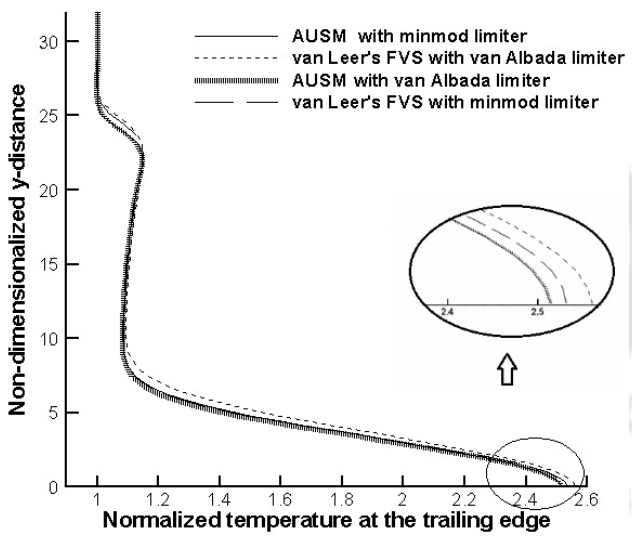

Fig. 5.6. Normalized-temperature profiles at the trailing edge for problem-1 under adiabatic-wall condition using higher-order-accurate AUSM and van Leer's FVS schemes.

The higher-order versions of the DRLLF and DRLLFV schemes are implemented with the limiter proposed by Jameson for the higher-order-accurate computation of the CUSP scheme [5], referred to in the present work as the CUSP limiter. The AUSM and van Leer's schemes are used in conjunction with the minmod and van Albada limiter. Figure 5.6 shows the normalized-temperature

profiles at the trailing edge of the flat plate under adiabatic-wall condition using the minmod and van Albada limiters with the AUSM and van Leer's FVS schemes. It is seen than that the AUSM scheme with the minmod limiter and van Albada limiters provide much better resolutions of the temperature field than the higher-order-accurate versions of the van Leer's FVS scheme. The AUSM scheme coupled with the minmod limiter shows marginally improved results over the AUSM scheme in conjunction with the van Albada limiter. Figure 5.7 shows the normalized-temperature profiles at the trailing edge of the plate under the adiabatic-wall condition computed by using the higher-order-accurate DRLLF and DRLLFV schemes and compares the results with the second-order AUSM scheme with the minmod limiter. Clearly, even in the higher-order-accurate computation also the DRLLFV scheme resolves the temperature field better than the DRLLF scheme and nearly as accurately as the AUSM scheme.

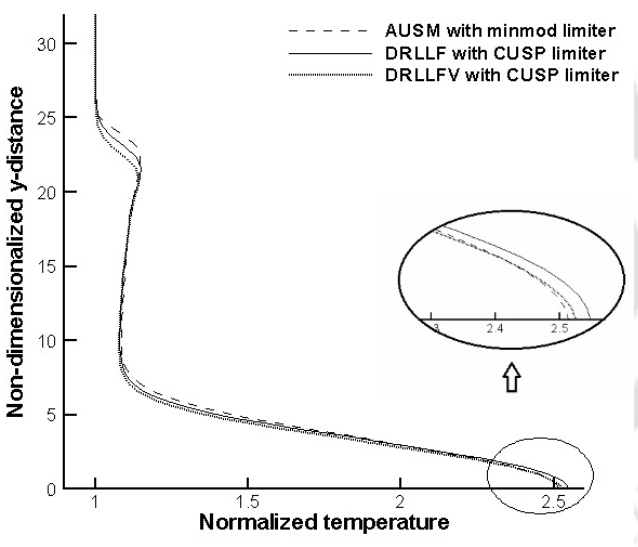

Fig. 5.7. Normalized-temperature profiles at the trailing edge for problem-1 under adiabatic-wall condition using higher-order-accurate DRLLF, DRLLFV and AUSM schemes.

Figure 5.8 compares the normalized-u-velocity profiles at the trailing edge for adiabatic-wall condition of problem-1 computed by using the higher-order-accurate DRLLF, DRLLFV and AUSM schemes. It can be seen that in this case also, the DRLLFV scheme produces a less diffused hydrodynamic boundary layer compared with the AUSM scheme. This means that the skin-friction-coefficient

profile computed by using the higher-order-accurate DRLLFV scheme should be higher than that obtained by the higher-order-accurate AUSM scheme. Figure 5.9 corroborates this fact.

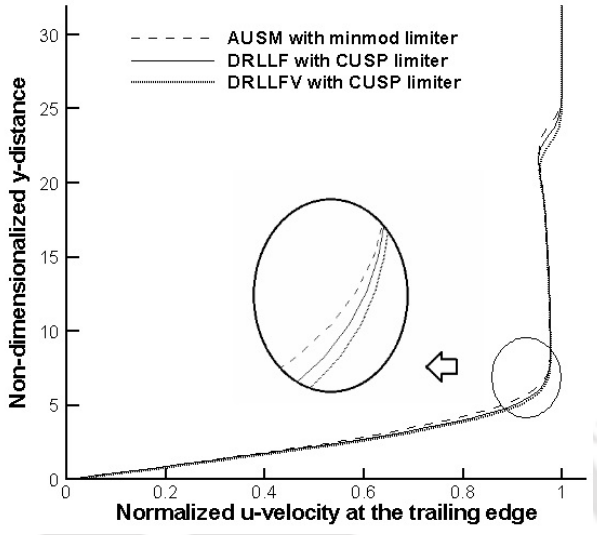

Fig. 5.8. normalized-u-velocity profiles at the trailing edge for problem-1 under adiabatic-wall condition using higher-order-accurate DRLLF, DRLLFV and AUSM schemes.

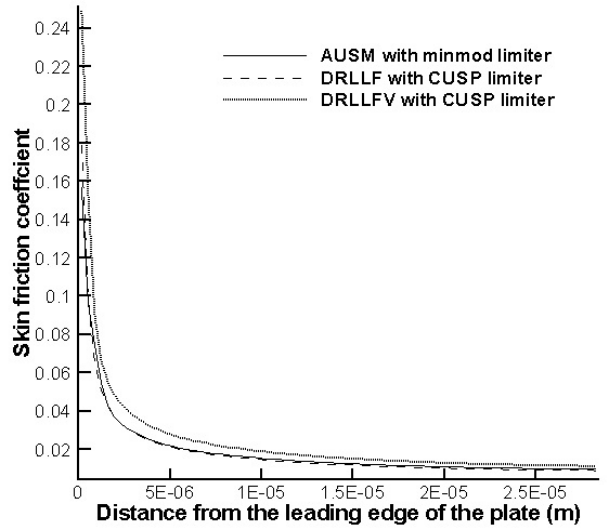

Fig. 5.9. Skin-friction profiles at the trailing edge for problem-1 under adiabatic-wall condition using higher-order-accurate DRLLF, DRLLFV and AUSM schemes.

For problem-2 when the ramp angle is greater than the incipient-separation angle [96], a separation bubble appears in the ramp junction due to adverse-pressure gradients. Figure 5.10 shows the u-velocity contours for the hypersonic

SWBLI problem, where, the free-stream stagnation temperature is 1080 K, free-stream Mach number is 6, length of the flat plate up to the ramp junction is 0.05 m, $\mathrm{Re}_\infty = 8 \times 10^5\ \mathrm{m}^{-1}$ and the wall-temperature is 300 K. The convective fluxes are computed by using the AUSM scheme with minmod limiter. The enlarged view of the separation bubble is shown in the encircled region. The leading-edge shock, the separation, as well as the re-attachment shocks and their merger further downstream of the ramp junction can also be seen in the figure.

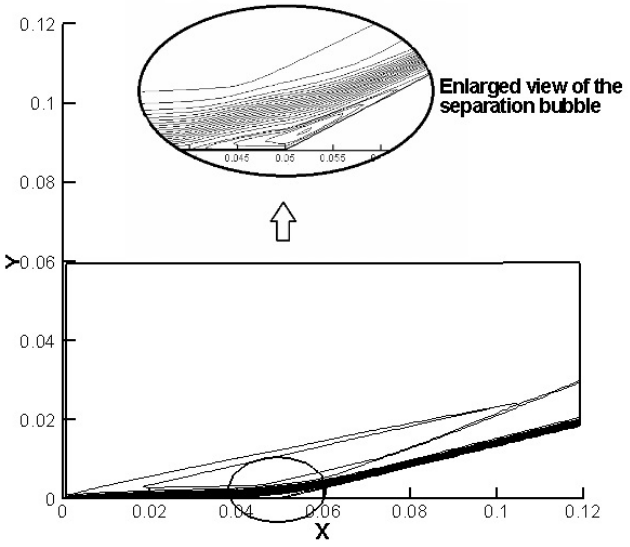

Fig. 5.10. u-velocity contours for problem-2 obtained using AUSM with minmod limiter.

A typical grid-independence test is done for problem-2. Here the free-stream stagnation temperature is 1080 K, free-stream Mach number is 6, length of the flat plate up to the ramp junction is 0.05 m, $\mathrm{Re}_\infty = 8 \times 10^5\ \mathrm{m}^{-1}$ and the wall-temperature is 300 K. The computations are carried out on 144×100, 168×120, 192×140, 216×160 and 240×180 grids. Figure 5.11 shows the grid-independence test with the skin-friction-coefficient profile along the ramped surface computed by using the AUSM scheme with minmod limiter. The plot shows that grid-independent solutions are reached for the 192×140 mesh. Hence subsequent results are shown for this grid only.

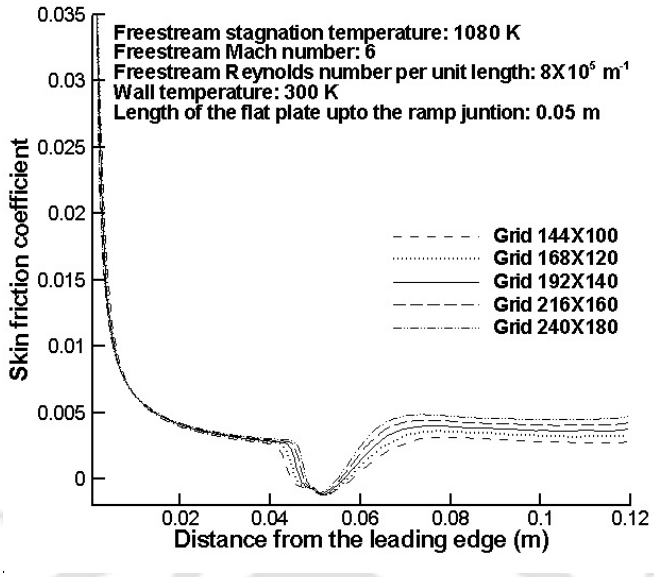

Fig. 5.11. Grid-independence test for problem-2 using higher-order AUSM scheme with minmod limiter.

For further validation of the HSVFS, the computed results for problem-2 are also compared with published numerical and experimental results. Figure 5.12 compares the skin-friction profiles along the ramped surface for the same problem using the second-order AUSM scheme with the published results [102]. The results are found to be in nice agreement, thus validating the solver. The improved performance of the DRLLFV scheme in resolving the hypersonic shock wave-boundary layer interaction can be seen from the skin-friction profile along the plate as shown in figure 5.13. In conformity with the observations of figures 5.5 and 5.9, for this problem also, the DRLLFV scheme computes a better-resolved skin-friction profile comparable with the AUSM scheme. The DRLLF and van Leer's FVS schemes badly fail to capture the same. Another important aspect that can be noticed is that in the post-reattachment zone, the skin-friction coefficient computed by using the DRLLFV scheme is on the higher side compared with the AUSM scheme. It is known that in hypersonic shock wave-boundary layer interactions, a point is reached after the re-attachment where the boundary layer becomes very thin [69]. This point is considered crucial for hypersonic-vehicle design since it corresponds to high-skin friction as well as high-heat transfer. There is a possibility that a more diffusive numerical flux scheme might lead to under-estimation of the skin friction and heat-transfer rates, especially in the post-reattachment zone owing

to a smeared boundary layer. Thus the present scheme holds good promise.

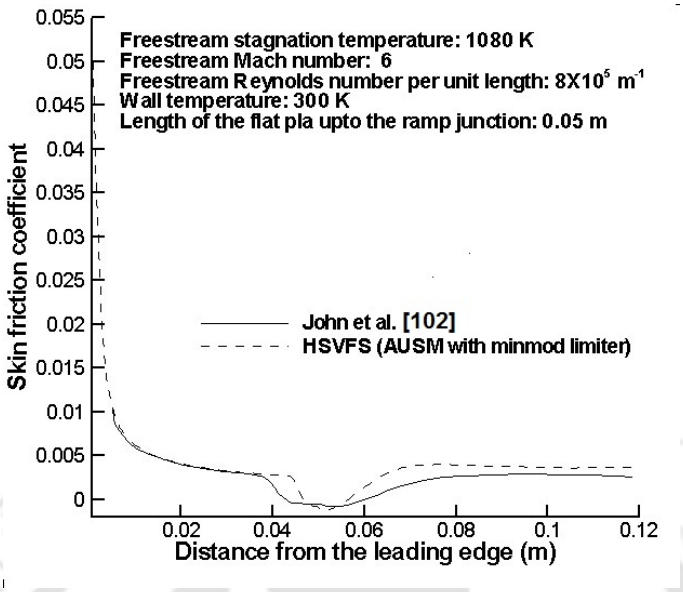

Fig. 5.12. Comparison of skin-friction profiles for problem-2 obtained by the HSVFS with John et al.'s computational results [102].

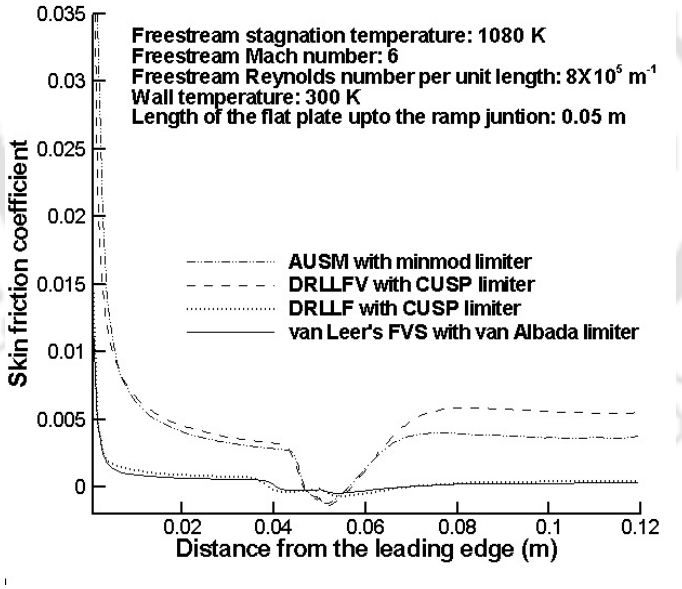

Fig. 5.13. Comparison of skin-friction profiles for problem-2 using the higher-order-accurate schemes.

Figure 5.14 compares the wall-heat-flux rates computed by using higher-order-accurate AUSM and DRLLFV schemes with the published results of John et al. [102]. The results are in close agreement with each other. As expected from the observation of figure 5.13, the peak-heat flux in the post re-attachment zone com-

puted by using the DRLLFV scheme is the highest. Thus, excellent performance of the DRLLFV scheme for high-speed viscous computations is demonstrated for this case as well.

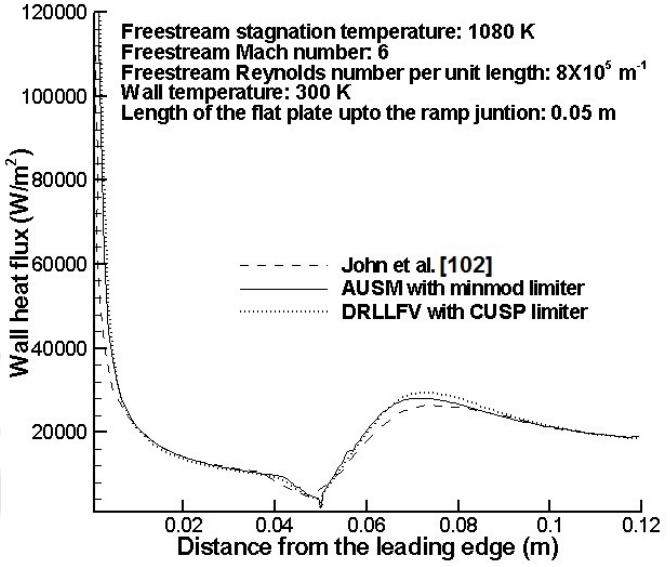

Fig. 5.14. Comparison of wall-heat fluxes for problem-2 with John et al.'s computational results [102].

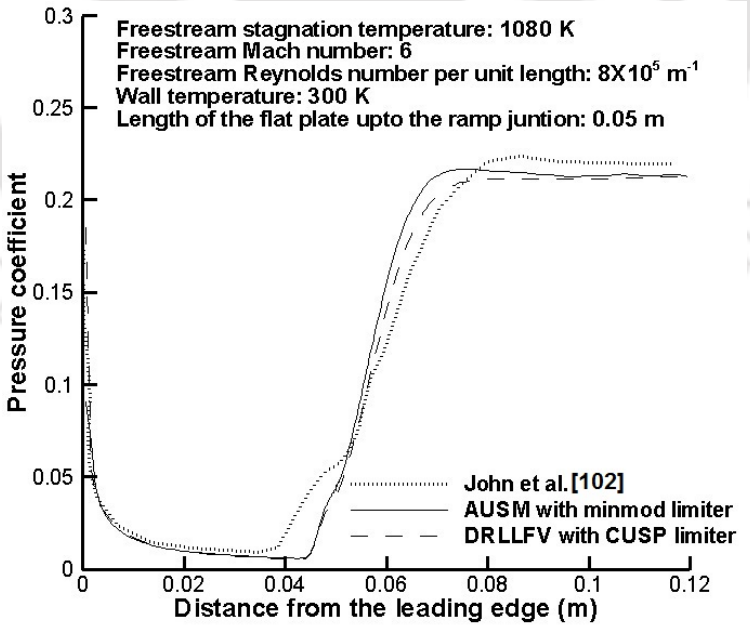

Fig. 5.15. Comparison of pressure-coefficient profiles for problem-2 with John et al.'s computational results [102].

Accurate computation of the pressure coefficient is crucial for computing the wave-drag force. Figure 5.15 compares the pressure coefficient for problem-2 using

the higher-order-accurate AUSM and DRLLFV schemes with the published results [102]. The results are in good agreement, except that for the present computation the lengths of the upstream-influence zones are slightly smaller for both the schemes. In conformity with figures 5.12, 5.13 and 5.14, the difference might be due to the difference in the smearing of the computed boundary layer by different schemes. A more diffusive scheme computes a longer zone of upstream influence by adding to the physical viscosity.

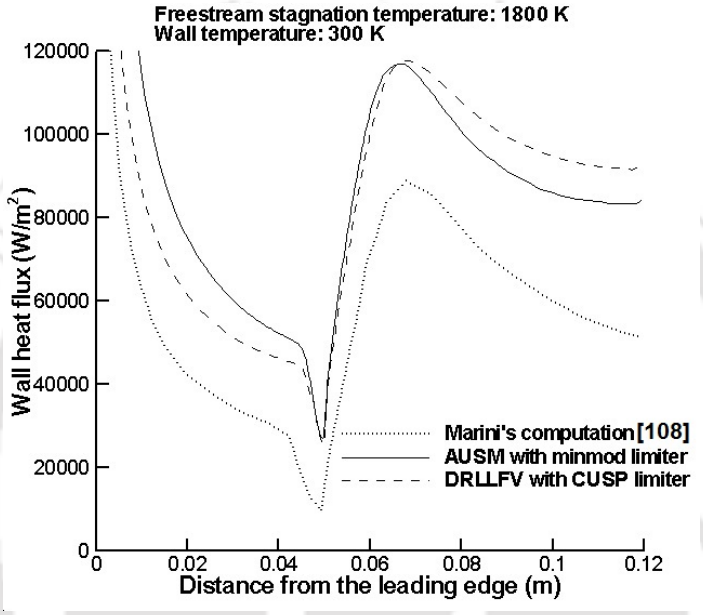

Fig. 5.16. Comparison of wall-heat fluxes for problem-2 with Marini's computational results [108].

Further cases of high-enthalpy-hypersonic flows are studied. Figure 5.16 compares the wall-heat fluxes for problem-2 computed by using higher-order AUSM and DRLLFV schemes with computed results of Marini [108]. The free-stream stagnation temperature for this case is 1800 K and wall-temperature is 300 K. The rest of the free-stream and geometric parameters are the same as in figures 5.11 to 5.15. The DRLLFV scheme computes the wall-heat flux for this case also in agreement with the AUSM scheme and the computed results of Marini [108]. In general, it is seen that both DRLLFV and AUSM schemes estimate the heat-flux on the higher side compared with the computed results of Marini. The higher resolution of the schemes in the present computation can be attributed to this observation. This is further substantiated by the fact that the wall-heat fluxes computed by using the higher-order-accurate AUSM and DRLLFV schemes are in

excellent agreement with Marini's experimental results [108] as can be seen from figure 5.17.

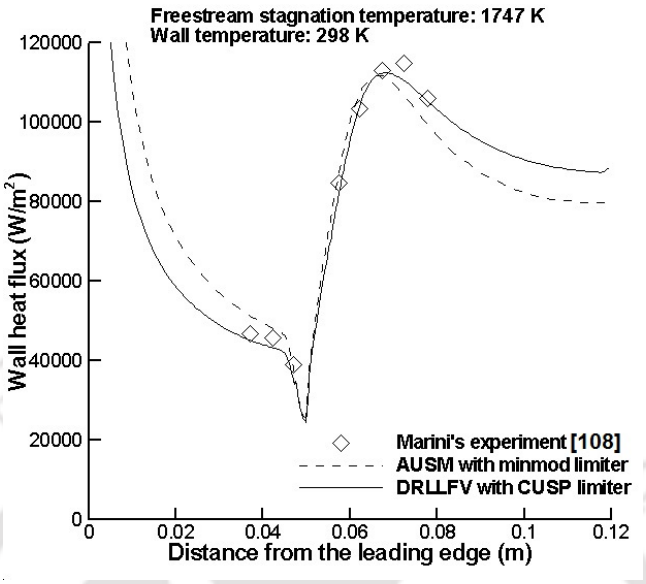

Fig. 5.17. Comparison of wall-heat fluxes for problem-2 with Marini's experimental results [108].

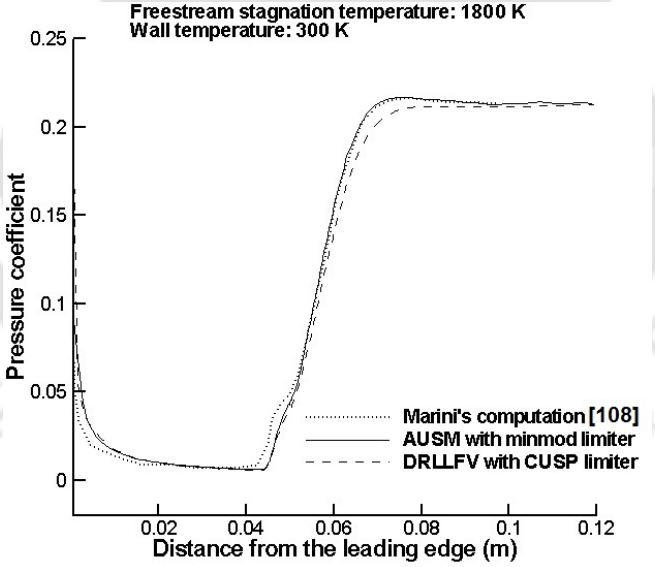

Fig. 5.18. Comparison of pressure-coefficient profiles for problem-2 with Marini's computational results [108].

Figure 5.18 compares the pressure-coefficient profiles computed by using the higher-order AUSM and DRLLFV schemes for problem-2 with the computational results of Marini [108]. The present computations are in nice agreement with the reference. The pressure-coefficient profiles for problem-2 computed with higher-order AUSM and DRLLFV schemes are compared with the experimental results of

Marini [108] in figure 5.19. For this case also the present computations are found in good agreement with the experimental data.

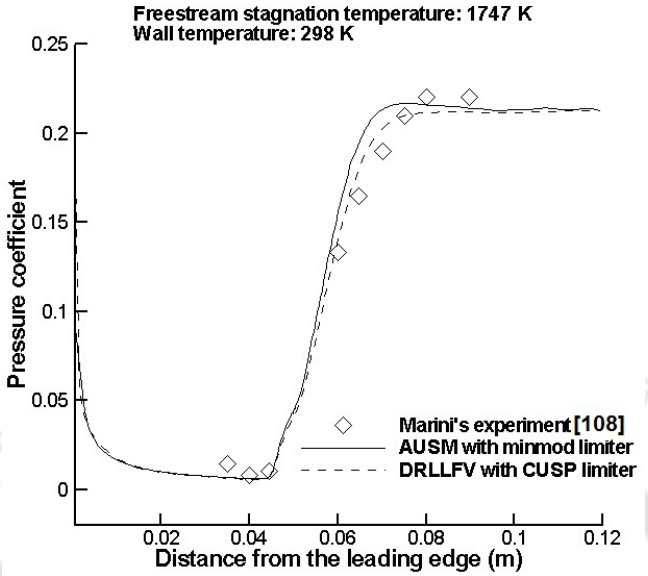

Fig. 5.19. Comparison of pressure-coefficient profiles for problem-2 with Marini's experimental results [108].

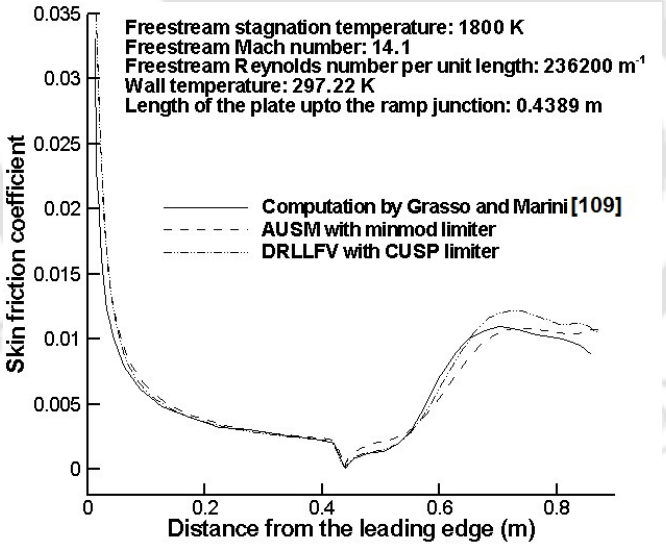

Fig. 5.20. Comparison of skin-friction profiles for problem-2 with Grasso and Marini's computational results [109].

A case of high-Mach number and high-enthalpy hypersonic flow in problem-2 is also considered in the present work. It involves flow over a ramped surface at Mach 14.1. The free-stream Reynolds number per unit length is 263200 m^{-1}. The length of the flat plate up to the ramp junction is 0.4389 m. The wall-temperature is 297.22 K. and the ramp angle is 15^0 [109]. Under these free-stream conditions,

this ramp angle is less than the incipient-separation angle suggested by Needhaam and Stollery [96]. Figure 5.20 shows that the skin-friction profiles computed by using the higher-order AUSM and DRLLFV schemes are in good agreement with the results of Grasso and Marini [109]. It deserves to be mentioned that the DRLLF and van Leer's FVS schemes produce under-estimations of the skin-friction profile. Thus, the improvement of the DRLLFV scheme over the DRLLF scheme for high-Mach number viscous computations is also demonstrated.

5.4 Conclusions

An improved version of the DRLLF scheme is developed for the accurate computation of high-speed-viscous flows. This new method, named as the DRLLF-Viscous (DRLLFV) scheme, works based upon a boundary-layer sensor that reduces the DR parameter only inside the boundary layer by using a scaling function. The function is formulated in a manner such that the scaling down of the DR parameter is the maximum on the solid wall and outside the boundary layer the scheme works like the original DRLLF scheme. Thus, the new scheme intends to control the numerical diffusion in the presence of strong physical diffusion and still retaining the numerical stability. The numerical effectiveness of the DRLLFV scheme is demonstrated by comparing the computed results of standard test cases involving supersonic flow over a flat plate and hypersonic flow over a ramped surface involving shock wave-boundary layer interactions with existing computational and experimental results. Excellent agreement of the results computed by using the DRLLFV scheme with the experimental results is observed. The new scheme is found to perform significantly better than the DRLLF and van Leer's FVS schemes. It is, therefore, not surprising that, for high-speed-viscous-flow computations, the DRLFLV scheme can capture many flow features even better than the AUSM scheme. Inside the boundary layer, the new scheme resolves the flow-separation and reattachment as accurately as the AUSM scheme, whereas, in the inviscid zone, it captures the weak shocks better than the latter.

Chapter 6

A Novel Hybrid Approach with Multidimensional-like Effects for Compressible-Flow Computations

6.1 Introduction

A multidimensional scheme achieves good resolution of strong and weak shocks irrespective of whether the discontinuities are aligned with or inclined to the grid. However, these schemes are computationally expensive. In this chapter we present a method which is computationally inexpensive and yet produces multidimensional-like effects. This is achieved by hybridizing two schemes, namely, AUSM and DRLLF and coupling them through a novel shock switch that operates – unlike existing switches – on the gradient of the Mach number across the cell-interface[1]. The schemes that are hybridized have contrasting properties. The AUSM scheme captures grid-aligned (and strong) shocks crisply but it is not so good for non-grid-aligned weaker shocks, whereas the DRLLF scheme achieves sharp resolution of non-grid-aligned weaker shocks, but is not as good for grid-aligned strong shocks. It is our experience that if conventional shock switches based on variables like density, pressure or Mach number are used to combine the schemes, the desired effect of crisp resolution of grid-aligned and non-grid-aligned discontinuities are not obtained. To circumvent this problem we design a

[1]This work is published in *Journal of Computational Physics*, Elsevier, Vol. 340 (2017)

shock switch based – for the first time – on the gradient of the cell-interface Mach number with very impressive results. Thus the strategy of hybridizing two carefully selected schemes together with the innovative design of the shock switch that couples them, affords a method that produces the effects of a multidimensional scheme with a lower computational cost. It is further seen that hybridization of the AUSM scheme with the recently developed DRLLFV scheme using the present shock switch gives another scheme that provides crisp resolution for both shocks and boundary layers. Merits of the schemes are established through a carefully selected set of numerical experiments.

The performance of a self-adjusting hybrid method greatly depends on the proper functioning of the shock switch. If the switch gets activated in smooth regions or assumes large values in zones involving weaker shocks, it may contaminate the solution leading to poorly resolved shock structures. On the other hand inability of the switch to recognize zones of moderate shock strength may lead to spurious numerical oscillations. Shock switches with varied applicability and complexity have been reported in the literature [33–37, 40, 41, 110–114]. The present work explores a new route for designing a shock switch which is simple yet effective. The switch is designed as a quadratic function of the contravariant-Mach-number gradient across the cell-interfaces. As a result it gets activated in such a way as to capture both strong and weak discontinuities crisply. Another advantage of this shock switch is that it relies on few user-adjustable parameters and therefore is relatively straightforward.

The choice of two Finite Volume Method (FVM)-based schemes is crucial in the design of a self-adjusting hybrid scheme that offers multidimensional upwinding-like effects with simplicity. In this context it is shown in chapter 3 that for inviscid flows the AUSM scheme resolves the grid-aligned shocks better than the DRLLF scheme, whereas the DRLLF scheme outperforms the AUSM scheme in resolving weak shocks inclined to the grid. Accordingly in chapter 5, we modified the DRLLF scheme for computing viscous flows involving weak shocks only, using a boundary-layer sensor. This scheme is named as the DRLLF-Viscous (DRLLFV) scheme. The DRLLFV scheme outperforms the AUSM scheme both inside and outside the viscous shear layer in flows involving weak-leading-edge

shocks and hypersonic shock wave-boundary layer interaction problems involving weak shocks. The contrasting performances of the AUSM and DRLLF/DRLLFV schemes in resolving strong and weak shocks offer an opportunity to hybridize the schemes for accurate-shock resolution irrespective of its inclination with the grid. This provided the motivation to hybridize the AUSM scheme with the DRLLF/DRLLFV schemes using the novel shock switch. The scheme is simple yet robust and produces "multidimensional-like" effects. For inviscid flows the hybrid method combines the AUSM and DRLLF schemes and it is termed the AUSM-DRLLF Self-Adjusting Hybrid (ADSAH) scheme. Similarly, for viscous flows the scheme combines the AUSM and DRLLFV schemes and the resultant method is termed the AUSM-DRLLF Self-Adjusting Hybrid Viscous (ADSAHV) scheme. It is found that the ADSAH/ADSAHV schemes achieve high accuracy in problems involving stationary and moving, strong as well as weak shocks in compressible inviscid and viscous flows.

All computations with the present methods are carried out using cell-centered FVM codes based on programming language "C". The present chapter is organized in five sections. The mathematical formulations of the new shock switch along with the self-adjusting hybrid methods for inviscid and viscous flows are presented in section 6.2. Sections 6.3 and 6.4 present the results of the ADSAH and ADSAHV schemes, respectively, for inviscid and viscous compressible flows. In these sections the superior performances of the new schemes are also highlighted by comparison with analytical, computational and experimental results available in the literature. Concluding remarks are made in section 6.5.

6.2 The new shock switch and the hybrid methodology

In the present work the smoothness of the flow-field is assessed based on the gradient of the contravariant Mach number across a cell interface. The Mach number is chosen as a smoothness-indicating parameter because it changes across both shocks as well as contact discontinuities. This is not the case with parameters like pressure and velocity as they remain unchanged across a contact discontinuity. Although parameters like density, entropy etc. can also be used in the design of shock

switches yet the contravariant Mach number is chosen in this work for devising the new switch. This is because density and entropy are static properties that are independent of the direction, whereas Mach number is direction-dependent. The use of Mach number as a parameter to design a shock switch has the potential of producing multidimensional-like effects. In our experience a switch that is based on the jump in contravariant Mach number may not be effective in capturing moving normal shocks in cases where the absolute flows across the shock remain subsonic, as in Sod's 1st shock tube problem [65]. The new shock switch based on the gradient of the contravariant Mach number overcomes this problem. Moreover the strategy of basing the switch on Mach-number gradient takes better cognizance of the strong and weak shocks, grid-aligned or otherwise. The mathematical formulation of the sensor is based on the fact that for a cell-face aligned with a shock, the gradient of the Mach number normal to the cell-interface increases as the shock strength increases and it decreases with increased inclination of the shocks. This approach has two benefits: firstly it can distinguish zones of strong shocks from weaker-shock zones or smooth regions. Accordingly the switch can assume higher or lower values. Therefore, a hybrid scheme using this switch can attain a genuinely-multidimensional-like quality, provided the constituent schemes are properly chosen. Secondly, in this approach the gradient of contravariant Mach number is high for strong shocks or shocks aligned with the grid irrespective of whether the absolute flow across the shock is subsonic or supersonic.

In what follows the mathematical formulation of the proposed switch is explained for a 1D flow for clarity. The same methodology can be easily extended to more than one dimensions by replacing the Mach numbers with the corresponding contravariant terms and the changes of the parameters with their components along the direction normal to the cell-face, as presented in Appendix G. Figures 6.1(a)-(b) depict the schematics for the present shock switch design in case of a 1D flow, where the variations of normalized Mach number along the flow-direction (i.e. x-axis) for a typical formulation are plotted. A shock is shown starting at cell I in figure 6.1(a). Many a times undesirable numerical oscillations arise in the vicinity of the shock. In order to show how these oscillations are eradicated, figure 6.1(a) considers a non-monotonous solution developed at cell $I-1$. Figure 6.1(b)

shows a flow-field with a smooth extremum at cell $I-1$. To calculate the shock switch $\theta_{I+\frac{1}{2}}$ across the cell-interface $(I+\frac{1}{2})$, the gradients of the normalized Mach number across the cell-interfaces $(I-\frac{3}{2})$, $(I-\frac{1}{2})$ and $(I+\frac{1}{2})$ are computed as:

$$\begin{aligned} g_{I-\frac{3}{2}} &= \frac{\nabla_{I-1}\left(\overline{M}\right)}{\nabla_{I-1}\left(\overline{X}\right)} \\ g_{I-\frac{1}{2}} &= \frac{\nabla_{I}\left(\overline{M}\right)}{\nabla_{I}\left(\overline{X}\right)} \\ g_{I+\frac{1}{2}} &= \frac{\nabla_{I+1}\left(\overline{M}\right)}{\nabla_{I+1}\left(\overline{X}\right)}, \end{aligned} \tag{6.1}$$

where $\overline{M}$ is the normalized value of the Mach number, $\overline{X}$ is the normalized x-coordinate of the cell-centroid and ∇ is the backward-difference operator. The Mach number is normalized by

$$\overline{M} = \frac{M}{\max|M|}. \tag{6.2}$$

The normalized coordinates $\overline{X}$ of the cell-centroids are given by

$$\overline{X} = \frac{X}{\max|X|}, \tag{6.3}$$

where X is the x-coordinate of the cell-centroid. The backward-difference operator for any parameter Θ is given by

$$\nabla_I(\Theta) = \Theta_I - \Theta_{I-1}. \tag{6.4}$$

In the presence of a shock, gradient of the normalized Mach-number curve across a cell-face becomes steep. Therefore, the angle γ_g made by the curve with the x-axis at a cell-face is generally large (close to $\pi/2$). On the other hand for the cells within the shock or in smooth zones, the gradients of the curve across the upstream and downstream faces of a cell do not change appreciably. Accordingly, γ_g is expressed in terms of the gradient g as follows:

$$\begin{aligned} (\gamma_g)_{I-\frac{3}{2}} &= \tan^{-1}\left(g_{I-\frac{3}{2}}\right) \\ (\gamma_g)_{I-\frac{1}{2}} &= \tan^{-1}\left(g_{I-\frac{1}{2}}\right) \\ (\gamma_g)_{I+\frac{1}{2}} &= \tan^{-1}\left(g_{I+\frac{1}{2}}\right). \end{aligned} \tag{6.5}$$

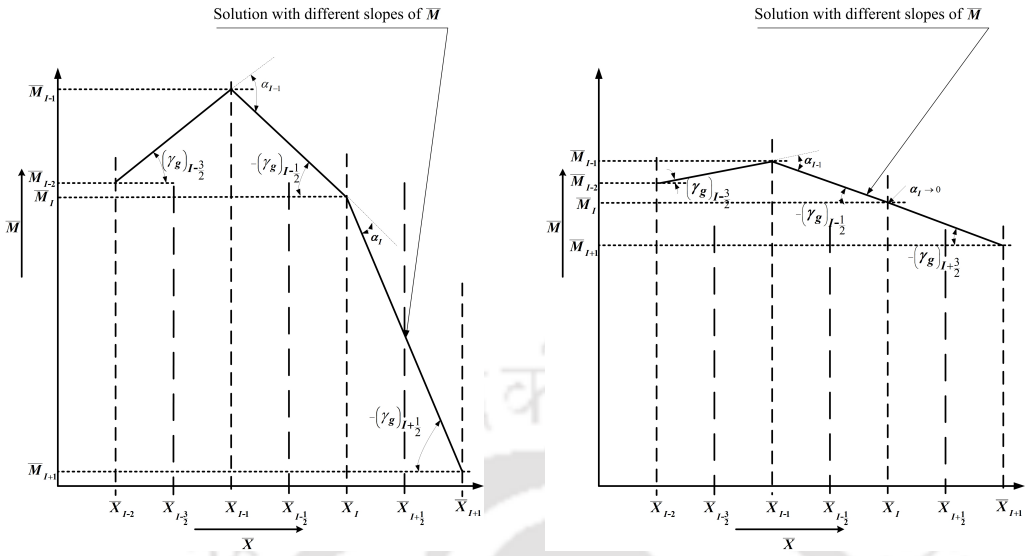

(a) (b)

Fig. 6.1. Schematics for shock-switch computation in case of 1D flow: (a) Flow with a shock at I and a sharp extremum at $I-1$, (b) Flow with a smooth extremum at $I-1$.

The difference α of the angles γ_g across each of a pair of adjacent cell-faces is a measure of departure from smoothness in the flow-field at a particular cell bounded by the two faces. For cells $I-1$ and I these angles are written as

$$\alpha_{I-1} = \left|(\gamma_g)_{I-\frac{1}{2}} - (\gamma_g)_{I-\frac{3}{2}}\right|, \tag{6.6}$$

$$\alpha_I = \left|(\gamma_g)_{I+\frac{1}{2}} - (\gamma_g)_{I-\frac{1}{2}}\right|. \tag{6.7}$$

It is desirable that the shock switch assumes higher values with increase in the smoothness-indicating angle α and asymptotically approaches zero in smooth-flow zones. A quadratic function of $\sin\alpha$ fulfils this requirement. Also to limit the shock-switch value to a maximum of unity, we propose the following relation to compute the shock switch:

$$\theta_{I+\frac{1}{2}} = \min\left[\kappa \sin^2\left\{\max\left(\alpha_{I-1}, \alpha_I\right)\right\}, 1\right], \tag{6.8}$$

where κ can be assigned any value greater than unity. Choosing κ close to unity results in less sensitivity of the switch to the change in Mach-number gradients. On the other hand if κ is assigned very large values, the switch tends to get activated even in smooth zones. Based on a series of numerical experiments we recommend

a value of $\kappa = 2.5$, which works satisfactorily for a wide range of problems. Figure 6.2 shows the variation of the shock switch with the angle α for $\kappa = 2.5$. Equations 6.1-6.8 also show that the shock switch requires a stencil size of four cells for its operation. It is preferable to choose the computational domain in such a way that the flow is smooth at the boundary. Otherwise the value of the switch at the boundary can be judiciously estimated from the interior.

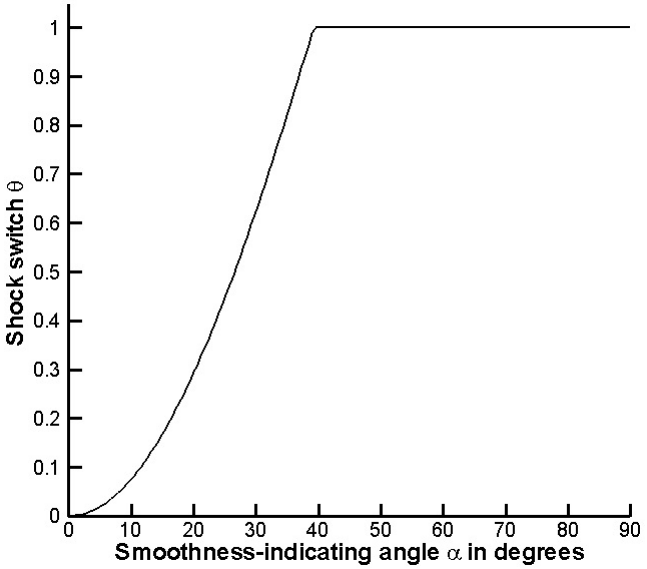

Fig. 6.2. Variation of the shock switch (θ) with the smoothness-indicating angle (α) for $\kappa = 2.5$.

Equation 6.8 indicates that even in non-monotonous zones the shock switch assumes higher values, thereby inhibiting numerical oscillations as it choses the maximum of the smoothness-indicating angles α_{I-1} and α_I. This can be seen from figure 6.1(a), which shows that as the Mach-number profile attains a sharp extremum at cell $I-1$, the angle α_{I-1} attains a value higher than α_I and accordingly value of the shock switch $\theta_{I+\frac{1}{2}}$ also increases. Further it may be noted that the computation of the shock switch using the relative angles α of the normalized Mach-number curve offers the additional advantage of assuming small values in smooth extrema. For example as shown in figure 6.1(b), if the cell $I-1$ contains a smooth extremum, then the angle α_{I-1} will assume a very small nonzero value and the angle α_I will approach zero. In that case the shock switch will equal $\kappa \sin^2(\alpha_{I-1})$, which will also be very small. Therefore, the nature of equation 6.8 ensures that the switch assumes high values near a sharp extremum such as cell

$I-1$ in figure 6.1(a), but it does not shoot up near a smooth extremum such as cell $I-1$ in figure 6.1(b).

Here it needs to be mentioned that in the extension of the switch to computation of 2D flows with weak-oblique shocks, the changes in gradients of the contravariant Mach numbers across neighbouring cell-interfaces are relatively less, resulting in smaller values of α. As indicated by figure 6.2 the shock switch across a weak shock assumes smaller values with increased inclination of the shock, producing a benign transition from strong shocks to weaker shocks.

Finally, for the Euler equations, the flux at the cell-interface is obtained by hybridizing the AUSM and DRLLF schemes through the shock switch as follows:

$$F_{I+\frac{1}{2}} = \theta_{I+\frac{1}{2}} \left(F_{I+\frac{1}{2}}\right)_{\text{AUSM}} + \left(1-\theta_{I+\frac{1}{2}}\right) \left(F_{I+\frac{1}{2}}\right)_{\text{DRLLF}}. \tag{6.9}$$

As mentioned previously this scheme is termed AUSM-DRLLF Self Adjusting Hybrid (ADSAH) scheme. The above scheme works close to the DRLLF scheme in smooth regions. It has, however, been observed in chapter 5 that the DRLLF scheme becomes over-dissipative for viscous-flow computations and for such flows the DRLLFV scheme is found to be much more accurate. Hence for the Navier-Stokes equations, the flux at the cell-interface is computed by hybridizing the AUSM with the DRLLFV scheme as

$$F_{I+\frac{1}{2}} = \theta_{I+\frac{1}{2}} \left(F_{I+\frac{1}{2}}\right)_{\text{AUSM}} + \left(1-\theta_{I+\frac{1}{2}}\right) \left(F_{I+\frac{1}{2}}\right)_{\text{DRLLFV}}. \tag{6.10}$$

We term this scheme as AUSM-DRLLF Self Adjusting Hybrid Viscous (ADSAHV) scheme. It may be noted that while hybridizing the AUSM with the DRLLF or DRLLFV schemes, higher-order accuracy can be obtained by blending the higher-order versions of the constituent schemes.

6.3 Inviscid-compressible-flow results

To check the numerical performance of the ADSAH scheme a number of test cases of inviscid-compressible flows involving strong as well as weak shocks including subsonic, supersonic and hypersonic flows are considered. In the next seven subsections (6.3.1-6.3.7) we present the results and comparative analysis of the Sod's 1D shock tube problems [65], Quasi-1D flow through a converging-diverging nozzle

[2], 2D flow through a converging-diverging nozzle, oblique-shock reflection [40], supersonic flow through a ramped channel [40], 2D Riemann problem [49–52, 115] and hypersonic flow over a semi-cylinder with perfect gas and equilibrium-air models [77].

6.3.1 Sod's shock tube problems

Sod's shock tube problems are famous bench-marking problems because they offer a variety of compressible-flow features such as shock waves, contact discontinuities, expansion waves and sonic points. Additional advantage enjoyed by these problems is the fact that they possess analytical solutions to compare the results with.

Figures 6.3(a)-(b) plot the first-order-accurate solutions of the two shock tube problems using the AUSM, DRLLF, Radespiel-Kroll Hybrid [18] and ADSAH schemes to compare with the analytical solutions. All the numerical computations are done on 200 cells. The ADSAH scheme captures the shocks and contact discontinuities more crisply than the AUSM and Radespiel-Kroll Hybrid schemes. In moving shock problems where the absolute flows across the shock remain subsonic the DRLLF scheme exhibits numerical oscillations near the shock, which are overcome by the ADSAH scheme (see figure 6.3(a)). It can further be seen from the encircled region in figure 6.3(b) that the DRLLF and the ADSAH schemes are free from the sonic-point error that the AUSM scheme suffers from. Figures 6.4(a)-(b) show the shock-switch profiles along the length of the shock tube. As the shock switch is based on the gradient of the Mach number, expectedly it assumes high values near the beginning and end-points of the shocks. Across a contact discontinuity the change in Mach number over a finite distance between the adjacent cells is somewhat less compared with that across a shock. Therefore, for a contact discontinuity the shock switch assumes moderate values near its starting and end-points. Owing to the same reason the shock switch peaks locally near the terminal points of the expansion waves. In smooth zones, since the gradients of the Mach number do not change much, the switch-value is close to zero. These observations are in agreement with the construction of the equations 6.1-6.8.

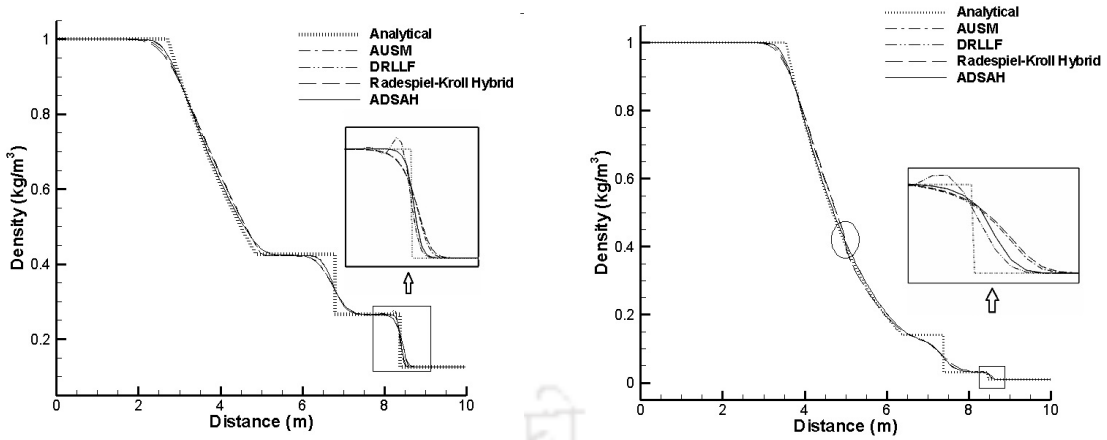

Fig. 6.3. Density variation for Sod's shock tube problems: (a) Sod's 1st problem and (b) Sod's 2nd problem.

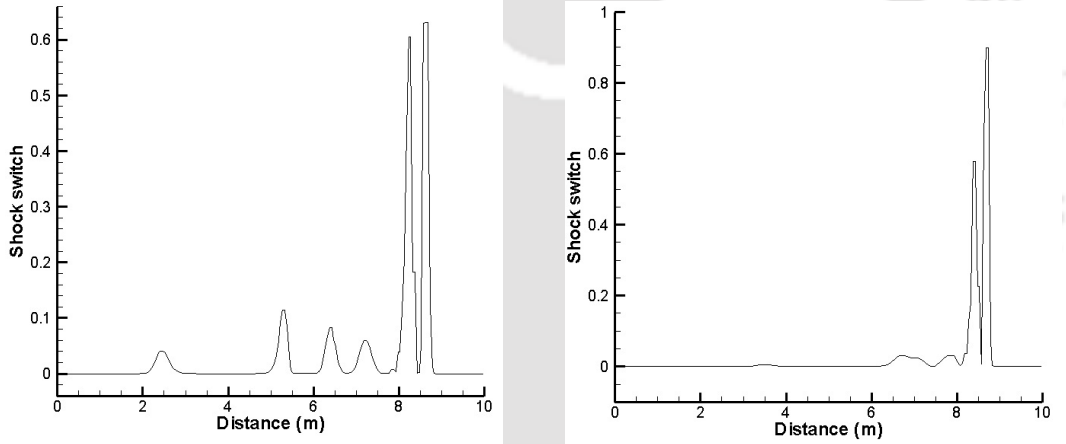

Fig. 6.4. Variation of the shock switch with the ADSAH scheme along the tube: (a) Sod's 1st problem and (b) Sod's 2nd problem.

6.3.2 Quasi-1D flow through a converging-diverging nozzle

In quasi-1D flow all the flow parameters as well as the cross-sectional area are functions of the axial coordinate x. The geometric and free-stream details for quasi-1D flow through a converging-diverging nozzle are listed in table 6.1. Under steady state, a standing-normal shock exists in the diverging portion of the nozzle at the assigned back pressure. This problem also offers the advantage of possessing

an analytical solution.

Table. 6.1. The geometric and flow parameters for quasi-1D converging-diverging nozzle-flow.

Parameter	**Value**
Length of the nozzle (L)	3 m
Cross-sectional area of the nozzle $A(x)$	$A(x) = 1 + 2.2\,(x - 1.5)^2$
Reservoir pressure (p_0)	101325 N/m^2
Reservoir temperature (T_0)	300 K
Back pressure (p_b)	$0.7\,(p_0)$

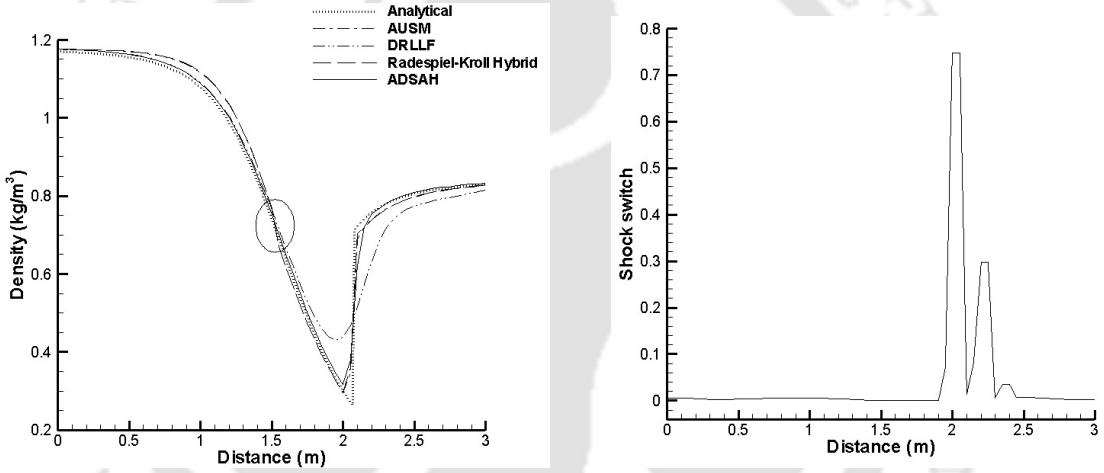

(a) (b)

Fig. 6.5. Quasi-1D flow problem: (a) Variation of density along the nozzle and (b) The shock-switch profile.

The density variation and the shock-switch profile along the nozzle for the quasi-1D-flow problem are plotted in figures 6.5(a)-(b). The number of cells in the computational domain is 60 for this computation. Figure 6.5(a) shows that the ADSAH scheme resolves the standing-normal shock with much less smearing like the AUSM and Radespiel-Kroll Hybrid schemes and much better than the DRLLF scheme. It can be seen from figure 6.5(b) that the shock switch assumes high value only in the vicinity of the shock and does not get activated in smooth regions. In conformity with equations 6.1-6.8, the switch approaches unity near the upstream end of the shock since there is a sharp change of the Mach-number

gradient in that location. Within the shock the gradient does not change abruptly across neighbouring cell-faces and therefore the value of the shock switch drops. Near the downstream end of the shock the change in the Mach-number gradient is milder compared to that in the upstream end. This fact gets reflected in the unequal peaks in figure 6.5(b). Owing to this reason the ADSAH scheme acts close to the AUSM scheme near the end-points of the shock and close to the DRLLF scheme within the shock as given by equation 6.9.

6.3.3 2D flow through a converging-diverging nozzle

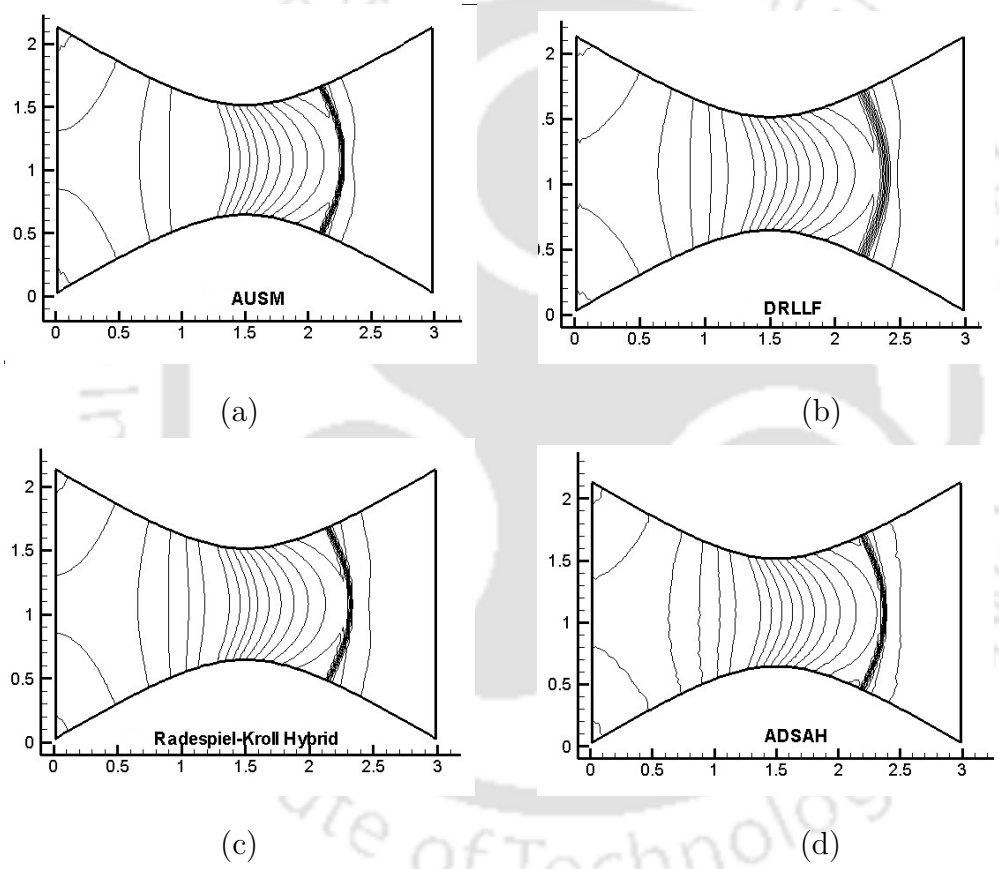

Fig. 6.6. Pressure contours for 2D flow through a converging-diverging nozzle using (a) AUSM, (b) DRLLF, (c) Radespiel-Kroll Hybrid and (d) ADSAH schemes.

The same problem mentioned in table 6.1 is computed by using a 2D formulation. The 2D Euler equations governing the flow are solved on a 120×51 grid. Figure 6.6(b) shows that the DRLLF scheme resolves the normal shock poorly. But the ADSAH scheme captures the normal shock with less smearing comparable with the AUSM and Radespiel-Kroll Hybrid schemes as seen in figures 6.6(a), 6.6(c) and 6.6(d). The centreline pressure and Mach-number variations with the AUSM,

DRLLF, Radespiel-Kroll Hybrid and ADSAH schemes are shown in figures 6.7(a)-(b). Expectedly the DRLLF scheme captures a more smeared shock compared with the AUSM scheme. On the other hand the present hybrid scheme resolves the shock almost as crisply as the AUSM and Radespiel-Kroll Hybrid schemes. In addition the ADSAH scheme is free from the sonic-glitch problem exhibited by the AUSM scheme as shown by the encircled region in figures 6.7(a)-(b).

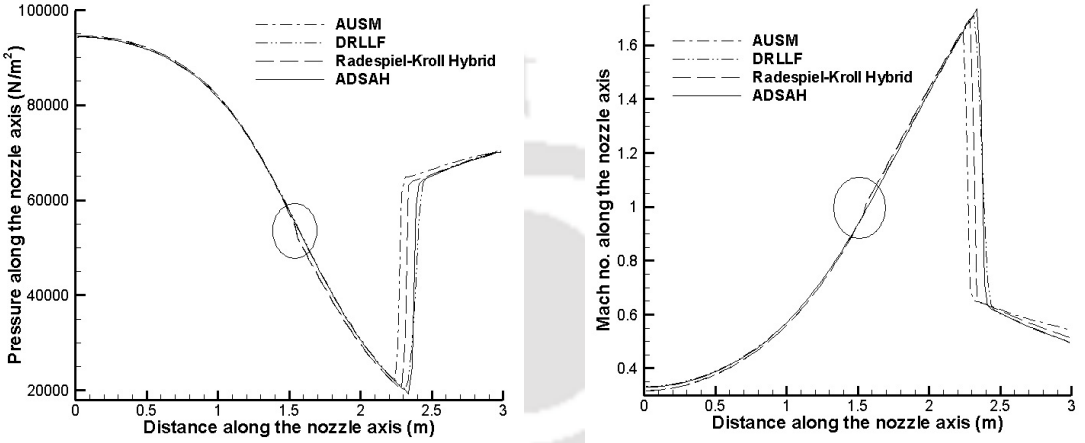

(a) (b)

Fig. 6.7. Variations along the axis for 2D flow through a converging-diverging nozzle: (a) pressure and (b) Mach number.

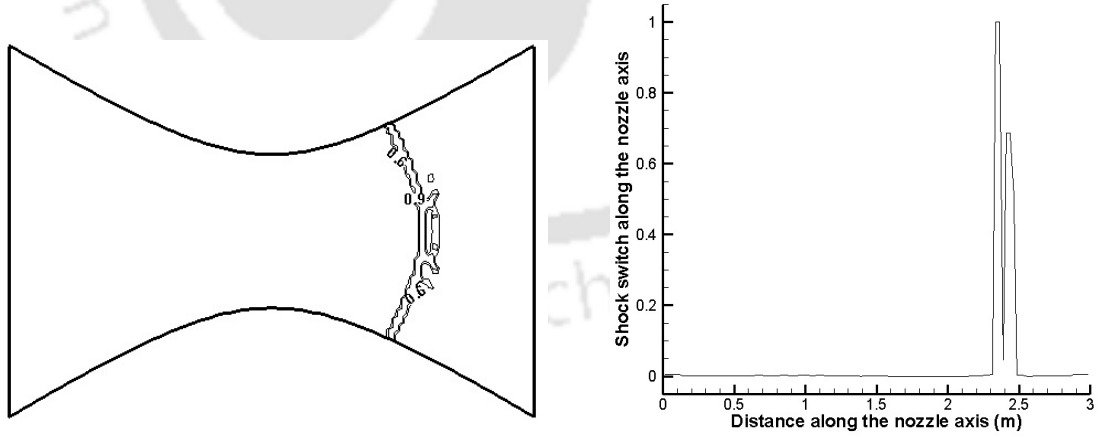

(a) (b)

Fig. 6.8. The shock-switch profile with the ADSAH scheme for the 2D flow through a converging-diverging nozzle: (a) contours and (b) variation along the nozzle axis.

Figures 6.8(a)-(b) show the shock-switch contours and the variation of the shock switch along the nozzle axis, respectively, for the ADSAH scheme. Similarly to the quasi-1D flow problem the switch attains a value close to unity at the end-points of the standing-normal shock. In addition the switch does not shoot up in the smooth regions including the cells contained within the shock and approaches zero. As a result the ADSAH scheme acts close to the AUSM scheme near the end-points of the standing-normal shock and like the DRLLF scheme in the smooth regions including the cells contained within the shock.

6.3.4 Oblique-shock-reflection problem

The geometric and free-stream parameters for the oblique-shock-reflection problem are shown in table 6.2. A 120×90 grid is used for all the computations. Figures 6.9(a)-(d) compare the pressure contours for the oblique-shock-reflection problem that reveals the improved performance of the ADSAH scheme. The DRLLF scheme resolves the oblique shock much better than the AUSM scheme. The ADSAH scheme outperforms the AUSM and Radespiel-Kroll Hybrid schemes in capturing the incident and reflected shocks and resolves them almost as good as the DRLLF scheme. Figures 6.10(a)-(b) compare the pressure and Mach-number variations at a height of 1/3 m from the plate obtained by the four schemes. It reaffirms the superior performance of the ADSAH scheme over the AUSM and Radespiel-Kroll Hybrid schemes in resolving weak shocks.

Table. 6.2. The geometric and flow parameters for oblique-shock reflection.

Parameter	**Value**
Length of the plate (L)	3
free-stream Mach number (M_∞)	3
free-stream pressure (p_∞)	101325 N/m^2
free-stream temperature (T_∞)	300 K
Incident wave angle (β)	30^0

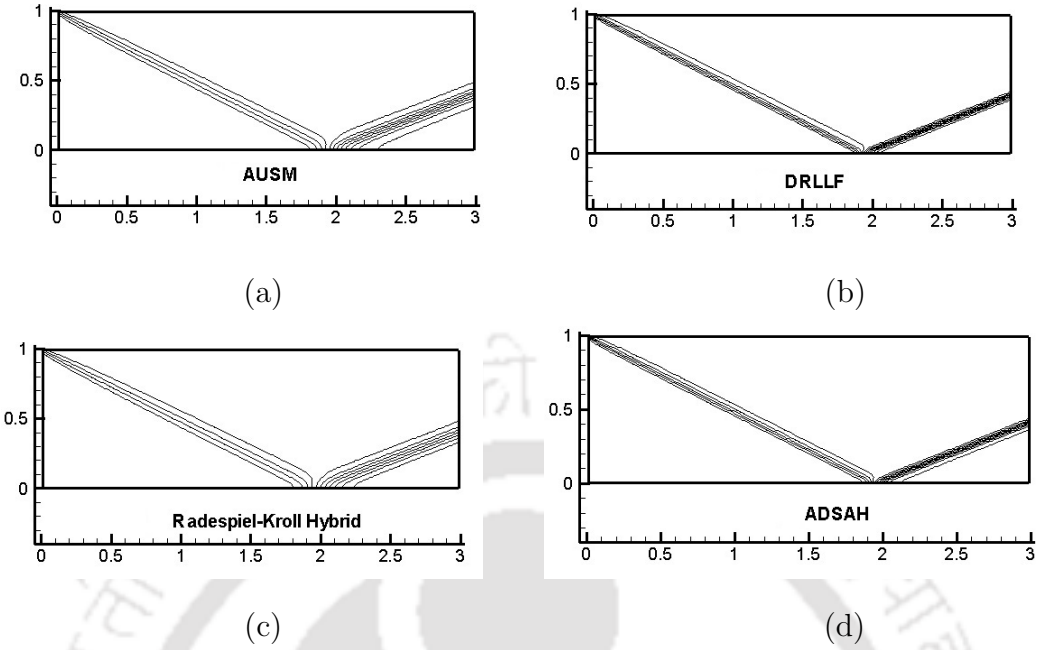

Fig. 6.9. Pressure contours for the oblique-shock-reflection problem using (a) AUSM, (b) DRLLF, (c) Radespiel-Kroll Hybrid and (d) ADSAH schemes.

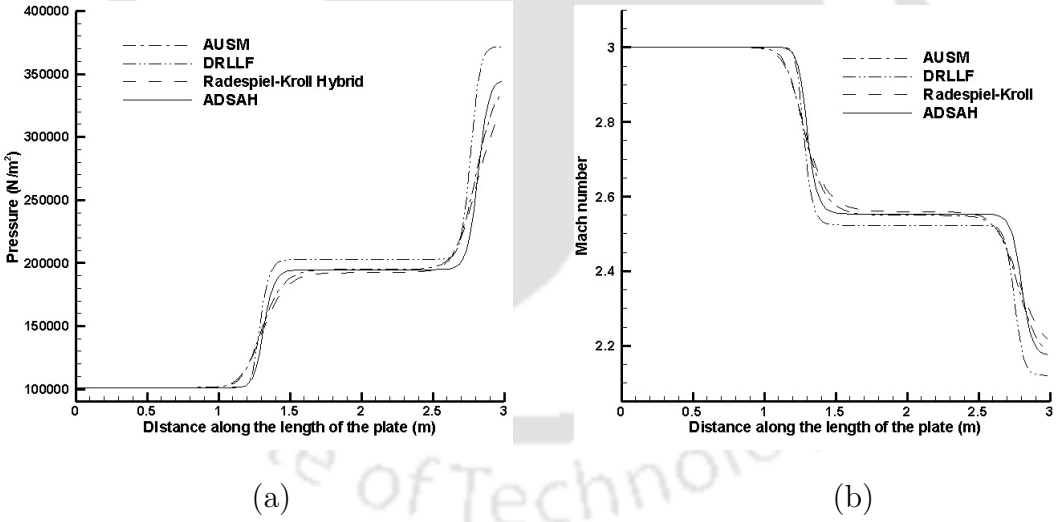

Fig. 6.10. Variations at a height of 1/3 m from the plate for the oblique-shock-reflection problem: (a) pressure and (b) Mach number.

It is desirable that across the cell-interfaces intercepted by weak-oblique shocks, the shock switch should assume smaller values compared with those crossed by stronger shocks. Figures 6.11(a)-(b) show the shock-switch contours and the variation of the shock switch at a height of 1/3 m from the plate. The zoomed region in figure 6.11(a) shows that the maximum value of the shock switch within the

captured shock is less than 0.4. Figure 6.11(b) reaffirms this fact.

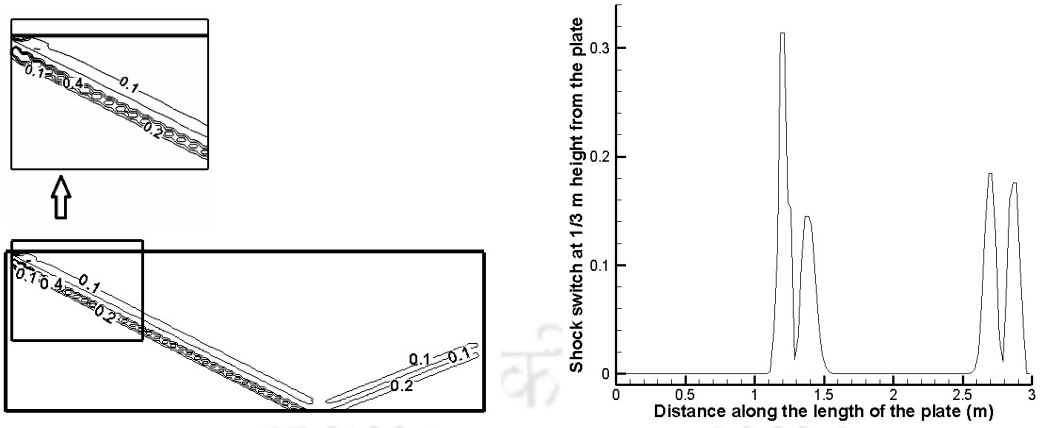

(a) (b)

Fig. 6.11. The shock-switch profile for the oblique-shock-reflection problem: (a) contours and (b) variation along a line at a height of 1/3 m from the plate.

6.3.5 Supersonic flow through a ramped channel

This problem involves the interaction between an oblique-reflected shock and an expansion wave centred on an expansion-corner. The geometric and free-stream parameters for this problem are shown in table 3.4. All the results are reported for a 120×90 grid.

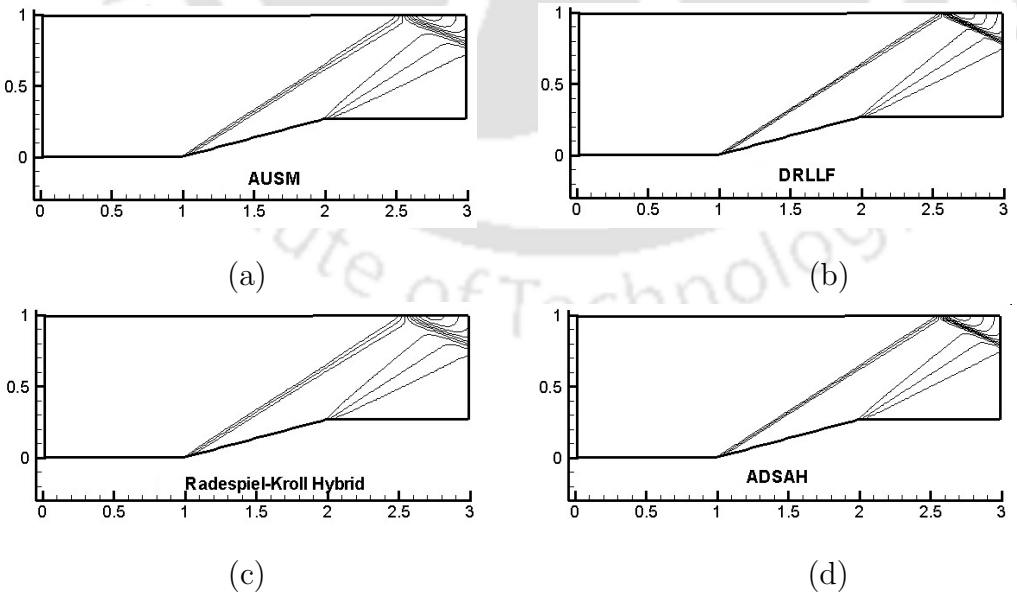

(a) (b)

(c) (d)

Fig. 6.12. Pressure contours for the supersonic flow through a ramped surface with (a) AUSM, (b) DRLLF, (c) Radespiel-Kroll Hybrid and (d) ADSAH schemes.

The AUSM and Radespiel-Kroll Hybrid schemes resolve the oblique shocks poorly compared with the DRLLF scheme. However, the ADSAH scheme succeeds in resolving these flow features comparable with the DRLLF scheme. Figures 6.12(a)-(d) corroborate this fact.

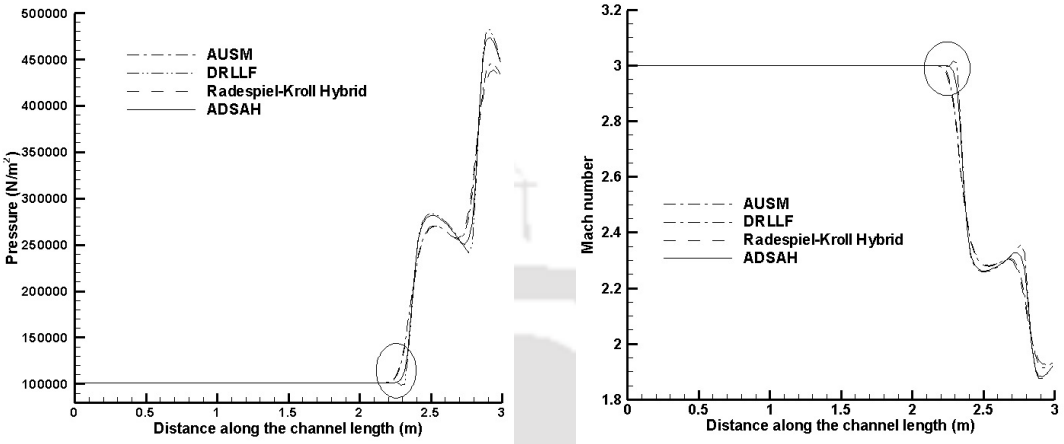

(a) (b)

Fig. 6.13. Variations at a height of 0.88 m for the ramp-in-a-channel problem: (a) pressure and (b) Mach number.

The variations of pressure and Mach number along a line at a height of 0.88 m with all these schemes are compared in figures 6.13(a)-(b). The crisp resolution of the weak shocks offered by the ADSAH scheme is evident from the figure. It may be noted that the ADSAH scheme creates less numerical diffusion than the AUSM and marginally more numerical diffusion than the DRLLF scheme in capturing weak shocks, as seen in figures 6.10 and 6.13. The same trend is also observed for moving normal shocks as seen in figures 6.3(a)-(b). In case of stationary strong shocks, the numerical diffusion of the ADSAH scheme assumes a smaller value than the DRLLF and slightly higher value than the AUSM scheme as evident from figures 6.5(a), 6.6 and 6.7. Thus the numerical diffusion of the ADSAH scheme gets self-adjusted based on the type of shocks. It can also be seen from figures 6.10(a) and 6.13(a) that as the numerical diffusion increases the computed pressure downstream of the shock decreases. Figures 6.13(a) and 6.13(b) show that the ADSAH scheme also eliminates the numerical oscillation produced by the DRLLF scheme near the shock emanating from the compression-corner, which is shown by the encircled regions in these figures. It is important to note from figure 6.13(b) that the gradient of the Mach number reverses sign at the point of

intersection between the centred expansion wave and the reflected shock wave.

Figures 6.14(a)-(b) show the contours of the shock switch and the variation of the shock-switch values at a height of 0.88 m. The shock switch peaks near the end-points of the oblique shocks. At the intersection point of the reflected shock and the centred expansion wave the switch reaches unity owing to the large change in the contravariant-Mach-number gradient.

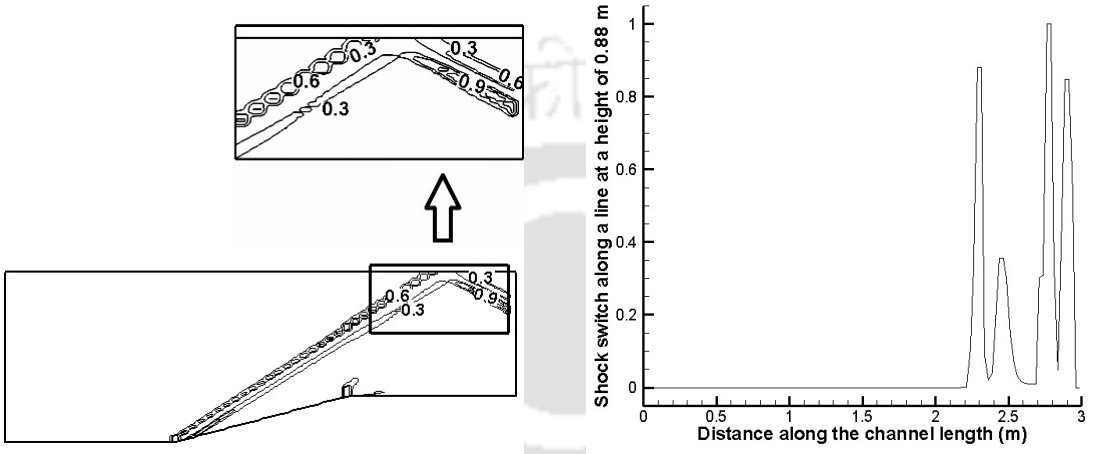

(a) (b)

Fig. 6.14. The shock-switch profile for the ramp-in-a-channel problem: (a) contours and (b) variation along a line at a height of 0.88 m.

6.3.6 2D Riemann problem

Schulz-Rinne et al. [116] demonstrated the importance of multidimensional Riemann problems for testing the efficiency of numerical schemes. The initial conditions were explicitly specified by Brio et al. [115] and have been used as test cases in the recent literature on multidimensional Riemann solvers [49–52]. The performance of the ADSAH scheme in computing a 2D Riemann problem is tested and compared with the AUSM, DRLLF and Radespiel-Kroll Hybrid schemes. The initial conditions in the four quadrants are specified in table 6.3. A computational domain of $[-1, 1] \times [-1, 1]$ is considered. A 400×400 grid is used for the computations with a CFL number of 0.9. The solutions are obtained at time $t = 1.1$.

Table. 6.3. The initial conditions for the 2D Riemann problem.

x- and y- locations	Parameters
$x > 0,\ y > 0$	$p = 1.5,\ \rho = 1.5,\ u = 0,\ v = 0$
$x < 0,\ y > 0$	$p = 0.3,\ \rho = 0.5323,\ u = 1.206,\ v = 0$
$x < 0,\ y < 0$	$p = 0.029,\ \rho = 0.1379,\ u = 1.206,\ v = 1.206$
$x > 0,\ y < 0$	$p = 0.3,\ \rho = 0.5323,\ u = 0,\ v = 1.206$

(The symbols p, ρ, u and v in the table denote the pressure, density, x-velocity and y-velocity, respectively.)

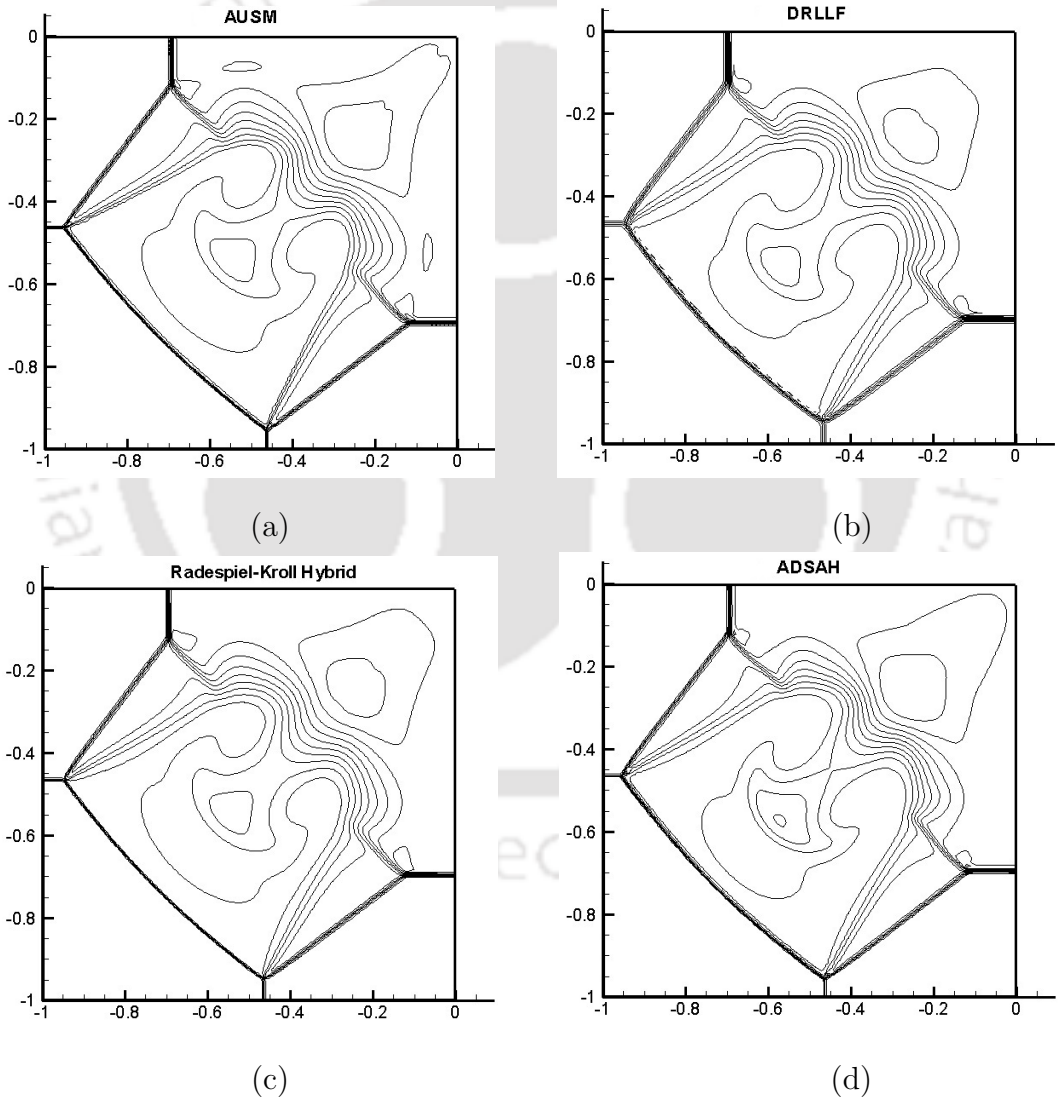

Fig. 6.15. Density contours for the 2D Riemann problem with (a) AUSM, (b) DRLLF, (c) Radespiel-Kroll Hybrid and (d) ADSAH schemes in the lower-left quadrant using 15 contour levels in the interval [0.2, 1.6].

For the given initial conditions the 2D Riemann problem results in simultaneous interaction of four shocks with double-Mach reflection and shock-propagation at 45^0 to the mesh. Figures 6.15(a)-(d) compare the density contours in the lower-left quadrant computed with the first-order-accurate AUSM, DRLLF, Radespiel-Kroll Hybrid and ADSAH schemes. Owing to the presence of the Mach-stems and strong-shock interactions the DRLLF scheme exhibits more diffusive nature than the other schemes. The Radespiel-Kroll Hybrid scheme resolves the non-grid aligned strong shock better than the other schemes. This is due to the robustness contributed by the van Leer's FVS part of the hybrid scheme, which imparts higher accuracy for strong shocks [18]. However, both ADSAH and AUSM schemes capture the non-grid aligned weak shocks better than the Radespiel-Kroll's scheme. The slip lines using the ADSAH scheme are less diffused than those of the DRLLF and Radespiel-Kroll's schemes, and are comparable to those of the AUSM scheme. Thus it is observed that the ADSAH scheme adjusts itself close to either the AUSM or the DRLLF scheme, whichever performs more accurately for any particular flow-situation.

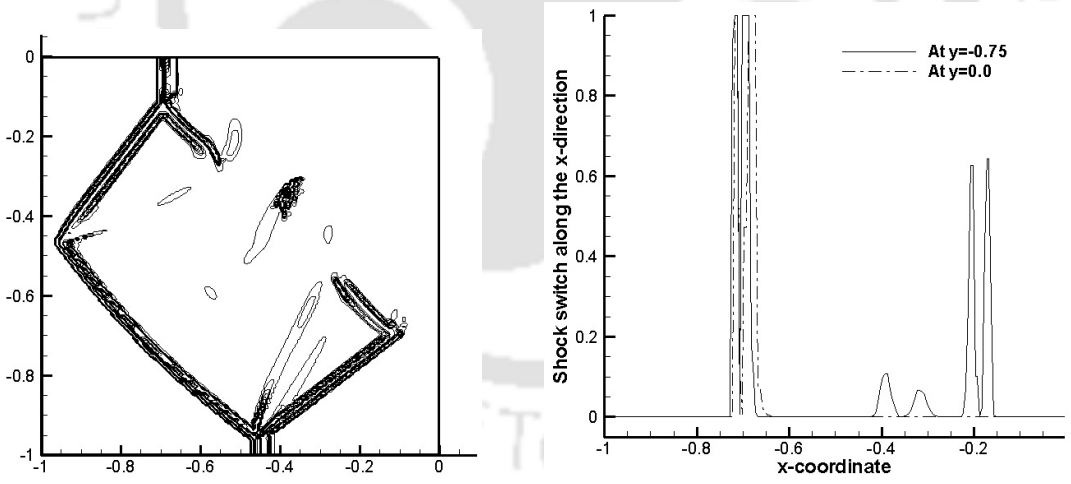

(a) (b)

Fig. 6.16. The shock-switch variation of the ADSAH scheme for the 2D Riemann problem: (a) contours in the lower-left quadrant using 10 contour levels in the range [0.05, 1.0] and (b) variations along the x-direction at two different y-locations.

Figure 6.16(a) shows the shock-switch contours in the lower-left quadrant and figure 6.16(b) presents the shock-switch profiles along the x-direction at $y = -0.75$

and $y = 0$. Expectedly the strong shock inclined at 45^0 to the gridlines gives the highest value of unity.

6.3.7 Hypersonic flow over a semi-cylinder

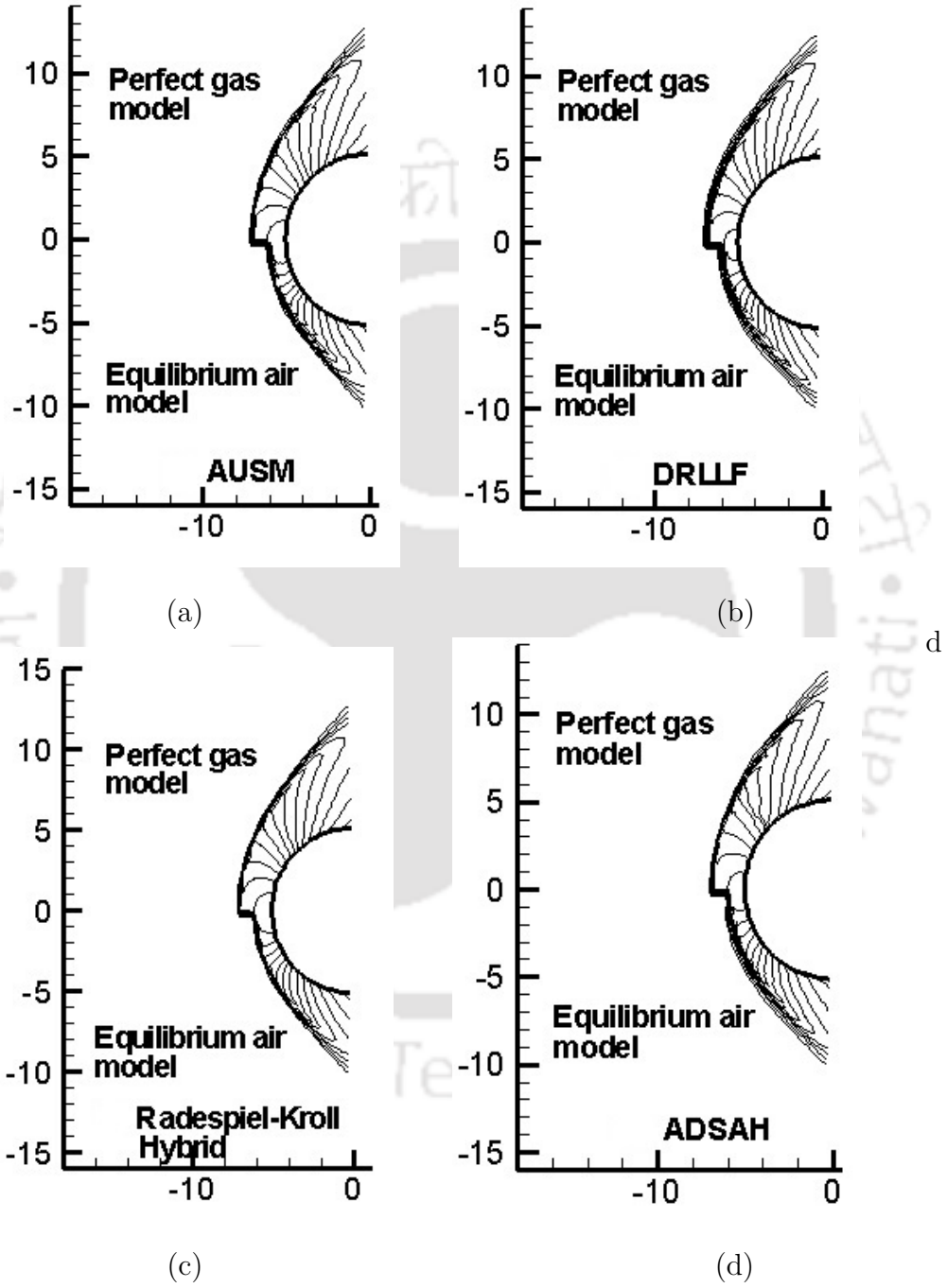

Fig. 6.17. Pressure contours for hypersonic flow ($M_\infty = 15$) over a semi-cylinder using (a) AUSM, (b) DRLLF, (c) Radespiel-Kroll Hybrid and (d) ADSAH schemes.

The hypersonic flow over a semi-cylinder involves a detached bow shock located at a certain stand-off distance from the solid body. The shock is the strongest in front of the nose of the blunt body where it resembles a normal shock. Away from the nose, the strength of the shock gradually becomes weaker till it becomes a Mach wave. Thus this problem offers itself as a single test case involving shock waves of various strengths. The present work considers flow at free-stream Mach number $M_\infty = 15$, free-stream pressure $p_\infty = 1197\,\mathrm{N/m^2}$ and free-stream temperature $T_\infty = 226.5\,\mathrm{K}$ over a semi-cylinder of diameter 10 m [77].

Figures 6.17(a)-(d) show the pressure contours for hypersonic flow over the semi-cylinder using the AUSM, DRLLF, Radespiel-Kroll Hybrid and ADSAH schemes. The results for the perfect-gas model and the equilibrium-air model of Tannehill and Mugge [73] are shown on the upper and lower halves of the semi-cylinder. To obtain a contrast of the shock resolutions a coarse grid of size 51×51 is used for all the computations. The ability of the ADSAH scheme to compute reacting-air flow is also demonstrated here.

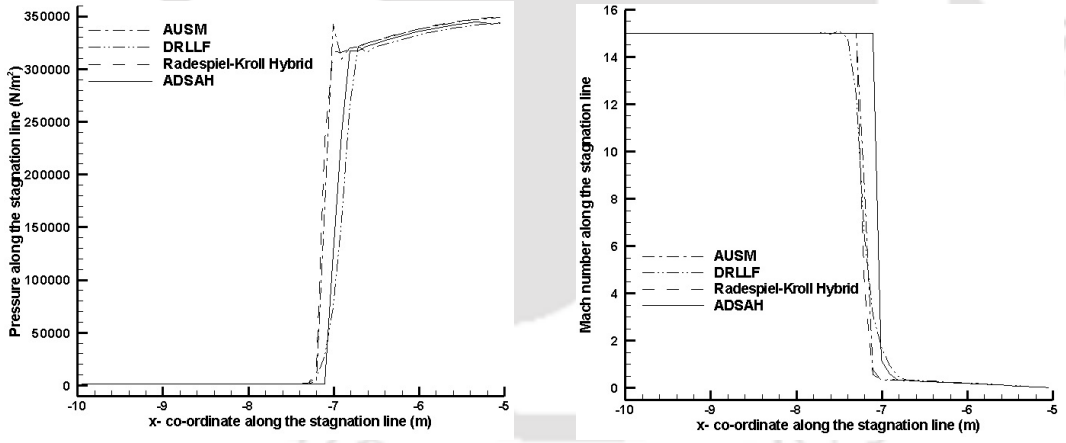

(a) (b)

Fig. 6.18. Variation along the stagnation line for hypersonic flow ($M_\infty = 15$) over a semi-cylinder (perfect-gas model): (a) pressure and (b) Mach number.

Figures 6.18-6.19 compare the pressure and Mach-number variations along the stagnation line with various schemes for the perfect-gas model and the equilibrium-air model, respectively. It is clear that the shock-stand-off distance for the equilibrium-air model is less than that for the perfect-gas model. The figures also indicate that the AUSM scheme produces large overshoots in the pressure field just behind the

shock, which are reduced to a large extent by the ADSAH scheme with a little more smearing of the shock. The reason for this improvement is that for standing-normal shocks the ADSAH scheme performs like the AUSM scheme at the end-points of a standing-normal shock and it acts close to the DRLLF scheme in cells lying within the shock. Therefore the AUSM part of the scheme offers low-numerical diffusion, resulting in a crisp-shock structure. On the other hand the DRLLF part of the scheme, which is highly diffusive across standing-normal shocks, contributes towards resisting the kinks in the computed pressure fields.

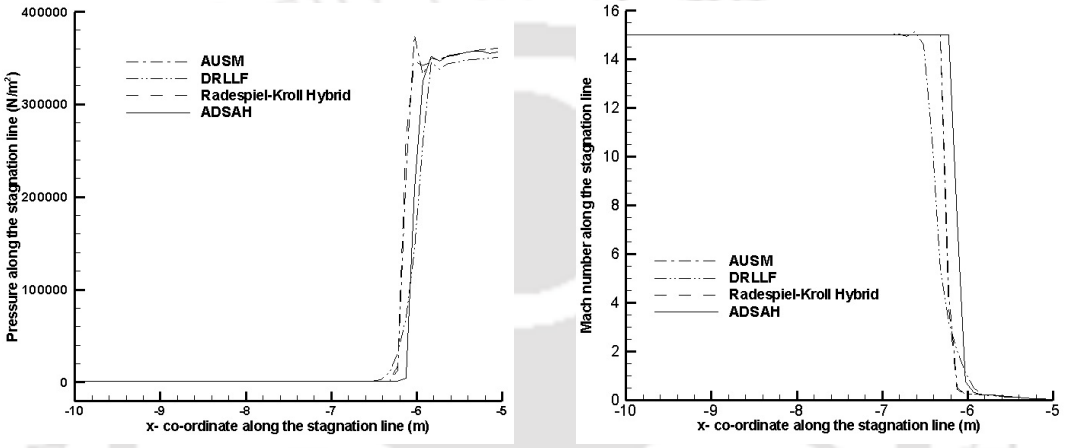

(a) (b)

Fig. 6.19. Variation along the stagnation line for hypersonic flow ($M_\infty = 15$) over a semi-cylinder (equilibrium-air model model): (a) pressure and (b) Mach number.

6.4 Viscous-compressible-flow results

In the next two subsections (6.4.1-6.4.2) we present the results of our second hybrid scheme ADSAHV developed for computing viscous-compressible flows. Test problems from both supersonic and hypersonic regimes are considered. The supersonic-test problem involves laminar-boundary layer for flow over a flat plate with a sharp-leading edge. The hypersonic-test problems deal with shock-wave boundary layer interaction (SWBLI) in flows over a ramped surface. The test cases are computed by incorporating the ADSAHV scheme in the High-speed Viscous Flow Solver (HSVFS) presented in chapter 5. Higher-order accuracies of the AUSM and Radespiel-Kroll Hybrid schemes are obtained by the MUSCL approach [38] with the minmod limiter [64]. Higher-order accuracy of the DRLLF scheme is obtained

through the reconstruction approach using CUSP limiter [5] as has been done for the higher-order-accurate DRLLFV scheme presented in section 5.3.

6.4.1 Viscous-supersonic flow over a flat plate

This problem involves viscous supersonic flow of air over a flat plate with a sharp-leading edge at a zero incidence. The geometric and free-stream parameters that are listed in table 4.1 are so chosen that the flow remains laminar throughout the length of the plate [93].

It has been found in section 5.3 that mesh-independence for this problem is achieved for an 80×100 grid and hence all the results are shown for this grid. Figures 6.20(a)-(b) show the normalized-temperature profiles at the trailing edge of an adiabatic-flat plate using the first-order and higher-order-accurate AUSM, DRLLF, Radespiel-Kroll Hybrid and ADSAHV schemes. The non-dimensionalized y-distance is calculated as suggested by Van Driest [105]. Inside the boundary layer the ADSAHV scheme resolves the flow-field with high resolution comparable with the AUSM scheme. The former scheme performs better than the latter in resolving the weak-leading-edge shock outside the boundary layer. The DRLLF and Radespiel-Kroll Hybrid schemes prove to be over-dissipative for viscous computations in that they predict a much higher adiabatic-wall temperatures.

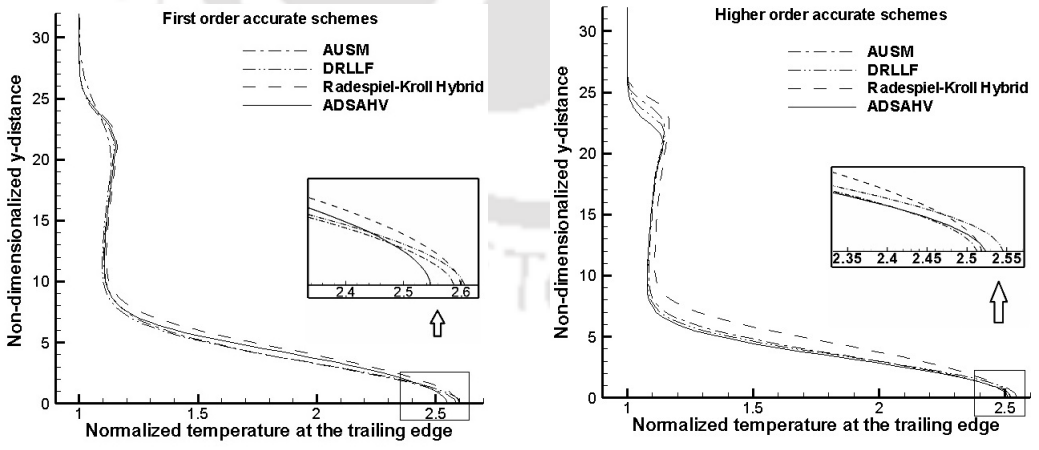

(a) (b)

Fig. 6.20. Temperature profiles at the trailing edge of the flat plate under adiabatic-wall condition: (a) first-order and (b) higher-order-accurate schemes.

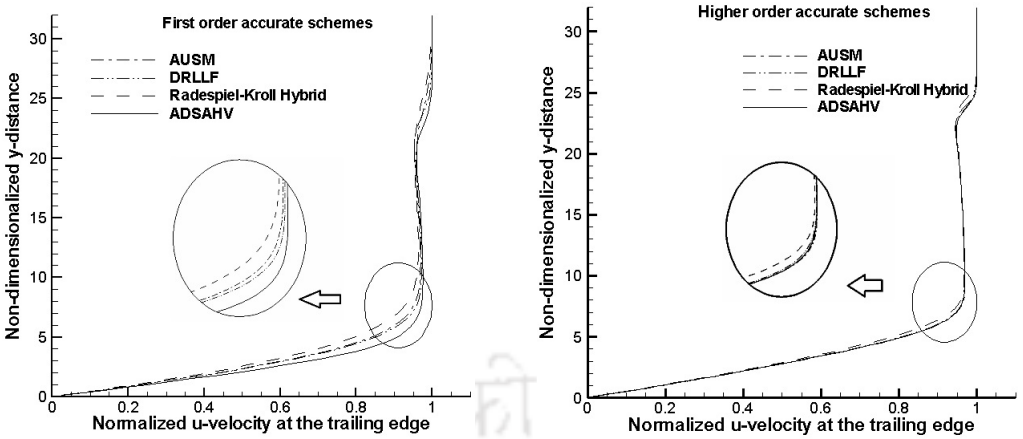

(a) (b)

Fig. 6.21. Velocity profiles at the trailing edge of the flat plate under the adiabatic-wall condition: (a) first-order and (b) higher-order-accurate schemes.

Figures 6.21(a)-(b) show the comparative plots for the non-dimensionalized velocity profiles at the trailing edge of the plate for the first-order and higher-order-accurate schemes. It can be seen that the ADSAHV scheme resolves the edge of the boundary layer marginally better than the AUSM and Radespiel-Kroll Hybrid schemes as shown by the zoomed-in encircled regions. Accordingly the ADSAHV scheme predicts a higher skin-friction-coefficient profile as evident from Figures 6.22(a)-(b).

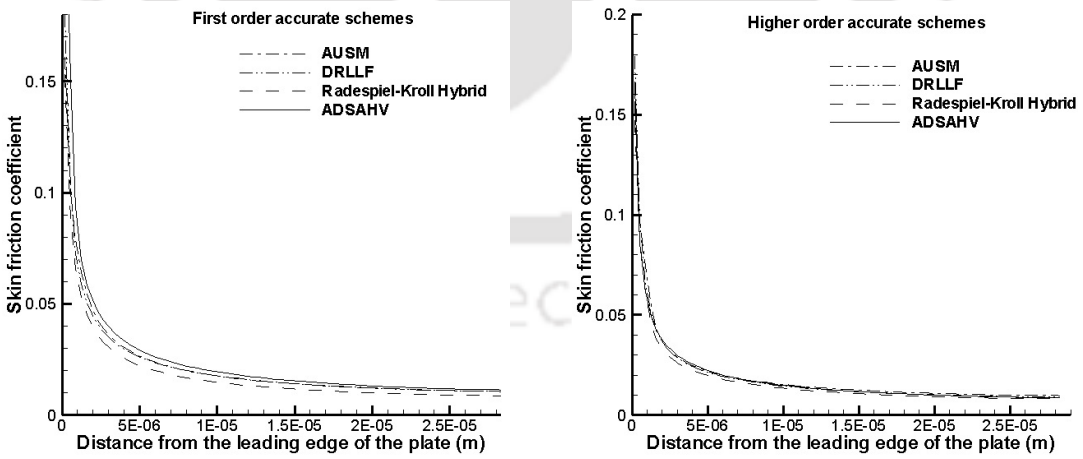

(a) (b)

Fig. 6.22. Skin-friction-coefficient profiles at the trailing edge of the flat plate under the adiabatic-wall condition: (a) first-order and (b) higher-order-accurate schemes.

6.4.2 Hypersonic shock wave-boundary layer interaction

This problem involves the interaction of a laminar boundary layer with a ramp-induced shock for hypersonic flow over a plate having a compression-corner. The ramp-angle is higher than the incipient-separation angle suggested by Needham and Stollery [96]. As a result a separation bubble is formed at the compression-corner. The geometric and free-stream parameters for this problem [98, 108] are listed in table 5.1.

For comparing our results with the literature [98, 108], computations are carried out using higher-order-accurate schemes on a 192×140 mesh that provides the mesh-independent solutions. The skin-friction and wall-heat-flux profiles for the hypersonic SWBLI problem [98] are shown in figures 6.23(a)-(b). The ADSAHV scheme produces significantly less smearing of the boundary layer because of which the skin friction coefficient obtained by this scheme is on the higher side as seen from figure 6.23(a). The reduced numerical diffusion succeeds in overcoming the under-prediction of the wall-heat flux. This is corroborated by figure 6.23(b). It can further be seen that the DRLLF and Radespiel-Kroll Hybrid schemes highly under-predict the skin-friction and wall-heat-flux profiles.

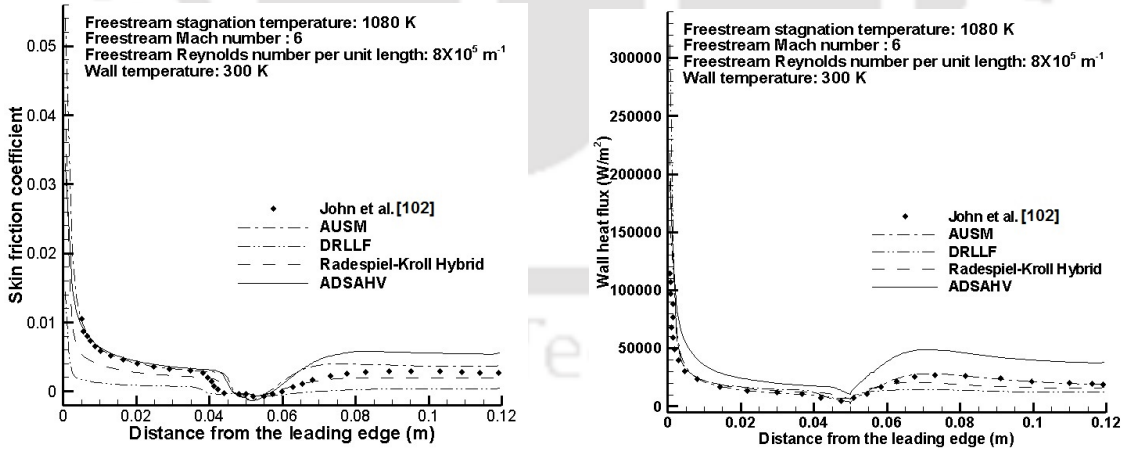

(a) (b)

Fig. 6.23. Hypersonic SWBLI problem [98]: Comparison with John et al.'s computational results [102] of (a) skin-friction and (b) wall-heat flux profiles.

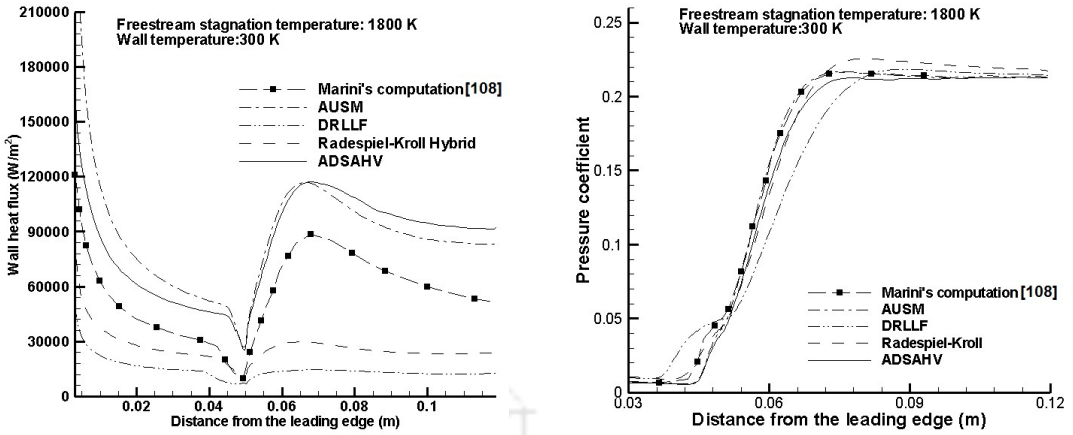

(a) (b)

Fig. 6.24. Hypersonic SWBLI problem with Marini's computational results [108]: Comparison of (a) Wall-heat-flux and (b) pressure-coefficient profiles.

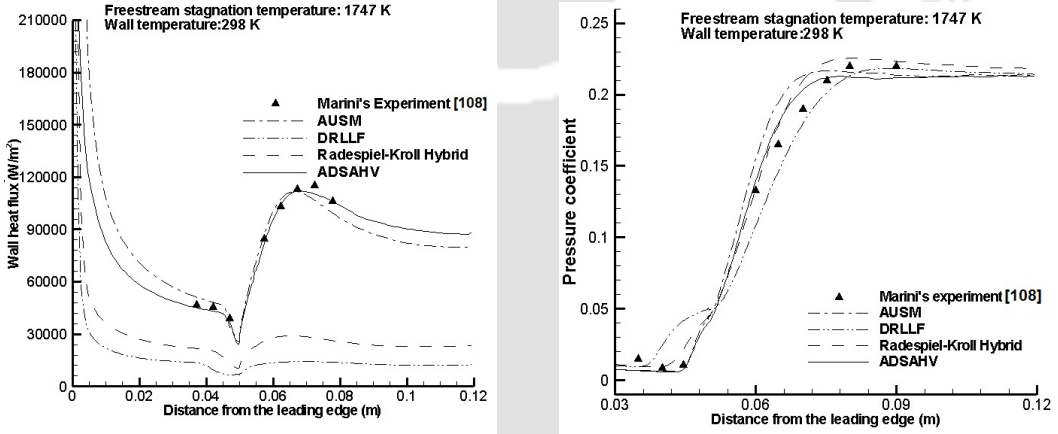

(a) (b)

Fig. 6.25. Hypersonic SWBLI problem with Marini's experimental results [108]: Comparison of (a) Wall-heat-flux and (b) pressure-coefficient profiles.

Further cases of higher-enthalpy flows having computational and experimental data of Marini [108] are also computed. Figure 6.24(a) compares the wall-heat fluxes for the SWBLI problem using higher-order AUSM, DRLLF, Radespiel-Kroll Hybrid and ADSAHV schemes with computed results of Marini [108]. The free-stream stagnation and wall-temperatures are 1800 K and 300 K, respectively. The rest of the free-stream and geometric parameters are the same as given in figures 6.23(a)-(b). The wall-heat-flux profiles using the ADSAHV and AUSM schemes are in nice agreement with each other. In general it is seen that both ADSAHV

and AUSM schemes estimate the heat-flux on the higher side compared with the computed results of Marini. However, the wall-heat fluxes using the ADSAHV and AUSM schemes are in much better agreement with Marini's experimental results, where the free-stream stagnation and wall-temperatures are 1747 K and 298 K, respectively, as seen in figure 6.25(a). It can further be seen that the ADSAHV scheme agrees with the experimental wall-heat-flux profile closer than even the AUSM scheme, especially in the post-reattachment zone. In both the computational and experimental test cases, the Radespiel-Kroll Hybrid and DRLLF schemes severely under-predict the wall-heat flux. From these observations it can be concluded that the higher-order ADSAHV scheme is able to resolve the SWBLI with marginally better resolution than the higher-order AUSM scheme and much better than the computations of Marini [108]. As can be observed from figure 6.24(b) and figure 6.25(b), the pressure-coefficient profiles for both the cases obtained by using the AUSM, Radepsiel-Kroll Hybrid and ADSAHV schemes are in reasonable agreement with Marini's results [108]. However, the DRLLF scheme expectedly computes much larger zones of upstream influence owing to the highly diffusive nature of the scheme for viscous-flow computations.

6.5 Conclusions

For computing viscous and inviscid flows the necessity of a numerical scheme with provisions for controlling dissipation so as to sharply capture both grid-aligned and inclined strong and weak shocks cannot be overemphasized. To that end we develop a self-adjusting hybrid methodology that results in two schemes, one for inviscid and the other for viscous flows. For inviscid-compressible flows, the ADSAH scheme combines AUSM scheme with DRLLF scheme whereas for viscous-compressible flows the ADSAHV scheme combines AUSM scheme with the very recently developed DRLLFV scheme. The numerical experiments demonstrate the superior capability of the ADSAH scheme to sharply capture both grid-aligned and inclined strong and weak shocks for a wide range of Mach numbers. The viscous counterpart of the scheme, namely ADSAHV, computes boundary layer and shock-boundary layer interaction problems very accurately with sharp resolution of both boundary layer and inclined shocks for a wide range of Mach numbers. The su-

perior performance of the scheme over the large range of Mach numbers can be ascribed not only to the careful selection of the constituent schemes that are hybridized but also to the novel strategy adopted to design the shock switch. In a significant departure from the earlier shock-switch-design strategies, the present shock switch is based on the cell-interface gradient of the Mach number. This ingenuity equips the switch with the quality of benign transition from strong shock to weak shock to smooth-flow regions. This is what makes the schemes highly suitable for computing flows with both strong and weak shocks, thus giving the schemes built-in ability to produce effects similar to multidimensional schemes. Unlike many hybrid schemes that are efficient only for a specified range of Mach numbers, the present schemes are highly robust producing results for low supersonic to hypersonic Mach numbers and at the same time retaining their ability to provide sharp resolution of discontinuities. The schemes also display excellent-sonic-point behaviour absent in many of the established schemes. One notable property of the schemes is their ability to capture contact discontinuities crisply; for example in the Sod's shock-tube problem the ADASH scheme does not smear the shock and contact discontinuity as much as the AUSM scheme. Unlike many of the popular schemes, the ADSAH scheme is free from the pre- and post-shock undershoots and overshoots in the wide variety of problems studied. For 2D inviscid-flow computations the ADSAH scheme resolves both strong and weak shocks with good resolution comparable with the AUSM and DRLLF schemes, respectively. The test problems demonstrate the capability of the ADSAH scheme to adjust itself close to either the AUSM or the DRLLF scheme, whichever performs more accurately for any particular-flow situation. For viscous flows such as the flow over a flat plate the present ADSAHV scheme resolves the boundary layer comparable to the AUSM scheme and the leading-edge shock better than it. The accuracy of the ADSAHV scheme is further reaffirmed by the excellent agreement of its results with the available numerical and experimental results for the ramp-induced hypersonic shock wave-boundary layer interaction problems. Thus the present schemes are important additions to the existing family of hybrid schemes in that they are robust, versatile and accurate with the extra ability to produce multidimensional-like effects without being as expensive.

Chapter 7

Summary and Conclusions

This chapter highlights the major achievements of the thesis and enlists the scope of future work that can be taken up based on the experience gained from the present work. Whenever an observation is made or an inference drawn, the work done is also briefly described so as to set the context.

All the results in this work are produced by codes developed in the programming language "C" with meticulous care to ensure that the merits and demerits of the schemes, developed and used, get accurately reflected in the results presented. The inviscid part of the solver has the provision for using various numerical-flux expressions of existing and newly-developed schemes. For computing viscous flows, viscous-flux discretization has been incorporated in the same solver using more than one method to ensure accuracy through comparison. Sufficient care has been taken to present grid-independent results unless a coarse grid is deliberately used to study the relative diffusive behaviour of various schemes.

The thesis focuses on the analysis and regulation of numerical diffusion for accurate computations of both inviscid and viscous-compressible flows. Towards this end, the work can be divided in the following stages:

1. Carrying out a qualitative study on the effects of numerical diffusion present in various schemes in the computation of inviscid flows.

2. Exploring the possibility of using reduced-numerical diffusion in viscous-flow computations.

3. Development of an accurate diffusion-regulated scheme for accurate computation of the compressible Navier-Stokes equations using a novel boundary layer sensor which enables differential numerical diffusion to be used in and outside the shear layer. The knowledge of dissipation-control gained in the earlier stages becomes useful here.

4. The observation that the schemes developed in the preceding stages gave improved results mainly for computation of flow situations involving weak and grid-inclined shocks, made it necessary to devise diffusion-regulated schemes that work equally well for strong and weak shocks, whether grid-aligned or otherwise. This is accomplished in the final stage of the work. Here a hybrid approach using a cleverly designed shock switch is developed so that both inviscid and viscous flows involving grid-aligned and grid-inclined shocks can be accurately computed with less computational cost than the conventional multidimensional schemes.

In the course of what follows these works will be briefly described in conjunction with explanatory observations and comments.

As already indicated, initially we study the role of numerical diffusion and its regulation in the computation of high-speed-inviscid flows and compare the performances of two recent diffusion-regulated methods with established-numerical-flux schemes. The study is done at various levels, namely, 1D and quasi-1D flows, 2D supersonic flows, and hypersonic flows. For the 1D and quasi-1D flows Sod's 1^{st} shock tube problem and flow through a converging-diverging nozzle, both having analytical solutions are chosen as the test cases. The performance of the Diffusion-Regulated Local Lax-Friedrichs (DRLLF) scheme is studied with varying levels of numerical diffusion. Reduction in numerical diffusion leads to less smearing of the captured discontinuities but augments nonphysical oscillations. This indicates that amount of artificial diffusion to be added should be based upon a balance between the solution-resolution and numerical stability. The most appropriate value of a variable δ for computing the Diffusion-Regulation (DR) parameter is found to be problem-dependent. The scheme is also compared with other established schemes. It is observed that for moving normal shocks where the absolute flows

across the shock remain subsonic the DRLLF scheme captures the shock with the least smearing. However, in computing the flow in a converging-diverging nozzle with a standing shock in the divergent part, the jump in Mach number across the cell-interface is large providing a relatively high value of the DR parameter. Thus for flows involving grid-aligned stationary normal shocks, the DRLLF scheme does not compare favourably with established schemes like AUSM and van Leer's Flux Vector Splitting (FVS). To have a better understanding of the diffusive behaviour of various schemes a number of 2D test cases are also solved. Expectedly the DRLLF scheme performs worse than AUSM in resolving normal and strong shocks; however, it scores over the other schemes in resolving oblique shocks that arise, for example, in problems like supersonic flow over a ramped channel where grid-inclined-weak shocks are generated from a compression-corner and when it gets reflected from another solid surface. Further the DRLLF scheme is tested for hypersonic flows including chemical-equilibrium-air model to get an idea as to whether diffusion control can be effectively used to compute such flows. However, in computing axisymmetric-hypersonic flow over a hemisphere, the scheme is found to produce numerical oscillations. The original method of computing the DR parameter is modified to successfully enforce monotonicity for such cases. The main achievement of this phase of work however is to get an idea about the types of problems where diffusion-regulation can be effectively used and to recognize that a scope exists for designing a versatile-diffusion-regulation scheme for accurate capture of discontinuities irrespective of their strength or grid-inclination.

An attempt is now made to explore the possibility of regulating numerical diffusion in computing compressible-viscous-flow problems. It is well known that for such flows viscous-flux discretization has to be coupled to inviscid-flux discretization mentioned above. However, presence of physical viscosity suggests that it might be possible to regulate numerical viscosity lower that it was originally suggested for Euler computations. To examine this, two test cases, namely, viscous-supersonic flow over a flat plate with a laminar-boundary layer and viscous-hypersonic flow over a ramped surface that leads to shock wave-boundary layer interaction (SWBLI) with a laminar separation are taken up. For the flat-plate problem reduced diffusion ($\delta = 0.2$ as against originally suggested value of 0.5)

throughout the domain gives better overall accuracy because it resolves the boundary layer as accurately as the AUSM and, additionally, resolves the leading-edge shock better than the AUSM and van Leer's FVS schemes. Limitation of the van Leer's FVS scheme for viscous-flow computations due to high numerical diffusion is affirmed again. For the isothermal-wall condition, the location of the maximum temperature shifts outward from the wall when the numerical diffusion increases. For the adiabatic-wall condition, a more diffusive scheme predicts a higher-wall temperature. Also it is found that on a regular orthogonal grid, the Green's theorem is comparable with the central-differencing method for the computation of the gradients across the cell-interfaces. The higher-order-inviscid-flux discretization is also employed to study the effect of limiters. However, it is found that choice of limiters generally does not have a highly-significant effect.

Effect of reducing numerical diffusion all over the computational domain in computing the hypersonic SWBLI problem also gives improved results. For this problem the value of the parameter δ can be as low as 0.1 (a lower value of δ indicates lower numerical diffusion); however, it is to some extent problem-dependent and the most suitable value is better chosen based upon the various flow parameters such as free-stream Mach number, pressure, temperature, stagnation temperature etc. It is seen that high-numerical diffusion leads to under-prediction of the wall-shear stress owing to a diffused-boundary layer. Further it is seen that laminar-separation-bubble length increases with numerical diffusion.

So far, for accurate-viscous-flow computations, numerical diffusion is uniformly reduced all over the computational domain that includes viscous-boundary-layer region and the outer-inviscid region alike. Encouraging results obtained provide the motivation to explore whether or not it is possible to scale down numerical diffusion even more in the viscous-shear layer where viscous effects are concentrated. Effort in this direction resulted in an accurate scheme for viscous-flow computations, which we call the DRLLF-Viscous (DRLLV) scheme. The scheme is based on a newly developed boundary-layer sensor that reduces numerical diffusion only inside the boundary layer by using a polynomial that scales down the diffusion-regulation parameter to the maximum on the solid wall and outside the boundary layer the scheme works like the original DRLLF scheme. To

demonstrate the effectiveness of the new scheme it is employed to compute the supersonic-viscous flow over a flat plate and the shock wave-boundary layer interaction problems described earlier. Excellent agreement of the results computed by the DRLLFV scheme with the experimental results is observed. The new scheme is found to perform significantly better than the DRLLF and van Leer's FVS schemes. It is, therefore, not surprising that, for high-speed-viscous-flow computations, the DRLFLV scheme can capture many flow-features even better than the AUSM scheme. Inside the boundary layer, the new scheme resolves the flow-separation and reattachment as accurately as the AUSM scheme, whereas, in the inviscid zone, it captures the weak shocks better than the latter.

For computing viscous and inviscid flows the necessity of a numerical scheme with provisions for controlling dissipation so as to sharply capture both grid-aligned and inclined strong and weak discontinuities cannot be overemphasized. To that end we develop a self-adjusting hybrid methodology that results in two schemes, one for inviscid and the other for viscous flows. For inviscid-compressible flows, the ADSAH scheme combines AUSM scheme with DRLLF scheme whereas for viscous-compressible flows the ADSAHV scheme combines AUSM scheme with the very recently developed DRLLFV scheme. We have detected that shock switches developed so far to hybridize schemes have a general weakness in that they are based on the cell-interface parameters like normal Mach number, pressure, entropy etc. In a significant departure from this approach we design a shock switch that is based on the gradient of the normal Mach number at cell-interface. The importance of this novel shock switch is readily understood from the facts that (i) The ADSAH scheme demonstrates superior capability to sharply capture both grid-aligned and inclined strong and weak shocks for a wide range of Mach numbers, (ii) The ADSAHV scheme computes boundary layer and shock-boundary layer interaction problems very accurately with sharp resolution of both boundary layer and inclined shocks for a wide range of Mach numbers. The superior performance of the schemes over the large range of Mach numbers can be ascribed not only to the careful selection of the constituent schemes that are hybridized but also to the novel strategy adopted to design the shock switch. The ingenuity of using the cell-interface gradient of the Mach number equips the switch with the qual-

ity of benign transition from strong shock to weak shock to smooth-flow regions. This is what makes the schemes highly suitable for computing flows with both strong and weak shocks, thus giving the schemes built-in ability to produce effects similar to multidimensional schemes. Unlike many hybrid schemes that are efficient only for a specified range of Mach numbers, the present schemes are highly robust producing results for low-supersonic to hypersonic Mach numbers and at the same time retaining their ability to provide sharp resolution of discontinuities. The schemes also display excellent-sonic-point behaviour absent in many of the established schemes. One notable property of the schemes is their ability to capture contact discontinuities crisply; for example in the Sod's shock-tube problem the ADASH scheme does not smear the shock and contact discontinuity as much as the AUSM scheme. Unlike many of the popular schemes, the ADSAH scheme is free from the pre- and post-shock undershoots and overshoots in the wide variety of problems studied. For 2D inviscid-flow computations the ADSAH scheme resolves both strong and weak shocks with good resolution comparable with the AUSM and DRLLF schemes, respectively. For viscous flows such as the flow over a flat plate the ADSAHV scheme resolves the boundary layer comparable to the AUSM scheme and the leading-edge shock better than it. These schemes are thus important additions to the existing family of hybrid schemes in that they are robust, versatile and accurate with the extra ability to produce multidimensional-like effects without being as expensive.

Thus it will not be unreasonable to to claim that the goal we set ourselves at the outset has been fulfilled to a large extent in that the volume of work is substantial and the element of novelty is significant.

Scope for future work

The present work opens up a number of possibilities for pursuing further research. Some of these are mentioned below.

1. A mathematical framework can be developed for exact assessment of the error due to numerical diffusion in compressible-flow computations.

2. A scope exists to investigate more deeply the sonic-point behaviour of the DRLLF scheme.

3. The diffusion-regulated scheme using the novel boundary layer sensor can be extended with suitable modifications for solving problems with mixed grids.

4. A study can be carried out on the performance of other boundary-layer sensors like the Ducros sensor or the blending function used in the Menter $k - \omega$ model, to regulate the numerical diffusion of the DRLLF scheme in viscous-flow computations.

5. Detailed studies can be carried out on the performance of DRLLFV scheme in computing vortical flows.

6. Attempts can be made to extend the present hybrid schemes to unstructured-grid applications.

7. Further studies on the higher-order-accurate extensions of the DRLLF, ADSAH and ADSAHV schemes can be carried out.

8. The present hybrid scheme can be tested in high-Reynolds-number situations.

9. The DRLLF, ADSAH and ADSAHV schemes can be extended to three dimensions.

10. The possibility can be explored to develop a hybrid approach for viscous-flow computations that works as the AUSM scheme for the major portion of flow, including shear layers and blends in DRLLF only in the presence of shocks and sonic transitions.

Appendix A

Non-dimensionalization of the Euler equations of gas dynamics

The 3D Euler equations of gas dynamics can be written in compact form as follows:

$$\frac{\partial \mathbf{U}}{\partial t} + \frac{\partial \mathbf{F}}{\partial x} + \frac{\partial \mathbf{G}}{\partial y} + \frac{\partial \mathbf{H}}{\partial z} = 0, \tag{A.1}$$

where the the vector of conserved variables $\mathbf{U}$ and flux vectors along the x-, y- and z-directions $\mathbf{F}$, $\mathbf{G}$ and $\mathbf{H}$, respectively are given by

$$\mathbf{U} = \begin{bmatrix} \rho \\ \rho u \\ \rho v \\ \rho w \\ \rho e_m \end{bmatrix}, \tag{A.2a}$$

$$\mathbf{F} = \begin{bmatrix} \rho u \\ p + \rho u^2 \\ \rho uv \\ \rho uw \\ (p + \rho e_m)u \end{bmatrix}, \tag{A.2b}$$

$$\mathbf{G} = \begin{bmatrix} \rho v \\ \rho uv \\ p + \rho v^2 \\ \rho vw \\ (p + \rho e_m)v \end{bmatrix}, \tag{A.2c}$$

$$\mathbf{H} = \begin{bmatrix} \rho w \\ \rho u w \\ \rho v w \\ p + \rho w^2 \\ (p + \rho e_m) w \end{bmatrix}. \tag{A.2d}$$

The symbols have their usual meanings. To carry out the non-dimensionalization of the Euler equations of gas dynamics given by equation A.1, the variables are normalized as follows:

$$\begin{aligned} x^* &= \frac{x}{L} \\ y^* &= \frac{y}{L} \\ z^* &= \frac{z}{L} \\ t^* &= \frac{tU_\infty}{L} \\ u^* &= \frac{u}{U_\infty} \\ v^* &= \frac{v}{U_\infty} \\ w^* &= \frac{w}{U_\infty} \\ \rho^* &= \frac{\rho}{\rho_\infty} \\ p^* &= \frac{p}{\rho_\infty U_\infty^2} \\ T^* &= \frac{T}{T_\infty} \\ e_m^* &= \frac{e_m}{U_\infty^2}, \end{aligned} \tag{A.3}$$

where L is the characteristic length, U_∞ is the free-stream velocity, ρ_∞ is the free-stream density, and T_∞ is the free-stream temperature.

The continuity equation is

$$\frac{\partial \rho}{\partial t} + \frac{\partial (\rho u)}{\partial x} + \frac{\partial (\rho v)}{\partial y} + \frac{\partial (\rho w)}{\partial z} = 0. \tag{A.4}$$

Introducing the normalization of the variables given by equations A.3, equation A.4 can be non-dimensionalized as

$$\frac{\partial (\rho^* \rho_\infty)}{\partial \left(\frac{t^* L}{U_\infty}\right)} + \frac{\partial (\rho^* \rho_\infty u^* U_\infty)}{\partial (x^* L)} + \frac{\partial (\rho^* \rho_\infty v^* U_\infty)}{\partial (y^* L)} + \frac{\partial (\rho^* \rho_\infty w^* U_\infty)}{\partial (z^* L)} = 0$$

$$\frac{\rho_\infty U_\infty}{L}\left[\frac{\partial \rho^*}{\partial t^*}+\frac{\partial\left(\rho^* u^*\right)}{\partial x^*}+\frac{\partial\left(\rho^* v^*\right)}{\partial y^*}+\frac{\partial\left(\rho^* w^*\right)}{\partial z^*}\right]=0$$

$$\frac{\partial \rho^*}{\partial t^*}+\frac{\partial\left(\rho^* u^*\right)}{\partial x^*}+\frac{\partial\left(\rho^* v^*\right)}{\partial y^*}+\frac{\partial\left(\rho^* w^*\right)}{\partial z^*}=0. \tag{A.5}$$

Equation A.5 is the non-dimensionalized form of the continuity equation.

The x-momentum equation is

$$\frac{\partial(\rho u)}{\partial t}+\frac{\partial\left(p+\rho u^2\right)}{\partial x}+\frac{\partial(\rho u v)}{\partial y}+\frac{\partial(\rho u w)}{\partial z}=0. \tag{A.6}$$

Using equations A.3 to normalize the parameters in equation A.6 one obtains

$$\frac{\partial\left(\rho^* \rho_\infty u^* U_\infty\right)}{\partial\left(\frac{t^* L}{U_\infty}\right)}+\frac{\partial\left\{p^* \rho_\infty U_\infty^2+\rho^* \rho_\infty\left(u^* U_\infty\right)^2\right\}}{\partial\left(x^* L\right)}$$

$$+\frac{\left(\rho^* \rho_\infty u^* U_\infty v^* U_\infty\right)}{\partial\left(y^* L\right)}+\frac{\left(\rho^* \rho_\infty u^* U_\infty w^* U_\infty\right)}{\partial\left(z^* L\right)}=0$$

$$\frac{\rho_\infty U_\infty^2}{L}\left[\frac{\partial\left(\rho^* u^*\right)}{\partial t^*}+\frac{\partial\left\{p^*+\rho*\left(u^*\right)^2\right\}}{\partial x^*}+\frac{\partial\left(\rho^* u^* v^*\right)}{\partial y^*}+\frac{\partial\left(\rho^* u^* w^*\right)}{\partial z^*}\right]=0, \tag{A.7a}$$

$$\frac{\partial\left(\rho^* u^*\right)}{\partial t^*}+\frac{\partial\left\{p^*+\rho*\left(u^*\right)^2\right\}}{\partial x^*}+\frac{\partial\left(\rho^* u^* v^*\right)}{\partial y^*}+\frac{\partial\left(\rho^* u^* w^*\right)}{\partial z^*}=0. \tag{A.7b}$$

Equation A.7b represents the non-dimensionalized form of the x-momentum equation. Proceeding in a similar fashion the non-dimensionalized forms of the y- and z-momentum equations can be written as

$$\frac{\partial\left(\rho^* v^*\right)}{\partial t^*}+\frac{\partial\left(\rho^* u^* v^*\right)}{\partial x^*}+\frac{\partial\left\{p^*+\rho*\left(v^*\right)^2\right\}}{\partial y^*}+\frac{\partial\left(\rho^* v^* w^*\right)}{\partial z^*}=0, \tag{A.8}$$

$$\frac{\partial\left(\rho^* w^*\right)}{\partial t^*}+\frac{\partial\left(\rho^* u^* w^*\right)}{\partial x^*}+\frac{\partial\left(\rho^* v^* w^*\right)}{\partial y^*}+\frac{\partial\left\{p^*+\rho*\left(w^*\right)^2\right\}}{\partial z^*}=0. \tag{A.9}$$

The energy equation is

$$\frac{\partial\left(\rho e_m\right)}{\partial t}+\frac{\partial\left\{\left(p+\rho e_m\right) u\right\}}{\partial x}+\frac{\partial\left\{\left(p+\rho e_m\right) v\right\}}{\partial y}+\frac{\partial\left\{\left(p+\rho e_m\right) w\right\}}{\partial z}=0. \tag{A.10}$$

Applying the normalization of the variables given by equations A.3 in equation A.10 one obtains

$$\frac{\partial\left(\rho^* \rho_\infty e_m^* U_\infty^2\right)}{\partial\left(\frac{t^* L}{U_\infty}\right)}+\frac{\partial\left[\left\{p^* \rho_\infty U_\infty^2+\rho^* \rho_\infty e_m^* U_\infty^2\right\} u^* U_\infty\right]}{\partial\left(x^* L\right)}$$

$$+\frac{\partial\left[\left\{p^* \rho_\infty U_\infty^2+\rho^* \rho_\infty e_m^* U_\infty^2\right\} v^* U_\infty\right]}{\partial\left(y^* L\right)}$$

$$+\frac{\partial\left[\left\{p^*\rho_\infty U_\infty^2+\rho^*\rho_\infty e_m^* U_\infty^2\right\}w^* U_\infty\right]}{\partial\left(z^* L\right)}=0$$

$$\frac{\rho_\infty U_\infty^3}{L}\frac{\partial\left(\rho^* e_m^*\right)}{\partial t^*}+\frac{\rho_\infty U_\infty^3}{L}\frac{\partial\left\{\left(p^*+\rho^* e_m^*\right)u^*\right\}}{\partial x^*}$$
$$+\frac{\rho_\infty U_\infty^3}{L}\frac{\partial\left\{\left(p^*+\rho^* e_m^*\right)v^*\right\}}{\partial y^*}+\frac{\rho_\infty U_\infty^3}{L}\frac{\partial\left\{\left(p^*+\rho^* e_m^*\right)w^*\right\}}{\partial z^*}=0$$

$$\frac{\partial\left(\rho^* e_m^*\right)}{\partial t^*}+\frac{\partial\left\{\left(p^*+\rho^* e_m^*\right)u^*\right\}}{\partial x^*}$$
$$+\frac{\partial\left\{\left(p^*+\rho^* e_m^*\right)v^*\right\}}{\partial y^*}+\frac{\partial\left\{\left(p^*+\rho^* e_m^*\right)w^*\right\}}{\partial z^*}=0. \quad \text{(A.11)}$$

Equation A.11 represents the non-dimensionalized form of the energy equation. Combining equations A.5, A.7b, A.8, A.9 and A.11 and dropping the superscript '*' for ease of representation, the non-dimensionalized form of the 3D Euler equations are obtained in the form given by equation 2.1.

Further, the equation of state for a perfect gas can be non-dimensionalized as follows:

$$\begin{aligned}
p &= \rho \mathrm{R} T \\
p^*\rho_\infty U_\infty^2 &= \rho^*\rho_\infty \mathrm{R} T^* T_\infty \\
p^* &= \frac{\gamma \mathrm{R} T_\infty}{\gamma U_\infty^2}\rho^* T^* \\
&= \frac{a_\infty^2}{\gamma U_\infty^2}\rho^* T^* \\
&= \frac{1}{\gamma M_\infty^2}\rho^* T^*. \qquad \text{(A.12)}
\end{aligned}$$

For a perfect gas, the non-dimensionalized total energy per unit mass e_m^* is obtained in terms of the non-dimensionalized temperature and non-dimensionalized velocities as follows:

$$\begin{aligned}
e_m &= c_v T+\frac{1}{2}\left(u^2+v^2+w^2\right) \\
e_m^* U_\infty^2 &= \frac{\mathrm{R}}{\gamma-1}T^* T_\infty+\frac{U_\infty^2}{2}\left\{\left(u^*\right)^2+\left(v^*\right)^2+\left(w^*\right)^2\right\} \\
e_m^* &= \frac{\gamma \mathrm{R} T_\infty}{\gamma\left(\gamma-1\right)U_\infty^2}T^*+\frac{1}{2}\left\{\left(u^*\right)^2+\left(v^*\right)^2+\left(w^*\right)^2\right\} \\
&= \frac{T^*}{\gamma\left(\gamma-1\right)M_\infty^2}+\frac{1}{2}\left\{\left(u^*\right)^2+\left(v^*\right)^2+\left(w^*\right)^2\right\}. \qquad \text{(A.13)}
\end{aligned}$$

Appendix B

Non-dimensionalization of the Compressible Navier-Stokes equations

The Navier-Stokes equations for 3D compressible flow are given by

$$\frac{\partial \mathbf{U}}{\partial t} + \frac{\partial \mathbf{F}_\mathrm{I}}{\partial x} + \frac{\partial \mathbf{G}_\mathrm{I}}{\partial y} + \frac{\partial \mathbf{H}_\mathrm{I}}{\partial z} = \frac{\partial \mathbf{F}_\mathrm{v}}{\partial x} + \frac{\partial \mathbf{G}_\mathrm{v}}{\partial y} + \frac{\partial \mathbf{H}_\mathrm{v}}{\partial z}, \tag{B.1}$$

where $\mathbf{U}$ is the vector of conserved variables, $\mathbf{F}_\mathrm{I}$, $\mathbf{G}_\mathrm{I}$ and $\mathbf{H}_\mathrm{I}$ are the inviscid-flux vectors and $\mathbf{F}_\mathrm{v}$, $\mathbf{G}_\mathrm{v}$ and $\mathbf{H}_\mathrm{v}$ are the viscous-flux vectors. The conserved variable vector for the compressible Navier-Stokes equations have the same expressions as the corresponding terms for the Euler equations and are given by equation A.2a. The inviscid-flux vectors have the same expressions as those of the Euler-flux terms given by equations A.2b-A.2d. The expressions for the viscous-flux vectors are as follows:

$$\mathbf{F}_\mathrm{v} = \begin{bmatrix} 0 \\ \tau_{xx} \\ \tau_{xy} \\ \tau_{xz} \\ u\tau_{xx} + v\tau_{xy} + w\tau_{xz} - q_x \end{bmatrix}, \tag{B.2a}$$

$$\mathbf{G}_{\mathrm{v}} = \begin{bmatrix} 0 \\ \tau_{yx} \\ \tau_{yy} \\ \tau_{yz} \\ u\tau_{yx} + v\tau_{yy} + w\tau_{yz} - q_y \end{bmatrix}, \tag{B.2b}$$

$$\mathbf{H}_{\mathrm{v}} = \begin{bmatrix} 0 \\ \tau_{zx} \\ \tau_{zy} \\ \tau_{zz} \\ u\tau_{zx} + v\tau_{zy} + w\tau_{zz} - q_z \end{bmatrix}. \tag{B.2c}$$

Assuming Stokes' hypothesis for a Newtonian fluid the stress and heat-flux terms in the visous-flux vectors can be expressed by

$$\tau_{xx} = \frac{4}{3}\mu\frac{\partial u}{\partial x} - \frac{2}{3}\mu\left(\frac{\partial v}{\partial y} + \frac{\partial w}{\partial z}\right), \tag{B.3a}$$

$$\tau_{yy} = \frac{4}{3}\mu\frac{\partial v}{\partial y} - \frac{2}{3}\mu\left(\frac{\partial u}{\partial x} + \frac{\partial w}{\partial z}\right), \tag{B.3b}$$

$$\tau_{zz} = \frac{4}{3}\mu\frac{\partial w}{\partial z} - \frac{2}{3}\mu\left(\frac{\partial u}{\partial x} + \frac{\partial v}{\partial y}\right), \tag{B.3c}$$

$$\tau_{xy} = \mu\left(\frac{\partial u}{\partial y} + \frac{\partial v}{\partial x}\right) = \tau_{yx}, \tag{B.3d}$$

$$\tau_{yz} = \mu\left(\frac{\partial v}{\partial z} + \frac{\partial w}{\partial y}\right) = \tau_{zy}, \tag{B.3e}$$

$$\tau_{zx} = \mu\left(\frac{\partial w}{\partial x} + \frac{\partial u}{\partial z}\right) = \tau_{xz}, \tag{B.3f}$$

$$q_x = -k\frac{\partial T}{\partial x}, \tag{B.4a}$$

$$q_y = -k\frac{\partial T}{\partial y}, \tag{B.4b}$$

$$q_z = -k\frac{\partial T}{\partial z}, \tag{B.4c}$$

where μ is the coefficient of dynamic viscosity and k is the thermal conductivity of the fluid. The coefficient of dynamic viscosity is obtained as a function of the absolute temperature using the Sutherland's law of viscosity:

$$\mu = \mu_0\left(\frac{T}{T_0}\right)^{3/2}\left(\frac{T_0 + 111}{T + 111}\right), \tag{B.5}$$

where the parameter μ_0 is the reference viscosity at the reference temperature T_0. For a fluid with a Prandtl number Pr and specific heat at constant pressure c_p, the thermal conductivity k is obtained using the following relation:

$$k = \frac{\mu c_p}{\mathrm{Pr}}. \tag{B.6}$$

For the non-dimensionalization of equation B.1 the variables are normalized as follows:

$$\begin{aligned}
x^* &= \frac{x}{L} \\
y^* &= \frac{y}{L} \\
z^* &= \frac{z}{L} \\
t^* &= \frac{tU_\infty}{L} \\
u^* &= \frac{u}{U_\infty} \\
v^* &= \frac{v}{U_\infty} \\
w^* &= \frac{w}{U_\infty} \\
\rho^* &= \frac{\rho}{\rho_\infty} \\
p^* &= \frac{p}{\rho_\infty U_\infty^2} \\
T^* &= \frac{T}{T_\infty} \\
e_m^* &= \frac{e_m}{U_\infty^2} \\
\mu^* &= \frac{\mu}{\mu_\infty},
\end{aligned} \tag{B.7}$$

where L is the characteristic length, U_∞ is the free-stream velocity, ρ_∞ is the free-stream density, T_∞ is the free-stream temperature, and μ_∞ is the free-stream dynamic-viscosity coefficient. The continuity equation for the Navier-Stokes equations given by equation B.1 is the same as that for the Euler equations (equation A.1). Using the variable-normalization given by equations B.7 and following the procedure adopted in Appendix A, the non-dimensionalized form of the continuity equation for 3D viscous compressible flow can be written as

$$\frac{\partial \rho^*}{\partial t^*} + \frac{\partial \left(\rho^* u^*\right)}{\partial x^*} + \frac{\partial \left(\rho^* v^*\right)}{\partial y^*} + \frac{\partial \left(\rho^* w^*\right)}{\partial z^*} = 0. \tag{B.8}$$

The x-momentum equation is

$$\begin{aligned}
\frac{\partial(\rho u)}{\partial t}+\frac{\partial\left(p+\rho u^2\right)}{\partial x}+\frac{\partial(\rho uv)}{\partial y}+\frac{\partial(\rho uw)}{\partial z} &= \frac{\partial\tau_{xx}}{\partial x}+\frac{\partial\tau_{yx}}{\partial y}+\frac{\partial\tau_{zx}}{\partial z} \\
\frac{\partial(\rho u)}{\partial t}+\frac{\partial\left(p+\rho u^2\right)}{\partial x}+\frac{\partial(\rho uv)}{\partial y}+\frac{\partial(\rho uw)}{\partial z} &= \frac{\partial\left\{\frac{4}{3}\mu\frac{\partial u}{\partial x}-\frac{2}{3}\mu\left(\frac{\partial v}{\partial y}+\frac{\partial w}{\partial z}\right)\right\}}{\partial x} \\
&\quad+\frac{\partial\left\{\mu\left(\frac{\partial u}{\partial y}+\frac{\partial v}{\partial x}\right)\right\}}{\partial y} \\
&\quad+\frac{\partial\left\{\mu\left(\frac{\partial w}{\partial x}+\frac{\partial u}{\partial z}\right)\right\}}{\partial z}.
\end{aligned} \tag{B.9}$$

Equation B.9 can be non-dimensionalized using the normalization given by equations B.7. Introducing variable-normalization the first term on the right-hand side of equation B.9 can be written as

$$\begin{aligned}
\frac{\partial\left\{\frac{4}{3}\mu\frac{\partial u}{\partial x}-\frac{2}{3}\mu\left(\frac{\partial v}{\partial y}+\frac{\partial w}{\partial z}\right)\right\}}{\partial x} &= \frac{\partial\left(\frac{4}{3}\mu\frac{\partial u}{\partial x}\right)}{\partial x} \\
&\quad-\frac{\partial\left\{\frac{2}{3}\mu\left(\frac{\partial v}{\partial y}+\frac{\partial w}{\partial z}\right)\right\}}{\partial x} \\
&= \frac{\partial\left\{\frac{4}{3}\mu^*\mu_\infty\frac{\partial(u^*U_\infty)}{\partial(x^*L)}\right\}}{\partial(x^*L)} \\
&\quad-\frac{\partial\left[\frac{2}{3}\mu^*\mu_\infty\left\{\frac{\partial(v^*U_\infty)}{\partial(y^*L)}+\frac{\partial(w^*U_\infty)}{\partial(z^*L)}\right\}\right]}{\partial(x^*L)} \\
&= \frac{\mu_\infty U_\infty}{L^2}\frac{\partial\left(\frac{4}{3}\mu^*\frac{\partial u^*}{\partial x^*}\right)}{\partial x^*} \\
&\quad-\frac{\mu_\infty U_\infty}{L^2}\frac{\partial\left\{\frac{2}{3}\mu^*\left(\frac{\partial v^*}{\partial y^*}+\frac{\partial w^*}{\partial z^*}\right)\right\}}{\partial x^*}.
\end{aligned} \tag{B.10}$$

Proceeding in a similar fashion, the non-dimensionalized forms of the second and third terms on the right-hand side of equation B.9 can be obtained as follows:

$$\frac{\partial\left\{\mu\left(\frac{\partial u}{\partial y}+\frac{\partial v}{\partial x}\right)\right\}}{\partial y} = \frac{\mu_\infty U_\infty}{L^2}\frac{\partial\left\{\mu^*\left(\frac{\partial u^*}{\partial y^*}+\frac{\partial v^*}{\partial x^*}\right)\right\}}{\partial y^*}, \tag{B.11}$$

$$\frac{\partial\left\{\mu\left(\frac{\partial w}{\partial x}+\frac{\partial u}{\partial z}\right)\right\}}{\partial z} = \frac{\mu_\infty U_\infty}{L^2}\frac{\partial\left\{\mu^*\left(\frac{\partial w^*}{\partial x^*}+\frac{\partial u^*}{\partial z^*}\right)\right\}}{\partial z^*}. \tag{B.12}$$

It may be noted that the left-hand side of the x-momentum equation from the system of Euler equations given by equation A.6 and that of the x-momentum equation from the system of compressible Navier-Stokes equations given by equation B.9 are exactly the same. Moreover, equations A.3 and B.7 show that the normalization strategies in both cases are identical, except that in the latter equation,

the variable μ is normalized in addition to the rest. Accordingly, after introducing normalization of the variables, the left-hand side of the non-dimensionalized form of equation B.9 is identical to equation A.7a. Therefore, the left-hand side of equation B.9 can be written using equation A.7a as

$$\frac{\partial(\rho u)}{\partial t}+\frac{\partial\left(p+\rho u^2\right)}{\partial x}+\frac{\partial(\rho uv)}{\partial y}+\frac{\partial(\rho uw)}{\partial z} = \frac{\rho_\infty U_\infty^2}{L}\left[\frac{\partial\left(\rho^* u^*\right)}{\partial t^*}+\frac{\partial\left\{p^*+\rho*\left(u^*\right)^2\right\}}{\partial x^*}+\frac{\partial\left(\rho^* u^* v^*\right)}{\partial y^*}+\frac{\partial\left(\rho^* u^* w^*\right)}{\partial z^*}\right]. \quad \text{(B.13)}$$

Substituting equations B.10-B.13 in equation B.9 one obtains

$$\frac{\rho_\infty U_\infty^2}{L}\left[\frac{\partial\left(\rho^* u^*\right)}{\partial t^*}+\frac{\partial\left\{p^*+\rho*\left(u^*\right)^2\right\}}{\partial x^*}+\frac{\partial\left(\rho^* u^* v^*\right)}{\partial y^*}+\frac{\partial\left(\rho^* u^* w^*\right)}{\partial z^*}\right] = \frac{\mu_\infty U_\infty}{L^2}\frac{\partial\left(\frac{4}{3}\mu^*\frac{\partial u^*}{\partial x^*}\right)}{\partial x^*}\frac{\mu_\infty U_\infty}{L^2}\frac{\partial\left\{\frac{2}{3}\mu^*\left(\frac{\partial v^*}{\partial y^*}+\frac{\partial w^*}{\partial z^*}\right)\right\}}{\partial x^*} + \frac{\mu_\infty U_\infty}{L^2}\frac{\partial\left\{\mu^*\left(\frac{\partial u^*}{\partial y^*}+\frac{\partial v^*}{\partial x^*}\right)\right\}}{\partial y^*}+\frac{\mu_\infty U_\infty}{L^2}\frac{\partial\left\{\mu^*\left(\frac{\partial w^*}{\partial x^*}+\frac{\partial u^*}{\partial z^*}\right)\right\}}{\partial z^*}. \quad \text{(B.14)}$$

Dividing both sides of equation B.14 by $\frac{\rho_\infty U_\infty^2}{L}$ we get

$$\frac{\partial\left(\rho^* u^*\right)}{\partial t^*}+\frac{\partial\left\{p^*+\rho*\left(u^*\right)^2\right\}}{\partial x^*}+\frac{\partial\left(\rho^* u^* v^*\right)}{\partial y^*}+\frac{\partial\left(\rho^* u^* w^*\right)}{\partial z^*} = \frac{\mu_\infty}{\rho_\infty U_\infty L}\frac{\partial\left(\frac{4}{3}\mu^*\frac{\partial u^*}{\partial x^*}\right)}{\partial x^*}-\frac{\mu_\infty}{\rho_\infty U_\infty L}\frac{\partial\left\{\frac{2}{3}\mu^*\left(\frac{\partial v^*}{\partial y^*}+\frac{\partial w^*}{\partial z^*}\right)\right\}}{\partial x^*} + \frac{\mu_\infty}{\rho_\infty U_\infty L}\frac{\partial\left\{\mu^*\left(\frac{\partial u^*}{\partial y^*}+\frac{\partial v^*}{\partial x^*}\right)\right\}}{\partial y^*}+\frac{\mu_\infty}{\rho_\infty U_\infty L}\frac{\partial\left\{\mu^*\left(\frac{\partial w^*}{\partial x^*}+\frac{\partial u^*}{\partial z^*}\right)\right\}}{\partial z^*}. \quad \text{(B.15)}$$

Equation B.15 can be recast as

$$\frac{\partial\left(\rho^* u^*\right)}{\partial t^*}+\frac{\partial\left\{p^*+\rho*\left(u^*\right)^2\right\}}{\partial x^*}+\frac{\partial\left(\rho^* u^* v^*\right)}{\partial y^*}+\frac{\partial\left(\rho^* u^* w^*\right)}{\partial z^*} = \frac{1}{\mathrm{Re}_L}\frac{\partial\left(\frac{4}{3}\mu^*\frac{\partial u^*}{\partial x^*}\right)}{\partial x^*}-\frac{1}{\mathrm{Re}_L}\frac{\partial\left\{\frac{2}{3}\mu^*\left(\frac{\partial v^*}{\partial y^*}+\frac{\partial w^*}{\partial z^*}\right)\right\}}{\partial x^*} + \frac{1}{\mathrm{Re}_L}\frac{\partial\left\{\mu^*\left(\frac{\partial u^*}{\partial y^*}+\frac{\partial v^*}{\partial x^*}\right)\right\}}{\partial y^*}+\frac{1}{\mathrm{Re}_L}\frac{\partial\left\{\mu^*\left(\frac{\partial w^*}{\partial x^*}+\frac{\partial u^*}{\partial z^*}\right)\right\}}{\partial z^*}. \quad \text{(B.16)}$$

where $\mathrm{Re}_L=\frac{\rho_\infty U_\infty L}{\mu_\infty}$ is the Reynolds number based on the free-stream flow properties and the characteristic length L. Equation B.16 can be further recast in compact non-dimensional form of the x-momentum equation as

$$\frac{\partial\left(\rho^* u^*\right)}{\partial t^*}+\frac{\partial\left\{p^*+\rho*\left(u^*\right)^2\right\}}{\partial x^*}+\frac{\partial\left(\rho^* u^* v^*\right)}{\partial y^*}+\frac{\partial\left(\rho^* u^* w^*\right)}{\partial z^*} = \frac{\partial \tau_{xx}^*}{\partial x^*}+\frac{\partial \tau_{yx}^*}{\partial y^*}+\frac{\partial \tau_{zx}^*}{\partial z^*}, \quad \text{(B.17)}$$

where

$$\tau_{xx}^*=\frac{\mu^*}{\mathrm{Re}_L}\left\{\frac{4}{3}\frac{\partial u^*}{\partial x^*}-\frac{2}{3}\left(\frac{\partial v^*}{\partial y^*}+\frac{\partial w^*}{\partial z^*}\right)\right\}, \quad \text{(B.18a)}$$

$$\tau_{yx}^*=\frac{\mu^*}{\mathrm{Re}_L}\left(\frac{\partial u^*}{\partial y^*}+\frac{\partial v^*}{\partial x^*}\right)=\tau_{xy}^*, \quad \text{(B.18b)}$$

$$\tau_{zx}^*=\frac{\mu^*}{\mathrm{Re}_L}\left(\frac{\partial w^*}{\partial x^*}+\frac{\partial u^*}{\partial z^*}\right)=\tau_{xz}^*. \quad \text{(B.18c)}$$

Proceeding in a manner similar to equations B.9-B.17, we can obtain the non-dimensionalized forms of the y- and z-momentum equations as follows:

$$\frac{\partial\left(\rho^* v^*\right)}{\partial t^*}+\frac{\partial\left(\rho^* u^* v^*\right)}{\partial x^*}+\frac{\partial\left\{p^*+\rho*\left(v^*\right)^2\right\}}{\partial y^*}+\frac{\partial\left(\rho^* v^* w^*\right)}{\partial z^*} = \frac{\partial \tau_{xy}^*}{\partial x^*}+\frac{\partial \tau_{yy}^*}{\partial y^*}+\frac{\partial \tau_{zy}^*}{\partial z^*}, \quad \text{(B.19)}$$

$$\frac{\partial\left(\rho^* w^*\right)}{\partial t^*}+\frac{\partial\left(\rho^* u^* w^*\right)}{\partial x^*}+\frac{\partial\left(\rho^* v^* w^*\right)}{\partial y^*}+\frac{\partial\left\{p^*+\rho*\left(w^*\right)^2\right\}}{\partial z^*} = \frac{\partial \tau_{xz}^*}{\partial x^*}+\frac{\partial \tau_{yz}^*}{\partial y^*}+\frac{\partial \tau_{zz}^*}{\partial z^*}, \quad \text{(B.20)}$$

where

$$\tau_{yy}^*=\frac{\mu^*}{\mathrm{Re}_L}\left\{\frac{4}{3}\frac{\partial v^*}{\partial y^*}-\frac{2}{3}\left(\frac{\partial u^*}{\partial x^*}+\frac{\partial w^*}{\partial z^*}\right)\right\}, \quad \text{(B.21a)}$$

$$\tau_{zz}^*=\frac{\mu^*}{\mathrm{Re}_L}\left\{\frac{4}{3}\frac{\partial w^*}{\partial z^*}-\frac{2}{3}\left(\frac{\partial u^*}{\partial x^*}+\frac{\partial v^*}{\partial y^*}\right)\right\}, \quad \text{(B.21b)}$$

$$\tau_{yz}^*=\frac{\mu^*}{\mathrm{Re}_L}\left(\frac{\partial v^*}{\partial z^*}+\frac{\partial w^*}{\partial y^*}\right)=\tau_{zy}^*. \quad \text{(B.21c)}$$

The energy equation is

$$\frac{\partial\left(\rho e_m\right)}{\partial t}+\frac{\partial\left\{\left(p+\rho e_m\right)u\right\}}{\partial x}+\frac{\partial\left\{\left(p+\rho e_m\right)v\right\}}{\partial y}+\frac{\partial\left\{\left(p+\rho e_m\right)w\right\}}{\partial z} = \frac{\partial\left(u\tau_{xx}+v\tau_{xy}+w\tau_{xz}+k\frac{\partial T}{\partial x}\right)}{\partial x}+\frac{\partial\left(u\tau_{yx}+v\tau_{yy}+w\tau_{yz}+k\frac{\partial T}{\partial y}\right)}{\partial y} + \frac{\partial\left(u\tau_{zx}+v\tau_{zy}+w\tau_{zz}+k\frac{\partial T}{\partial z}\right)}{\partial z}. \quad \text{(B.22)}$$

The first term on the right-hand side of equation B.22 can be expanded as follows:

$$\frac{\partial\left(u\tau_{xx}+v\tau_{xy}+w\tau_{xz}+k\frac{\partial T}{\partial x}\right)}{\partial x} = \frac{\partial\left(u\tau_{xx}\right)}{\partial x}+\frac{\partial\left(v\tau_{xy}\right)}{\partial x}+\frac{\partial\left(w\tau_{xz}\right)}{\partial x}+\frac{\partial\left(k\frac{\partial T}{\partial x}\right)}{\partial x}. \quad \text{(B.23)}$$

The first term on the right-hand side of equation B.23 can be written in non-dimensional form using the normalized variables given by equations B.7 as follows:

$$\begin{aligned}\frac{\partial\left(u\tau_{xx}\right)}{\partial x} &= \frac{\partial\left[u\left\{\frac{4}{3}\mu\frac{\partial u}{\partial x}-\frac{2}{3}\mu\left(\frac{\partial v}{\partial y}+\frac{\partial w}{\partial z}\right)\right\}\right]}{\partial x}\\ &= \frac{\partial\left[u^*U_\infty\left\{\frac{4}{3}\mu^*\mu_\infty\frac{\partial(u^*U_\infty)}{\partial(x^*L)}\right\}\right]}{\partial\left(x^*L\right)}\\ &\quad -\frac{\partial\left[u^*U_\infty\left\{\frac{2}{3}\mu^*\mu_\infty\frac{\partial(v^*U_\infty)}{\partial(y^*L)}\right\}\right]}{\partial\left(x^*L\right)}-\frac{\partial\left[u^*U_\infty\left\{\frac{2}{3}\mu^*\mu_\infty\frac{\partial(w^*U_\infty)}{\partial(z^*L)}\right\}\right]}{\partial\left(x^*L\right)}\\ &= \frac{\mu_\infty U_\infty^2}{L^2}\frac{\partial\left[u^*\mu^*\left\{\frac{4}{3}\frac{\partial u^*}{\partial x^*}-\frac{2}{3}\left(\frac{\partial v^*}{\partial y^*}+\frac{\partial w^*}{\partial z^*}\right)\right\}\right]}{\partial x^*}. \end{aligned} \quad \text{(B.24)}$$

Proceeding in a similar fashion as in equation B.24, the second and third terms on the right-hand side of equation B.23 can be written in non-dimensional form as

$$\frac{\partial\left(v\tau_{xy}\right)}{\partial x} = \frac{\mu_\infty U_\infty^2}{L^2}\frac{\partial\left\{v^*\mu^*\left(\frac{\partial u^*}{\partial y^*}+\frac{\partial v^*}{\partial x^*}\right)\right\}}{\partial x^*}, \quad \text{(B.25)}$$

$$\frac{\partial\left(w\tau_{xz}\right)}{\partial x} = \frac{\mu_\infty U_\infty^2}{L^2}\frac{\partial\left\{w^*\mu^*\left(\frac{\partial w^*}{\partial x^*}+\frac{\partial u^*}{\partial z^*}\right)\right\}}{\partial x^*}. \quad \text{(B.26)}$$

The fourth term in equation B.23 can be non-dimensionalized as

$$\begin{aligned}\frac{\partial\left(k\frac{\partial T}{\partial x}\right)}{\partial x} &= \frac{\partial\left\{\frac{\mu c_p}{\mathrm{Pr}}\frac{\partial(T^*T_\infty)}{\partial(x^*L)}\right\}}{\partial\left(x^*L\right)}\\ &= \frac{\partial\left\{\frac{\gamma\mu^*\mu_\infty \mathrm{R}}{(\gamma-1)\,\mathrm{Pr}}\frac{\partial(T^*T_\infty)}{\partial(x^*L)}\right\}}{\partial\left(x^*L\right)}\\ &= \frac{\mu_\infty\gamma \mathrm{R}T_\infty}{(\gamma-1)\,\mathrm{Pr}\,L^2}\frac{\partial\left(\mu^*\frac{\partial T^*}{\partial x^*}\right)}{\partial x^*}\\ &= \frac{\mu_\infty U_\infty^2}{(\gamma-1)\,M_\infty^2\,\mathrm{Pr}\,L^2}\frac{\partial\left(\mu^*\frac{\partial T^*}{\partial x^*}\right)}{\partial x^*}. \end{aligned} \quad \text{(B.27)}$$

Substituting equations B.24-B.27 in equation B.23 we get

$$\frac{\partial\left(u\tau_{xx}+v\tau_{xy}+w\tau_{xz}+k\frac{\partial T}{\partial x}\right)}{\partial x} = \frac{\mu_\infty U_\infty^2}{L^2}\frac{\partial\left[u^*\mu^*\left\{\frac{4}{3}\frac{\partial u^*}{\partial x^*}-\frac{2}{3}\left(\frac{\partial v^*}{\partial y^*}+\frac{\partial w^*}{\partial z^*}\right)\right\}\right]}{\partial x^*}$$

$$+\frac{\mu_\infty U_\infty^2}{L^2}\frac{\partial\left\{v^*\mu^*\left(\frac{\partial u^*}{\partial y^*}+\frac{\partial v^*}{\partial x^*}\right)\right\}}{\partial x^*}+\frac{\mu_\infty U_\infty^2}{L^2}\frac{\partial\left\{w^*\mu^*\left(\frac{\partial w^*}{\partial x^*}+\frac{\partial u^*}{\partial z^*}\right)\right\}}{\partial x^*}+\frac{\mu_\infty U_\infty^2}{(\gamma-1)M_\infty^2\,\mathrm{Pr}\,L^2}\frac{\partial\left(\mu^*\frac{\partial T^*}{\partial x^*}\right)}{\partial x^*}. \quad \text{(B.28)}$$

Proceeding in a line similar to deriving equation B.28, one obtains

$$\frac{\partial\left(u\tau_{yx}+v\tau_{yy}+w\tau_{yz}+k\frac{\partial T}{\partial y}\right)}{\partial y}=\frac{\mu_\infty U_\infty^2}{L^2}\frac{\partial\left\{u^*\mu^*\left(\frac{\partial u^*}{\partial y^*}+\frac{\partial v^*}{\partial x^*}\right)\right\}}{\partial y^*}+\frac{\mu_\infty U_\infty^2}{L^2}\frac{\partial\left[v^*\mu^*\left\{\frac{4}{3}\frac{\partial v^*}{\partial y^*}-\frac{2}{3}\left(\frac{\partial u^*}{\partial x^*}+\frac{\partial w^*}{\partial z^*}\right)\right\}\right]}{\partial y^*}+\frac{\mu_\infty U_\infty^2}{L^2}\frac{\partial\left\{w^*\mu^*\left(\frac{\partial v^*}{\partial z^*}+\frac{\partial w^*}{\partial y^*}\right)\right\}}{\partial y^*}+\frac{\mu_\infty U_\infty^2}{(\gamma-1)M_\infty^2\,\mathrm{Pr}\,L^2}\frac{\partial\left(\mu^*\frac{\partial T^*}{\partial y^*}\right)}{\partial y^*}, \quad \text{(B.29)}$$

$$\frac{\partial\left(u\tau_{zx}+v\tau_{zy}+w\tau_{zz}+k\frac{\partial T}{\partial z}\right)}{\partial z}=\frac{\mu_\infty U_\infty^2}{L^2}\frac{\partial\left\{u^*\mu^*\left(\frac{\partial u^*}{\partial z^*}+\frac{\partial w^*}{\partial x^*}\right)\right\}}{\partial z^*}+\frac{\mu_\infty U_\infty^2}{L^2}\frac{\partial\left\{v^*\mu^*\left(\frac{\partial v^*}{\partial z^*}+\frac{\partial w^*}{\partial y^*}\right)\right\}}{\partial z^*}+\frac{\mu_\infty U_\infty^2}{L^2}\frac{\partial\left[w^*\mu^*\left\{\frac{4}{3}\frac{\partial w^*}{\partial z^*}-\frac{2}{3}\left(\frac{\partial u^*}{\partial x^*}+\frac{\partial v^*}{\partial y^*}\right)\right\}\right]}{\partial z^*}+\frac{\mu_\infty U_\infty^2}{(\gamma-1)M_\infty^2\,\mathrm{Pr}\,L^2}\frac{\partial\left(\mu^*\frac{\partial T^*}{\partial z^*}\right)}{\partial z^*}. \quad \text{(B.30)}$$

Applying the normalization of variables by using equations B.7 and following the steps adopted in equation A.11 it can be shown that

$$\frac{\partial\left(\rho e_m\right)}{\partial t}+\frac{\partial\left\{\left(p+\rho e_m\right)u\right\}}{\partial x}+\frac{\partial\left\{\left(p+\rho e_m\right)v\right\}}{\partial y}+\frac{\partial\left\{\left(p+\rho e_m\right)w\right\}}{\partial z}=\frac{\rho_\infty U_\infty^3}{L}\frac{\partial\left(\rho^* e_m^*\right)}{\partial t^*}+\frac{\rho_\infty U_\infty^3}{L}\frac{\partial\left\{\left(p^*+\rho^* e_m^*\right)u^*\right\}}{\partial x^*}+\frac{\rho_\infty U_\infty^3}{L}\frac{\partial\left\{\left(p^*+\rho^* e_m^*\right)v^*\right\}}{\partial y^*}+\frac{\rho_\infty U_\infty^3}{L}\frac{\partial\left\{\left(p^*+\rho^* e_m^*\right)w^*\right\}}{\partial z^*}. \quad \text{(B.31)}$$

Applying equations B.28-B.31 in equation B.22 we obtain

$$\begin{aligned}
&\frac{\rho_\infty U_\infty^3}{L}\frac{\partial\left(\rho^* e_m^*\right)}{\partial t^*}+\frac{\rho_\infty U_\infty^3}{L}\frac{\partial\left\{\left(p^*+\rho^* e_m^*\right)u^*\right\}}{\partial x^*}\\
&\quad+\frac{\rho_\infty U_\infty^3}{L}\frac{\partial\left\{\left(p^*+\rho^* e_m^*\right)v^*\right\}}{\partial y^*}+\frac{\rho_\infty U_\infty^3}{L}\frac{\partial\left\{\left(p^*+\rho^* e_m^*\right)w^*\right\}}{\partial z^*}\\
&\quad=\frac{\mu_\infty U_\infty^2}{L^2}\frac{\partial\left[u^*\mu^*\left\{\frac{4}{3}\frac{\partial u^*}{\partial x^*}-\frac{2}{3}\left(\frac{\partial v^*}{\partial y^*}+\frac{\partial w^*}{\partial z^*}\right)\right\}\right]}{\partial x^*}\\
&\qquad+\frac{\mu_\infty U_\infty^2}{L^2}\frac{\partial\left\{v^*\mu^*\left(\frac{\partial u^*}{\partial y^*}+\frac{\partial v^*}{\partial x^*}\right)\right\}}{\partial x^*}\\
&\qquad+\frac{\mu_\infty U_\infty^2}{L^2}\frac{\partial\left\{w^*\mu^*\left(\frac{\partial w^*}{\partial x^*}+\frac{\partial u^*}{\partial z^*}\right)\right\}}{\partial x^*}\\
&\qquad+\frac{\mu_\infty U_\infty^2}{\left(\gamma-1\right)M_\infty^2\,\mathrm{Pr}\,L^2}\frac{\partial\left(\mu^*\frac{\partial T^*}{\partial x^*}\right)}{\partial x^*}\\
&\qquad+\frac{\mu_\infty U_\infty^2}{L^2}\frac{\partial\left\{u^*\mu^*\left(\frac{\partial u^*}{\partial y^*}+\frac{\partial v^*}{\partial x^*}\right)\right\}}{\partial y^*}\\
&\quad+\frac{\mu_\infty U_\infty^2}{L^2}\frac{\partial\left[v^*\mu^*\left\{\frac{4}{3}\frac{\partial v^*}{\partial y^*}-\frac{2}{3}\left(\frac{\partial u^*}{\partial x^*}+\frac{\partial w^*}{\partial z^*}\right)\right\}\right]}{\partial y^*}\\
&\qquad+\frac{\mu_\infty U_\infty^2}{L^2}\frac{\partial\left\{w^*\mu^*\left(\frac{\partial v^*}{\partial z^*}+\frac{\partial w^*}{\partial y^*}\right)\right\}}{\partial y^*}\\
&\qquad+\frac{\mu_\infty U_\infty^2}{\left(\gamma-1\right)M_\infty^2\,\mathrm{Pr}\,L^2}\frac{\partial\left(\mu^*\frac{\partial T^*}{\partial y^*}\right)}{\partial y^*}\\
&\qquad+\frac{\mu_\infty U_\infty^2}{L^2}\frac{\partial\left\{u^*\mu^*\left(\frac{\partial u^*}{\partial z^*}+\frac{\partial w^*}{\partial x^*}\right)\right\}}{\partial z^*}\\
&\qquad+\frac{\mu_\infty U_\infty^2}{L^2}\frac{\partial\left\{v^*\mu^*\left(\frac{\partial v^*}{\partial z^*}+\frac{\partial w^*}{\partial y^*}\right)\right\}}{\partial z^*}\\
&\quad+\frac{\mu_\infty U_\infty^2}{L^2}\frac{\partial\left[w^*\mu^*\left\{\frac{4}{3}\frac{\partial w^*}{\partial z^*}-\frac{2}{3}\left(\frac{\partial u^*}{\partial x^*}+\frac{\partial v^*}{\partial y^*}\right)\right\}\right]}{\partial z^*}\\
&\qquad+\frac{\mu_\infty U_\infty^2}{\left(\gamma-1\right)M_\infty^2\,\mathrm{Pr}\,L^2}\frac{\partial\left(\mu^*\frac{\partial T^*}{\partial z^*}\right)}{\partial z^*}. \qquad \text{(B.32)}
\end{aligned}$$

Dividing both sides of equation B.32 with $\frac{\rho_\infty U_\infty^3}{L}$ we get

$$\begin{aligned}
&\frac{\partial\left(\rho^* e_m^*\right)}{\partial t^*}+\frac{\partial\left\{\left(p^*+\rho^* e_m^*\right)u^*\right\}}{\partial x^*}+\frac{\partial\left\{\left(p^*+\rho^* e_m^*\right)v^*\right\}}{\partial y^*}+\frac{\partial\left\{\left(p^*+\rho^* e_m^*\right)w^*\right\}}{\partial z^*}\\
&\quad=\frac{\mu_\infty}{\rho_\infty U_\infty L}\frac{\partial\left[u^*\mu^*\left\{\frac{4}{3}\frac{\partial u^*}{\partial x^*}-\frac{2}{3}\left(\frac{\partial v^*}{\partial y^*}+\frac{\partial w^*}{\partial z^*}\right)\right\}\right]}{\partial x^*}\\
&\qquad+\frac{\mu_\infty}{\rho_\infty U_\infty L}\frac{\partial\left\{v^*\mu^*\left(\frac{\partial u^*}{\partial y^*}+\frac{\partial v^*}{\partial x^*}\right)\right\}}{\partial x^*}
\end{aligned}$$

$$
\begin{aligned}
&+\frac{\mu_\infty}{\rho_\infty U_\infty L}\frac{\partial\left\{w^*\mu^*\left(\frac{\partial w^*}{\partial x^*}+\frac{\partial u^*}{\partial z^*}\right)\right\}}{\partial x^*}\\
&+\frac{\mu_\infty}{(\gamma-1)\,\rho_\infty U_\infty L M_\infty^2\,\mathrm{Pr}}\frac{\partial\left(\mu^*\frac{\partial T^*}{\partial x^*}\right)}{\partial x^*}\\
&+\frac{\mu_\infty}{\rho_\infty U_\infty L}\frac{\partial\left\{u^*\mu^*\left(\frac{\partial u^*}{\partial y^*}+\frac{\partial v^*}{\partial x^*}\right)\right\}}{\partial y^*}\\
&+\frac{\mu_\infty}{\rho_\infty U_\infty L}\frac{\partial\left[v^*\mu^*\left\{\frac{4}{3}\frac{\partial v^*}{\partial y^*}-\frac{2}{3}\left(\frac{\partial u^*}{\partial x^*}+\frac{\partial w^*}{\partial z^*}\right)\right\}\right]}{\partial y^*}\\
&+\frac{\mu_\infty}{\rho_\infty U_\infty L}\frac{\partial\left\{w^*\mu^*\left(\frac{\partial v^*}{\partial z^*}+\frac{\partial w^*}{\partial y^*}\right)\right\}}{\partial y^*}\\
&+\frac{\mu_\infty}{(\gamma-1)\,\rho_\infty U_\infty L M_\infty^2\,\mathrm{Pr}}\frac{\partial\left(\mu^*\frac{\partial T^*}{\partial y^*}\right)}{\partial y^*}\\
&+\frac{\mu_\infty}{\rho_\infty U_\infty L}\frac{\partial\left\{u^*\mu^*\left(\frac{\partial u^*}{\partial z^*}+\frac{\partial w^*}{\partial x^*}\right)\right\}}{\partial z^*}\\
&+\frac{\mu_\infty}{\rho_\infty U_\infty L}\frac{\partial\left\{v^*\mu^*\left(\frac{\partial v^*}{\partial z^*}+\frac{\partial w^*}{\partial y^*}\right)\right\}}{\partial z^*}\\
&+\frac{\mu_\infty}{\rho_\infty U_\infty L}\frac{\partial\left[w^*\mu^*\left\{\frac{4}{3}\frac{\partial w^*}{\partial z^*}-\frac{2}{3}\left(\frac{\partial u^*}{\partial x^*}+\frac{\partial v^*}{\partial y^*}\right)\right\}\right]}{\partial z^*}\\
&+\frac{\mu_\infty}{(\gamma-1)\,\rho_\infty U_\infty L M_\infty^2\,\mathrm{Pr}}\frac{\partial\left(\mu^*\frac{\partial T^*}{\partial z^*}\right)}{\partial z^*}. \qquad \text{(B.33)}
\end{aligned}
$$

Equation B.33 can be written in a compact non-dimensional form of the energy equation:

$$
\begin{aligned}
&\frac{\partial\left(\rho^* e_m^*\right)}{\partial t^*}+\frac{\partial\left\{\left(p^*+\rho^* e_m^*\right)u^*\right\}}{\partial x^*}+\frac{\partial\left\{\left(p^*+\rho^* e_m^*\right)v^*\right\}}{\partial y^*}+\frac{\partial\left\{\left(p^*+\rho^* e_m^*\right)w^*\right\}}{\partial z^*}\\
&=\frac{\partial\left(u^*\tau_{xx}^*+v^*\tau_{xy}^*+w^*\tau_{xz}^*-q_x^*\right)}{\partial x^*}\\
&+\frac{\partial\left(u^*\tau_{yx}^*+v^*\tau_{yy}^*+w^*\tau_{yz}^*-q_y^*\right)}{\partial y^*}\\
&+\frac{\partial\left(u^*\tau_{zx}^*+v^*\tau_{zy}^*+w^*\tau_{zz}^*-q_z^*\right)}{\partial z^*}, \qquad \text{(B.34)}
\end{aligned}
$$

where

$$q_x^*=-\frac{\mu^*}{(\gamma-1)\,\mathrm{Re}_L M_\infty^2\,\mathrm{Pr}}\frac{\partial T^*}{\partial x^*}, \qquad \text{(B.35)}$$

$$q_y^*=-\frac{\mu^*}{(\gamma-1)\,\mathrm{Re}_L M_\infty^2\,\mathrm{Pr}}\frac{\partial T^*}{\partial y^*}, \qquad \text{(B.36)}$$

$$q_z^*=-\frac{\mu^*}{(\gamma-1)\,\mathrm{Re}_L M_\infty^2\,\mathrm{Pr}}\frac{\partial T^*}{\partial z^*}. \qquad \text{(B.37)}$$

Combining equations B.8, B.17, B.19, B.20, and B.34 and dropping the superscript '*' for ease of representation, the non-dimensionalized form of the 3D Compressible Navier-Stokes equations are obtained in the form given by equation 2.3.

Appendix C

Analytical aspects of the one-dimensional Euler equations of gas dynamics

The 1D Euler equations of gas dynamics in conservative form are given by

$$\frac{\partial \mathbf{U}}{\partial t} + \frac{\partial \mathbf{F}}{\partial x} = 0, \tag{C.1}$$

where

$$\mathbf{U} = \begin{bmatrix} \rho \\ \rho u \\ \rho e_m \end{bmatrix}, \tag{C.2a}$$

$$\begin{aligned} \mathbf{F} &= \begin{bmatrix} \rho u \\ p + \rho u^2 \\ (p + \rho e_m) u \end{bmatrix} \\ &= \begin{bmatrix} \rho u \\ p + \rho u^2 \\ \rho u h_0 \end{bmatrix}. \end{aligned} \tag{C.2b}$$

In equation C.2b, e_m is the total energy of the fluid per unit mass and h_0 is the specific stagnation enthalpy that are obtained as follows:

$$\begin{aligned} e_m &= c_v T + \frac{1}{2} u^2 \\ &= \frac{p}{(\gamma - 1)\,\rho} + \frac{1}{2} u^2, \end{aligned} \tag{C.3a}$$

$$\begin{aligned} h_0 &= h + \frac{1}{2}u^2 \\ &= \frac{\gamma p}{(\gamma-1)\,\rho} + \frac{1}{2}u^2. \end{aligned} \tag{C.3b}$$

Using chain rule equation C.1 can be recast as

$$\begin{aligned} \frac{\partial \mathbf{U}}{\partial t} + \frac{\mathrm{d}\mathbf{F}}{\mathrm{d}\mathbf{U}}\frac{\partial \mathbf{U}}{\partial x} &= 0 \\ \frac{\partial \mathbf{U}}{\partial t} + \mathbf{A}\frac{\partial \mathbf{U}}{\partial x} &= 0, \end{aligned} \tag{C.4}$$

where $\mathbf{A} = \frac{\mathrm{d}\mathbf{F}}{\mathrm{d}\mathbf{U}}$ is the flux Jacobian. It can be demonstrated that the Euler fluxes exhibit what is known as the homogeneity property. The vector of conserved variables $\mathbf{U}$ and the flux vector $\mathbf{F}$ can be written as follows:

$$\begin{aligned} \mathbf{U} &= \begin{bmatrix} U_1 \\ U_2 \\ U_3 \end{bmatrix} \\ &= \begin{bmatrix} \rho \\ \rho u \\ \rho e_m \end{bmatrix}, \end{aligned} \tag{C.5}$$

$$\begin{aligned} \mathbf{F} = \begin{bmatrix} F_1 \\ F_2 \\ F_3 \end{bmatrix} &= \begin{bmatrix} \rho u \\ p + \rho u^2 \\ (p + \rho e_m)\, u \end{bmatrix} \\ &= \begin{bmatrix} U_2 \\ (\gamma-1)\left(U_3 - \frac{U_2^2}{2U_1}\right) + \frac{U_2^2}{U_1} \\ (\gamma-1)\left(U_3 - \frac{U_2^2}{2U_1}\right)\frac{U_2}{U_1} + \frac{U_2 U_3}{U_1} \end{bmatrix} = \begin{bmatrix} U_2 \\ (\gamma-1)\,U_3 + \left(\frac{3-\gamma}{2}\right)\frac{U_2^2}{U_1} \\ \gamma\frac{U_2 U_3}{U_1} - \left(\frac{\gamma-1}{2}\right)\frac{U_2^3}{U_1^2} \end{bmatrix}. \end{aligned} \tag{C.6}$$

The flux Jacobian $\mathbf{A}$ can be expressed in terms of the conserved variables as follows:

$$\begin{aligned} \mathbf{A} = \mathbf{A}(\mathbf{U}) &= \frac{\partial(F_1, F_2, F_3)}{\partial(U_1, U_2, U_3)} \\ &= \begin{bmatrix} \frac{\partial F_1}{\partial U_1} & \frac{\partial F_1}{\partial U_2} & \frac{\partial F_1}{\partial U_3} \\ \frac{\partial F_2}{\partial U_1} & \frac{\partial F_2}{\partial U_2} & \frac{\partial F_2}{\partial U_3} \\ \frac{\partial F_3}{\partial U_1} & \frac{\partial F_3}{\partial U_2} & \frac{\partial F_3}{\partial U_3} \end{bmatrix} = \begin{bmatrix} 0 & 1 & 0 \\ \frac{\gamma-3}{2}\frac{U_2^2}{U_1^2} & (3-\gamma)\frac{U_2}{U_1} & \gamma-1 \\ -\frac{\gamma U_2 U_3}{U_1^2} + (\gamma-1)\frac{U_2^3}{U_1^3} & \frac{\gamma U_3}{U_1} - \frac{3(\gamma-1)}{2}\frac{U_2^2}{U_1^2} & \frac{\gamma U_2}{U_1} \end{bmatrix}. \end{aligned} \tag{C.7}$$

We know that $\mathbf{F}$ is a nonlinear function of $\mathbf{U}$, i.e., $\mathbf{F} = \mathbf{F}(\mathbf{U})$ and $\frac{\partial \mathbf{F}}{\partial x} = \frac{\mathrm{d}\mathbf{F}}{\mathrm{d}\mathbf{U}}\frac{\partial \mathbf{U}}{\partial x} = \mathbf{A}\frac{\partial \mathbf{U}}{\partial x}$. Using equations C.2a, C.2b and C.7 it can be shown that, $\mathbf{F} = \mathbf{A}\mathbf{U}$.

This is known as the homogeneity property. It can further be shown that the unsteady Euler equations are hyperbolic. If $\mathbf{A}$ has all real eigenvalues with distinct eigenvectors, then (1D) Euler equations are hyperbolic [2]. As seen from equation C.7, matrix $\mathbf{A}$ is somewhat unwieldy and the process of finding the eigenvalues is tedious. From the nonconservative form of the Euler equations we will generate another matrix $\widetilde{\mathbf{A}}$ that is easier to handle and has the same eigenvalues as $\mathbf{A}$. Thus for finding the eigenvalues of $\mathbf{A}$ one can conveniently use the matrix $\widetilde{\mathbf{A}}$.

Expressing e_m in terms of the primitive variables using equation C.3a, the conservative form of the 1D Euler equations can also be written as

$$\frac{\partial}{\partial t}\begin{bmatrix} \rho \\ \rho u \\ \frac{p}{\gamma-1}+\frac{1}{2}\rho u^2 \end{bmatrix} + \frac{\partial}{\partial x}\begin{bmatrix} \rho u \\ p+\rho u^2 \\ \frac{\gamma p u}{\gamma-1}+\frac{1}{2}\rho u^3 \end{bmatrix} = 0. \tag{C.8}$$

Carrying out the differentiation and rearranging we obtain the following nonconservative form:

$$\frac{\partial \rho}{\partial t} + u\frac{\partial \rho}{\partial x} + \rho\frac{\partial u}{\partial x} = 0, \tag{C.9a}$$

$$\frac{\partial u}{\partial t} + u\frac{\partial u}{\partial x} + \frac{1}{\rho}\frac{\partial p}{\partial x} = 0, \tag{C.9b}$$

$$\frac{\partial p}{\partial t} + u\frac{\partial p}{\partial x} + \gamma p\frac{\partial u}{\partial x} = 0. \tag{C.9c}$$

Equations C.9a-C.9c can be written in terms of the following primitive variable vector:

$$\mathbf{V} = \begin{bmatrix} \rho \\ u \\ p \end{bmatrix}. \tag{C.10}$$

The Euler equations can now be written in terms of $\mathbf{V}$ as follows:

$$\frac{\partial}{\partial t}\begin{bmatrix} \rho \\ u \\ p \end{bmatrix} + \begin{bmatrix} u & \rho & 0 \\ 0 & u & \frac{1}{\rho} \\ 0 & \gamma p & u \end{bmatrix}\frac{\partial}{\partial x}\begin{bmatrix} \rho \\ u \\ p \end{bmatrix} = 0$$

$$\frac{\partial \mathbf{V}}{\partial t} + \widetilde{\mathbf{A}}\frac{\partial \mathbf{V}}{\partial x} = 0, \tag{C.11}$$

where

$$\widetilde{\mathbf{A}} = \begin{bmatrix} u & \rho & 0 \\ 0 & u & \frac{1}{\rho} \\ 0 & \gamma p & u \end{bmatrix}. \tag{C.12}$$

It can be shown that matrix $\mathbf{A}$ can be expressed as $\mathbf{A} = \mathbf{N}\widetilde{\mathbf{A}}\mathbf{N}^{-1}$ (similarity transformation) so that both the matrices have the same set of eigenvalues.

$$\begin{aligned}
\mathbf{U} &= \begin{bmatrix} \rho \\ \rho u \\ \frac{p}{\gamma-1} + \frac{1}{2}\rho u^2 \end{bmatrix} \\
\mathrm{d}\mathbf{U} &= \mathrm{d}\begin{bmatrix} \rho \\ \rho u \\ \frac{p}{\gamma-1} + \frac{1}{2}\rho u^2 \end{bmatrix} \\
&= \begin{bmatrix} \mathrm{d}\rho \\ \rho \mathrm{d}u + u\mathrm{d}\rho \\ \frac{\mathrm{d}p}{\gamma-1} + \rho u \mathrm{d}u + \frac{1}{2}u^2\mathrm{d}\rho \end{bmatrix} \\
&= \begin{bmatrix} 1 & 0 & 0 \\ u & \rho & 0 \\ \frac{1}{2}u^2 & \rho u & \frac{1}{\gamma-1} \end{bmatrix} \begin{bmatrix} \mathrm{d}\rho \\ \mathrm{d}u \\ \mathrm{d}p \end{bmatrix}. \qquad \text{(C.13)}
\end{aligned}$$

Equation C.13 shows that

$$\mathrm{d}\mathbf{U} = \mathbf{N}\mathrm{d}\mathbf{V}, \qquad \text{(C.14a)}$$

$$\frac{\partial \mathbf{U}}{\partial t} = \mathbf{N}\frac{\partial \mathbf{V}}{\partial t}, \qquad \text{(C.14b)}$$

$$\frac{\partial \mathbf{U}}{\partial x} = \mathbf{N}\frac{\partial \mathbf{V}}{\partial x}. \qquad \text{(C.14c)}$$

Premultiplying equation C.11 by $\mathbf{N}$ one obtains

$$\begin{aligned}
\mathbf{N}\frac{\partial \mathbf{V}}{\partial t} + \mathbf{N}\widetilde{\mathbf{A}}\frac{\partial \mathbf{V}}{\partial x} &= 0 \\
\mathbf{N}\frac{\partial \mathbf{V}}{\partial t} + \mathbf{N}\widetilde{\mathbf{A}}\mathbf{N}^{-1}\left(\mathbf{N}\frac{\partial \mathbf{V}}{\partial x}\right) &= 0 \\
\frac{\partial \mathbf{U}}{\partial t} + \mathbf{N}\widetilde{\mathbf{A}}\mathbf{N}^{-1}\frac{\partial \mathbf{U}}{\partial x} &= 0. \qquad \text{(C.15)}
\end{aligned}$$

Comparing equation C.15 with equation C.4 we get that the flux Jacobian $\mathbf{A} = \mathbf{N}\widetilde{\mathbf{A}}\mathbf{N}^{-1}$ (similarity transformation) and hence $\lambda(\mathbf{A}) = \lambda\left(\widetilde{\mathbf{A}}\right)$. This can be proved as follows:

Let λ be an eigenvalue of $\widetilde{\mathbf{A}}$ so that

$$\widetilde{\mathbf{A}}\mathbf{x} = \lambda\mathbf{x}$$

$$\mathbf{N}\widetilde{\mathbf{A}}\mathbf{x} = \lambda\mathbf{N}\mathbf{x}. \tag{C.16}$$

Let $\mathbf{x} = \mathbf{N}^{-1}\mathbf{y}$. Then substituting $\mathbf{x} = \mathbf{N}^{-1}\mathbf{y}$ in equation C.16 we get

$$\mathbf{N}\widetilde{\mathbf{A}}\mathbf{N}^{-1}\mathbf{y} = \lambda\mathbf{N}\mathbf{N}^{-1}\mathbf{y}$$

$$\mathbf{A}\mathbf{y} = \lambda\mathbf{y}. \tag{C.17}$$

Equation C.17 shows that λ is also an eigenvalue of $\mathbf{A}$ and the corresponding eigenvector is $\mathbf{y} = \mathbf{N}\mathbf{x}$ (as $\mathbf{x} = \mathbf{N}^{-1}\mathbf{y}$). Now we see that in order to find the eigenvalues of $\mathbf{A}$ it is possible to use $\widetilde{\mathbf{A}}$ instead. The characteristic equation for $\widetilde{\mathbf{A}}$ is

$$\begin{aligned}
\left|\widetilde{\mathbf{A}} - \lambda\mathbf{I}\right| &= 0 \\
\begin{bmatrix} u-\lambda & \rho & 0 \\ 0 & u-\lambda & \frac{1}{\rho} \\ 0 & \gamma p & u-\lambda \end{bmatrix} &= 0 \\
(u-\lambda)\left[(u-\lambda)^2 - \frac{\gamma p}{\rho}\right] &= 0 \\
(u-\lambda)\left[(u-\lambda)^2 - a^2\right] &= 0 \\
\lambda &= u, u \pm a.
\end{aligned} \tag{C.18}$$

We see that matrix $\widetilde{\mathbf{A}}$, and hence $\mathbf{A}$, has real and distinct eigenvalues and hence the eigenvectors must also be distinct. Thus the system of equations $\frac{\partial \mathbf{U}}{\partial t} + \frac{\partial \mathbf{F}}{\partial x} = \frac{\partial \mathbf{U}}{\partial t} + \mathbf{A}\frac{\partial \mathbf{U}}{\partial x} = 0$, i.e., the 1D unsteady Euler equations are hyperbolic. It may be noted that the unsteady Euler equations are hyperbolic even in higher dimensions. Steady Euler equations are, however, elliptic for subsonic flows, parabolic for sonic flow and hyperbolic for supersonic flows. For transonic flows generally it is not possible to know the boundaries across which the mathematical character of the equations changes and compatible boundary conditions are difficult to formulate. Thus unsteady Euler equations are frequently used even to compute steady flows as the mathematical character of the unsteady equations remain hyperbolic all over the domain. We know that hyperbolic PDEs admit wavelike solutions. Let us now demonstrate the wavelike nature of the unsteady 1D Euler equations. We start with $\lambda(\mathbf{A}) = u, u \pm a$. If $\mathbf{r}_i$ $(i = 1, 2, 3)$ is a right eigenvector of $\mathbf{A}$ then

$$\mathbf{A}\mathbf{r}_i = \lambda_i\mathbf{r}_i \quad [\mathbf{r}_i \text{ is a three-component column vector }]. \tag{C.19}$$

If $\mathbf{l}_i$ $(i = 1, 2, 3)$ is a left eigenvector of $\mathbf{A}$ then

$$\mathbf{l}_i\mathbf{A} = \lambda_i\mathbf{l}_i \quad [\mathbf{l}_i \text{ is a three-component row vector }]\,. \tag{C.20}$$

Matrix of right eigenvectors of $\mathbf{A}$ is given by

$$\mathbf{R} = [\mathbf{r}_1 \;\; \mathbf{r}_2 \;\; \mathbf{r}_3]_{3\times 3}\,. \tag{C.21}$$

Matrix of left eigenvectors of $\mathbf{A}$ is given by

$$\mathbf{L} = \begin{bmatrix} \mathbf{l}_1 \\ \mathbf{l}_2 \\ \mathbf{l}_3 \end{bmatrix}_{3\times 3}\,. \tag{C.22}$$

$\mathbf{A}$ can be expressed in Jordan canonical form as

$$\mathbf{A} = \mathbf{R}\mathbf{\Lambda}\mathbf{L} = \mathbf{R}\mathbf{\Lambda}\mathbf{R}^{-1} = \mathbf{L}^{-1}\mathbf{\Lambda}\mathbf{L}, \tag{C.23}$$

where $\mathbf{\Lambda}$ is a diagonal matrix whose entries are the eigenvalues of $\mathbf{A}$. Thus

$$\mathbf{\Lambda} = \begin{bmatrix} \lambda_1 & 0 & 0 \\ 0 & \lambda_2 & 0 \\ 0 & 0 & \lambda_3 \end{bmatrix}. \tag{C.24}$$

For $\lambda_1 = u - a$, $\lambda_2 = u$ and $\lambda_3 = u + a$ it can be shown that

$$\mathbf{r}_1 = \begin{bmatrix} 1 \\ u - a \\ h_0 - ua \end{bmatrix}, \quad \mathbf{r}_2 = \begin{bmatrix} 1 \\ u \\ u^2/2 \end{bmatrix}, \quad \mathbf{r}_3 = \begin{bmatrix} 1 \\ u + a \\ h_0 + ua \end{bmatrix}. \tag{C.25}$$

Applying equation C.23 in the quasi-linear form of the Euler equations given by equation C.4 we get

$$\begin{aligned} \frac{\partial \mathbf{U}}{\partial t} + \mathbf{R}\mathbf{\Lambda}\mathbf{R}^{-1}\frac{\partial \mathbf{U}}{\partial x} &= 0 \\ \mathbf{R}^{-1}\frac{\partial \mathbf{U}}{\partial t} + \mathbf{\Lambda}\mathbf{R}^{-1}\frac{\partial \mathbf{U}}{\partial x} &= 0. \end{aligned} \tag{C.26}$$

If we freeze the Jacobian locally, then equation C.26 can be recast as

$$\begin{aligned} \frac{\partial\left(\mathbf{R}^{-1}\mathbf{U}\right)}{\partial t} + \mathbf{\Lambda}\frac{\partial\left(\mathbf{R}^{-1}\mathbf{U}\right)}{\partial x} &= 0 \\ \frac{\partial \widehat{\mathbf{U}}}{\partial t} + \mathbf{\Lambda}\frac{\partial \widehat{\mathbf{U}}}{\partial x} &= 0. \end{aligned} \tag{C.27}$$

If we write $\widehat{\mathbf{U}} = \left[\widehat{U}_1 \ \widehat{U}_2 \ \widehat{U}_3\right]$, then equation C.27 can be written in expanded form as

$$\frac{\partial}{\partial t}\begin{bmatrix}\widehat{U}_1\\ \widehat{U}_2\\ \widehat{U}_3\end{bmatrix} + \begin{bmatrix}\lambda_1 & 0 & 0\\ 0 & \lambda_2 & 0\\ 0 & 0 & \lambda_3\end{bmatrix}\frac{\partial}{\partial t}\begin{bmatrix}\widehat{U}_1\\ \widehat{U}_2\\ \widehat{U}_3\end{bmatrix} = 0. \tag{C.28}$$

Equation C.28 represents three (decoupled) wave equations:

$$\frac{\partial \widehat{U}_i}{\partial t} + \lambda_i \frac{\partial \widehat{U}_i}{\partial t} = 0, \quad i = 1, 2, 3. \tag{C.29}$$

Thus the eigenvalues λ_i of the Jacobian $\mathbf{A}$ correspond to the wave speeds. In other words $\widehat{U}_i$ is an invariant along $\frac{\mathrm{d}x}{\mathrm{d}t} = \lambda_i$ and is known as Riemann invariant. It can be shown that for $\lambda_1 = u - a$, $\lambda_2 = u$ and $\lambda_3 = u + a$ we can write the Riemann invariants as $\widehat{U}_1 = \frac{2a}{\gamma - 1} - u$, $\widehat{U}_2 = \frac{p}{\rho^\gamma}$ and $\widehat{U}_3 = \frac{2a}{\gamma - 1} + u$.

Appendix D

Finite Volume Method for two-dimensional compressible Navier-Stokes equations

Let us consider the 2D compressible Navier-Stokes equations:

$$\frac{\partial \mathbf{U}}{\partial t} + \frac{\partial \mathbf{F}_{\mathrm{I}}}{\partial x} + \frac{\partial \mathbf{G}_{\mathrm{I}}}{\partial y} = \frac{\partial \mathbf{F}_{\mathrm{v}}}{\partial x} + \frac{\partial \mathbf{G}_{\mathrm{v}}}{\partial y}, \tag{D.1}$$

where $\mathbf{U}$ is the vector of conserved variables, $\mathbf{F}_{\mathrm{I}}$ and $\mathbf{G}_{\mathrm{I}}$ are the inviscid flux vectors, and $\mathbf{F}_{\mathrm{v}}$ and $\mathbf{G}_{\mathrm{v}}$ are the viscous flux vectors that are given by

$$\mathbf{U} = \begin{bmatrix} \rho \\ \rho u \\ \rho v \\ \rho e_m \end{bmatrix}, \tag{D.2a}$$

$$\mathbf{F}_{\mathrm{I}} = \begin{bmatrix} \rho u \\ p + \rho u^2 \\ \rho u v \\ (p + \rho e_m) u \end{bmatrix}, \tag{D.2b}$$

$$\mathbf{G}_{\mathrm{I}} = \begin{bmatrix} \rho v \\ \rho u v \\ p + \rho v^2 \\ (p + \rho e_m) v \end{bmatrix}, \tag{D.2c}$$

$$\mathbf{F}_{\mathrm{v}} = \begin{bmatrix} 0 \\ \tau_{xx} \\ \tau_{xy} \\ u\tau_{xx} + v\tau_{xy} - q_x \end{bmatrix}, \tag{D.2d}$$

$$\mathbf{G}_{\mathrm{v}} = \begin{bmatrix} 0 \\ \tau_{yx} \\ \tau_{yy} \\ u\tau_{yx} + v\tau_{yy} - q_y \end{bmatrix}. \tag{D.2e}$$

Assuming Stokes' hypothesis for a Newtonian fluid the stress and heat-flux terms in the visous-flux vectors can be expressed by

$$\tau_{xx} = \frac{4}{3}\mu\frac{\partial u}{\partial x} - \frac{2}{3}\mu\frac{\partial v}{\partial y}, \tag{D.3a}$$

$$\tau_{yy} = \frac{4}{3}\mu\frac{\partial v}{\partial y} - \frac{2}{3}\mu\frac{\partial u}{\partial x}, \tag{D.3b}$$

$$\tau_{xy} = \mu\left(\frac{\partial u}{\partial y} + \frac{\partial v}{\partial x}\right) = \tau_{yx}, \tag{D.3c}$$

$$q_x = -k\frac{\partial T}{\partial x}, \tag{D.3d}$$

$$q_y = -k\frac{\partial T}{\partial y}, \tag{D.3e}$$

where μ is the coefficient of dynamic viscosity and k is the thermal conductivity of the fluid that are calculated using equations B.5 and B.6, respectively.

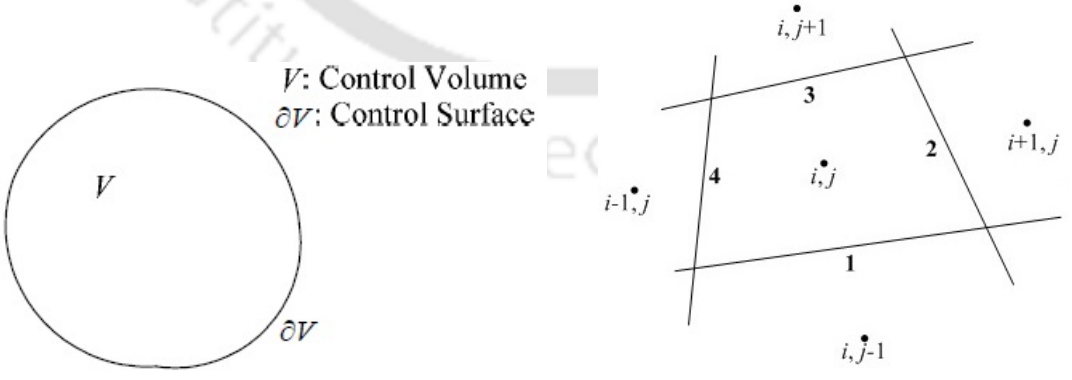

(a) (b)

Fig. D.1. (a) An arbitrary control volume and its control surface and (b) A rectangular finite volume.

Integrating equation D.1 over an arbitrary finite volume with volume V_{ij} and cell-centre i, j (see figure D.1(b)) one obtains

$$\int_{V_{i,j}} \frac{\partial \mathbf{U}}{\partial t} \mathrm{d}x\mathrm{d}y + \int_{V_{i,j}} \left(\frac{\partial \mathbf{F}_\mathrm{I}}{\partial x} + \frac{\partial \mathbf{G}_\mathrm{I}}{\partial y} \right) \mathrm{d}x\mathrm{d}y = \int_{V_{i,j}} \left(\frac{\partial \mathbf{F}_\mathrm{v}}{\partial x} + \frac{\partial \mathbf{G}_\mathrm{v}}{\partial y} \right) \mathrm{d}x\mathrm{d}y. \quad \text{(D.4)}$$

Let $\underline{\mathbf{Q}_\mathrm{I}} = \mathbf{i}_x\mathbf{F}_\mathrm{I} + \mathbf{i}_y\mathbf{G}_\mathrm{I}$, so that $\mathrm{div}\underline{\mathbf{Q}_\mathrm{I}} = \underline{\nabla}.\underline{\mathbf{Q}_\mathrm{I}} = \frac{\partial \mathbf{F}_\mathrm{I}}{\partial x} + \frac{\partial \mathbf{F}_\mathrm{I}}{\partial y}$. Also let $\underline{\mathbf{Q}_\mathrm{v}} = \mathbf{i}_x\mathbf{F}_\mathrm{v} + \mathbf{i}_y\mathbf{G}_\mathrm{v}$, so that $\mathrm{div}\underline{\mathbf{Q}_\mathrm{v}} = \underline{\nabla}.\underline{\mathbf{Q}_\mathrm{v}} = \frac{\partial \mathbf{F}_\mathrm{v}}{\partial x} + \frac{\partial \mathbf{F}_\mathrm{v}}{\partial y}$. Gauss-divergence theorem applied to equation D.4 yields

$$\int_{V_{i,j}} \frac{\partial \mathbf{U}}{\partial t} \mathrm{d}x\mathrm{d}y + \int_{\partial V_{i,j}} \underline{\mathbf{Q}_\mathrm{I}}.\mathbf{n}\mathrm{d}S = \int_{\partial V_{i,j}} \underline{\mathbf{Q}_\mathrm{v}}.\mathbf{n}\mathrm{d}S. \quad \text{(D.5)}$$

If $\mathbf{U}$ is constant within a cell with value $\overline{\mathbf{U}}$ which can be thought of as the cell average

$$\overline{\mathbf{U}} = \frac{\int \mathbf{U}\mathrm{d}x\mathrm{d}y}{\mathrm{d}x\mathrm{d}y}. \quad \text{(D.6)}$$

The first integral on the left-hand side of equation D.5 can be written using equation D.6 as

$$\int_{V_{i,j}} \frac{\partial \mathbf{U}}{\partial t} \mathrm{d}x\mathrm{d}y = V_{i,j} \frac{\mathrm{d}\overline{\mathbf{U}}}{\mathrm{d}t}. \quad \text{(D.7)}$$

For the quadrilateral finite volume with four edges the second integral on the left-hand side of equation D.5 can be written as

$$\int_{\partial V_{i,j}} \underline{\mathbf{Q}_\mathrm{I}}.\mathbf{n}\mathrm{d}S = \sum_{k=1}^{4} \left(\underline{\mathbf{Q}_\mathrm{I}}\right)_k.\mathbf{S}_k, \quad \text{(D.8)}$$

where $\mathbf{S}_k$ is the area vector for the k^{th} surface. Similarly, the integral on the right-hand side of equation D.5 can be written as

$$\int_{\partial V_{i,j}} \underline{\mathbf{Q}_\mathrm{v}}.\mathbf{n}\mathrm{d}S = \sum_{k=1}^{4} \left(\underline{\mathbf{Q}_\mathrm{v}}\right)_k.\mathbf{S}_k. \quad \text{(D.9)}$$

Thus equation D.5 can now be written as

$$V_{i,j}\frac{\mathrm{d}\overline{\mathbf{U}}}{\mathrm{d}t} + \sum_{k=1}^{4} \left(\underline{\mathbf{Q}_\mathrm{I}}\right)_k.\mathbf{S}_k = \sum_{k=1}^{4} \left(\underline{\mathbf{Q}_\mathrm{v}}\right)_k.\mathbf{S}_k$$

$$\frac{\mathrm{d}\overline{\mathbf{U}}}{\mathrm{d}t} = \frac{1}{V_{i,j}} \left\{ -\sum_{k=1}^{4} \left(\underline{\mathbf{Q}_\mathrm{I}}\right)_k.\mathbf{S}_k + \sum_{k=1}^{4} \left(\underline{\mathbf{Q}_\mathrm{v}}\right)_k.\mathbf{S}_k \right\}. \quad \text{(D.10)}$$

To show how the products $\left(\underline{\mathbf{Q}_\mathrm{I}}\right)_k.\mathbf{S}_k$ and $\left(\underline{\mathbf{Q}_\mathrm{v}}\right)_k.\mathbf{S}_k$ are evaluated for a typical 2D cell or finite volume, let us consider figure D.2.

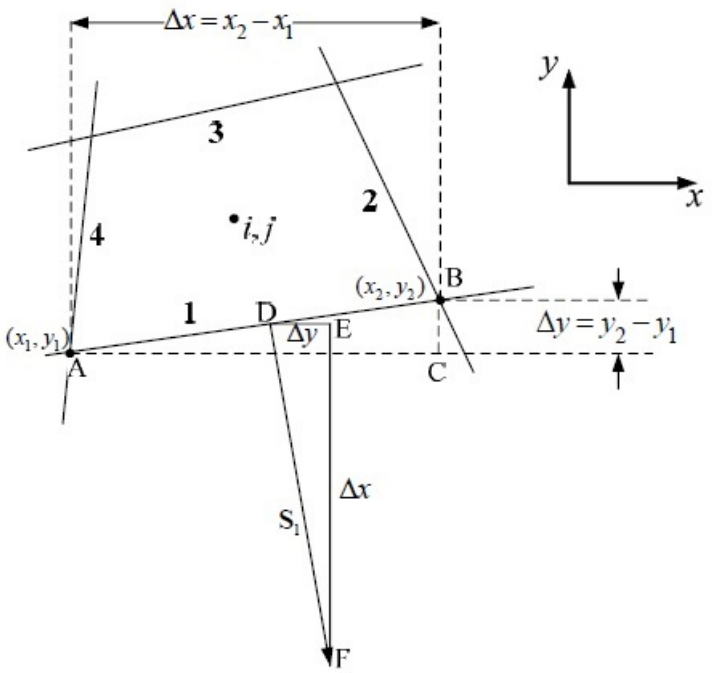

Fig. D.2. Face of a quadrilateral finite volume with components of the surface-area vector.

From figure D.2 it can be seen that

$$\Delta \mathrm{ABC} \cong \Delta \mathrm{DEF},$$
$$\mathrm{DE} = \Delta y,$$
$$\mathrm{EF} = \Delta x.$$

Therefore, the surface vector can be written

$$\begin{aligned} \mathbf{S} &= \mathbf{i}_x \Delta y - \mathbf{i}_y \Delta x \\ &= \mathbf{n}\,|\mathbf{S}| \\ &= \mathbf{n}\sqrt{(\Delta x)^2 + (\Delta y)^2}. \end{aligned} \tag{D.11}$$

The unit outward surface normal can be written as

$$\begin{aligned} \mathbf{n} &= \frac{\mathbf{S}}{|\mathbf{S}|} \\ &= \mathbf{I}_x \frac{\Delta y}{|\mathbf{S}|} - \mathbf{I}_y \frac{\Delta x}{|\mathbf{S}|} \\ &= \mathbf{I}_x n_x + \mathbf{i}_y n_y, \end{aligned}$$
$$\text{where } n_x = \frac{\Delta y}{|\mathbf{S}|}, \tag{D.12a}$$

$$n_y = -\frac{\Delta x}{|\mathbf{S}|}. \tag{D.12b}$$

Dropping the subscript 'k', the terms $\underline{\mathbf{Q}_\mathrm{I}}.\mathbf{S}$ and $\underline{\mathbf{Q}_\mathrm{v}}.\mathbf{S}$ appearing in equation D.10 can also be written as follows:

$$\begin{aligned}\underline{\mathbf{Q}_\mathrm{I}}.\mathbf{S} &= \underline{\mathbf{Q}_\mathrm{I}}.\mathbf{n}\,|\mathbf{S}| \\ &= \mathbf{Q}_{\mathrm{I}\perp}\,|\mathbf{S}|\,, \end{aligned} \tag{D.13a}$$

$$\begin{aligned}\underline{\mathbf{Q}_\mathrm{v}}.\mathbf{S} &= \underline{\mathbf{Q}_\mathrm{v}}.\mathbf{n}\,|\mathbf{S}| \\ &= \mathbf{Q}_{\mathrm{v}\perp}\,|\mathbf{S}|\,, \end{aligned} \tag{D.13b}$$

where $\mathbf{Q}_{\mathrm{I}\perp}$ and $\mathbf{Q}_{\mathrm{v}\perp}$ represent the components of the invicid and viscous flux vectors, respectively, normal to the (straight) cell-face having a unit normal vector $\mathbf{n}$. Therefore substituting equations D.13a and D.13b in equation D.10 we can write the semi-discrete equation on the FVM framework as follows:

$$\begin{aligned}\frac{\mathrm{d}\overline{\mathbf{U}}}{\mathrm{d}t} = \frac{1}{V_{i,j}}\left[-\left\{(\mathbf{Q}_{\mathrm{I}\perp})_1 \,.\, |\mathbf{S}_1| + (\mathbf{Q}_{\mathrm{I}\perp})_2 \,.\, |\mathbf{S}_2| + (\mathbf{Q}_{\mathrm{I}\perp})_3 \,.\, |\mathbf{S}_3| + (\mathbf{Q}_{\mathrm{I}\perp})_4 \,.\, |\mathbf{S}_4|\right\}\right] \\ + \frac{1}{V_{i,j}}\left[\left\{(\mathbf{Q}_{\mathrm{v}\perp})_1 \,.\, |\mathbf{S}_1| + (\mathbf{Q}_{\mathrm{v}\perp})_2 \,.\, |\mathbf{S}_2| + (\mathbf{Q}_{\mathrm{v}\perp})_3 \,.\, |\mathbf{S}_3| + (\mathbf{Q}_{\mathrm{v}\perp})_4 \,.\, |\mathbf{S}_4|\right\}\right]. \end{aligned} \tag{D.14}$$

If the fluid velocity is given by $\mathbf{q} = \mathbf{i}_x u + \mathbf{i}_y v$, then velocity normal to the cell-face or the contravariant velocity is

$$u_\perp = \mathbf{q}.\mathbf{n} = (\mathbf{i}_x u + \mathbf{i}_y v).(\mathbf{i}_x n_x + \mathbf{i}_y n_y) = u n_x + v n_y. \tag{D.15}$$

The inviscid flux vectors normal to an edge of a 2D finite volume $\mathbf{Q}_{\mathrm{I}\perp}$ is given by

$$\begin{aligned}\mathbf{Q}_{\mathrm{I}\perp} &= \underline{\mathbf{Q}_\mathrm{I}}.\mathbf{n} \\ &= (\mathbf{i}_x \mathbf{F}_\mathrm{I} + \mathbf{i}_y \mathbf{G}_\mathrm{I})\,.\,(\mathbf{i}_x n_x + \mathbf{i}_y n_y) \\ &= \mathbf{F}_\mathrm{I} n_x + \mathbf{G}_\mathrm{I} n_y \\ &= \begin{bmatrix} \rho u n_x \\ p n_x + \rho u^2 n_x \\ \rho v u n_x \\ (p + \rho e_m)\, u n_x \end{bmatrix} + \begin{bmatrix} \rho v n_y \\ \rho u v n_y \\ p n_y + \rho v^2 n_y \\ (p + \rho e_m)\, v n_y \end{bmatrix} \\ &= \begin{bmatrix} \rho\,(u n_x + v n_y) \\ p n_x + \rho u\,(u n_x + v n_y) \\ p n_y + \rho v\,(u n_x + v n_y) \\ (p + \rho e_m)\,(u n_x + v n_y) \end{bmatrix} \end{aligned}$$

$$= \begin{bmatrix} \rho u_\perp \\ p n_x + \rho u u_\perp \\ p n_y + \rho v u_\perp \\ (p + \rho e_m)\, u_\perp \end{bmatrix}. \tag{D.16}$$

Similarly the viscous flux vector normal to a cell-face $\mathbf{Q}_{\mathrm{v}\perp}$ is obtained as follows:

$$\begin{aligned}
\mathbf{Q}_{\mathrm{v}\perp} &= \underline{\mathbf{Q}_{\mathrm{v}}}.\mathbf{n} \\
&= (\mathbf{i}_x \mathbf{F}_{\mathrm{v}} + \mathbf{i}_y \mathbf{G}_{\mathrm{v}}) \,.\, (\mathbf{i}_x n_x + \mathbf{i}_y n_y) \\
&= \mathbf{F}_{\mathrm{v}} n_x + \mathbf{G}_{\mathrm{v}} n_y \\
&= \begin{bmatrix} 0 \\ \tau_{xx} n_x \\ \tau_{xy} n_x \\ \left(u\tau_{xx} + v\tau_{xy} + k\frac{\partial T}{\partial x}\right) n_x \end{bmatrix} + \begin{bmatrix} 0 \\ \tau_{yx} n_y \\ \tau_{yy} n_y \\ \left(u\tau_{yx} + v\tau_{yy} + k\frac{\partial T}{\partial y}\right) n_y \end{bmatrix} \\
&= \begin{bmatrix} 0 \\ \tau_{xx} n_x + \tau_{xy} n_y \\ \tau_{xy} n_x + \tau_{yy} n_y \\ \left(u\tau_{xx} + v\tau_{xy} + k\frac{\partial T}{\partial x}\right) n_x + \left(u\tau_{yx} + v\tau_{yy} + k\frac{\partial T}{\partial y}\right) n_y \end{bmatrix}.
\end{aligned} \tag{D.17}$$

From equations D.3a-D.3e and D.17 it is seen that computation of $\mathbf{Q}_{\mathrm{v}\perp}$ requires the values of u, v, k, μ at the cell-faces, which are obtained by volume-averaging of the corresponding cell-averages from the left and right cells sharing that face. Further, the computation of the stress and heat-flux terms require the gradients of u, v and T across the cell-faces. Appendix E presents two methods, namely, the Green's theorem and the cross-diffusion method for the computation of gradient of a scalar φ across a cell-face.

Appendix E

The Green's theorem and the Cross-Diffusion Method for gradient-computation

Gradient-computation using Green's theorem

Figure E.1 shows a finite volume centered at i, j and surrounded by its neighbouring cells. For a 2D structured grid application, each cell consists of four faces.

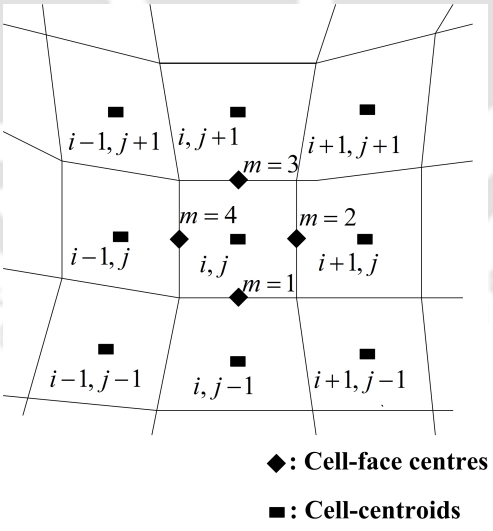

Fig. E.1. A cluster of finite-volume cells for gradient computation.

With reference to figure E.1, the gradients of any variable φ within an arbitrary cell centred at i, j is obtained as follows:

$$\left(\frac{\partial \varphi}{\partial x}\right)_{i,j} = \frac{1}{V_{i,j}} \int_{\partial V_{i,j}} \varphi \mathrm{d}S_x$$

$$\approx \frac{1}{V_{i,j}} \sum_{m=1}^{4} \varphi_m S_{x,m}, \tag{E.1a}$$

$$\left(\frac{\partial \varphi}{\partial y}\right)_{i,j} = \frac{1}{V_{i,j}} \int_{\partial V_{i,j}} \varphi \mathrm{d}S_y$$

$$\approx \frac{1}{V_{i,j}} \sum_{m=1}^{4} \varphi_m S_{y,m}, \tag{E.1b}$$

$$(\underline{\nabla}\varphi)_{i,j} = \mathbf{i}_x \left(\frac{\partial \varphi}{\partial x}\right)_{i,j} + \mathbf{i}_y \left(\frac{\partial \varphi}{\partial y}\right)_{i,j}, \tag{E.1c}$$

where $V_{i,j}$ is the cell-volume and S_x and S_y are the x- and y-components of the surface vector that are obtained as

$$\begin{aligned} S_x &= \Delta y \\ S_y &= -\Delta x \end{aligned} \tag{E.2}$$

in figure D.2 and equation D.11. It may be noted that φ_m is computed by volume-averaging based on the cells that share the m^{th} face. For example when $m = 1$, w.r.t figure E.1, φ_1 is computed as

$$\varphi_1 = \frac{\varphi_{i,j} V_{i,j} + \varphi_{i,j-1} V_{i,j-1}}{V_{i,j} + V_{i,j-1}}. \tag{E.3}$$

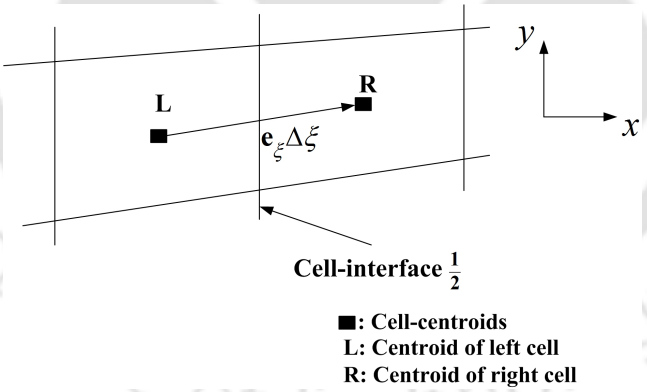

Fig. E.2. Two typical finite volume cells for computing the gradients across a cell face.

Figure E.2 shows a cell-interface $\frac{1}{2}$ between a left cell and a right cell with cell-centroids at L and R, respectively. In order to compute the gradient of φ at the cell-interface the gradients of φ within the left and right cells are obtained by applying equations E.1a-E.1c as follows:

$$\left(\frac{\partial \varphi}{\partial x}\right)_{\mathrm{L/R}} = \left(\frac{1}{V} \sum_{m=1}^{4} \varphi_m S_{x,m}\right)_{\mathrm{L/R}}, \tag{E.4a}$$

$$\left(\frac{\partial\varphi}{\partial y}\right)_{\mathrm{L/R}} = \left(\frac{1}{V}\sum_{m=1}^{4}\varphi_m S_{y,m}\right)_{\mathrm{L/R}}, \tag{E.4b}$$

$$(\underline{\nabla}\varphi)_{\mathrm{L/R}} = \mathbf{i}_x\left(\frac{\partial\varphi}{\partial x}\right)_{\mathrm{L/R}} + \mathbf{i}_y\left(\frac{\partial\varphi}{\partial y}\right)_{\mathrm{L/R}}. \tag{E.4c}$$

A provisional gradient at the midpoint of the cell-interface is obtained by averaging the gradients inside each adjoining control volumes L and R, which is given by [54]

$$\overline{(\underline{\nabla}\varphi)}_{\mathrm{prov}} = \frac{1}{2}\left[(\underline{\nabla}\varphi)_{\mathrm{L}} + (\underline{\nabla}\varphi)_{\mathrm{R}}\right]. \tag{E.5}$$

Now the gradient of φ along the direction from the left to the right cell-centroid is obtained as

$$\left(\frac{\partial\varphi}{\partial\xi}\right)_{\mathrm{LR}} \approx \frac{\varphi_{\mathrm{R}} - \varphi_{\mathrm{L}}}{\Delta\xi}, \tag{E.6}$$

where $\Delta\xi$ represents the distance between the cell-centroids L and R. If $\mathbf{e}_\xi$ is the unit vector in the direction from L and R, then

$$\begin{aligned}\mathbf{e}_\xi &= \frac{\mathbf{r}_{\mathrm{LR}}}{\Delta\xi}\\ &= \mathbf{i}_x\frac{x_{\mathrm{R}} - x_{\mathrm{L}}}{\Delta\xi} + \mathbf{i}_y\frac{y_{\mathrm{R}} - y_{\mathrm{L}}}{\Delta\xi},\end{aligned} \tag{E.7}$$

where $\mathbf{r}_{\mathrm{LR}} = \mathbf{r}_{\mathrm{R}} - \mathbf{r}_{\mathrm{L}}$ and $\mathbf{r}$ in general, represents the position vector of a point. Finally, the gradient across the cell-interface is obtained by

$$\overline{(\underline{\nabla}\varphi)}_{\frac{1}{2}} = \overline{(\underline{\nabla}\varphi)}_{\mathrm{prov}} - \left[\overline{(\underline{\nabla}\varphi)}_{\mathrm{prov}}.\mathbf{e}_\xi - \left(\frac{\partial\varphi}{\partial\xi}\right)_{\mathrm{LR}}\right]\mathbf{e}_\xi. \tag{E.8}$$

Gradient-computation using the cross-diffusion method

Let us consider a face ab as the interface between two cells with their centroids at L and R as shown in figure E.3. The gradient of any variable φ can be written as follows:

$$\underline{\nabla}\varphi = \mathbf{i}_x\frac{\partial\varphi}{\partial x} + \mathbf{i}_y\frac{\partial\varphi}{\partial y} = \mathbf{n}\frac{\partial\varphi}{\partial n} + \mathbf{e}_\eta\frac{\partial\varphi}{\partial\eta}, \tag{E.9}$$

where $\mathbf{n}$ and $\mathbf{e}_\eta$ are the unit vectors normal and tangential to face ab, respectively. If $\mathbf{e}_\xi$ represents the unit vector in the direction LR, then the expressions for $\mathbf{n}$, $\mathbf{e}_\eta$ and $\mathbf{e}_\xi$ are obtained as follows:

$$\mathbf{n} = \mathbf{i}_x\frac{y_{\mathrm{b}} - y_{\mathrm{a}}}{\Delta\eta} - \mathbf{i}_y\frac{x_{\mathrm{b}} - x_{\mathrm{a}}}{\Delta\eta}, \tag{E.10a}$$

$$\mathbf{e}_\eta = \mathbf{i}_x\frac{x_{\mathrm{b}} - x_{\mathrm{a}}}{\Delta\eta} + \mathbf{i}_y\frac{y_{\mathrm{b}} - y_{\mathrm{a}}}{\Delta\eta}, \tag{E.10b}$$

$$\mathbf{e}_\xi = \mathbf{i}_x \frac{x_\mathrm{R} - x_\mathrm{L}}{\Delta\xi} + \mathbf{i}_y \frac{y_\mathrm{R} - y_\mathrm{L}}{\Delta\xi}, \tag{E.10c}$$

$$\text{where } \Delta\eta = \sqrt{(x_\mathrm{b} - x_\mathrm{a})^2 + (y_\mathrm{b} - y_\mathrm{a})^2},$$

$$\Delta\xi = \sqrt{(x_\mathrm{R} - x_\mathrm{L})^2 + (y_\mathrm{R} - y_\mathrm{L})^2}.$$

By using the cross-diffusion term it can be shown that [55]

$$\mathbf{n}.\underline{\nabla}\varphi = \frac{\partial\varphi}{\partial n} = \frac{\mathbf{n}.\mathbf{n}}{\mathbf{n}.\mathbf{e}_\xi}\frac{\varphi_\mathrm{R} - \varphi_\mathrm{L}}{\Delta\xi} - \frac{\mathbf{e}_\xi.\mathbf{e}_\eta}{\mathbf{n}.\mathbf{e}_\xi}\frac{\varphi_\mathrm{b} - \varphi_\mathrm{a}}{\Delta\eta}, \tag{E.11}$$

The first term on the right-hand side of equation E.11 is called the direct-gradient term and the second term is called the cross-diffusion term. The values of φ_a and φ_b are obtained through volume-averaging based on the cells sharing the corresponding nodes.

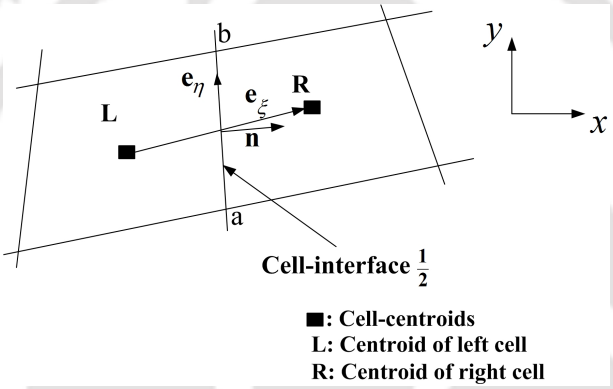

Fig. E.3. The method of cross diffusion terms for gradient computation.

Once $\frac{\partial\varphi}{\partial n}$ is known from equation E.11, the values of $\frac{\partial\varphi}{\partial x}$ and $\frac{\partial\varphi}{\partial y}$ are computed with reference to figure E.4 as follows:

$$\frac{\partial\varphi}{\partial x} = \frac{\partial\varphi}{\partial n}n_x - \frac{\partial\varphi}{\partial\eta}n_y, \tag{E.12a}$$

$$\frac{\partial\varphi}{\partial y} = \frac{\partial\varphi}{\partial n}n_y + \frac{\partial\varphi}{\partial\eta}n_x, \tag{E.12b}$$

where $\frac{\partial\varphi}{\partial\eta} = \frac{\varphi_\mathrm{b} - \varphi_\mathrm{a}}{\Delta\eta}$, $n_x = \frac{y_\mathrm{b} - y_\mathrm{a}}{\Delta\eta}$ and $n_y = -\frac{x_\mathrm{b} - x_\mathrm{a}}{\Delta\eta}$.

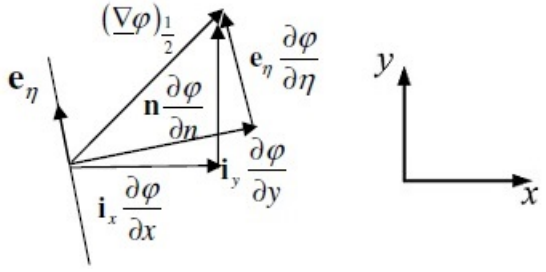

Fig. E.4. Relation among flow gradients along different directions.

Appendix F

Methodology adopted for finding the coefficients of the scaling polynomial

A second-order polynomial f in terms of the boundary-layer sensor is defined as

$$f = a + br_{\mathrm{vg}} + cr_{\mathrm{vg}}^2, \tag{F.1}$$

where the constants a, b and c are evaluated using three boundary conditions. The boundary conditions are:

$$r_{\mathrm{vg}} = 1,\ f = A,\ r_{\mathrm{vg}} = 0,\ f = 1 \text{ and } r_{\mathrm{vg}} = 0.5,\ f = B. \tag{F.2}$$

Depending on the chosen values of A and B one can get different polynomials for f. Many combinations for A and B may be considered. If the following combinations for A and B are chosen, five forms of f are obtained as follows:

Case 1: $A = 0.1$ and $B = 0.5$. On solving for the constants a, b and c one obtains

$$f_1 = 1 - 1.1r_{\mathrm{vg}} + 0.2r_{\mathrm{vg}}^2. \tag{F.3}$$

Case 2: $A = 0.1$ and $B = 0.2$. On solving for the constants a, b and c one obtains

$$f_2 = 1 - 2.3r_{\mathrm{vg}} + 1.4r_{\mathrm{vg}}^2. \tag{F.4}$$

Case 3: $A = 0.05$ and $B = 0.5$. On solving for the constants a, b and c one obtains

$$f_3 = 1 - 1.05r_{\mathrm{vg}} + 0.1r_{\mathrm{vg}}^2. \tag{F.5}$$

Case 4: $A = 0.05$ and $B = 0.1$. On solving for the constants a, b and c one obtains

$$f_4 = 1 - 2.65r_{\text{vg}} + 1.7r_{\text{vg}}^2. \tag{F.6}$$

Case 5: $A = 0.05$ and $B = 0.2$. On solving for the constants a, b and c one obtains

$$f_5 = 1 - 2.25r_{\text{vg}} + 1.3r_{\text{vg}}^2. \tag{F.7}$$

To isolate the effect of limiters from the inherent numerical diffusion of the schemes, the non-dimensionalized temperature profiles at the trailing edge of the plate are computed by the first-order-accurate AUSM, DRLLF ($\delta = 0.5$) and DRLLFV schemes using the polynomials f_1, f_2, f_3, f_4 and f_5. From section 4.2, it is seen that a scheme that produces the minimum smearing of the boundary layer and computes the least value of the adiabatic-wall temperature is the least diffusive.

Figure F.1 compares the temperature profiles at the trailing edge of the flat plate [93] obtained by using the polynomials f_1 and f_2 with the DRLLFV scheme. It shows that polynomial f_2 produces marginally less dissipative results than f_1.

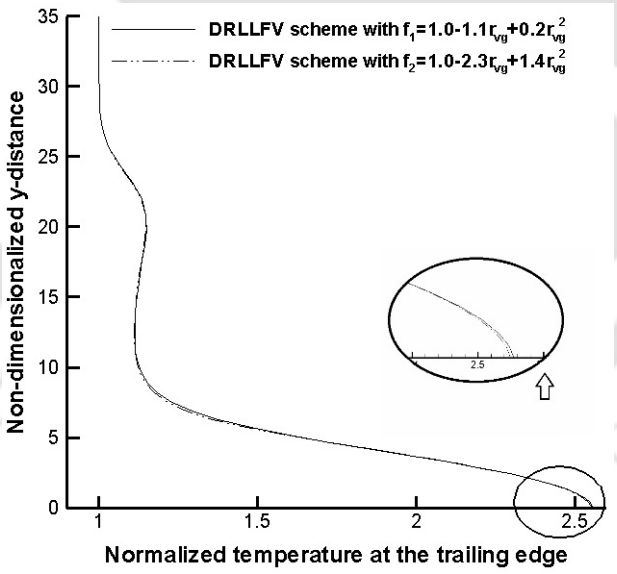

Fig. F.1. Comparison of the temperature profiles at the trailing edge of the adiabatic flat plate obtained by using the polynomials f_1 and f_2 with the DRLLFV scheme.

Figure F.2 compares the temperature profiles obtained by using the first-order DRLLFV scheme with the polynomials f_3, f_4 and f_5. It is seen that the polynomial f_3 produces the most diffused result among the three. The polynomial f_4 causes marginally less dissipation than f_5. However, keeping in mind that the

DRLLFV scheme is to be designed to compute flows at larger Mach numbers, a little accuracy is sacrificed with some anticipated robustness. Hence in figure F.3, the temperature profiles computed by the AUSM scheme, DRLLF ($\delta = 0.5$) and DRLLFV schemes using polynomials f_2 and f_5 are compared. It is seen that the DRLLFV scheme with both the scaling polynomials f_5 and f_2 produces results pretty close the AUSM scheme in terms of the adiabatic-wall temperature. Hence it can be inferred that there may be various combinations of the coefficients in the scaling polynomial f. However, empirically the coefficients used in equation 5.2 produced reasonably accurate results for all the test cases.

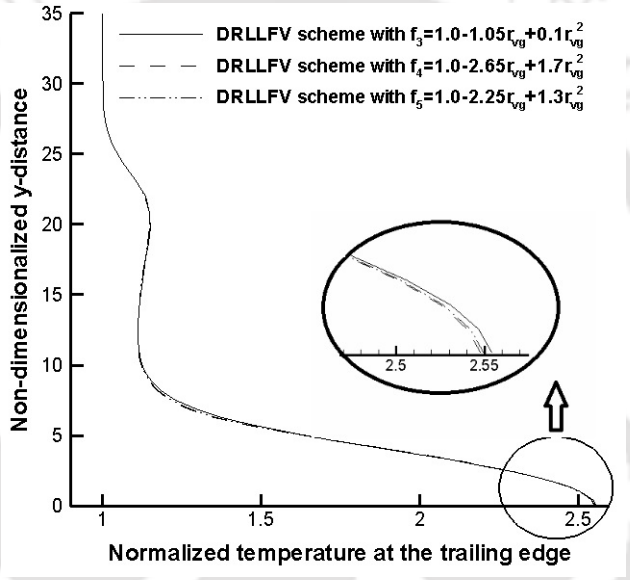

Fig. F.2. Comparison of the temperature profiles at the trailing edge of the adiabatic flat plate obtained by using the polynomials f_3, f_4 and f_5 with the DRLLFV scheme.

As a justification for the coefficients used in equation 5.4 it is to be noted that in case of separated flows, the parameter r_{vg} may attain value larger than 1. In that case, from equation F.7, the scaling polynomial $f_5$becomes negative. This will result in a negative-artificial-viscosity coefficient that may destabilize the computations. In fact physical dissipation tends to increase the tendency for separation. Thus, to maintain the accuracy of the computations, the numerical diffusion should be minimum in the vicinity of separated flows. Hence, inside the separation zone, where $r_{\mathrm{vg}} > 1$, the scaling polynomial f is assigned its minimum possible value, i.e. $f = 0.05$.

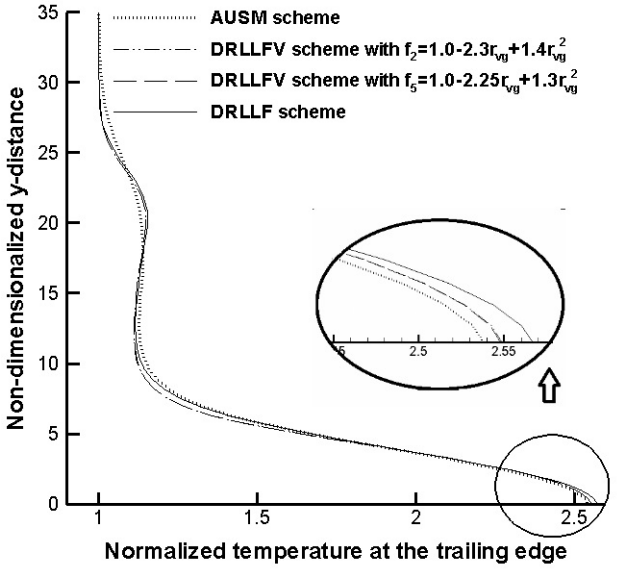

Fig. F.3. Comparison of the temperature profiles at the trailing edge of the flat plate obtained by using AUSM, DRLLF ($\delta = 0.5$) the DRLLFV scheme with the polynomials f_2 and f_5.

Appendix G

Computation of the new shock switch for two-dimensional flows

Let us consider a 2D structured grid-system as shown in figure G.1. The four faces of an arbitrary cell (i,j) are marked as Face-1, Face-2, Face-3 and Face-4. It may be noted that Face-3 and Face-4 of cell (i,j) are the same as Face-1 of cell $(i-1,j)$ and Face-2 of cell $(i,j-1)$, respectively, of course with opposite signs of corresponding unit outward normal vectors. In other words, for each cell, the shock switch is to be computed only for Face-1 and Face-2.

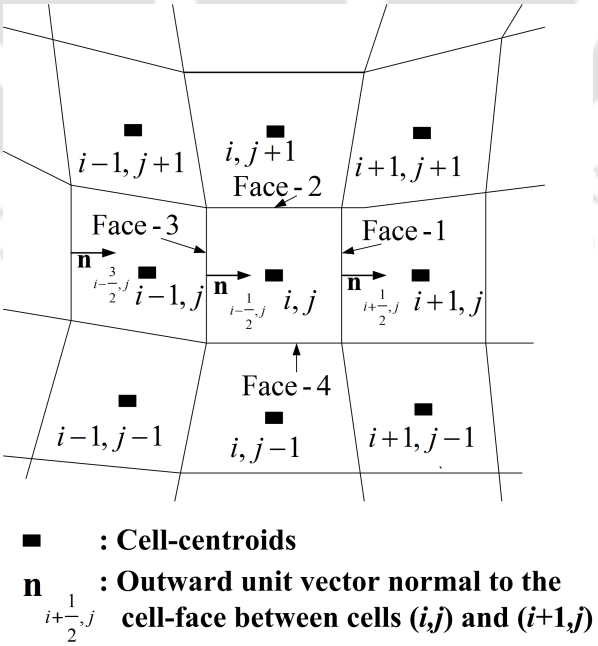

Fig. G.1. A cluster of finite-volume cells for shock-switch computation.

The methodology for computing the shock switch along Face-1 is discussed here. The same methodology can be adopted for Face-2 as well. First, the normalized contravariant Mach number at each cell $\left(\overline{M_\perp}\right)_{i,j}$ is obtained as follows:

$$\left(\overline{M_\perp}\right)_{i,j} = \frac{(M_\perp)_{i,j}}{\max|M|}, \tag{G.1}$$

where $(M_\perp)_{i,j} = \frac{\mathbf{q}_{i,j}.\mathbf{n}_{i+\frac{1}{2},j}}{a_{i,j}}$, $\mathbf{q}_{i,j} = \mathbf{i}_x u_{i,j} + \mathbf{i}_y v_{i,j}$ and $a_{i,j}$ is the speed of sound. The normalized position vector of a cell-centroid $\overline{\mathbf{r}}_{i,j}$ is computed as

$$\overline{\mathbf{r}}_{i,j} = \mathbf{i}_x \overline{x}_{i,j} + \mathbf{i}_y \overline{y}_{i,j}, \tag{G.2}$$

where $\overline{x}_{i,j}$ and $\overline{y}_{i,j}$ are the normalized x- and y-coordinates of the cell-centroids that are obtained as follows:

$$\overline{x}_{i,j} = \frac{x_{i,j}}{\max|x|}, \tag{G.3a}$$

$$\overline{y}_{i,j} = \frac{y_{i,j}}{\max|x|}. \tag{G.3b}$$

Now the gradients of the normalized Mach number across the cell-interfaces $(i-\frac{3}{2},j)$, $(i-\frac{1}{2},j)$ and $(i+\frac{1}{2},j)$ are computed as:

$$\begin{aligned} g_{i-\frac{3}{2},j} &= \frac{\nabla_{i-\frac{3}{2},j}\left(\overline{M_\perp}\right)}{\nabla_{i-\frac{3}{2},j}\left(\overline{\mathbf{r}}\right).\mathbf{n}_{i-\frac{3}{2},j}} \\ g_{i-\frac{1}{2},j} &= \frac{\nabla_{i-\frac{1}{2},j}\left(\overline{M_\perp}\right)}{\nabla_{i-\frac{1}{2},j}\left(\overline{\mathbf{r}}\right).\mathbf{n}_{i-\frac{1}{2},j}} \\ g_{i+\frac{1}{2},j} &= \frac{\nabla_{i+\frac{1}{2},j}\left(\overline{M_\perp}\right)}{\nabla_{i+\frac{1}{2},j}\left(\overline{\mathbf{r}}\right).\mathbf{n}_{i+\frac{1}{2},j}}, \end{aligned} \tag{G.4}$$

where $(i+\frac{1}{2},j)$ represents the cell-face between cells (i,j) and $(i+1,j)$, ∇ is the backward-difference operator, and $\mathbf{n}$ is the unit normal vector to a cell-face. The backward-difference operator for any parameter Θ is given by

$$\nabla_{i+\frac{1}{2},j}(\Theta) = \Theta_{i+1,j} - \Theta_{i,j}. \tag{G.5}$$

By using equations G.4, the gradients $g_{i-\frac{3}{2},j}$, $g_{i-\frac{1}{2},j}$ and $g_{i-\frac{1}{2},j}$ are converted to angles made by the normalized-Mach-number curve with the axis drawn along the cell-face-normal direction as

$$
\begin{aligned}
(\gamma_g)_{i-\frac{3}{2},j} &= \tan^{-1}\left(g_{i-\frac{3}{2},j}\right) \\
(\gamma_g)_{i-\frac{1}{2},j} &= \tan^{-1}\left(g_{i-\frac{1}{2},j}\right) \\
(\gamma_g)_{i+\frac{1}{2},j} &= \tan^{-1}\left(g_{i+\frac{1}{2},j}\right).
\end{aligned}
\tag{G.6}
$$

The angles $(\gamma_g)_{i-\frac{3}{2},j}$, $(\gamma_g)_{i-\frac{1}{2},j}$ and $(\gamma_g)_{i+\frac{1}{2},j}$ are used to find the smoothness-indicating angles using the following expressions:

$$
\begin{aligned}
\alpha_{i-1,j} &= \left|\gamma_{i-\frac{1}{2},j} - \gamma_{i-\frac{3}{2},j}\right| \\
\alpha_{i,j} &= \left|\gamma_{i+\frac{1}{2},j} - \gamma_{i-\frac{1}{2},j}\right|.
\end{aligned}
\tag{G.7}
$$

Finally, the shock switch across the cell-interface $(i+\frac{1}{2},j)$ is calculated using the following equation:

$$
\theta_{i+\frac{1}{2},j} = \min\left[\kappa \sin^2\left\{\max\left(\alpha_{i-1,j}, \alpha_{i,j}\right)\right\}, 1\right]. \tag{G.8}
$$

The suggested value of the parameter κ is 2.5 which is found to work satisfactorily for a wide range of flow-problems.

References

[1] J. von Neumann and R.D. Richtmyer. A method for the numerical calculation of hydrodynamic shocks. *Journal of Applied Physics*, 21:232–237, 1950.

[2] J. D. Anderson, Jr. *Computational Fluid Dynamics: The Basics with Applications*. McGraw-Hill Inc., New York, USA, international edition, 1995.

[3] S. Jaisankar and S.V. Raghurama Rao. A central Rankine-Hugoniot solver for hyperbolic conservation laws. *Journal of Computational Physics*, 228:770–798, 2009.

[4] A. Harten. High resolution schemes for hyperbolic conservation laws. *Journal of Computational Physics*, 49:357–393, 1983.

[5] A. Jameson. Analysis and design of numerical schemes for gas dynamics, 1: artificial diffusion, upwind biasing, limiters and their effect on accuracy and multigrid convergence. *International Journal of Computational Fluid Dynamics*, 4(3-4):171–218, 1995.

[6] R. P Dwight. Heuristic a posteriori estimation of error due to dissipation in finite volume schemes and application to mesh adaptation. *Journal of Computational Physics*, 227(5):2845–2863, 2008.

[7] M.S. Liou and C. J. Steffen, Jr. A new flux splitting scheme. *Journal of Computational Physics*, 107:23–39, 1993.

[8] B. van Leer. Flux vector splitting for the 1990s. In *Proceedings of Computational Fluid Dynamics Symposium on Aero-propulsion, NASA*, pages 203–214, 1991.

[9] C. B. Laney. *Computational Gasdynamics*. Cambridge University Press, Cambridge, UK, first edition, 1998.

[10] S. K. Godunov. A difference scheme for numerical computation of discontinuous solutions of the equations of hydrodynamics. *Mat. Sbornik*, 47:271–306, 1959.

[11] P. Woodward and P. Colella. The numerical simulation of two-dimensional fluid flow with strong shocks. *Journal of Computational Physics*, 54:115–173, 1984.

[12] J. L. Steger and R.F. Warming. Flux vector splitting of the inviscid gasdynamic equations with application to finite-difference methods. *Journal of Computational Physics*, 40:263–293, 1981.

[13] P. L. Roe. Approximate riemann solvers, parameter vectors, and difference schemes. *Journal of Computational Physics*, 43:357–372, 1981.

[14] B. van Leer. Flux vector splitting for Euler equations. In *Lecture notes in Physics*, pages 507–519, New York, 1982. Springer-Verlag.

[15] J.R. Edwards. A low-diffusion flux-splitting scheme for Navier-Stokes calculations. *Computers & Fluids*, 26:635–659, 1997.

[16] Wada Y. and Liou M. S. An accurate and robust flux splitting scheme for shock and contact discontinuities. *SIAM Journal on Scientific Computing*, 18:633–657, 1997.

[17] M. S. Liou. A sequel to ausm, part II: AUSM$^+$-up for all speeds. *Journal of Computational Physics*, 214:137–170, 2006.

[18] R. Radespiel and N. Kroll. Accurate flux vector splitting for shocks and shear layers. *Journal of Computational Physics*, 121:66–78, 1995.

[19] S. Kim, C. Kim, O. Rho, and S. K. Hong. Cures for the shock instability: Development of a shock-stable Roe scheme. *Journal of Computational Physics*, 185:342–374, 2003.

[20] K. H. Kim, C. Kim, and O. Rho. Methods for the accurate computations of hypersonic flows: I. AUSMPW+ scheme. *Journal of Computational Physics*, 174, 2001.

[21] B. van Leer. Upwind and high-resolution methods for compressible flow: From donor cell to residual distribution schemes. *Communications in Computational Physics*, 1:192–206, 2006.

[22] P. D. Lax. Weak solutions of nonlinear hyperbolic equations and their numerical computation. *Communications on Pure and Applied Mathematics*, 7:159–193, 1954.

[23] P. D. Lax and B. Wendroff. Systems of conservation laws. *Communications on Pure and Applied Mathematics*, 13:217–237, 1960.

[24] V. V. Rusanov. Calculation of interaction of non-steady shock waves with obstacles. *Journal of Computational Mathematics and Physics*, 1:267–279, 1961.

[25] R.W. MacCormack. The effect of viscosity in hypervelocity cratering. In *AIAA Paper 69-354*, 1969.

[26] B. van Leer. Towards the ultimate conservative difference scheme. II. Monotonicity and conservation combined in a second-order scheme. *Journal of Computational Physics*, 14:361–370, 1974.

[27] P. K. Sweby. High resolution schemes using flux limiters for hyperbolic conservation laws. *SIAM Journal on Numerical Analysis*, 21:995–1011, 1984.

[28] S. Osher and S. Chakravarthy. High resolution schemes and the entropy condition. *SIAM Journal on Numerical Analysis*, 21:955–984, 1984.

[29] H. C. Yee. Construction of explicit and implicit symmetric TVD schemes and their applications. *Journal of Computational Physics*, 68:151–179, 1987.

[30] J.P. Boris and D.L. Book. Flux-corrected transport. I. SHASTA, a fluid transport algorithm that works. *Journal of Computational Physics*, 11:38–69, 1973.

[31] S.T. Zalesak. Fully multidimensional flux-corrected transport algorithms for fluids. *Journal of Computational Physics*, 31:335–362, 1979.

[32] A. Harten and G. Zwas. Self-adjusting hybrid schemes for shock computations. *Journal of Computational Physics*, 9:568–583, 1972.

[33] A. Harten and G. Zwas. Switched numerical shuman filters for shock calculations. *Journal of Engineering Mathematics*, 6:207–216, 1972.

[34] A. Harten. The artificial compression method for computation of shocks and contact discontinuities. III. Self-adjusting hybrid schemes. *Mathematics of Computation*, 32:363–389, 1978.

[35] A. Jameson, W. Schmidt, and E. Turkel. Numerical solutions of the Euler equations by finite volume methods using Runge-Kutta time stepping schemes. In *AIAA Paper 81-1259*, 1981.

[36] M. Khoshab, A.A. Dehghan, V. Esfahanian, and H.M Darian. Numerical assessment of a shock-detecting sensor for low dissipative high-order simulation of shock-vortex interactions. *International Journal for Numerical Methods in Fluids*, 77:18–42, 2015.

[37] J. Peng and Y. Shen. A novel weighting switch function for uniformly high-order hybrid shock-capturing schemes. *International Journal for Numerical Methods in Fluids*, DOI:10.1002/fld.4285, 2016.

[38] B. van Leer. Towards the ultimate conservative difference scheme. V. A second-order sequel to Godunov's method. *Journal of Computational Physics*, 32:101–16, 1979.

[39] V. Venkatakrishnan. Convergence to steady-state solutions of the Euler equations on unstructured grids with limiters. *Journal of Computational Physics*, 118:120–130, 1995.

[40] S. Jaisankar and S. V. Raghurama Rao. Diffusion regulation for Euler solvers. *Journal of Computational Physics*, 221:577–599, 2007.

[41] S. Jaisankar and T. S. Sheshadri. Directional diffusion regulator (DDR) for some numerical solvers of hyperbolic conservation laws. *Journal of Computational Physics*, 233:83–99, 2013.

[42] A. Kurganov and Y. Liu. New adaptive artificial viscosity method for hyperbolic systems of conservation laws. *Journal of Computational Physics*, 231:8114–8132, 2012.

[43] E.F. Toro and M.E. Vázquez-Cendón. Flux splitting schemes for the Euler equations. *Computers & Fluids*, 70:1–12, 2012.

[44] W. Xie, H. Li, Z. Tian, and S. Pan. A low diffusion flux splitting method for inviscid compressible flows. *Computers & Fluids*, 112:83–93, 2015.

[45] C.L. Rumsey, P.L. Roe, D.W. Levy, K.G. Powell, and B. van Leer. A multidimensional flux function with applications to the Euler and Navier-Stokes equations. *Journal of Computational Physics*, 105:306–323, 1993.

[46] H. Nishikawa and K. Kitamura. Very simple, carbuncle-free, boundary-layer-resolving, rotated-hybrid Riemann solvers. *Journal of Computational Physics*, 227:2560–2581, 2008.

[47] L.M. Mesaros. *Multi-dimensional fluctuation splitting schemes for the Euler equations on unstructured grids*. PhD thesis, University of Michigan, 1995.

[48] R. Abgrall and D.D. Santis. Linear and non-linear high order accurate residual distribution schemes for the discretization of the steady compressible Navier-Stokes equations. *Journal of Computational Physics*, 283:329–359, 2015.

[49] D. S. Balsara. Multidimensional HLLE Riemann solver: Application to Euler and Magnetohydrodynamic flows. *Journal of Computational Physics*, 229:1970–1993, 2010.

[50] D. S. Balsara. A two-dimensional HLLC Riemann solver for conservation laws: Application to Euler and Magnetohydrodynamic flows. *Journal of Computational Physics*, 231:7476–7503, 2012.

[51] D. S. Balsara, M. Dumbser, and R. Abgrall. Multidimensional HLLC Riemann solver for unstructured meshes-with application to Euler and MHD flows. *Journal of Computational Physics*, 261:172–208, 2014.

[52] D. S. Balsara. Multidimensional Riemann problem with self-similar internal structure. Part I-Application to hyperbolic conservation laws on structured meshes. *Journal of Computational Physics*, 277:163–200, 2014.

[53] M. Dumbser and D. S. Balsara. A new efficient formulation of the HLLEM Riemann solver for general conservative and non-conservative hyperbolic systems. *Journal of Computational Physics*, 304:275–319, 2016.

[54] J. Blazek. *Computational Fluid Dynamics: Principles and Applications*. Elsevier, Kidlington, Oxford, UK, first edition, 2001.

[55] H. K. Versteeg and W. Malalasekera. *An Introduction to Computational Fluid Dynamics The Finite Volume Method*. Pearson, Harlow. England, second edition, 2009.

[56] D. D. Knight. *Elements of Numerical Methods for Compressible Flows*. Cambridge University Press, New York. USA, first edition, 2006.

[57] W. K. Anderson, J. L. Thomas, and B. van Leer. Comparison of finite volume flux vector splittings for the Euler equations. *AIAA Journal*, 24:1453–1460, 1986.

[58] P. Colella and P. Woodward. The piecewise parabolic method (PPM) for gas-dynamical simulations. *Journal of Computational Physics*, 54:17–201, 1984.

[59] A. Harten and S. Osher. Uniformly high-order accurate nonoscillatory schemes. I. *SIAM Journal on Numerical Analysis*, 24:279–309, 1987.

[60] A. Harten, B. Engquist, S. Osher, and S. R. Chakravarthy. Uniformly high order accurate essentially non-oscillatory schemes. Ill. *Journal of Computational Physics*, 71:231–303, 1987.

[61] T.J. Barth and D.C Jespersen. The design and application of upwind schemes on unstructured meshes. In *AIAA Paper 89-0366*, 1989.

[62] C. Hirch. *Numerical Computation of Internal and External Flows. Vol. 2.* John Wiley and Sons, Chichester, England, second edition, 1998.

[63] G.D. van Albada, B. van Leer, and W. W. Roberts. A comparative study of computational methods in cosmic gas dynamics. *Astronomy and Astrophysics*, 108:76–84, 1982.

[64] P. L. Roe. Characteristic-based schemes for the Euler equations. *Annual Review on Fluid Mechanics*, 18:337–365, 1986.

[65] G. A. Sod. A survey of several finite difference methods for systems of non-linear hyperbolic conservation laws. *Journal of Computational Physics*, 27:1–31, 1978.

[66] G. C. Zha. Numerical tests of upwind scheme performance for entropy condition. *AIAA Journal*, 37:1005–1007, 1999.

[67] G. C. Zha and Z. Huy. Calculation of transonic internal flows using an efficient high resolution upwind scheme. In *AIAA Paper 2004-1097*, 2004.

[68] J. D. Anderson, Jr. *Modern Compressible Flow with Historical Perspective.* McGraw-Hill Inc., New York, USA, third edition, 2002.

[69] J. D. Anderson, Jr. *Hypersonic and High Temperature Gas Dynamics.* American Institute of Aeronautics and Astronautics, Reston, Virginia, second revised edition, 2006.

[70] M. S. Liou. Mass flux schemes and connections to shock instability. *Journal of Computational Physics*, 160:623–648, 2000.

[71] M. Pandolfi and D. Ambrosio. Numerical instabilities in upwind methods: Analysis and cures for the "Carbuncle" phenomenon. *Journal of Computational Physics*, 166:271–301, 2001.

[72] M. Dumbser, J. Moschetta, and J. Gressier. A matrix stability analysis of the carbuncle phenomenon. *Journal of Computational Physics*, 197:647–670, 2004.

[73] J. C. Tannehill and P. H. Mugge. Improved curve fits for the thermodynamic properties of equilibrium air suitable for numerical computations using time-dependent or shock-capturing methods. In *NASA, CR-2470*, 1974.

[74] S. M. Deshpande. Boltzmann schemes for continuum gas dynamics. *Sadhana*, 18:405–430, 1993.

[75] H.O. Kreiss. Initial boundary value problems for hyperbolic systems. *Communications in Pure and Applied Mathematics*, 23:277–298, 1970.

[76] K. A. Hoffmann and S. T. Chiang. *Computational Fluid Dynamics, Vol 2*. Engineering Education System, Wichita, Kansas, USA, fourth edition, 2000.

[77] R. Kumar and A. K. Dass. Aspects of computation of hypersonic flow over blunt bodies. In *Proceedings of the 4th International and 37th National Conference on Fluid Mechanics and Fluid Power, IIT Madras, Paper ID FMFP10-HS-04*, 2010.

[78] E.R.G. Eckert. Survey of heat transfer at high speeds. In *WADC Technical Report, 54-70*, 1954.

[79] S.K. Aliabadi, S. E. Ray, and T. E. Tezduyar. SUPG finite element computation of viscous compressible flows based on the conservation and entropy variables formulations. *Commputational Mechanics*, 11:300–312, 1993.

[80] A. D. Savelyev. Numerical simulation of laminar viscous supersonic flow past a two-dimensional cavity. *Fluid Dynamics*, 29:759–764, 1994.

[81] D. Drikakis and F. Durst. A numerical study of the viscous supersonic flow past a flat plate at large angles of incidence. *Physics of Fluids (1994-present)*, 6:1553–1573, 1994.

[82] K. Aoki and K. Kanba S. Takata. Numerical analysis of a supersonic rarefied gas flow past a flat plate. *Physics of Fluids (1994-present)*, 9:1144–1161, 1997.

[83] V. Deshpande, S. Eshpuniani, and S. Sanghi. Computation of supersonic flow over a flat plate with moving protrusion. In *Proceedings of the 4th International and 37th National Conference on Fluid Mechanics and Fluid Power, IIT Madras, Paper ID FMFP10-HS-01*, 2010.

[84] Q. Abbas and J. Nordström. Weak versus strong no-slip boundary conditions for the Navier-Stokes equations. *Engineering Applications of Computational Fluid Mechanics*, 4:29–38, 2010.

[85] D. Arnal and O. Vermeersch. Compressibility effects on laminar-turbulent boundary layer transition. *International Journal of Engineering Systems Modelling and Simulation*, 3:26–35, 2011.

[86] P. Tsoutsanis, A. F. Antoniadis, and D. Drikakis. WENO schemes on arbitrary unstructured meshes for laminar, transitional and turbulent flows. *Journal of Computational Physics*, 256:254–276, 2014.

[87] B. John and V. Kulkarni. Numerical assessment of correlations for shock wave boundary layer interaction. *Computers & Fluids*, 90:42–50, 2014.

[88] S. Matsuyama. Performance of all-speed AUSM-family schemes for DNS of low Mach number turbulent channel flow. *Computers & Fluids*, 91:130–143, 2014.

[89] P. S. Iyer, S. Muppidi, and K. Mahesh. Boundary layer transition in high-speed flows due to roughness. In *AIAA Paper 2012-1106*, 2012.

[90] J. Fang, Z. Li, and L. Lu. An optimized low-dissipation monotonicity-preserving scheme for numerical simulations of high-speed turbulent flows. *Journal of Scientific Computing*, 56:67–95, 2013.

[91] L. Xu and P. Weng. High order accurate and low dissipation method for unsteady compressible viscous flow computation on helicopter rotor in forward flight. *Journal of Computational Physics*, 258:470–488, 2014.

[92] R. Kannan and Z. Wang. Improving the high order spectral volume formulation using a diffusion regulator. *Communications in Computational Physics*, 12:247–260, 2012.

[93] J. Tu, G.H. Yeoh, and C. Liu. *Computational Fluid Dynamics: A Practical Approach*. Butterworth-Heinemann, Burlington, USA, first edition, 2007.

[94] A. Jayantha and I.W. Turner. A comparison of gradient approximations for use in finite-volume computational models for two-dimensional diffusion equations. *Numerical Heat Transfer: Part B: Fundamentals*, 40:367–390, 2001.

[95] D. R. Chapman, D. M. Kuehn, and H.K. Larson. Investigation of separated flows in supersonic and subsonic streams with emphasis on the effect of transition. In *NACA TN 3869, NACA Rep. 1356*, 1957.

[96] D. Needham and J. Stollery. Boundary layer separation in hypersonic flow. In *3rd and 4th Aerospace Sciences Meeting*, 1966.

[97] M.S. Holden and J.R. Moselle. Theoretical and experimental studies of the shock wave-boundary layer interaction on compression surfaces in hypersonic flow. In *ARL 70-0002, Aerospace Research Laboratories*, 1970.

[98] M. C. Coet, B. Chanetz, and J.M. Delery. Shock-wave boundary layer interaction with entropy layer effect in hypersonic flow. In *ONERA, Colloque sur les Ecoulements Hypersoniques*, 1992.

[99] M.S. Holden. Boundary-layer displacement and leading-edge bluntness effects on attached and separated laminar boundary layers in a compression corner. part I: Theoretical study. *AIAA Journal*, 8:2179–2188, 1970.

[100] M. S. Holden. Boundary-layer displacement and leading-edge bluntness effects on attached and separated laminar boundary layers in a compression corner. II-Experimental study. *AIAA Journal*, 9:84–93, 1971.

[101] D. Rizzetta and K. Mach. Comparative numerical study of hypersonic compression ramp flows. In *AIAA Paper 89-1877*, 1989.

[102] B. John, V. N. Kulkarni, and G. Natarajan. Shock wave boundary layer interactions in hypersonic flows. *International Journal of Heat and Mass Transfer*, 70:81–90, 2014.

[103] T. Cebeci, J.P. Shao, F. Kafyeke, and E. Laurendeau. *Computational Fluid Dynamics for Engineers*. Horizons Publishing Inc., Long Beach, California, first edition, 2005.

[104] B. John. *Numerical Investigations of Shock Wave Boundary Layer Interaction in Hypersonic Flows*. PhD thesis, Indian Institute of Technology Guwahati, India, 2014.

[105] E.R. Van Driest. Investigation of laminar boundary layer in compressible fluids using the Crocco method. In *NACA Technical Note 2597*, 1952.

[106] G. Puppo. Numerical entropy production on shocks and smooth transitions. *Journal of Scientific Computing*, 17:263–271, 2002.

[107] R. C. Swanson, R. Radespiel, and E. Turkel. On some numerical dissipation schemes. *Journal of Computational Physics*, 147:518–544, 1998.

[108] M. Marini. Effects of flow and geometry parameters on shock wave-boundary layer interaction in hypersonic flow. In *AIAA Paper*, pages 319–329, 1998.

[109] F. Grasso and M. Marini. Analysis of hypersonic shock wave laminar boundary layer interaction phenomena. *Computers & Fluids*, 25:561–581, 1996.

[110] R.W. MacCormack and B.S. Baldwin. A numerical method for solving the navier-stokes equations with application to shock boundary layer interactions. In *AIAA Paper 75-0001*, 1975.

[111] R.C. Swanson and E. Turkel. On central-difference and upwind schemes. *Journal of Computational Physics*, 101:292–306, 1992.

[112] H.C. Yee, N.D. Sandham, and M.J. Djomehri. Low-dissipative high-order shock-capturing methods using characteristic-based filters. *Journal of Computational Physics*, 150:199–238, 1999.

[113] B. Sjögreen and H.C. Yee. Multiresolution wavelet based adaptive numerical dissipation control for high order methods. *Journal of Scientific Computing*, 20:211–255, 2004.

[114] L.V. Yu, C.S. Yee, and I. Matthias. An entropy-residual shock detector for solving conservation laws using high-order discontinuous galerkin methods. *Journal of Computational Physics*, 322:448–472, 2016.

[115] M. Brio, A.R. Zakharian, and G.M. Webb. Two-dimensional Riemann solver for Euler equations of gas dynamics. *Journal of Computational Physics*, 167:177–195, 2001.

[116] C.W. Schulz-Rinne, J.P. Collins, and H.M. Glaz. Numerical solution of the riemann problem for two-dimensional gas dynamics. *SIAM Journal on Scientific Computing*, 14:1394–1414, 1993.

Publications from the present PhD work

International Journals

1. P. Kalita, A. K. Dass, and A. Sarma. Effects of numerical diffusion on the computation of viscous supersonic flow over a flat plate. *International Journal of Applied and Computational Mathematics*, Springer, 2:663-678, 2016.

2. P. Kalita and A. K. Dass. A diffusion-regulated scheme for the compressible Navier–Stokes equations using a boundary-layer sensor, *Computers and Fluids*, Elsevier, 129:91-100, 2016.

3. P. Kalita and A. K. Dass. A novel hybrid approach with multidimensional-like effects for compressible flow computations, *Journal of Computational Physics*, Elsevier, 340:55-68, 2017.

International/National Conferences

1. P. Kalita and A. K. Dass. Aspects of Computation of 2D Planar and Axisymmetric High-Speed Flows through Nozzles. *4th International Congress on Computational Mechanics and Simulation, Indian Institute of Technology Hyderabad, India*, 2012.

2. P. Kalita and A. K. Dass. Computation of high speed flows using diffusion regulation. *Proceedings of the 40th National Conference on Fluid Mechanics and Fluid Power, National Institute of Technology, Hamirpur, India, pp. 1231-1239*, 2013.

3. P. Kalita, R. Kumar and A. K. Dass. Aspects of a diffusion-regulated scheme applied to hypersonic flow. *Proceedings of the 5th International and 41st National Conference on Fluid Mechanics and Fluid Power, Indian Institute of Technology Kanpur, Paper ID FMFP14-C-400*, 2014.

4. P. Kalita and A. K. Dass. Effect of numerical diffusion on the computation of hypersonic shock wave boundary layer interaction. *Proceedings of International Symposium on Aspects of Mechanical Engineering and Technology for Industry, NERIST, Arunachal Pradesh, India, pp. 306-313*, 2014.

5. P. Kalita and A. K. Dass. Effect of limiter on the computation of viscous supersonic flow over a flat plate. *Proceedings of the International Conference on Frontiers in Mathematics, Gauhati University, pp. 135-141*, 2015.